

NASA SPACE ENGINEERING RESEARCH CENTER
FOR UTILIZATION OF LOCAL PLANETARY RESOURCES

**ANNUAL
PROGRESS REPORT
1991**

APR-91/F

Director: T.Triffet, Principal Investigators: K.Ramohalli, J.Lewis

**THE UNIVERSITY OF ARIZONA
4717 E. Ft. Lowell Rd./AML
Tucson, AZ 85712**

Telephone: (602) 322-2304 FAX: (602) 326-0938

**ORIGINAL PAGE
COLOR PHOTOGRAPH
PAGE**

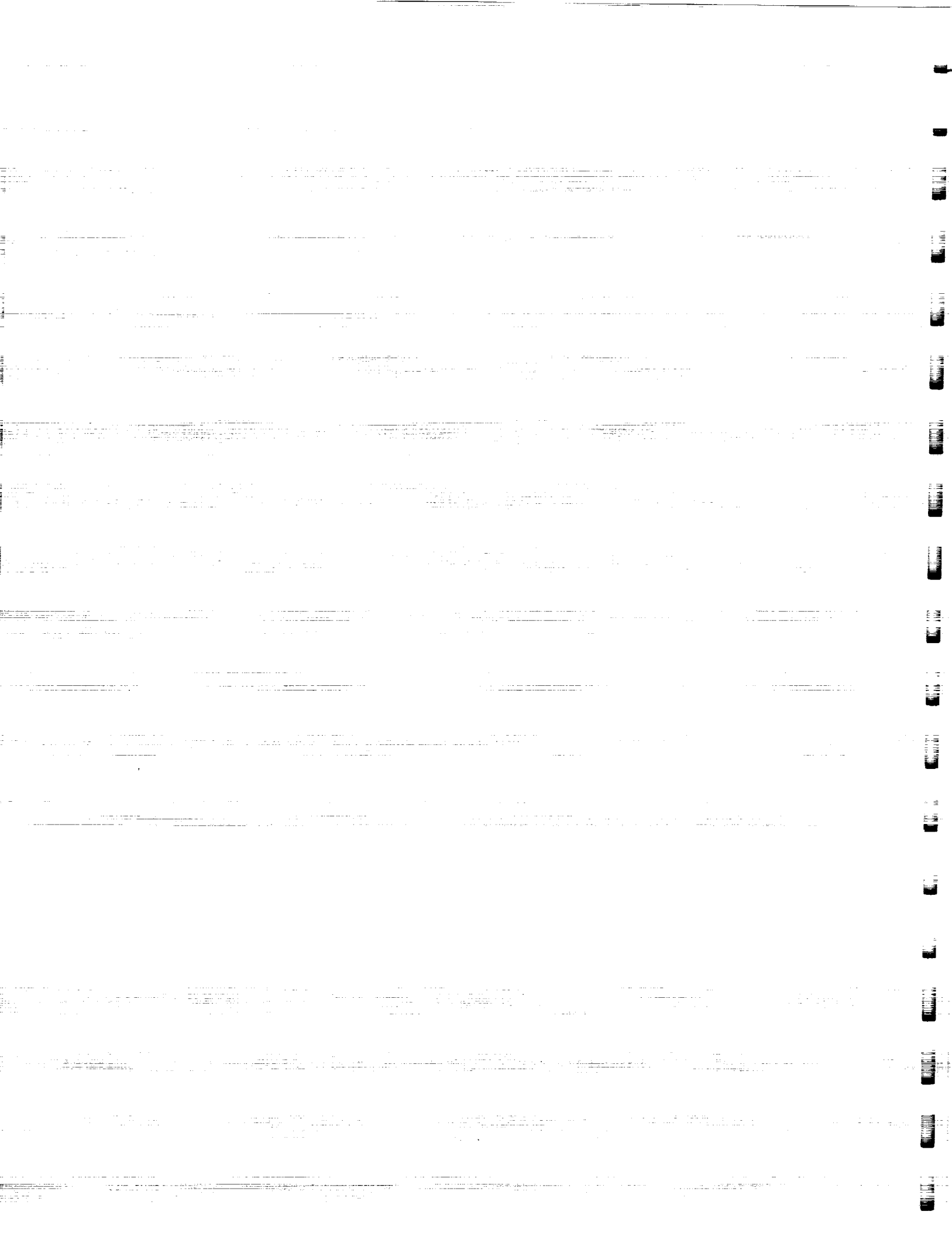


TABLE OF CONTENTS

	Page
Executive Summary.....	v
Publications.....	x

I. PROCESSING OF PROPELLANTS, VOLATILES AND METALS

A. Reduction of Lunar Regolith

Extraction of Volatiles and Metals from Extraterrestrial Materials	
J.S. Lewis.....	IA-1
Production of Oxygen from Lunar Ilmenite.....	IA-9
F. Shadman, Y. Zhao and C. Massieon	
"Cold" Plasma Processing of Local Planetary Ores for Oxygen and	
Metallurgically Important Metals.....	IA-69
D. Bullard and D.C. Lynch	
Innovative Techniques for the Production of Energetic Radicals	
for Lunar Materials Processing Including Photogeneration Via	
Concentrated Solar Energy.....	IA-78
D.E. Osborn and D.C. Lynch	
Oxygen and Iron Production by Electrolytic Smelting	
of Lunar Soil.....	IA-89
R. O. Colson and L.A. Haskin	
Experimental Study of the Electrolysis of Silicate Melts.....	IA-100
R. Keller	

B. Reduction of Carbon Dioxide

Electrochemical Separation of Oxygen from Carbon	
Dioxide.....	IB-1
K.R. Sridhar and P. Kaloupis	
Design and Optimization of Sub-Systems in the Martian Oxygen	
Production Plant.....	IB-23
K.R. Sridhar and V. Iyer	
Full System Engineering Design and Operation of an.....	IB-34
Oxygen Plant	
J. Colvin, P. Schallhorn and K. Ramohalli	
Carbon Monoxide Removal From Electrochemical Cell	
Discharge Gas.....	IB-52
D.C. Lynch, A.H.Cutler and P. Nolan	

C. Reduction of Carbonaceous Materials

Modal Abundance & Dehydration Kinetics of Volatile Bearing Phases in Carbonaceous Chondrites.....	IC-1
J. Ganguly and K. Bose	

II. PRODUCTION OF STRUCTURAL AND REFRACTORY MATERIALS

Processing of Glass-Ceramics from Lunar Resources.....	II-1
B.D. Fabes, W.H. Polsl, and D. Allen	
Design of High Temperature Seals.....	II-8
K.R. Sridhar, M. Yalcintas, G. Honea	
Recovery of Precious Metals from Space.....	II-26
H. Freiser and S. Muralidharan	
Development and Mechanical Properties of Structural Materials from Lunar Simulant.....	II-39
C.S. Desai	
Large Area Solar Cells from Lunar Materials.....	II-49
P. Calvert, B. Fabes, J. Hodges and J. Corley	
Feasibility of Solar Concentrator Fabrication from Indigenous Lunar and Martian Materials.....	II-56
SAIC/R. Davenport	

III. RESOURCE DISCOVERY AND CHARACTERIZATION

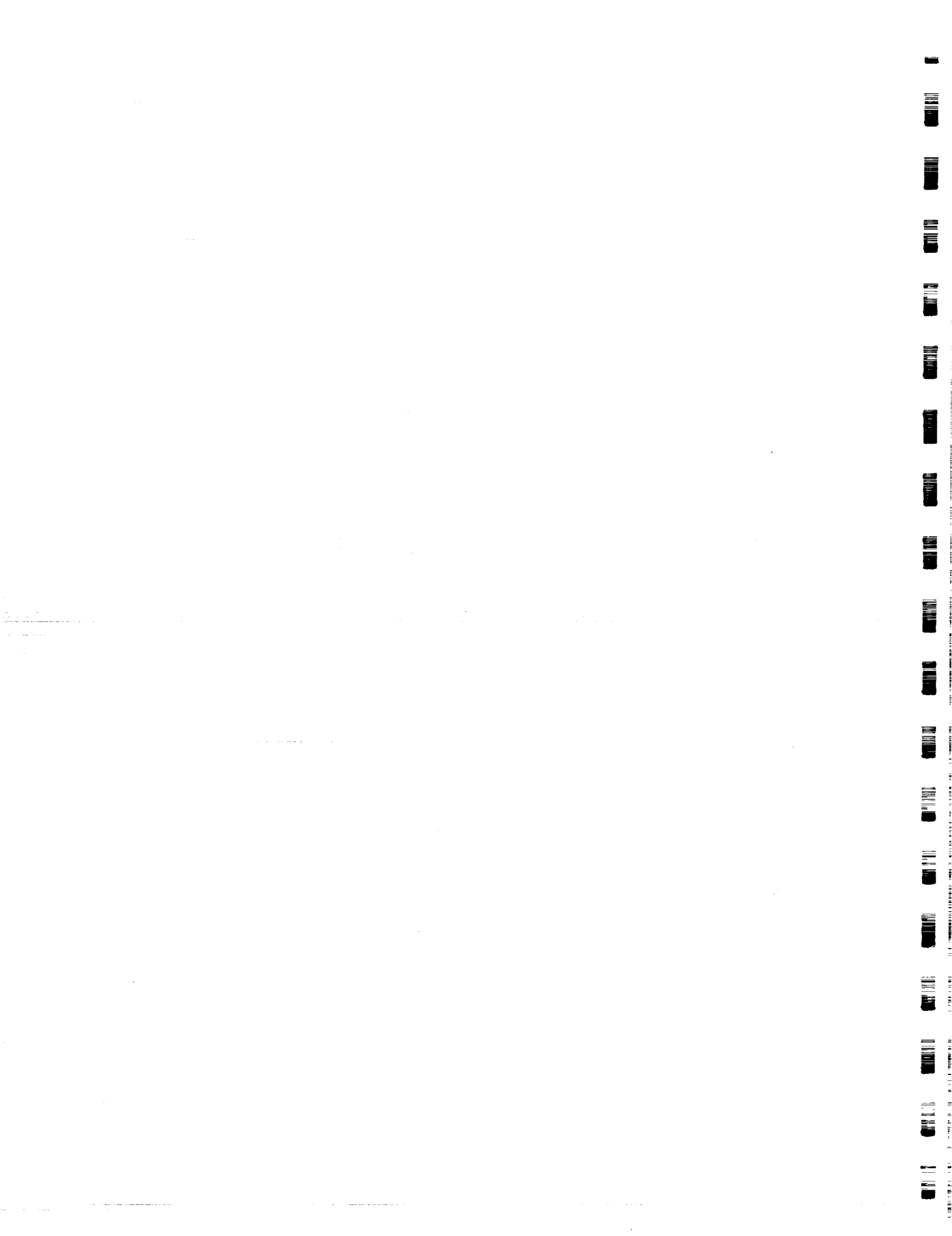
Continuous Monitoring of the Lunar or Martian Subsurface Using On-Board Pattern Recognition and Neural Processing of Rover Geophysical Data.....	III-1
C.E. Glass and R.V. Boyd	
Determination of Lunar Ilmenite Abundances from Remotely Sensed Data.....	III-20
R.B. Singer, S.M. Larson, J.R. Johnson and D.E. Melendrez	
Compositions of Near-Earth Asteroids.....	III-25
L.A. Lebofsky and M.L. Nelson	
Spacewatch Discovery of Near-Earth Asteroids.....	III-30
T. Gehrels	
Abundance of He-3 and Other Solar-Wind-Derived Volatiles in Lunar Soil.....	III-35
T. Swindle	

IV. SYSTEM AUTOMATION AND OPTIMIZATION

Further Development of A Figure-of-Merit for Space Missions.....	IV-1
B. Preiss and K.R. Ramohalli	
Automation and Control of an Oxygen Extraction Plant.....	IV-11
L.Schooley, F.Cellier, A.Doser, G.Farrenkopf, J.Kim, Y.Pan, and B.Williams	
Quantitative Simulation of Extraterrestrial Engineering Devices.....	IV-31
A. Arabyan, P.E. Nikraves and T.L. Vincent	
In-Situ Materials Processing Systems and Bioregenerative	
Life Support Systems Interrelationships.....	IV-35
R. Frye and G.V. Mignon	

V. DATABASE DEVELOPMENT

The Steward Observatory Asteroid	
Relational Database.....	V-1
Mark V. Sykes and E.M. Alvarez del Castillo	
Near-Earth Asteroids: Observer Alert Network and	
Database Analysis.....	V-6
D.R. Davis and C.R. Chapman	



EXECUTIVE SUMMARY

EXECUTIVE SUMMARY

1991

Because of a change in the NASA funding cycle, the present reporting period covers only the six months from March to September 1991. Nevertheless, remarkable progress was made in a number of areas, some of the most noteworthy of which are:

Engineering operation of a breadboard $\text{CO}_2 \rightarrow \text{O}_2$ demonstration plant that produced over 10 grams of oxygen per day during several runs of over 100 hours each with a single electrolytic cell. Complete automation of controls, monitoring of various inputs/outputs and critical internal variables, diagnostics, and emergency shutdown in an orderly manner were also included. Moreover, 4-cell and 16-cell units, capable of much higher rates of production, were assembled and tested.

Demonstration of a 200 % increase in the carbothermal reduction of ilmenite through vapor deposition of carbon layers on particles of that material.

Demonstration of the deposition of strong iron films from carbonyl chemical vapor deposition, establishing the crucial role of additive gases in governing the process.

Discovery of an apparent 800% increase in the conversion rates of a modified ilmenite simulant in a plasma-augmented reactor, including direct enhancement by solar radiation absorption.

Proof that test specimens of lunar soil with small amounts of metallic additives, recrystallized at moderate temperatures, exhibit an improvement of several orders of magnitude in ductility/tensile strength.

Experiments establishing the feasibility of producing silicon-based polymers from indigenous lunar materials.

Application of CCD technology to the production of maps of TiO_2 abundance, defining primary ilmenite deposits, on the disk of the full moon.

Attainment of a discovery rate of approximately 3 new near-Earth asteroids per month by Spacewatch, more than doubling the previous global rate.

Coordination of industry and university magma electrolysis investigations in a workshop designed to define remaining problem areas and propose critical experiments.

These, together with the accomplishments of a wide variety of other projects, led by Professor Kumar Ramohalli, PI for Engineering, and Professor John Lewis, PI for Science, are briefly discussed on the following pages.

Full system operation of the breadboard oxygen plant was demonstrated by students led by professor Ramohalli. Extensive data were obtained on the oxygen output, temperature and voltage control of the cell, post-test micro-examination of the uncontaminated cell material, and a host of parameters related to plant efficiency. Another of his graduate students then used these to extend the earlier concept of a Figure-of-Merit for space missions in general, and ISRU/ISMU missions in particular, to develop a systematic optimization methodology.

Proprietary restrictions of the sole industrial supplier of the electrolytic cells required for the $\text{CO}_2 \rightarrow \text{O}_2$ reactor led to a breakthrough in cell production. Significant progress was made in producing yttria-stabilized zirconia cells, and several other alternative types, in-house; and the necessary technologies for leak-proofing electrodes and electrical leads through the ceramic/metal interface were developed.

Concurrently, material selection and cell design were greatly improved by professor Sridhar, who also completed the thermal design of 4-cell and 16-cell assemblies for scale-up, and characterized candidate cell operations in terms of oxygen production rate as a function of voltage, temperature, flow rate and pressure. The 16-cell assembly was shown to require far less than sixteen times the power needed by a single tube to function; and the analysis also suggested operating the reactor at a slightly lower temperature (900°C), which demonstrated remarkable improvements in reliability and life expectancy, though at a slight expense in production rates. This engineering tradeoff was optimized by further experimentation.

Steps were also taken to expand the capabilities of this small pilot plant by adding hydrogen to the CO_2 -rich exhaust stream and interposing, at laboratory bench scale, a Sabatier reactor to produce methane, and a water electrolysis unit to complete the cycle. This work was sponsored by Martin Marietta and further supported by Hamilton Standard through the loan of a full-scale water electrolysis unit, soon to be delivered. In effect, the full range of possibilities available to organic chemistry will then become available, and it is confidently expected that many new products, such as polymers and lubricants, can easily be produced.

Quantitative simulations of the entire pilot plant, capable of automatically calculating changing values of key interface variables, were used by professors Nikraves and Arabyan to guide these advanced designs. The high-resolution graphical software required for the purpose was also developed in-house, and some of the images generated have been selected by NASA Headquarters for inclusion in a forthcoming USERC publication.

Closely related were the studies by Professor Lynch aimed at reducing the compression requirements of carbon dioxide through recycling. Removal of carbon monoxide from the spent stream was shown to be the most efficient way to reclaim the high pressure, high temperature carbon dioxide. A number of ceramic and metallic materials were tested as catalysts for the disproportionation of carbon monoxide to produce solid carbon and carbon dioxide. Ruthenium was examined between 200° and 600°C , and it was shown that saturation occurred within 20 minutes. Copper chloride was identified as another promising catalyst.

Professors Cellier and Schooley completely automated the breadboard oxygen production plant through the use of smart sensors and digital controls. This included emergency procedures - battery backup with graceful shutdown - and the dependability of the system was successfully proven during several thunderstorms which caused power outages. An event-based intelligent controller with time windows was set up to perform fault diagnoses.

Communication protocols were modified to allow remote command/control of the oxygen plant, with a choice of any of several remote VAX/VMS or SUN/UNIX commanders and multiple observers. This will be used to monitor and control the oxygen plant from a campus site six miles distant with no cable connections.

In other of his studies Professor Lynch demonstrated an 800% increase in the conversion rates of ilmenite samples in a plasma augmented reactor. This was achieved with metal ions which have a large cross-section. Also, direct augmentation through solar radiation absorption was demonstrated for the first time, suggesting that ultra-compact reactors may be possible for use in space. Specifically, sixty percent of the TiO_2 was reduced to Ti_2O_3 in 11 minutes, and in the solar UV assisted reaction, significant rate enhancement (60% contrasted with 40% reduction in 60 minutes) was proven between 260°C and 360°C.

In studies independent of the $\text{CO}_2 \rightarrow \text{O}_2$ plant, professor Shadman discovered an increase of more than 200% in the carbothermal reduction of ilmenite after successfully applying a monolayer of carbon to the particles by vapor deposition. Because of the extraordinary potential of the process, this concept has been chosen for incorporation in a demonstration unit that will produce scaled-up quantities of oxygen. A synthetic ilmenite with complete $\text{Fe}^{2+}/\text{Fe}^{3+}$ authenticity, also developed in his laboratory, will be used for the demonstration unit.

Professor Singer continued his investigations into the distribution of lunar titanium dioxide, defining the boundaries of rich ilmenite deposits. By utilizing the charge-coupled device technology now in place, the project will produce the best possible TiO_2 abundance maps.

Continuing his experiments and analyses of the thermodynamics and kinetics of crystallization of simulated lunar glasses, professor Fabes formed large glass monoliths and subjected them to a variety of heat treatments to produce polycrystalline, fine-grained ceramics. For materials of small grain sizes, tensile strengths greater than 300 MPa were demonstrated. Professors Calvert and Fabes also made an excellent start on producing large area solar cells from lunar materials. Siloxane polymers were selected for synthesis and a novel chlorosiloxane polymer was prepared and partly characterized.

Professor Desai obtained valuable new data on creating composites from lunar soil. Test specimens of Minnesota simulant, mixed with small percentages of metallic fibers and recrystallized, were shown to exhibit enhanced ductility arising from increased tensile strength. In related studies SAIC, San Diego, conducted an extensive analysis of the production techniques for solar concentrator dishes utilizing authentically simulated lunar soils and, after demonstrating success for a 14" diameter dish, turned to formulating general principles that could introduce greater economy in energy use.

In a close and fruitful interaction with consultant William C. Jenkin, professor Lewis has addressed the problem of how best to handle iron carbonyl extracted from non-terrestrial ferrous metal alloys-- iron being the dominant constituent of native metals in meteorites and asteroidal fragments found in lunar regolith, the dominant metal in cathode deposits produced by electrolysis of molten lunar silicates, and formed in large quantities during the reduction of lunar ilmenite. Experiments using ammonia, water vapor, and especially carbon dioxide as additives in the process produced direct deposition of thin iron films with desirable physical properties. Further experiments involving lower pressures, outgassing at higher temperatures, and codeposition of iron and nickel are underway.

Also, during this period the efforts of professor Freiser to develop efficient and economical large-scale separation and recovery methods for platinum-group and other precious and strategic metals resulted in the development of a novel process. Centrifugal Partition

Chromatography, as he has named it, promises to be the most efficient separation method known, well-suited for scale-up.

In early August a workshop devoted to magma electrolysis, a possible alternative process for producing volatiles and metals in space, was held in Tucson. Professor Haskin and his colleague Dr. Colson presented the latest results of their continuing research program at Washington University, stressing recently completed calculations of steady-state electrolysis cell compositions, experiments focussed on the solubilities of metals in silicate melts--especially the role of iron, and studies directed toward identifying and determining the behavior of gaseous components at the cathode.

Closely related investigations underway at SERC by professors Lewis and Cutler, at EMEC by Dr. Keller, at Rockwell International by Dr. Waldron and Mr. McCullough, and at the University of North Dakota by Dr. Ness were also described. And in the discussion that followed common problem areas, suggesting critical experiments that should be performed to evaluate the process, were identified. For example, emphasis was placed on closing the system and measuring the quantities of oxygen actually produced at various power and temperature levels. A SERC Workshop Report summarizing these findings will be published in the near future.

Pursuing related aspects of space resource utilization, professor Ganguly performed studies on the modal abundance of volatile-bearing phases in C2 carbonaceous chondrites, and accumulated experimental data on the dehydration kinetics of talc preparatory to development of a computer simulation of volatile release. And professor Swindle, in studies defining the magnitude of systematic variations in solar wind influence with lunar location, generated maps of estimated abundances of valuable solar wind-implanted volatiles such as He-3, hydrogen, carbon and nitrogen.

Of special interest was a new low-level project led by Dr. Mignon of ERL, which explored the interrelationships of these in-space resource utilization processes with life support systems through bioregenerative interactions. A broad spectrum of by-products were examined. It was shown that a high level of synergism exists, and that substantial economy can be achieved through a properly planned match of the ISRU/ISMU activities with life-support systems.

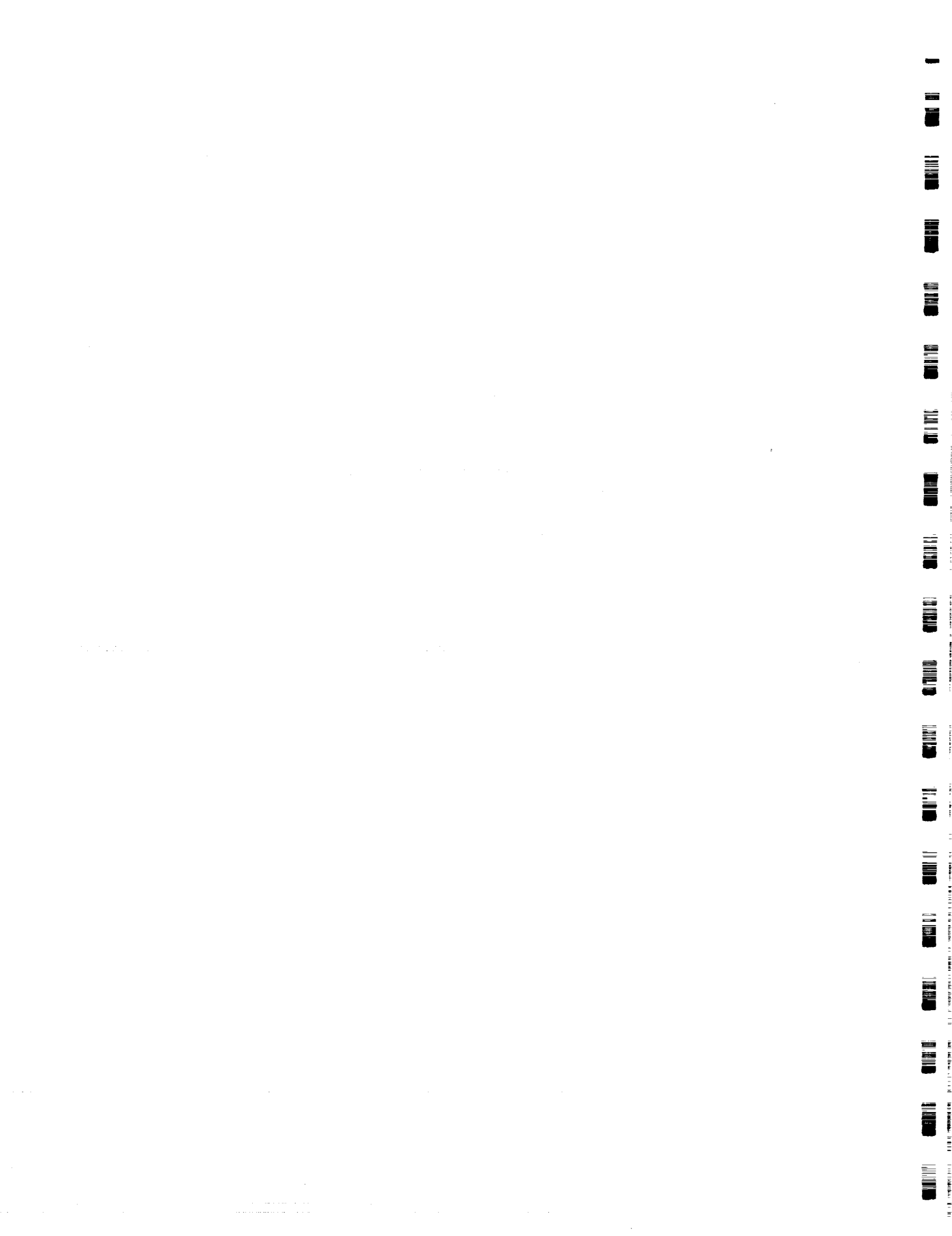
This period also saw the automation of the neural network processing, ground-penetrating radar system developed by professors Glass and Sternberg, with the intention of achieving easy pattern recognition for precisely targeting extraterrestrial mining.

Major successes were also scored by other projects in the SERC exploration program, most notably by professor Gehrels. During this reporting period no less than 15 new near-Earth asteroids were discovered by his spacewatch facility and fully confirmed by other observers around the world. Also, studies conducted by professor Lebofsky to determine whether any such asteroids contain hydrosilicate minerals resulted in a computational model which is now being tested. In close support of this work professor Sykes completed an extensive compilation of the data available on asteroids, and developed a single menu-driven database program and interface for SERC investigators. A browse capability was added as well as a 12,000-entry bibliography.

Theoretical studies of two methods of providing energy for Earth from space were also conducted by professor Lewis and his students: building solar power satellites from asteroidal materials in highly eccentric earth orbit, and returning He-3 from the atmosphere of Uranus for use as a clean fusion fuel. Related studies of transportation system architectures defined three bootstrapping schemes for the return of non-terrestrial propellants and metals to near-Earth space: use of the stations in such orbits as fuel manufacturing sites, near-Earth asteroids as sources of water, and both solar and nuclear thermal "steam rockets" as means of transport.

From the above it will be clear that our program of research has continued to prosper during this reporting period, and that the integration of its engineering and science aspects continues to increase. What may not be apparent is the effect the program is having on science and technology education at the University of Arizona, in particular by preparing outstanding young men and women for careers in space science and engineering. Each of the professors whose work is described employs one or more graduate students as assistants, and often several additional undergraduates -- a total of nineteen of the former and fifteen of the latter in 1991.

Not only do these students contribute significantly to the project work, in a regular seminar series they learn to make technical presentations, and every year one issue of the SERC Newsletter is devoted entirely to technical papers they have written. Remarkably often the result is improved academic performance as well, and a sense of mission not often found in other fields. This we believe to be an equally important aspect of the Center's program.



PUBLICATIONS

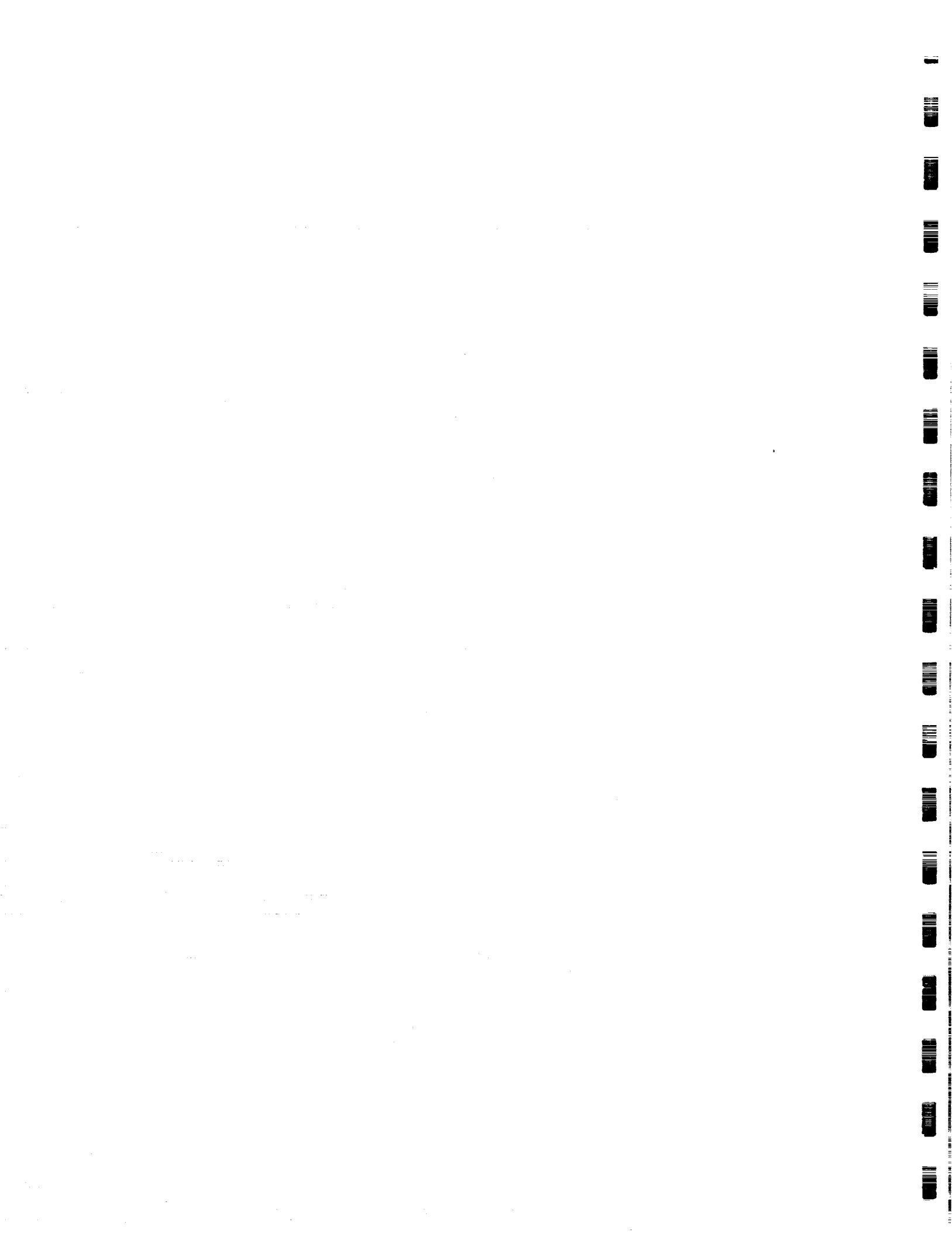


SERC/culpr PUBLICATIONS

The following publications of the Center are available without charge to qualified organizations and may be obtained by written request to the Director.

Those marked with an asterisk are finished products featuring overviews for corporate, government and university management, while those preceded by a dash are designed for the primary purpose of attracting potential students. The remainder contain detailed technical information on research and development projects, and are published in simplified form, with standardized binding and slightly non-uniform format, to permit rapid dissemination of results.

*PR-89	Program Brochure 1988-89
*AER-90	Annual Executive Report 1989-90
*Newsletter	Vol.1, Nos. 1-4, 1989-90 Vol.2, Nos. 1-4, 1990-91
- AF-88	Advanced Flyer 1987-88
- CP-88	Center Poster 1987-88
APR-89	Annual Progress Report 1988-89
APR-90	Annual Progress Report 1989-90
APR-91/S	Annual Progress Report 1990-91
APR-91/F	Annual Progress Report 1991
First Annual Symposium on Space Resources of Near-Earth Space 1990	
AIS-89/A	Abstracts
AIS-89	Proceedings
Second Annual Symposium on Resources of Near-Earth Space 1990	
AIS-90/A	Abstracts
WR-89/1	Automation of Extraterrestrial Sources of Oxygen Production Workshop (AESOP) Report
WR-91/1	Magmaelectrolysis of Indigenous Space Materials (MISM) Report
TM-90/1	Mining Lunar Soils for He -3 1990



I. PROCESSING OF PROPELLANTS, VOLATILES AND METALS



A. REDUCTION OF LUNAR REGOLITH



Extraction of Volatiles and Metals from Extraterrestrial Materials

J. S. Lewis

**Lunar and Planetary Laboratory
University of Arizona**

Abstract:

We have made substantial progress in defining desirable transportation system architectures for the use of non-terrestrial volatiles and metals, including a) the delivery of propellants to near-Earth space, b) the refuelling of SEI-type expeditions, c) the construction and resupply of Solar Power Satellite constellations in various Earth orbits, including GEO and Highly Eccentric Earth Orbit (HEEO), and d) the retrieval of large amounts of ^3He for use as a clean fusion fuel on Earth. Laboratory studies of volatilization and deposition of ferrous metal alloys have led to the first successful demonstration of deposition of strong iron films from carbonyl chemical vapor deposition (CVD), showing the crucial role of additive gases in governing the CVD process.

General Research Program

This project includes research into three basic areas: carbonyl processing of nonterrestrial ferrous native metals; prospects for accelerating the development of non-terrestrial sources of energy for Earth using non-terrestrial propellants and structural materials; and transportation system studies on the most efficient return of non-terrestrial materials to near-Earth space for use in large-scale future space activities. In addition, this project includes oversight over SERC science program activities and travel for the purposes of developing research collaborations at other research centers and in industry. These activities are treated separately below.

Gaseous Carbonyl Process

The most important results arising in this project over the past few months have been the result of a close and fruitful interaction with a consultant, William C. Jenkin, who is perhaps the leading developer of carbonyl chemical vapor deposition (CVD) technology in the world. We have been working with him for over a year on the problem of how best to handle iron carbonyl extracted from non-terrestrial ferrous metal alloys. Iron is the dominant constituent (40 to 93%) of native metals found in meteorites and in asteroidal metal fragments found in the lunar regolith. It is also the dominant metal in the metallic cathode deposits produced by electrolysis of molten lunar silicates, and is formed in large quantities and with a rather high degree of purity (99%) during the reduction of lunar ilmenite. Carbonyl extraction of iron from native Fe-Ni alloy has been demonstrated in our own laboratory, but the disposition of the resulting iron pentacarbonyl vapor and liquid is unclear. Iron carbonyl CVD is never used for manufacture of strong metal components because of the tendency to precipitate a very fine-grained powder during thermal decomposition. This iron powder is of exceptional purity and of great metallurgical interest; indeed, it is the source of almost all the analytical-grade iron in the world market. However, the iron powder was something of a disappointment compared to the results of nickel tetracarbonyl CVD, which can quickly fill molds with bright, full-density, very strong nickel. Under similar circumstances, iron carbonyl leaves a mechanically weak, black deposit with a high carbon content. Jenkin, however, brought to our attention some unpublished laboratory experiments in which ammonia is added to the iron carbonyl to suppress carbon codeposition during production of analytical-grade iron powder. He suggested that we examine the effects of addition of ammonia during attempts to plate out tough iron films. Also, based on his own earlier experience, he suggested a similar experiment with water vapor as an additive. (All runs have added hydrogen and carbon dioxide).

The experiments with ammonia turned out promising results: two runs at 210 and 230°C with both ammonia and carbon dioxide added both produced bright, tough films, but unfortunately both developed stress cracks and partially peeled off the mandrel surface. But a run with water vapor, carbon dioxide and no ammonia looked even better, without spalling, and remained mirror-bright as long as deposition continued, but closer examination of the surface again shows extensive cracking. The literature does not report reactions of ammonia with iron carbonyls to displace carbon monoxide (as happens with nickel carbonyl), and it is possible that the participation of ammonia begins with partial decomposition of ammonia and leads to nitriding of the iron surface, and hence to embrittlement.

Analyses of the metal film deposited without ammonia show about 3.9% oxygen and 1.6% carbon, nearly the same proportion as in carbon dioxide. Adsorbed and trapped carbon dioxide gas, not a bizarre alloy, may be responsible for this contamination. Jenkin suggests that deposition at lower pressures may alleviate this problem.

In general, carbon dioxide helps reduce the carbon content of the deposit, but increases the oxygen content. Water, at high concentrations, of course also is an important source of oxygen. Hydrogen suppresses the oxidation of the deposit by carbon dioxide, while helping keep the carbon content low. The impurity then approaches a C:O molar ratio of 1:2.

It seemed reasonable to try a run with only carbon dioxide as the carrier gas. The resulting

deposit was bright, tough, adherent, and had a high deposition rate-- the best yet! Again, the impurity had the stoichiometry of carbon dioxide, and may be susceptible to removal by exposure to lower pressures or higher temperatures. A similar run with a little added hydrogen produced chemically similar results but had an even higher deposition rate.

We are making clear progress toward the goal of direct deposition of iron with desirable physical properties. Experiments involving lower pressures, outgassing at higher temperatures, and codeposition of iron and nickel are all planned.

Energy for Earth from Space

We have carried out studies of two different schemes for providing energy for Earth from space. We find that the energy needs of Earth in the 21st century can plausibly be met economically and with diminished environmental impact by either building Solar Power Satellites from asteroidal materials in Highly Eccentric Earth Orbit (HEEO) or by returning ^3He from the atmosphere of Uranus for use as a clean fusion fuel in reaction with terrestrial deuterium.

HEEO (in our reference example, 6000 to 400000 km altitude) has several considerable advantages relative to GEO as a site for construction of SPS constellations: 1) It is more accessible than GEO via chemical launch from Earth, the Moon, and near-Earth asteroids. 2) From HEEO there is much easier access to Earth than from GEO (a ΔV of under 100 m/s vs. 1461 m/s for return to atmospheric entry), easier access to the Moon than from GEO (2900 vs. 3500 m/s), and easier access to the typical NEA than from GEO (3000 vs. 5400 m/s). 3) The radiation hazard in HEEO is no worse than in GEO, and the cost of providing shielding from any source will always be less in HEEO. 4) The high MPBRs available for return of asteroidal material suggested a careful look at a variety of bootstrapping schemes for return of large masses of asteroidal material to HEEO, using propellants derived from asteroids. The missions considered in this study are summarized in Table 1. The corresponding ΔV requirements and single-mission mass payback ratios are given in Tables 2 and 3, respectively.

Alternatively, commercial production of electric power from fusion of ^3He with deuterium may be shown to be technically feasible. If so, then: 5) the preferred source for the ^3He is the atmosphere of Uranus, 6) ^3He return from Uranus requires two crucial items of new technology: a nuclear rocket stage using hydrogen as the working fluid and a "hot air balloon" filled with warm hydrogen to suspend the processing package in the uranian atmosphere. 7) Processing of the ambient atmosphere to separate helium from hydrogen and methane and to separate the isotopes of helium can be done using a small subset of the equipment required to extract ^3He from lunar regolith. Among the features of the lunar scheme that may be omitted entirely are a) the need to mine 10^8 tonnes of dirt per tonne of ^3He , b) the need to beneficiate and size minerals, c) the energy needed to heat 10^8 tonnes of regolith to roughly 1000°C , d) the need for high process temperatures, e) the need to design around a two-week very hot day and a two-week very cold night, which creates severe temperature-cycling stresses and interrupts continuous processes, and f) the need to handle a wide range of reactive gases along with the ^3He .

Transportation System Architectures

Motivated in large part by the study of possible locations for SPS constellations summarized above, we have looked at a variety of bootstrapping schemes for return of nonterrestrial propellants and metals to near-Earth space. These studies involve the use of stations in highly eccentric Earth orbit as fuel-manufacture sites, near-Earth asteroids as sources of water, and both solar thermal and nuclear thermal "steam rockets" as the means of transport. Constraining the spacecraft specific impulse to 180 to 220 seconds (cool thrust chambers; very long operational lifetimes) and allowing a spacecraft operational life of 10 to 15 years (three round trips to a carbonaceous NEA by each spacecraft) we can demonstrate that real mission sequences to know near-Earth asteroids of probable C-type composition can provide mass payback ratios of 100:1.

Near-Earth Asteroid Streams

During the present reporting period oversight of a special investigation of asteroid streams was also provided by Dr. Jack Drummond.

The seminal paper reporting the discovery of three near-Earth asteroid streams investigated 139 numbered and unnumbered Earth-approaching asteroids known through June 1990 (Icarus 89, 14-25, 1991). Fourteen asteroids comprised the three streams, i.e., 10% of NEAs were found to be members of streams. In the current study 176 asteroids known through mid-May 1991 were examined for streaming. One new member was added to Stream III, maintaining the ratio of asteroids in streams at about 10% (15/172.09).

Table 5 shows the members and orbital characteristics of the three streams, including the changes in Stream III. With the addition of a new member for Stream III, all streams now have five members, there are no four-member streams, and, interestingly, there are now three-member streams. However, these three-member streams are not yet considered real. The lack of a four-member stream will serve as the dividing line between real and random grouping. As more NEAs are discovered perhaps the number in these tentative streams will increase sufficiently so that the streams might be included among the major ones. At any rate, the three streams in Table 5 appear to be a new type of Hirayama family available for near-Earth study.

A phenomenon apparent in all three streams is that there is a bottleneck near perihelion where the orbits of all members pinch together. The size of these scrunch points is about 0.1AU in diameter. Located just outside the orbit of the Earth, the scrunch points are an ideal place to search for new members since the flux is greatest and most concentrated through these regions, which can be studied from anywhere along the Earth's orbit. Search parameters are addressed in a chapter written as part of this investigation: "On the Search for Near-Earth Asteroids" by J. Drummond, D. Rabinowitz and M. Hoffmann, to appear in *Resources of Near-Earth Space* edited by J.S. Lewis *et al.*

Finally, as part of this investigation, an invitation for amateurs to join an early evening search for meteors and fireballs from streams was extended in the May 1991 issue of *Sky and Telescope*. Thus far letters of interest have been received from approximately 100 people. However, it will take at least a year for results from these low-rate theoretical sunset meteor showers to come in, and few individuals may have the perseverance to maintain a watch for that long with so little activity.

Publications

1. J.S. Lewis and R.A. Lewis, Space Resources: Breaking the Bonds of Earth. 407 pp. Columbia University Press.
2. J.S. Lewis, Extraterrestrial Resources. In: Space Manufacturing 6, AIAA, Washington, D.C., 18 (1987).
3. J.S. Lewis, T.D. Jones and W.H. Farrand, Carbonyl Extraction of Lunar and Asteroidal Metals. In: Engineering, Construction and Operations in Space (S.W. Johnson and J.P. Wetzel, eds.), American Soc. Civil Engineers, N.Y., 111 (1988).
4. T.D. Jones, L.A. Lebofsky, J.S. Lewis and M.S. Marley, The Composition and Origin of the C, P and D Asteroids: Water as a Tracer of Thermal Evolution in the Outer Belt. Icarus, 88, 172-192 (1990).
5. J.S. Lewis, Lunar, Martian and Asteroidal Resources: Programmatic Considerations. In Proceedings of the 1989 Annual Invitational Symposium on Space Mining and Manufacturing. UA/NASA Space Engineering Research Center, 1-10 (1990).
6. J.S. Lewis, Non-terrestrial Resources. In: Space Manufacturing 7, 5-10 (1990).
7. J.S. Lewis, Asteroid Resources. In: Proceedings of the La Jolla Workshop on Space Resources. In press (1990).

8. J.S. Lewis, K. Ramohalli and T. Triffet, Extraterrestrial Resource Utilization for Economy In Space Missions. International Astronautical Federation, IAA 90-604 (1990).
9. T.D. Swindle, J.S. Lewis and L.A. McFadden, The Case for Planetary Sample Return Missions, 4: Asteroids. Submitted (1991).
10. J.S. Lewis, ^3He for Fusion Power: The Willie Sutton Principle. Submitted (1991).
11. J.S. Lewis, Construction Materials for an SPS Constellation in Highly Eccentric Earth Orbit. Submitted (1991).
12. J.S. Lewis and M.S. Matthews, eds., Resources of Near-Earth Space, Univ. of Arizona Press, Tucson. In press (1991).
13. M.L. Hutson and J.S. Lewis, Asteroidal Resource Opportunities Suggested by Meteorite Data. In: Resources of Near-Earth Space (J.S. Lewis and M.S. Matthews, eds.), Univ. of Arizona Press, Tucson, in press (1991).
14. J.S. Lewis, D.S. McKay and B.C. Clark, Using Resources from Near-Earth Space to Meet Human Needs. In: Resources of Near-Earth Space (J.S. Lewis and M.S. Matthews, eds.), Univ. of Arizona Press, Tucson. Submitted (1991).
15. J.S. Lewis, Cometary and Asteroidal Bombardment of Earth: Monte Carlo Simulation. In preparation (1991).
16. J.S. Lewis, Non-terrestrial Resources. In: Space Manufacturing 8, in press (1992).
17. J.S. Lewis, Non-terrestrial Resources of Economic Importance to Earth, IAF 91 (1991).
18. J.S. Lewis, Processing of Non-terrestrial Materials, SME, invited (1992).
19. J.S. Lewis, Logistical Implications of Water Extraction from Near-Earth Asteroids. Paper presented at the Conference on Near-Earth Asteroids, San Juan Capistrano, CA, June 1991.

Table 1
Mission Architectures Studied

Earth launch:

E1. Direct rocket launch from Earth

Moon resource retrieval:

- M1. Retrieval of lunar materials; all ΔV s are propulsive, using Earth propellants,
- M2. Retrieval of lunar materials; aerobraking is used where possible, and only Earth propellants are used for the other ΔV s,
- M3. All ΔV s are propulsive, with lunar-derived liquid oxygen (LLOX) used for all burns above LEO,
- M4. Aerobraking is used where possible, with LLOX used for all burns above LEO,
- M5. Aerobrakes made from lunar material are used where possible; LLOX used for all burns above LEO

Near-Earth Asteroid resource retrieval:

- A1. Retrieval of NEA materials; all ΔV s are propulsive, using Earth propellants,
- A2. Retrieval of NEA materials; aerobraking is used where possible, and only Earth propellants are used for all the other ΔV s,
- A3. All ΔV s are propulsive, with NEA-derived liquid water used for all ΔV s above LEO,
- A4. Aerobraking is used where possible, with water used for all ΔV s above LEO,
- A5. Aerobrakes made from NEA material are used where possible; water used for ΔV s above LEO

Table 2
Delta Vs for Eleven Mission Architectures
 ΔV (m/s)

Event	E1	M1,3	M2,4,5	A1,3	A2,4,5
Earth to LEO	8500	8500	8500	8500	8500
LEO to GTO	2491				
GTO to GEO	1461				
LEO to TO	3113				
TO to HEE0	63				
LEO to intercept		3113	3113	4000	4000
orbit match		812	812	1000	1000
landing		2100	2100	10	10
takeoff		2100	2100	10	10
to E intercept				500	500
capture LEO		3925	872	4800	60
+ trim to: GEO		1538	1538	3729	1480
HEEO		750	750	1690	63
Sum to LEO	8500	6025	2972	5310	570
Sum to GEO	12452	3638	3638	4239	1990
Sum to HEE0	11676	2850	2850	2200	573
	E1	M1,3	M2,4,5	A1,3	A2,4,5

Table 3
Mass Payback Ratios for Selected Mission Architectures
 (Single mission; typical "good" asteroid)

Mission	Return to LEO	To GEO	To HEE0
E1	1.000	0.334	0.418
M1	0.036	0.063	0.145
M2	0.118*	-	-
M3	0.202	0.502	0.707
M4	0.505*	-	-
M5	0.715*	-	-
A1	0.068	0.134	0.292
A2	0.615***	0.226***	0.804**
A3	1.672	2.710	5.65
A4	1.431***	0.978***	1.86**
A5	8.50***	5.40***	8.48**

* Assuming an aerobrake mass fraction of 0.1 (low energy dissipation)

** Assuming an aerobrake mass fraction of 0.2 (moderate energy dissipation)

*** Assuming an aerobrake mass fraction of 0.3 (high energy dissipation)

Table 4
Energy Consumption Comparison
 for Lunar- and Uranus-Derived ³He

	Gj per kg ³ He	
Operation	Moon ^a	Uranus
Transportation from Earth	2180	0.25
Excavation	13	0
Conveyance/ Beneficiation	4	0
Heating Regolith	4100 ^b	0
Compressor/ Refrigerator	67	5. ^c
Return to Earth	0.005	0.5
TOTAL	<u>6364</u>	<u>5.75</u>

^a University of Wisconsin data.

^b Using a ³He concentration of 10⁻⁸ g/g, a heat capacity of 0.25 cal/g K, and delta T = 800 K, we calculate an energy use of 10³ · 10⁻⁸ · 25 · 4 × 10⁷ · 800 = 80000 Gj/kg ³He. The total would then be 85264. The Wisconsin study very optimistically assumes 95% recovery of heat from heated lunar solids.

^c Using rejected LH₂ to precool the ingested gas stream with a thermal efficiency of 80%.

Table 5

Association I Orbital Elements

<u>Orbital elements</u>								
Asteroid	q	e	ω	Ω	i	π	D_{SH}	D'
QRS	1989 RC	1.13	0.513	180.8	139.7	7.4	320.5	.059
	1972 RB	1.10	0.487	152.4	176.8	5.2	329.2	.082
	1987 SF3	1.05	0.535	133.6	187.1	3.3	320.7	.086
	3102	1.18	0.449	154.3	171.7	8.4	326.0	.113
	1987 QB	1.13	0.595	156.0	152.9	3.5	308.9	.146
Average		1.12	0.516	156.8	164.2	5.4	321.0	.097

Association II Orbital Elements

<u>Orbital elements</u>								
Asteroid	q	e	ω	Ω	i	π	D_{SH}	D'
V	3551	1.07	0.487	193.0	173.4	9.5	6.4	.118
C	1989 VB	1.01	0.461	329.5	38.4	2.1	7.9	.128
V	3908	1.04	0.458	125.5	261.4	2.2	26.9	.134
TGC	2061	1.05	0.537	155.9	207.3	3.7	3.2	.114
	2202	1.12	0.512	217.3	169.7	8.8	27.0	.155
Average		1.06	0.491	194.5	179.7	4.0	14.2	.130

Association III Orbital Elements

<u>Orbital elements</u>								
Asteroid	q	e	ω	Ω	i	π	D_{SH}	D'
S	3757	1.02	0.447	16.8	74.5	3.9	91.3	.080
S	1980 AA	1.05	0.444	168.0	298.5	4.2	106.5	.145
QU	1980 WF 4688	1.08	0.514	212.8	241.1	6.4	93.9	.131
	1989 UP	0.98	0.473	17.2	52.8	3.9	70.0	.189
	1991 FA	1.095	0.447	91.5	339.0	3.1	70.5	
Average		1.03	0.470	136.7	313.7	0.8	90.4	.136
New Average		1.05	0.465	120.5	325.9	1.3	86.4	.420

PRODUCTION OF OXYGEN FROM LUNAR ILMENITE

F. Shadman, Y. Zhao, and C. Massleon
Department of Chemical Engineering
University of Arizona

Progress Report
August 30, 1991

Abstract

The high temperature reduction of ilmenite is investigated. The experiments were performed in a microgravimetric reactor system. The starting materials and products were characterized using X-ray diffraction (XRD) with Cu K α source, high-resolution scanning electron microscopy (SEM), energy-dispersive X-ray (EDX) and wavelength-dispersive X-ray (WDX) analyses, mercury porosimetry and Mossbauer spectrometry.

The procedures for the synthesis of lunar ilmenite simulant have been established. The simulants have been successfully prepared with desired physical and chemical properties. The significance of this work is that it is possible to generate the kinetics data even without having access to real lunar ilmenite, which is so precious and difficult to obtain at the present time.

The results of ilmenite reduction by a mixture of H₂ and CO indicate that the mechanism is similar to the reduction of ilmenite by H₂ or CO alone. However, the overall process is more complex because of the reaction between H₂ and CO₂ generated from the CO reduction of ilmenite.

It seems that the MgTiO₃ has some effect on the reduction of ilmenite. This depends on the reduction temperature and conversion. The results indicate a very important role for MgTiO₃ which has not been reported before. In addition to the expected Fe and TiO₂ product phases in the partially reduced sample, an unreduced core enriched in MgTiO₃ is observed. The movement of MgTiO₃ toward the core is a very significant factor affecting the reduction rate.

A new technique has been developed to deposit carbon on iron titanate with gas compositions from 2.7% to 21% carbon monoxide in nitrogen and at temperatures from 350 to 500°C.

Section 1

Synthesis of lunar ilmenite simulant

A possible activity on the Moon could be the production of oxygen from ilmenite, which is abundant on the lunar surface. An important aspect of investigating the reduction of lunar ilmenite is to prepare a simulant that has the same physical and chemical properties as the lunar ilmenite. Because first of all, the terrestrial mineral ilmenite is very different in composition from lunar ilmenite and far more reactive than its lunar namesake, and secondly, the lunar samples are very valuable and scarce.

Typical lunar ilmenite deviates from ideal FeTiO_3 mainly because of the incorporation of a significant amount of MgTiO_3 in the FeTiO_3 lattice. Substitutions other than Mg include Cr and Mn; rarer metals like Al, Zr, and V could also be present, but in quantities less than 0.1%. The metals Mg, Cr, and Mn are the most abundant substitutes in ilmenites of the high-Ti mare basalts, which are the lunar rocks rich in ilmenite and are the likeliest target for ilmenite mining. Literature data on the compositions of 133 ilmenites from high-Ti mare basalts give the distribution of compositions listed in Table 1.1.

In this present study, both synthetic ilmenite and the synthetic ilmenite containing MgTiO_3 are used as lunar ilmenite simulants. Only one impurity is added to the synthetic ilmenite at each time; this allows us to have a better understanding of the fate of impurities such as MgTiO_3 in the reduction of lunar ilmenite. Since both lunar ilmenite and terrestrial ilmenite contain at least three or four impurities, it is often difficult to interpret the mechanism of reduction of such samples. The results of present study are also applicable to the reduction of terrestrial ilmenite because of the presence of MgTiO_3 in it. In this section, the detailed procedures for the synthesis of ilmenite with MgTiO_3 are described. This is followed by the results for the characterization of the samples.

Synthesis Procedures

FeTiO_3 and MgTiO_3 were used as reactants for the synthesis of the $\text{FeTiO}_3\text{-MgTiO}_3$ solid-solid solution. The reason for the use of FeTiO_3 and MgTiO_3 as starting materials is that the use of Fe, TiO_2 , FeO, and MgO results in some unreacted Fe_2O_3 and Fe in the final sample (Briggs and Sacco 1991). The FeTiO_3 (99.9%, -325 mesh) and MgTiO_3 (99.9%, -325

mesh) were heated in a drying oven at 100°C for a minimum of 24 hours and then cooled under vacuum.

Appropriate proportion of these two components were weighed to produce about four grams of a synthetic ilmenite and geikilite mixture. The mixture was ground under 'spec-pure' acetone for approximately two hours and then dried under vacuum. Pellets, 12 mm in diameter and weighing 200-300 mg, were made and loaded into an alumina crucible with 15 mm I.D. and 23 mm height. Direct contact was avoided between the crucible and the pellets by putting a layer of FeTiO_3 - MgTiO_3 mixture on the bottom and along the wall of crucible. This layer of FeTiO_3 - MgTiO_3 is discarded at the end of each experiment. No significant reaction was observed between the alumina crucible and the mixture.

Table 1.1 Compositions for 133 Ilmenites* from High-Ti Mare Basalts

fraction	Average mole weight %	Average weight %	Std.dev. weight %	Range in
TiO_2	0.50	52.70	1.10	49.90-55.50
FeO	0.45	43.30	2.40	35.00-47.70
MgO	0.045	2.23	1.75	0.0-9.50
Cr_2O_3	0.0060	0.64	0.29	0.05-2.12
MnO	0.0040	0.42	0.14	0.00-0.95

*Compiled from the proceeding of the Lunar Science Conferences, 1970-1977.

Figure 1 shows the schematic diagram of the furnace used for the synthesis of the sample. It is a Deltech furnace (ModelDt-31-8) with eight molybdenum disilicide heating elements. Zirconia and high purity alumina insulation is employed to achieve a high operating temperature. The maximum operating temperature is 1750 °C. Silicone O-ring seals are used between a high purity alumina tube and sealing head parts which are water cooled in order to prevent the silicone O-rings from being overheated during the experiment. The ultra high purity argon with less than 2 ppm maximum oxygen content was used. In order to eliminate traces of oxygen, thin iron wire and titanium screen were placed above the alumina crucible. The furnace system was flushed for six hours with 1.2 std.l./min of UHP Argon to remove any remaining air before the furnace was heated

to the desired temperature. Temperature was measured with a Pt-6%Rh/Pt-30%Rh thermocouple installed near the heating elements and varied within $\pm 5^{\circ}\text{C}$ during a typical experiment. The crucible loaded with the pellets was kept at 1300°C for 16 hours. This time was sufficient for complete reaction as judged by microscopic examination of polished samples and X-ray diffraction study. During the baking period, the flow rate of UHP argon was kept at 250 std.cc/min.

Several techniques were used for chemical analysis and characterization of the starting materials and the synthesized samples. Mossbauer spectroscopy was employed to determine the oxidation state of iron in the ilmenite. X-ray diffraction (XRD) with a Cu K α source, high-resolution scanning electron microscopy (SEM), energy-dispersive X-ray (EDX) and wavelength-dispersive X-ray (WDX) analyses were employed to determine the chemical composition and elemental distribution in the samples.

Results and discussion

Since lunar ilmenite does not contain any Fe^{3+} , it is important to make sure that the iron in the synthetic sample is only Fe^{2+} . To confirm this, Mossbauer spectroscopy was performed on the synthetic ilmenite used in the studies. The amount of ilmenite used in a typical experiments is about 300mg. A typical Mossbauer spectrum of the synthetic ilmenite is shown in Figure 2b. The results indicate that the amount of impurities including Fe^{3+} was less than 0.8% on metal basis. The figure 3 shows that 2% of hematite (on a metal basis) in an ilmenite sample can be easily resolved with the Mossbauer spectrometer used in this study.

The polished cross-section of the pellets of the solid-solid solution was examined using both optical microscopy and SEM. An SEM secondary electron micrograph of the polished cross-section of the solid-solid flake after being heated for 16 hours at 1300°C is shown in Figure 4. The micrograph reveal only one phase. It also indicates the presence of small craters formed during the baking of samples.

To determine the homogeneity of the synthesized sample, both quantitative WDX and EDX were performed at randomly selected spots and lines. The results in Figure 5 and 6 show that the MgTiO_3 dissolved uniformly in the FeTiO_3 phase and the atomic ratio of iron and magnesium is the same as that of starting mixture. The WDX results are in good agreement with those obtained from EDX. These results confirm the SEM revealing.

The synthesized sample was also analyzed using XRD. The typical XRD pattern is shown in Figure 7. The peaks in Figure 7 are very sharp, which indicates that the synthesized sample is

homogeneous. As expected, there is some shift in each peak of the XRD pattern of the solid-solid solution as compared to those of pure ilmenite and geikielite, which are shown in Figure 3.7. This well characterized sample with desirable properties has been substantially investigated and the results are presented in section three.

Section 2

REDUCTION OF ILMENITE BY A MIXTURE OF HYDROGEN AND CARBON MONOXIDE

The purpose of this study is to understand the fundamental kinetics and mechanism of ilmenite reduction by mixtures of CO/H_2 . Both CO and H_2 would be present in an ilmenite reduction process shown in Figure 20, which is based on the use of carbonaceous waste. Hydrogen reduction of ilmenite is much faster than CO reduction of ilmenite. The carbothermal reduction is more favored thermodynamically than that by hydrogen. Both gases should be used to advantage in any process. The emphasis is on ilmenite with no ferric impurities present, since the Mossbauer study of Apollo 11 ilmenite found no detectable ferric iron (Mason and Melson, 1970). This is important in applying the results to the reduction of lunar ilmenite. The first part of this section deals with the literature on the reduction of ilmenite by a mixture of CO/H_2 . Then the experimental method and material used are described. This is followed by the results from the present study. Shomate (1946) concluded from his thermodynamic examination that carbon is better reducer of ilmenite than either hydrogen or carbon monoxide. El-Guindy and Davenport (1970) studied the reduction of synthetic ilmenite with graphite in the solid state by thermogravimetric analysis. They observed that the reduction initiated near 860°C at the contact points between the reactants. Up to 1020°C , solid state reduction appeared to be the main reduction mechanism, while above this temperature a rate increase was observed and was attributed to a change of mechanism to gaseous reduction of ilmenite by CO regenerated through the Boudouard reaction. Similarly, the mechanism of reduction of iron oxide by carbon is considered by Baldwin to be gaseous by the intermediary action of carbon monoxide which passes from the coke to iron oxide to form carbon dioxide which then returns to the coke to reform more carbon monoxide. This recycle continues until the completion of reduction.

Donnelly (1970) showed that cokes and chars containing hydrogen are even more active than carbon monoxide in establishing a cyclic gaseous reduction process. It is therefore of value to investigate the reduction of ilmenite by the mixture of H_2 and CO .

The only study on the reduction of ilmenite with mixtures of CO/H_2 was conducted by Donnelly (1970). The ilmenite beach sand concentrates used in the study was first oxidized with air and then reduced by a mixture of H_2/CO . The following four reactions were involved in the reduction process: (1) hydrogen reduction of ilmenite, (2) carbon monoxide reduction of ilmenite,

(3) water gas shift reaction, (4) CO disproportionation reaction. The reduction with the mixture was found to be slower at temperatures below 850 °C than with hydrogen alone. This is because carbon monoxide formed carbon and carbon dioxide. The carbon dioxide then reacted with hydrogen to form water via the water gas shift reaction. The water formed from this secondary reaction would set back the amount of water which could be generated by hydrogen reduction of ilmenite.

Above 850 °C, the reduction rate was much higher. At 900 °C and 1000 °C, the rate of reduction by 50/50 mixture of H₂/CO was as high as that with hydrogen alone, despite the dilution of the hydrogen by carbon monoxide. This was attributed to the fact that CO disproportionation reaction does not proceed to a significant extent at temperature above 900°C.

EL-Greassy et al. (1977) examined the reduction mechanism of pure Fe₂O₃ briquettes with CO/H₂ mixtures and found that the reaction mechanism depended on the original structure (porosity and grain size) as well as the reducing gas composition. These factors significantly affected the structure of the phases formed during reduction. They also reported that the reduction of dense briquettes with H₂ is chemically controlled at the initial stages, and then becomes controlled by both the chemical reaction and gaseous diffusion for reduction with either CO or CO/H₂ mixtures, with more contribution of the gaseous diffusion part as the CO fraction of the gas increases. The rate of reduction with CO was found to be much lower than those with H₂, and was intermediate for gas mixtures. Chemical rates predominate for reduction with H₂, but the formation of a porous iron carbide layer during reduction with CO causes diffusional resistance for gases which affects to the overall rate.

Experimental Approach

A schematic of the experimental apparatus is shown in Figure 8. The main components of this system are an electronic microbalance (Cahn Instruments, Inc., Model 1000), a quartz flow through reactor with inlet and outlet shown in figure 9, and a movable furnace with a PID controller. The composition of gaseous reactants was prepared using both a gas chromatograph and an infrared analyzer. The infrared analyzer also was employed to determine the concentration profile of carbon monoxide and carbon dioxide in the gaseous products of the reduction. Ilmenite was used in the form of thin flakes pressed from powder. Samples were suspended from the microbalance, which monitored weight changes during the course of an experiment. A thermocouple was used to monitor the temperature of the reactor around the flake. All experiments were performed under isothermal conditions at temperatures between 900 and

1100°C. The reducing gas entering the reactor contained CO, CO₂, H₂, and N₂. The ratio of CO to CO₂ was maintained at 99 to prevent carbon deposition due to the CO disproportionation reaction (Jones, 1975; Shomate, 1946). The gas flow rate was 660 std.cc/min, except in the experiments conducted to determine the effect of interphase mass transfer on the reduction rate.

Samples of starting material were prepared by cold pressing approximately 0.270 g of FeTiO₃ powder (with particles size less than 45 µm) in a die at 14,500 psi for 5 minutes to form disks. The disks were then cut into flakes approximately 10 mm by 8 mm. The thickness of the disks was 0.60 mm except for experiments conducted to determine the effect of intergranular diffusion resistance (transport through void space among grain particles).

Each experiment was started by first purging the reactor system at room temperature to reduce the concentration of oxygen to levels below 10 ppm. A mixture of CO/CO₂/H₂/N₂ was then introduced into the reactor. To initiate the reduction, the furnace was raised rapidly. Within three minutes the temperature in the reactor was within 1% of the set point temperature. The experiments were terminated at a desired conversion by rapidly lowering the furnace.

Similar analytical techniques mentioned before were used for chemical analysis and characterization of the reduced samples. X-ray diffraction (XRD) with a cobalt Ka source was used to identify the different crystalline phases in the products. High-resolution scanning electron microscopy (SEM) and energy-dispersive X-ray (EDX) analyses were employed to examine the polished cross section of both partially and completely reduced samples and to determine the elements present in each phase. For SEM and EDX analyses, the samples were mounted in an epoxy resin and polished to expose the cross-section of the grains.

Results and discussion

The reduction of ilmenite by a mixture of H₂ and CO consists of the following four reactions:

- (1) The reduction of ilmenite by H₂.
- (2) The reduction of ilmenite by CO.
- (3) Water gas shift reaction.
- (4) CO disproportion reaction.

However, the CO disproportion reaction can be suppressed by adding a small amount of CO₂ in the mixture of H₂ and CO. Two sets of experiments were conducted to determine the experimental conditions under which CO disproportion reaction does not occur. The results

indicate that CO disproportion does not take place if the ratio CO to CO₂ is at least 124 at temperature above 850°C with H₂% varying from 0 to 14.7%. All experiments were performed under this condition so that CO disproportion does not participate in the overall reduction of ilmenite.

The results of reduction of ilmenite with hydrogen indicates that the interphase resistance was not important if the gas flow rate was at least 660 std. cc/min at temperature of 1014°C, whereas the flowrate of 260 std. cc/min was high enough to eliminate the interphase resistance at temperature of 1100°C in the reduction of ilmenite by CO. The flowrate of 700 std. cc/min was used in the reduction of ilmenite by H₂/CO.

The effect of temperature on the initial rate of reaction is shown in Figure 10. The apparent activation energy calculated based on initial rates with 6.4% H₂ and 11.6% CO is 22.2 kcal/mole.

To understand the effect of hydrogen concentration in the gaseous mixture on the reaction rate of ilmenite by a mixture of CO/H₂, two sets of experiments were conducted at 945°C and 1000°C at 6.4% and 14.7% H₂ concentration and approximately 11% CO in the mixture. The results shown in Figures 11 and 12 suggest that the reduction rate of ilmenite by H₂/CO at 945°C and 1005°C and 1000°C with 6.4% hydrogen is almost equal to that by hydrogen and carbon monoxide combined. However, the reduction rate of ilmenite at 945°C and at 1005°C with 14.7% H₂ is nearly equal to that of hydrogen alone. The explanation of this is that the reaction rate between H₂ and CO₂ generated from the reduction of ilmenite by CO increases as hydrogen concentration in the gaseous mixture increases. The water formed from this secondary reaction would set back the amount of water which could be generated by hydrogen reduction of ilmenite.

These results suggest that the ratio of hydrogen to carbon monoxide is an important factor in the reduction of ilmenite by H₂/CO. Also as shown in Figure 13, 14 and 15, an increase in the hydrogen concentration results in an increase in the reduction rate and a decrease in the time required to attain any given conversion. For example, with 6.4% H₂ and 11.6% CO, the time to reach 95% conversion was 28 minutes at 945°C and 21 minutes at 1045°C. With 14.7% H₂ and 10.5% CO, the time to reach 95% conversion was 17 minutes at 945°C and 12 minutes at 1045°C.

The effect of CO concentration in the gaseous mixture was also examined. The results, shown in Figure 16 and 17, show that the effect of CO concentration on the reduction of ilmenite by H₂/CO becomes more significant at higher temperature as the CO concentration was increased from 10.5% to 18% at 14.7% H₂ concentration. An increase in CO concentration from 0 to 10.5% at 945°C and 1005°C does not increase the overall reduction rate with 14.7% hydrogen. This is because the CO₂ (from the CO reduction of ilmenite) reacts with H₂ to form

H₂O. This would reduce the amount of water which could be generated by hydrogen reduction of ilmenite.

As the CO concentration in gaseous mixture is increased from 10.5% to 18% with 14.7% hydrogen, the overall reduction rate increases at 945°C and 1005°C. This is probably due to the fact that the water gas shift reaction forms more H₂ and CO₂ as CO concentration increases from 10.5% to 18%. This increases the concentration of H₂ which reacts with ilmenite more faster than CO.

An SEM secondary electron micrograph of the polished cross-section of an ilmenite flake after partial reduction at 1,000°C is shown in Figure 18. The micrograph reveals three distinct regions which appear as bright, light gray and dark gray phases. To identify the phases present, quantitative EDX was performed at spots marked in Figure 18. The results and XRD observations (to be discussed later) show that the bright phase is primarily iron, the dark gray phase is made up of titanium dioxide and the light gray phase is unreacted FeTiO₃. These results suggest that there is a strong tendency toward the segregation of the products iron and titanium dioxide and that iron diffuses to the grain boundaries through the TiO₂ layer during the reduction.

The sample completely reduced at 1000°C, as shown in Figure 19, was also polished and analysed using SEM and EDX. The observed phases are Fe and TiO₂.

The XRD spectra of both completely and partially reduced samples were also obtained. The phases present after complete reduction at 874°C, 945°C, and 1048°C are iron and titanium dioxide; those present after partial reduction at 1049°C were iron, titanium dioxide, and unreacted ilmenite. These findings are in good agreement with the data obtained from EDX analysis.

The various observations described here suggest a mechanism consisting of the following main steps for the reaction in each grain:

Step 1. Diffusion of both CO and H₂ through the porous product layer of TiO₂ toward the unreacted core of the grain particles.

Step 2. Reactions of both H₂ and CO with the ilmenite core to produce TiO₂ and Fe.

Step 3. Water gas shift reaction involving H₂, CO, H₂O and CO₂.

Step 4. Migration of Fe through the TiO₂ layer away from the unreacted core toward the grain boundary.

Step 5. Formation of iron nuclei and their subsequent growth outside and around the reacted grain particles.

Step 4 and step 5 result in almost complete segregation of the two solid products, iron and titanium dioxide, in the scale of grains.

The SEM and XRD results suggest that the solid reduction mechanism of ilmenite is very similar to that by either H_2 or CO alone. However, the overall reduction of ilmenite by H_2/CO is more complex than by H_2 or CO alone because of the reaction between H_2 and CO_2 generated from the CO reduction of ilmenite.

The temporal profiles of conversion as shown in Figure 13, 14, and 15 indicate the presence of three different stages during the reduction of ilmenite by H_2/CO : induction, acceleration, and deceleration. In principle, the mechanism involved in this phenomena is the same as that in the reduction of ilmenite by either H_2 or CO alone. However, the overall process of ilmenite reduction by H_2/CO is more complicated than that by either H_2 or CO alone because of the involvement of water gas shift reaction.

Section 3

CARBOTHERMAL REDUCTION OF ILMENITE

Because the equilibrium conversion of carbon monoxide in the reaction $\text{CO} + \text{FeTiO}_3 \rightleftharpoons \text{CO}_2 + \text{Fe} + \text{TiO}_2$ is low, a large gas recycle stream must be used to extract oxygen from ilmenite. This large gas flow causes a large heating and cooling load, and thus high energy use. Reducing the ilmenite with carbon is one way to avoid this thermodynamic constraint. The carbon monoxide disproportionation reaction, $2\text{CO} \rightarrow \text{C} + \text{CO}_2$, has a high equilibrium conversion at reasonable temperatures, allows the deposition of carbon on ilmenite, and produces carbon dioxide for electrolysis. Also, iron, available as a reduction product, is an excellent catalyst for this reaction. A proposed flow sheet for the process is shown in Figure 20.

Experiments were performed to deposit carbon on iron titanate with gas compositions from 2.7% to 21% carbon monoxide in nitrogen and at temperatures from 350 to 500 °C. The iron titanate used was -44 μm powder. The sample was placed in a quartz pan on the TGA. Gas of the desired composition was prepared, using a nondispersive infrared detector and a gas chromatograph to measure the gas composition. The furnace was preheated to the desired temperature. The reaction was quickly initiated by raising the furnace. Mass changes were continuously monitored with the Cahn 1000 microbalance, and the carbon dioxide and carbon monoxide in the outlet were continuously monitored with the infrared analyser. See Figure 8 for a schematic of the reactor system.

Iron titanate was a poor catalyst for the reaction. Throughout the range of temperatures and gas compositions investigated, no measurable amount of carbon was deposited, and no carbon dioxide was observed in the outlet gas.

Since iron is available as a product on the outside of the reduced ilmenite grains (see sections 1 and 2), its role as a possible catalyst was investigated. The experimental procedure used was the same as for ilmenite, with -44 μm iron powder. Iron did not catalyze the reaction for a gas mixture of carbon monoxide in nitrogen. Thermodynamic calculations (Audier et al.) show that the temperatures and gas compositions where it would be a good catalyst are very limited due to the formation of cementite, Fe_3C , which deactivates the iron.

However, even low amounts of hydrogen on the gas stream causes iron to retain its catalytic activity (Walker et al., Turkdogan and Vinters). Walker et al. proposed that this is because the presence of hydrogen prevents the formation of cementite. They also found that hydrogen will convert cementite to iron, and regenerate the catalytic activity. Turkdogan and Vinters proposed that adsorbed hydrogen catalyses the disproportionation reaction, and also that the reaction $\text{H}_2 +$

$\text{CO} \rightarrow \text{C} + \text{H}_2\text{O}$ takes place . The carbon produced then dissolved in the iron, and migrated to a center of nucleation, where it left solution and formed carbon filaments.

Experiments were done to confirm the activity of hydrogen in this reaction. Powdered iron ($-43 \mu\text{m}$) was placed in the pan of the balance, and the gas was a mixture of 8.8% hydrogen, and 28.3% carbon monoxide in nitrogen. The product was a uniform, low density, black powder. No iron powder was visible, and all the powder was attracted to a magnet, indicating that the iron was distributed throughout the product. At 402°C , the rate of deposition dropped from the initial value, and then became constant. At 452°C and 502°C , the rate initially dropped, and then increased for the rest of the experiment. The increasing rate is probably due to fragmentation of the iron, which is reported for this reaction (Audler et al. , Turkdogan and Vinters). The reaction rate was fairly sensitive to temperature (see Figures 21 and 22).

These results show that the carbon monoxide disproportionation reaction could be used to deposit carbon on the ilmenite feedstock. The feedstock could be partially reduced to form iron on the outside of the ilmenite. The carbon deposited in this way would be evenly distributed on the ilmenite. Alternatively, some of the completely reduced ilmenite could be returned to the carbon deposition reactor, where the iron in it would act as a catalyst. Carbonaceous waste at the oxygen production plant could be used to make up the carbon lost in the exhausted feedstock. This waste would also contain hydrogen, which aids in both the deposition of carbon on iron and the reduction of ilmenite. This use of carbonaceous waste would solve the problem of resupplying the reagents which will be lost, and give value to the carbonaceous waste.

Section 4

EFFECT OF IMPURITIES ON THE REDUCTION OF LUNAR ILMENITE

This section deals with the reduction of ilmenite containing MgTiO_3 , which is a major impurity present in lunar ilmenite. This approach allows us to have a better understanding of the fate of the impurities such as MgTiO_3 in the process of lunar ilmenite reduction. Since terrestrial ilmenite contains MgTiO_3 , the results presented in this chapter are also applicable to the reduction of terrestrial ilmenite. The detailed procedures for the synthesis of ilmenite with MgTiO_3 is described in section 1. In this section, the literature is reviewed and the results of the reduction of the solid solution (FeTiO_3 - MgTiO_3) by H_2 is considered and compared to that of synthetic ilmenite.

While a number of papers have dealt with the solid state reduction of synthetic ilmenite using various reducing agents, as mentioned in section one, very little is available on the solid state reduction of synthetic ilmenite containing MgTiO_3 . The only study on the effect of MgTiO_3 on the reduction of synthetic ilmenite is conducted by D. Poggi, et al. They prepared their sample by melting a mixture of Fe_2O_3 , MgO , TiO_2 , Fe in molybdenum crucibles at 1450°C under an atmosphere of argon. The sample was maintained molten for about one minute before fast cooling. Analysis showed that sample contained approximately 1% molybdenum evenly distributed throughout the sample.

Microscopic examination of their samples reduced by CO shows that in pure synthetic ilmenite the metallic iron precipitates out on preferential planes and along the grain boundaries. However, in the MgO doped ilmenite, the metallic iron precipitates as very fine particles and is well disseminated in the reduced phase. Also, near the reduction interface a metallic iron barrier seems to have formed. Between this metallic iron barrier and the interface there is a strip of reduced ilmenite depleted of metallic iron. They also observed that the MgO doped ilmenite does not contain as much metallic iron at the grain boundaries as does pure ilmenite.

Experimental Approach

A schematic of the experimental apparatus is shown in Figure 8. This system has been discussed in section 2. The main components of this system are an electronic microbalance (Cahn Instruments, Inc., Model 1000), a quartz flow through reactor with inlet and outlet, as shown

in Figure 9, and a movable furnace with a PID controller. The composition of gaseous reactants and products was determined using an infrared analyzer and a gas chromatograph. Ilmenite containing MgTiO_3 was used in the form of thin flakes pressed from powder. Samples were suspended from the microbalance, which monitored weight changes during the course of an experiment. A thermocouple was used to monitor the temperature of the reactor around the flake. All experiments were performed under isothermal conditions at temperatures between 800 and 1045°C. The reducing gas entering the reactor contained H_2 and N_2 . The gas flow rate was 700 std.cc/min, except in the experiments conducted to determine the effect of interphase mass transfer on the reduction rate.

Samples of starting material were prepared by cold pressing approximately 0.270 g of $\text{FeTiO}_3\text{-MgTiO}_3$ powder (with particles size less than 45 μm) in a die at 14,500 psi for 5 minutes to form disks. The disks were then cut into flakes approximately 7 mm by 4 mm. The thickness of the disks was 0.60 mm except for experiments conducted to determine the effect of intergranular diffusion resistance (transport through void space among grain particles).

Each experiment was started by first purging the reactor system at room temperature to reduce the concentration of oxygen to levels below 25 ppm. A mixture of $\text{CO/CO}_2/\text{N}_2$ was then introduced into the reactor. To initiate the reduction, the furnace was raised rapidly. Within three minutes the temperature in the reactor was within 1% of the set point temperature. The experiments were terminated at a desired conversion by rapidly lowering the furnace.

Several techniques were used for chemical analysis and characterization of the starting and reduced samples. Mossbauer spectroscopy was employed to determine the oxidation state of iron in our synthetic ilmenite. X-ray diffraction (XRD) with a cobalt $\text{K}\alpha$ source was used to identify the different crystalline phases in the starting material and products. High-resolution scanning electron microscopy (SEM) and energy-dispersive X-ray (EDX) analyses were employed to examine the polished cross section of both partially and completely reduced samples and to determine the elements present in each phase. For SEM and EDX analyses, the samples were mounted in an epoxy resin and polished to expose the cross-section of the grains.

Results and Discussion

The effect of temperature on the initial reaction rate is shown in Figure 23. The apparent activation energy is 20.9 kcal/mole. This suggests that the addition of MgTiO_3 to synthetic ilmenite, up to 28.6 %, doesn't affect the sensitivity of the reduction process of ilmenite to temperature significantly.

It seems that the addition of MgTiO_3 to synthetic ilmenite didn't affect the rate of reduction significantly at the initial stage in the temperature range of 915 °C to 1014°C as shown in Figure 24 and 25. Retardation of reduction rate increase as the conversion increases. The retardation is more significant at lower temperature and at higher conversion. This is probably due to the fact that the diffusion of MgTiO_3 into the unreduced core of ilmenite (to be discussed below) affect the diffusional rate of Fe out of TiO_2 phase, which affect in turn the draining rate of pores in TiO_2 phase. This diffusional effect is more significant at lower temperature and is not important in the early stage of reduction. As conversion increases, the diffusion of MgTiO_3 into the center core affects the diffusion of Fe out of the TiO_2 phase to a greater extent because of the increase in diffusional length. The diffusion of MgTiO_3 into the unreacted core of ilmenite lowers the concentration of ilmenite. This probably also contributes to the decrease in the reduction rate of ilmenite.

Figure 26 indicates that the reaction order with respect to hydrogen is unity and Figure 24 shows that the effect of temperature on the reduction rate of ilmenite containing MgTiO_3 .

An SEM backscattered electron micrograph of the polished cross-section of an ilmenite flake containing 28.6 wt% of MgTiO_3 after partial reduction at 1000°C is shown in Figure 28. The micrograph reveals four distinct regions which appear as bright, light gray, dark gray phases. To find out what these phases are, quantitative EDX was performed at spots marked in Figure 29. The results and XRD observations (to be discussed later) show that the bright phase is primarily iron, the dark gray phase is made up of titanium dioxide, the dark phase is primarily MgTi_2O_5 .

The light gray phase is unreacted ilmenite but it is richer in MgTiO_3 than starting sample. To confirm this result, another grain reduced to a larger extent is analysed. The EDX was performed on the marked spot located in the unreduced ilmenite core. The result show that this spot contained more magnesium. Both EDX and XRD results suggest that some of the geikielite generated from the reduction of ilmenite-geikielite reacts with TiO_2 , forming MgTi_2O_5 around the unreduced core, and some of the geikielite diffuses through the TiO_2 layer and dissolves into the unreduced core, making the core richer in MgTiO_3 than the starting samples. Segregation of Fe from the other products and nucleation of Fe around each grain are similar to what was observed in the reduction of synthetic ilmenite by either CO or H_2 .

The polished cross-section of synthetic ilmenite flakes after partial reduction at 915°C was also examined by SEM and EDX. The results obtained, as shown in Figure 30 indicate that a similar mechanism of reduction is involved.

Similarly, the SEM photo of a partially reduced sample at 807°C was analyzed and is shown in Figure 31. It shows that the reduction of ilmenite containing MgTiO_3 at 807°C follows

the same mechanism as at 915°C and 1000°C. The only difference is that at 807°C the H₂ penetrates more into the core of ilmenite and causes the phases of TiO₂ and unreduced ilmenite to be mixed.

Table 3.1 XRD results of the lunar ilmenite reduction by hydrogen

Reduction Extent	Reduction Temperature (°C)	Phases Observed
partial	1000	Fe, TiO ₂ , FeTiO ₃ - MgTiO ₃ , MgTi ₂ O ₅
complete	1015	Fe, TiO ₂ , Mg ₂ TiO ₅
partial	915	Fe, TiO ₂ , FeTiO ₃ - MgTiO ₃
complete	915	Fe, TiO ₂ , MgTiO ₃ , MgTi ₂ O ₅
partial	807	Fe, TiO ₂ , FeTiO ₃ - MgTiO ₃
complete	807	Fe, TiO ₂ , MgTiO ₃

The XRD results are listed in Table 3.1. It is interesting to note that the MgTi₂O₅ is not detected in the partially reduced sample at 915°C. However, it is found in the completely reduced sample. The X-ray pattern of partially reduced FeTiO₃-MgTiO₃ sample is shown in Figure 32.

REFERENCE

- Audier M. et al, Carbon 21, No. 2, 93, 1983
- Bird R. B., W. E. Stewart and E. N. Lightfoot "Transport Phenomena" John Wiley & Sons, Inc. (1960)
- Briggs, R. et al, The High Fronties Newsletter Vol. XVI MARCH/APRIL 1990
- Bischoff, K. B. Chemical Engineering Science, Vol. 22, pp 783-784, 1965
- Cutler, A. H. Slag-Metal Equilibrium in Lunar Smelting and Arc Electroninning, Space Tech Sept. 23-25, 1985, Anaheim, California
- Costa, E. C. and J. M. Smith AIChE Journal, Vol. 17, No. 4 pp. 947, July 1971
- Dickson D. P. E. "Mossbauer Spectroscopy": Cambridge University Press 1986
- Donnelly, R. P. Australian Mining March 1970
- Froment F. and K. B. Bischoff "Chemical Reactor Analysis and Design", John Wiley & Sons 1979
- Fortini, A. and D. D. Perlmutter AIChE Journal Vol 35, No. 12, p1975 December 1989
- Gellner, O. H. and F. D. Richardson, Nature, No. 4262, July 7, 1951
- Glaeser, H. H. United States Patent, Dec. 16, 1975, 3, 926, 614
- Geassy A. A. El, K. A. Shehata and S. Y. FZZ Transaction ISIJ, 17, 629 (1977)
- Ishida, M. and Wen, C. Y. AIChE Journal Vol. 14, No. 2, pp 311, 1968
- Ishida, M. and C. Y. Wen, Chemical Engineering Science, Vol. 26, pp. 1031-1041, 1971
- Jones, D. G. J. Appli. Chem. Biotechnol. 1975, Vol. 25, p. 561-582
- Jones, D. G. Trans Instit Min Metall (Sect C: Mineral Process Extr Metall) 83 (1974) pp. L1-L9
- Jagtap, S. B. Industrial Engineering Chemistry Research, 29, 795-799, 1990
- Johnson, R. E. et al., American Journal of Science, Vol. 271, Oct. pp. 278-292, 1971
- Li, Guoxun and Rongjian, Cao. Acta Metallurgica Sinica Vol. 18, No. 3, June 1982
- Landler, P.F.J. and Komarek, K.L. Transations of the Metallurgical Society of AIME. Vol. 283, pp. 138, 1966
- Poggi, D. Ph.D. Dissertation, Universitge de Montreal (1974)
- Poggi, D. et al, Titanium Science and Technology, Vol. 1, pp. 691-695, Edited by R. I. Jaffee and H. M. Burte, Plenum Publishing Co. 1973
- Rumble, Douglas III, Mineralogical society of America Short Course Notes, Vol. 3, Nov. 1976
- Papanastassion, D. Metallurgical Transaction, Vol. 4, Feb. p. 477, 1973
- Rosenberg D.U.V. "Method for the Numerical Solution of Partial Differential Equations" American Elsevier Publishing Company, Inc., New York 1969

Smith, J. M. "Chemical Engineering Kinetics" McGraw-Hill Book Company (1981)
Shomate, G. H. et al. U.S. Bur. Mines Rep Invert 3864, 1946
Taylor, A. Earth and Planetary Science Lettersx 17 (1973) 357-364
Turkdogan, E.T. and Vinters, J. V. Metallurgical Transaction Vol. 5 1974
Wen, C.Y. Industrial and Chemistry Vol. 60, No. 9, Sept., p. 39, 1968
Wagman, D. D. et al. National Bureau of Standards, Rsearch Paper R10, 1634
Zhao, Y and F. Shadman, Industrial and Engineering Chemistry Research, August, 1991
Walker, P.L. et al Journal of Physical Chemistry, Vol., 63 1959

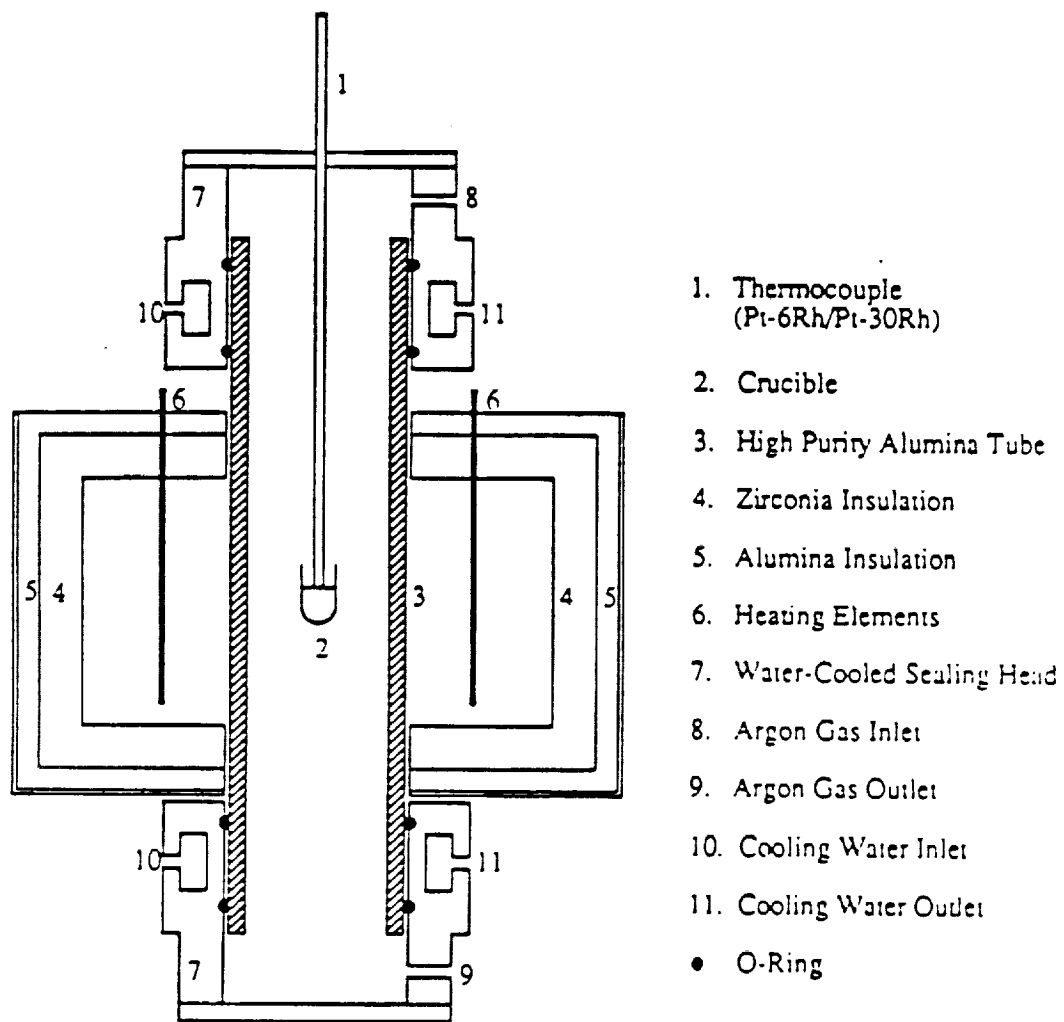


Figure 1 Schematic diagram of the furnace used for the synthesis of $\text{FeTiO}_3\text{-MgTiO}_3$.

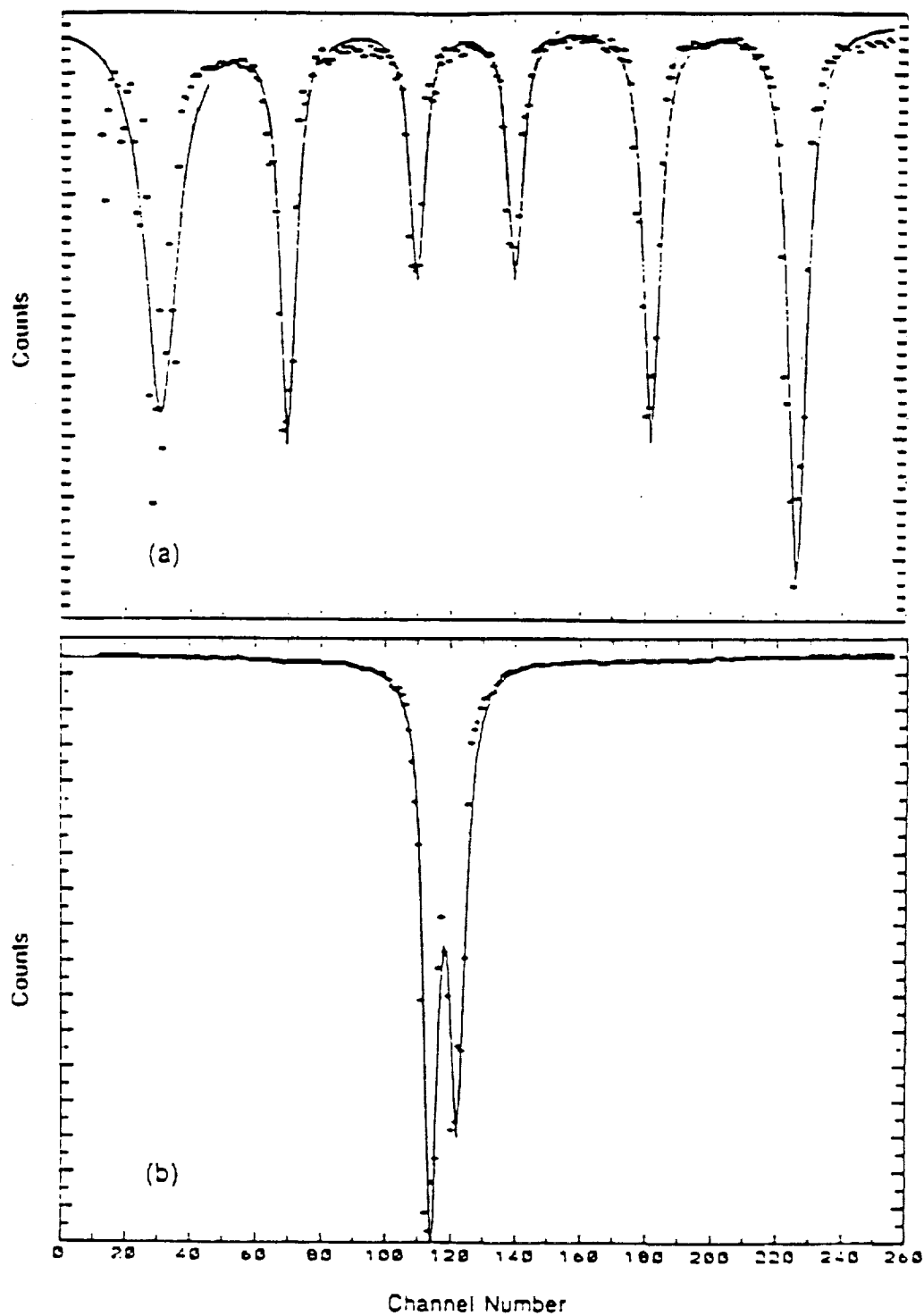


Figure 2 a Mossbauer velocity spectrum for hematite.
 2 b Mossbauer velocity spectrum for synthetic ilmenite.

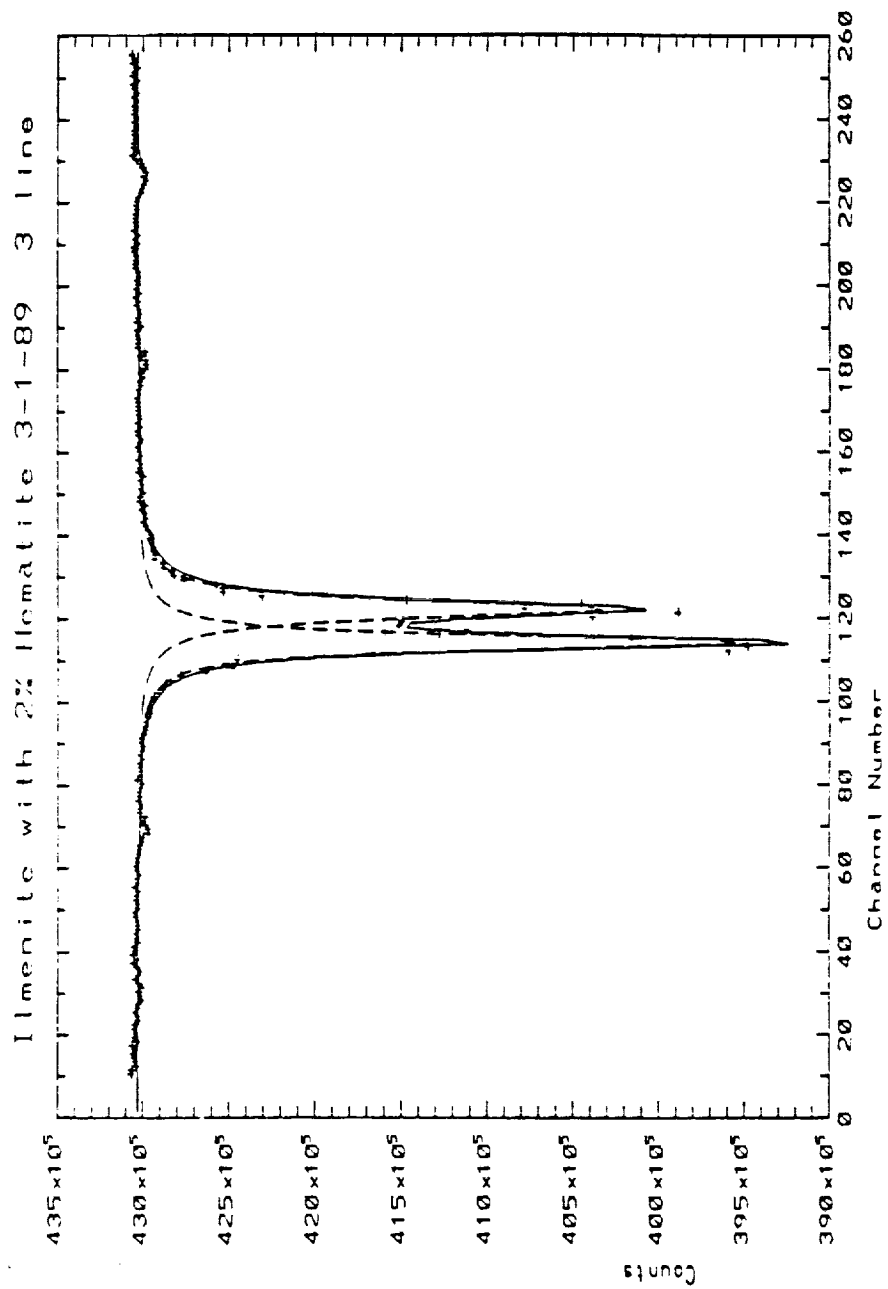


Figure 3 Mossbauer velocity spectrum for synthetic ilmenite
with 2% Fe^{3+} (hematite)

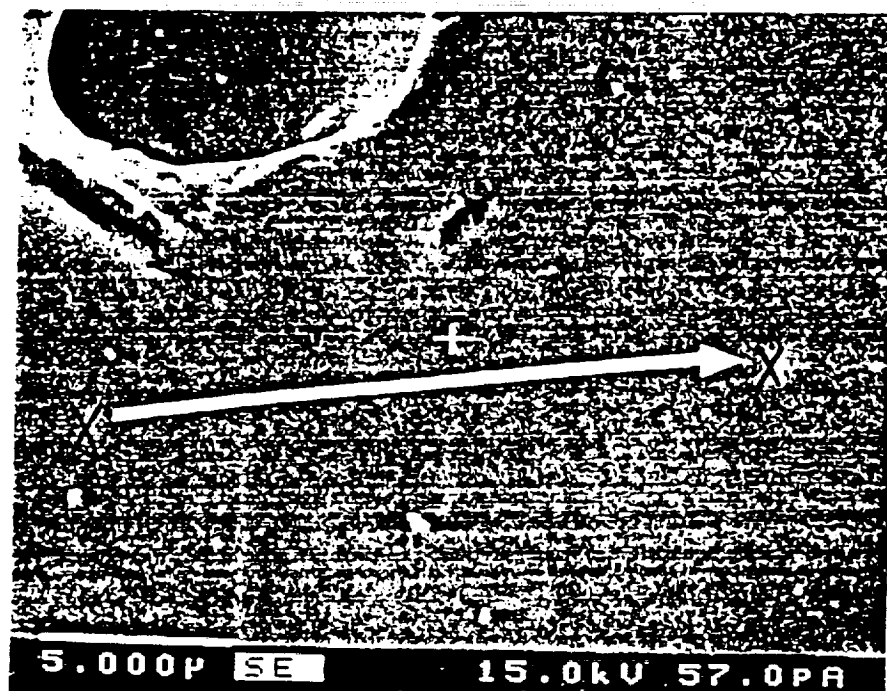


Figure 4 Secondary electron micrograph of the polished cross section of $\text{FeTiO}_3\text{-MgTiO}_3$ flake after being heated for 16 hrs at 1300°C .

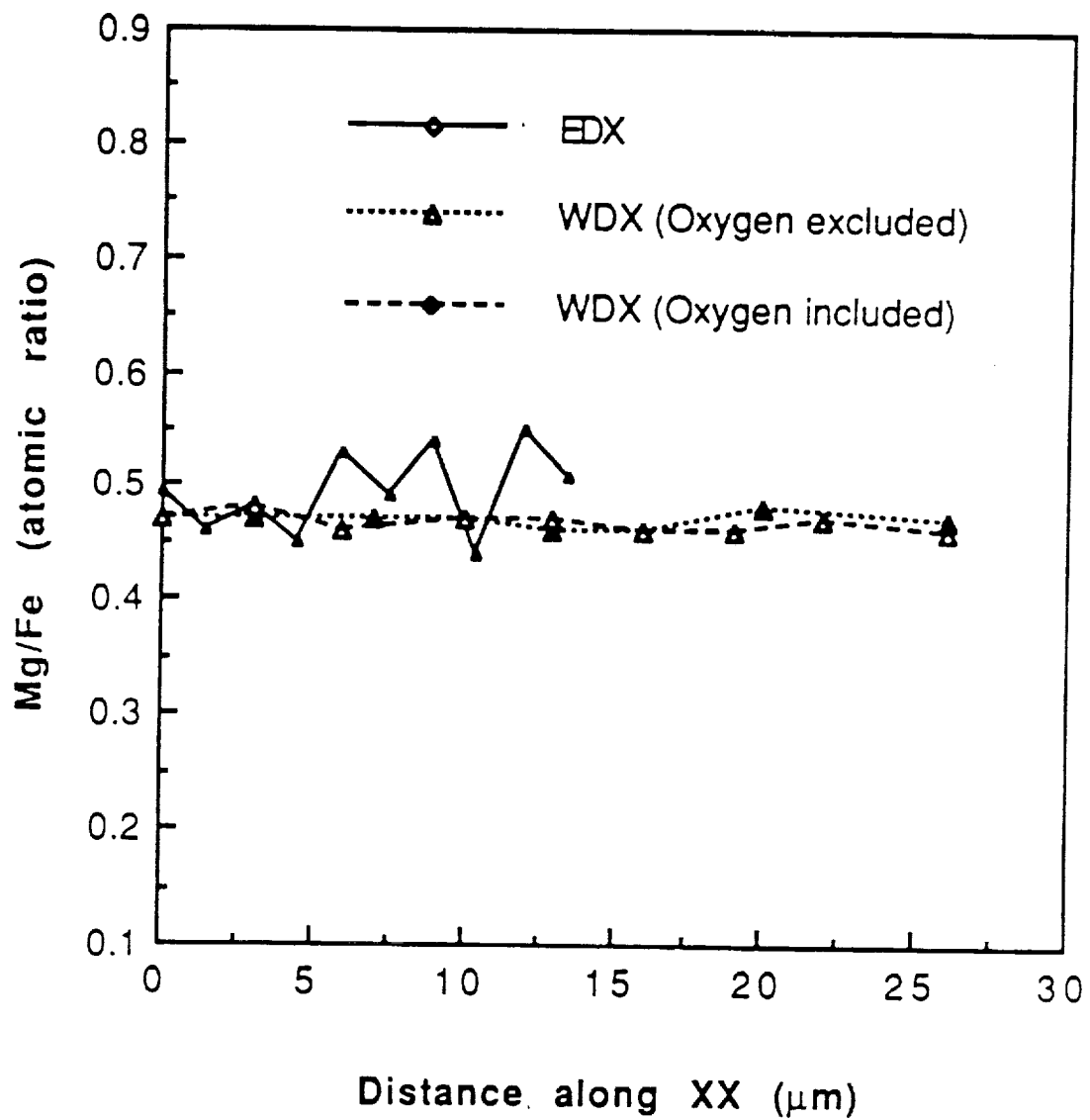


Figure 5 Variation in the magnesium to iron atomic ratio in flake (Figure 3.4)

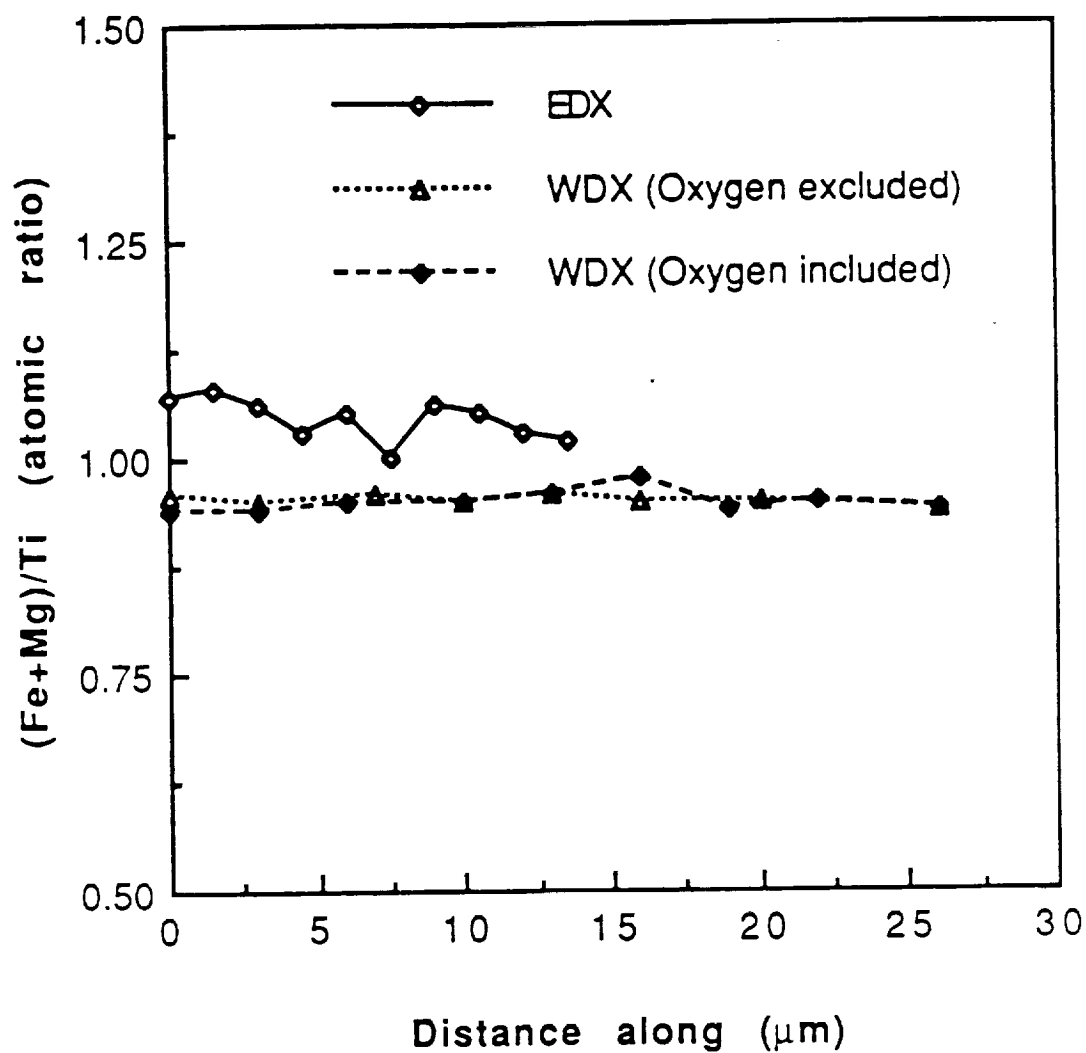


Figure 6 Variation in the magnesium plus iron to titanium atomic ratio in flake (Figure 3.4)

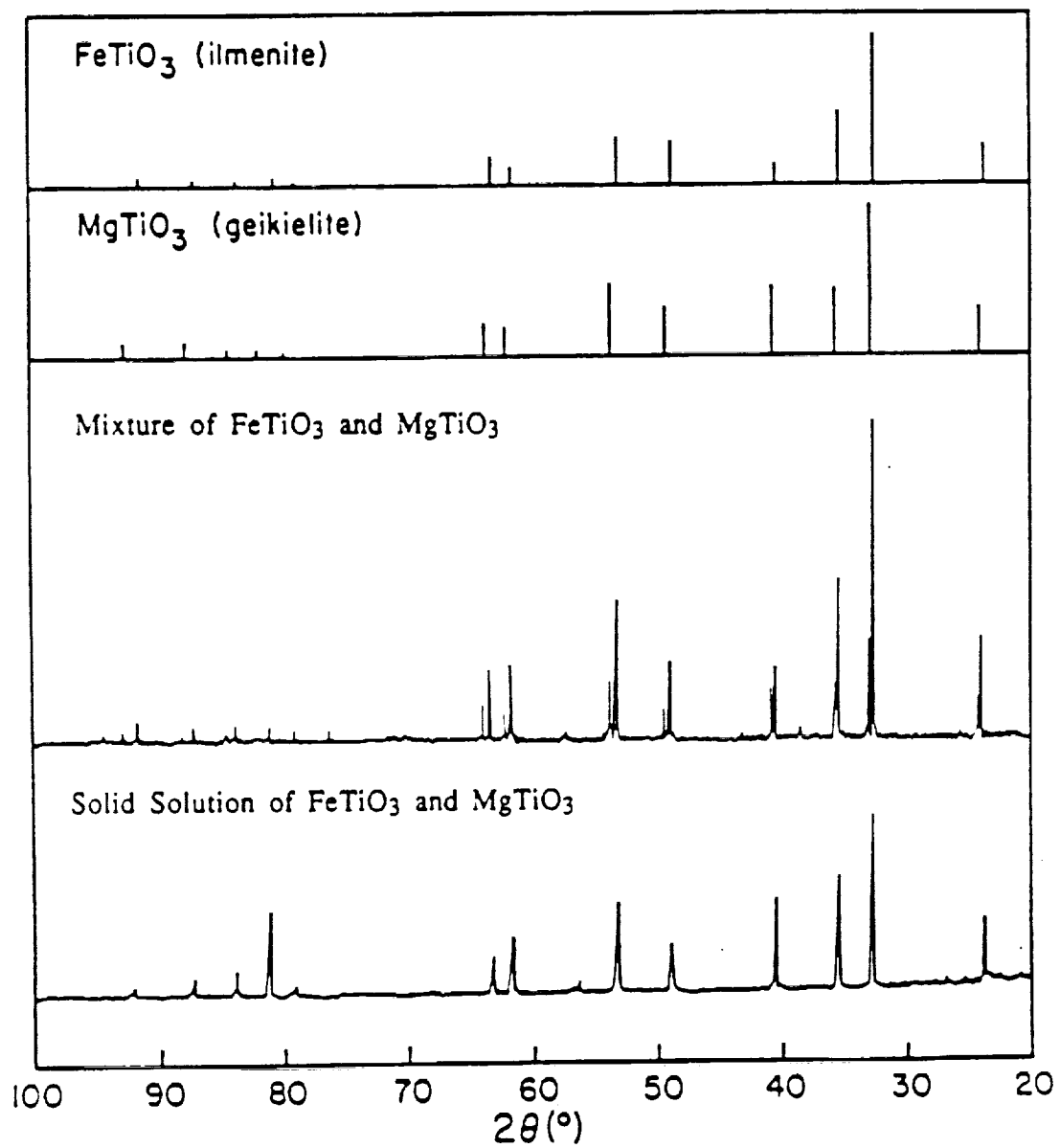


Figure 7 X-ray diffraction spectrum of solid solid solution of FeTiO₃-MgTiO₃.

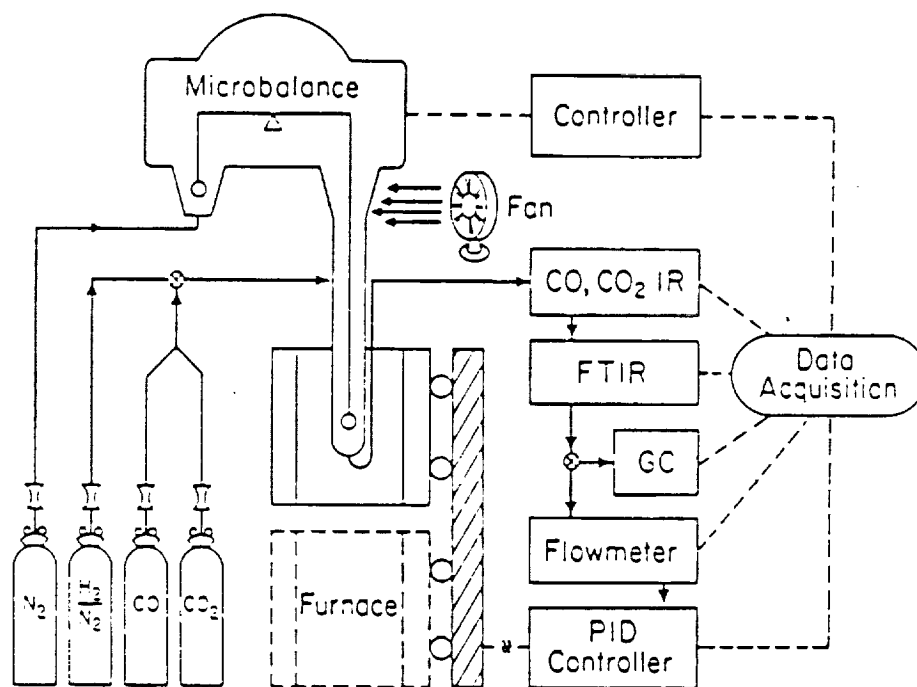


Figure 8 Schematic diagram of the reactor system.
 GC= gas chromatograph. IR=non-dispersive
 infrared analyzer, FTIR= Fourier transform
 infrared spectrometer

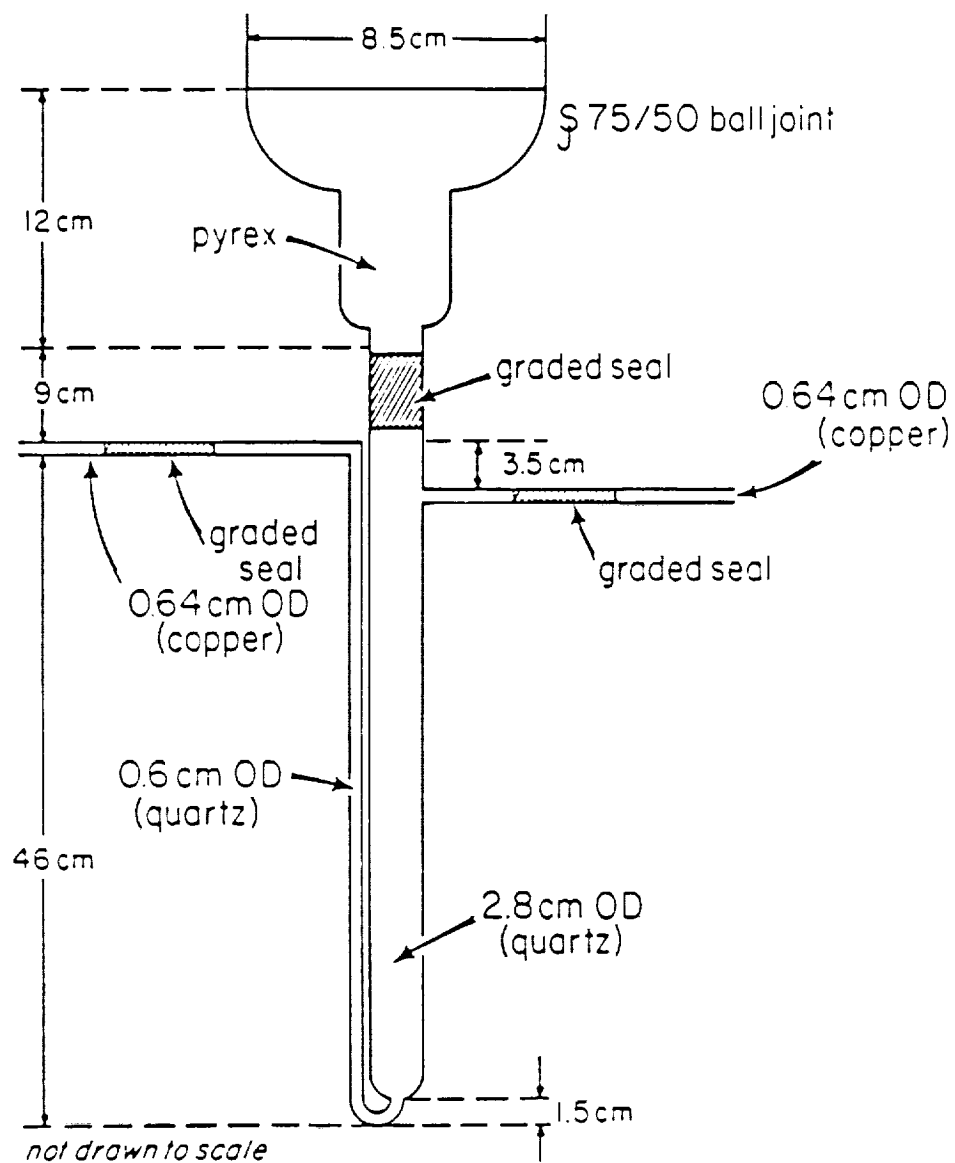


Figure 9 Microgravimetric quartz reactor details.

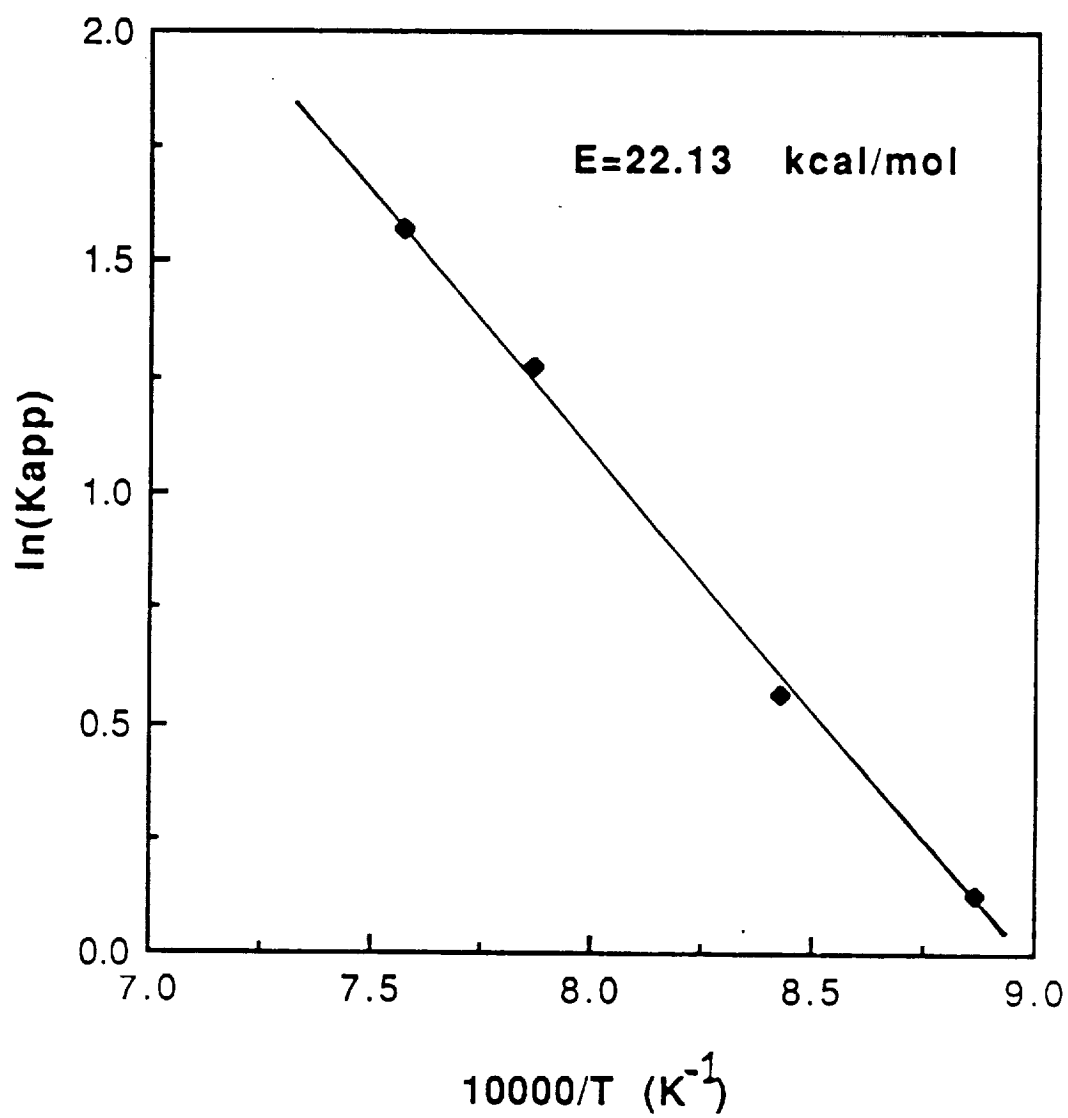


Figure 10 Temperature dependence of the apparent rate coefficient.

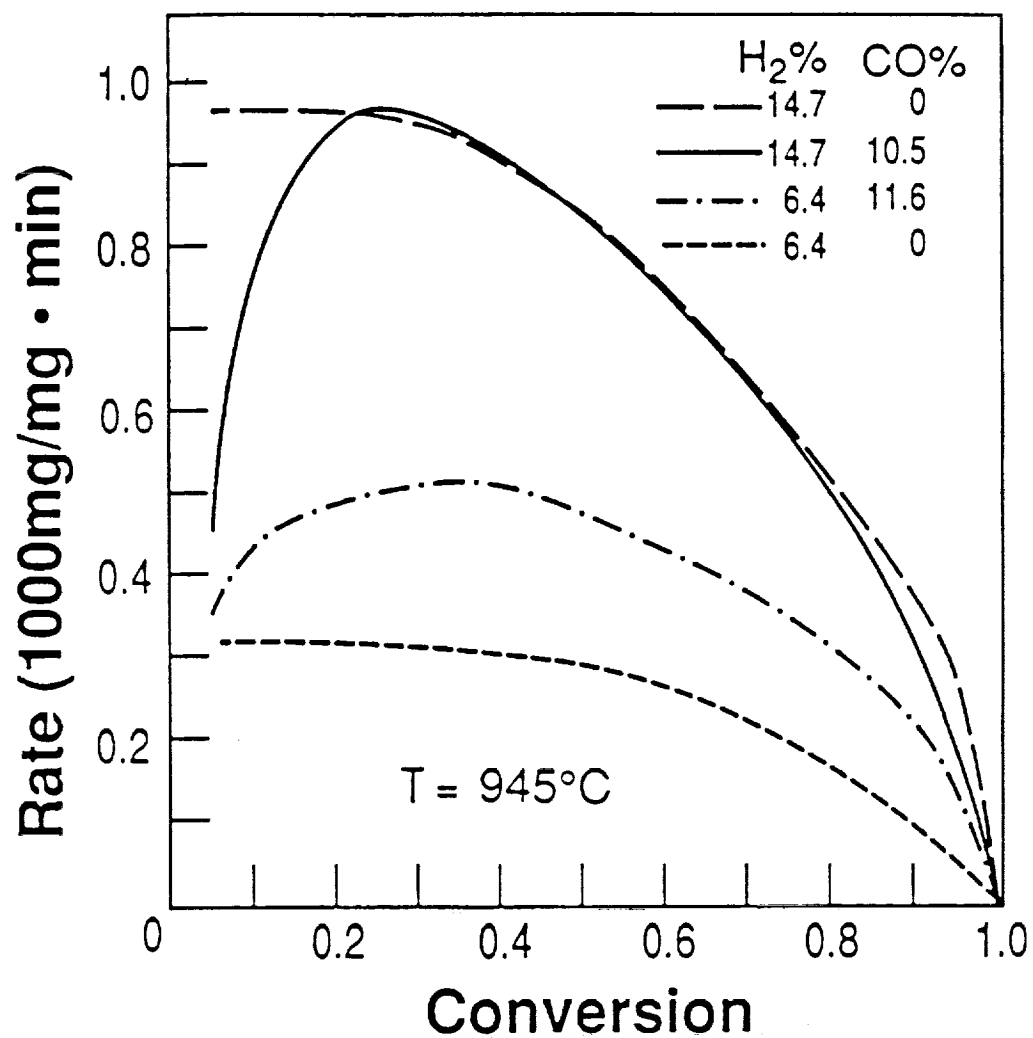


Figure 11 Effect of hydrogen concentration on the reduction rate of ilmenite by a mixture of H₂/CO. T=945°C

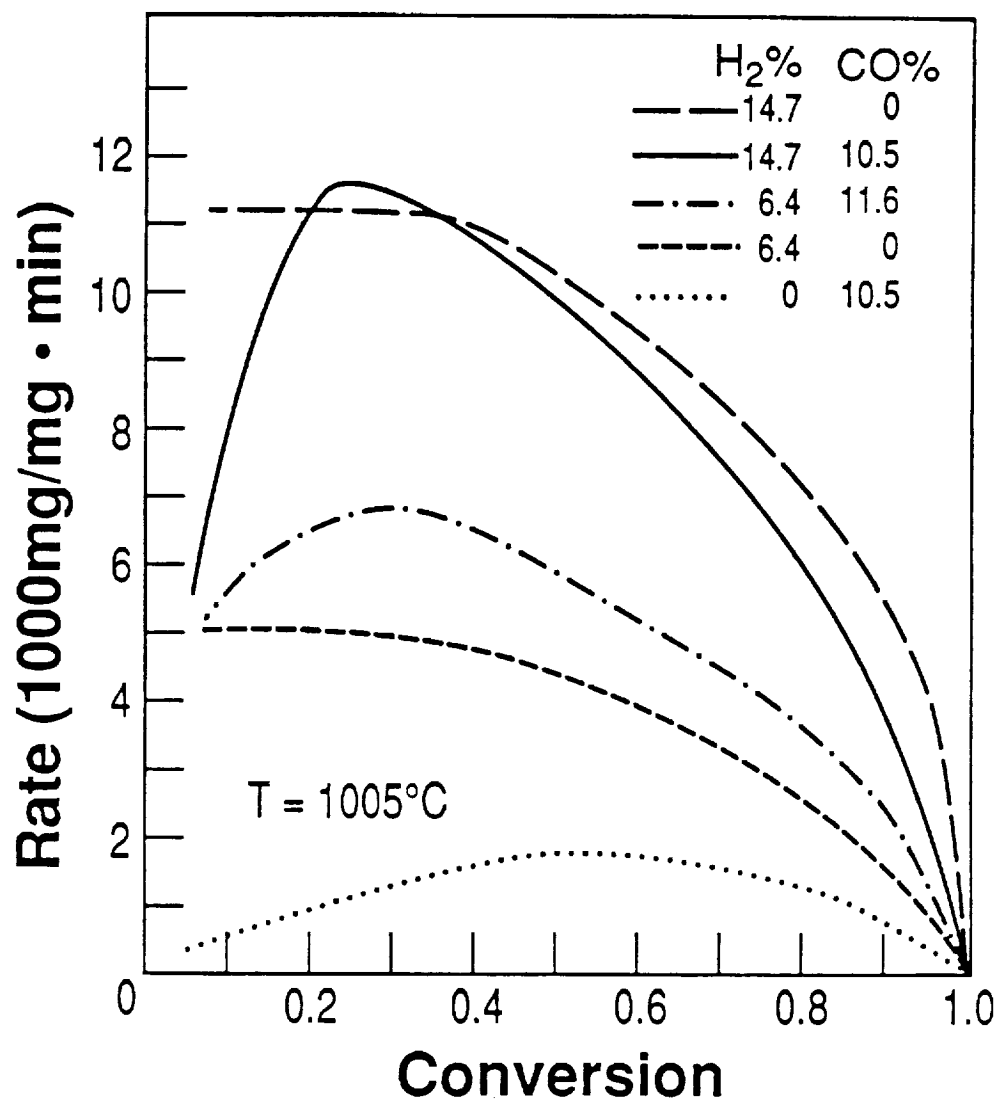


Figure 12 Effect of hydrogen concentration on the reduction rate of ilmenite by a mixture of H₂/CO. T=1005°C

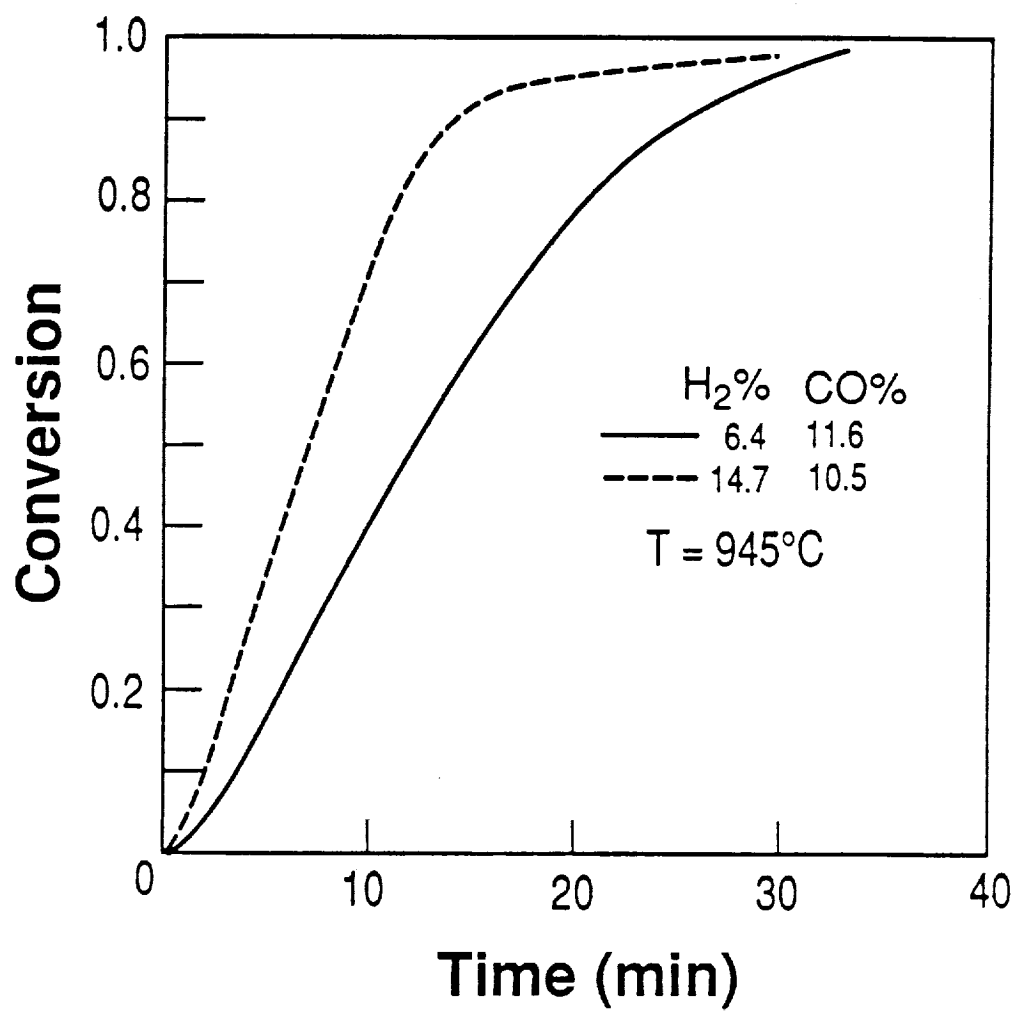


Figure 13 Effect of hydrogen concentration on the reduction of ilmenite by a mixture of H_2/CO . $T=945^{\circ}\text{C}$

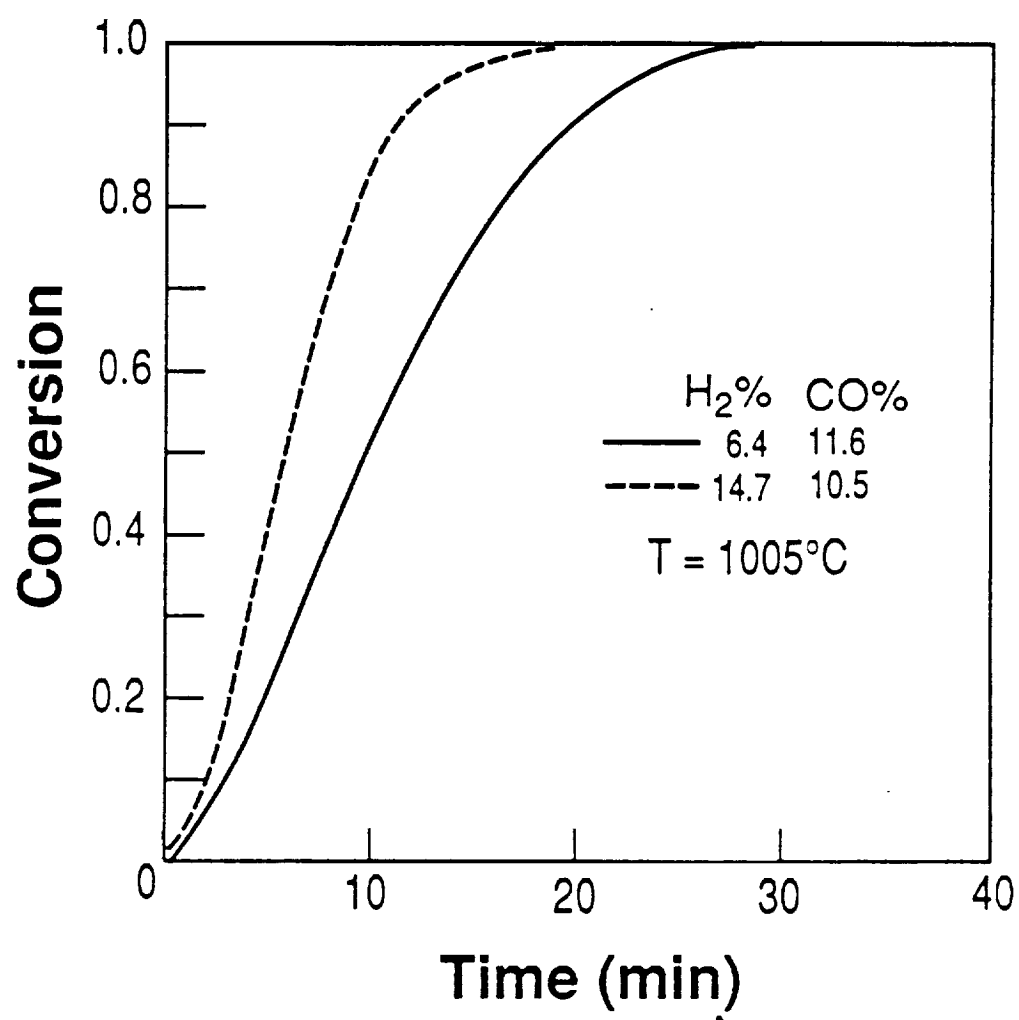


Figure 14 Effect of hydrogen concentration on the reduction of ilmenite by a mixture of H_2/CO . $T=1005^{\circ}\text{C}$

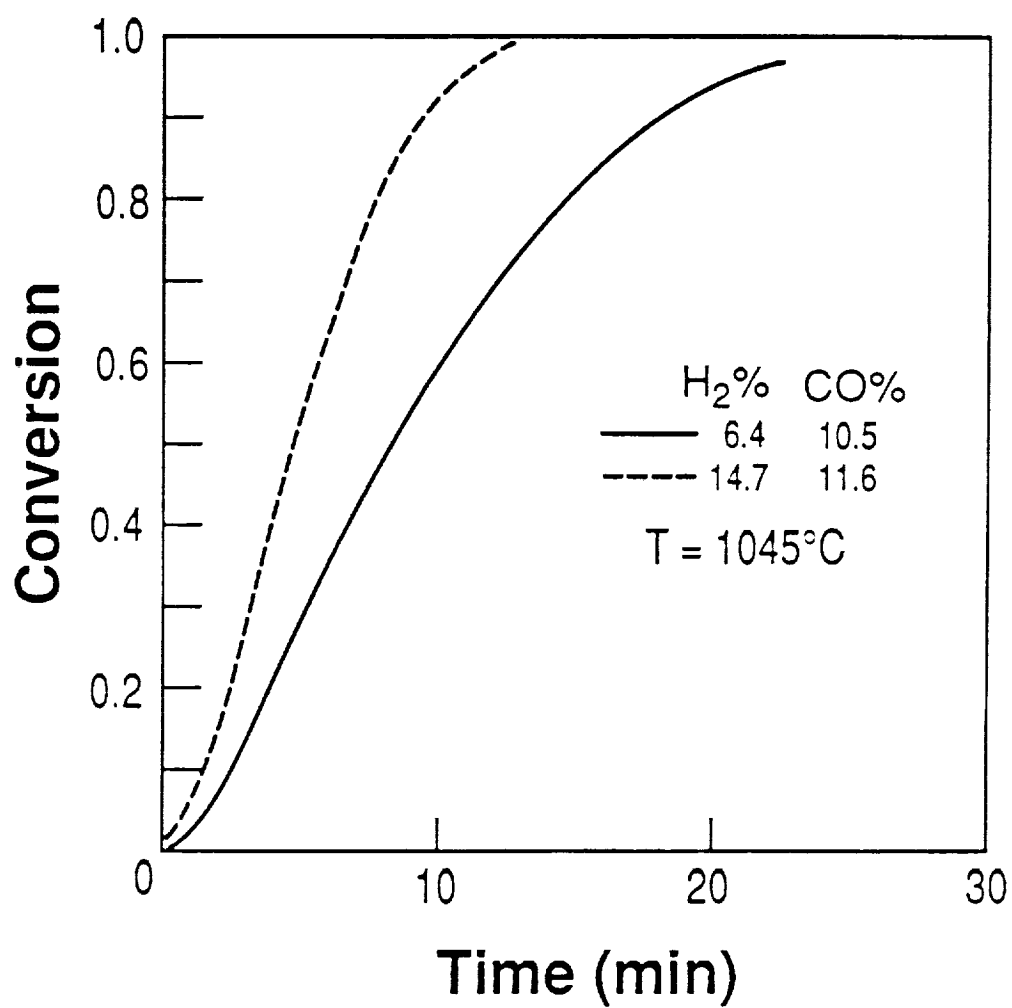


Figure 15 Effect of hydrogen concentration on the reduction of ilmenite by a mixture of H_2/CO . $T=1045^{\circ}\text{C}$

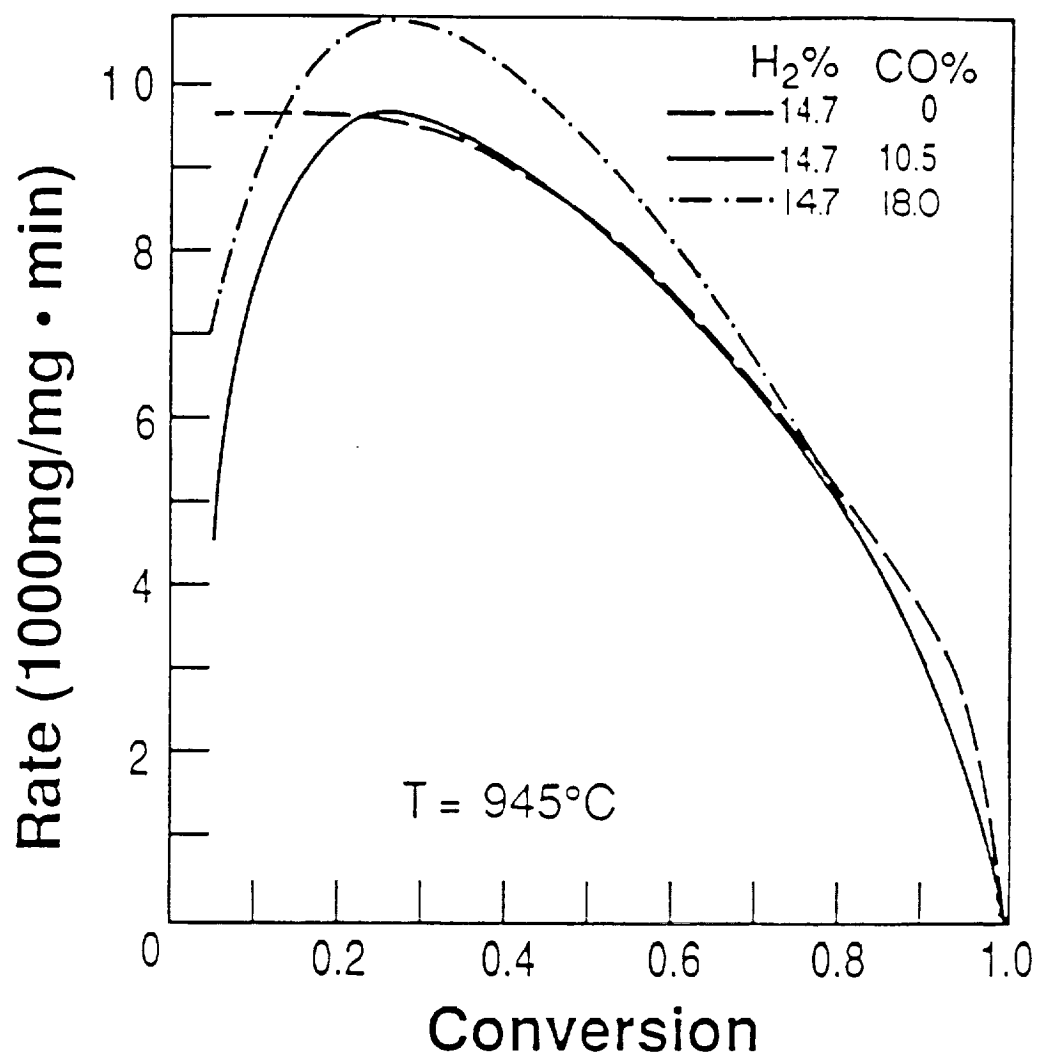


Figure 16 Effect of CO concentration on the reduction rate of ilmenite by a mixture of H₂/CO. T=945°C

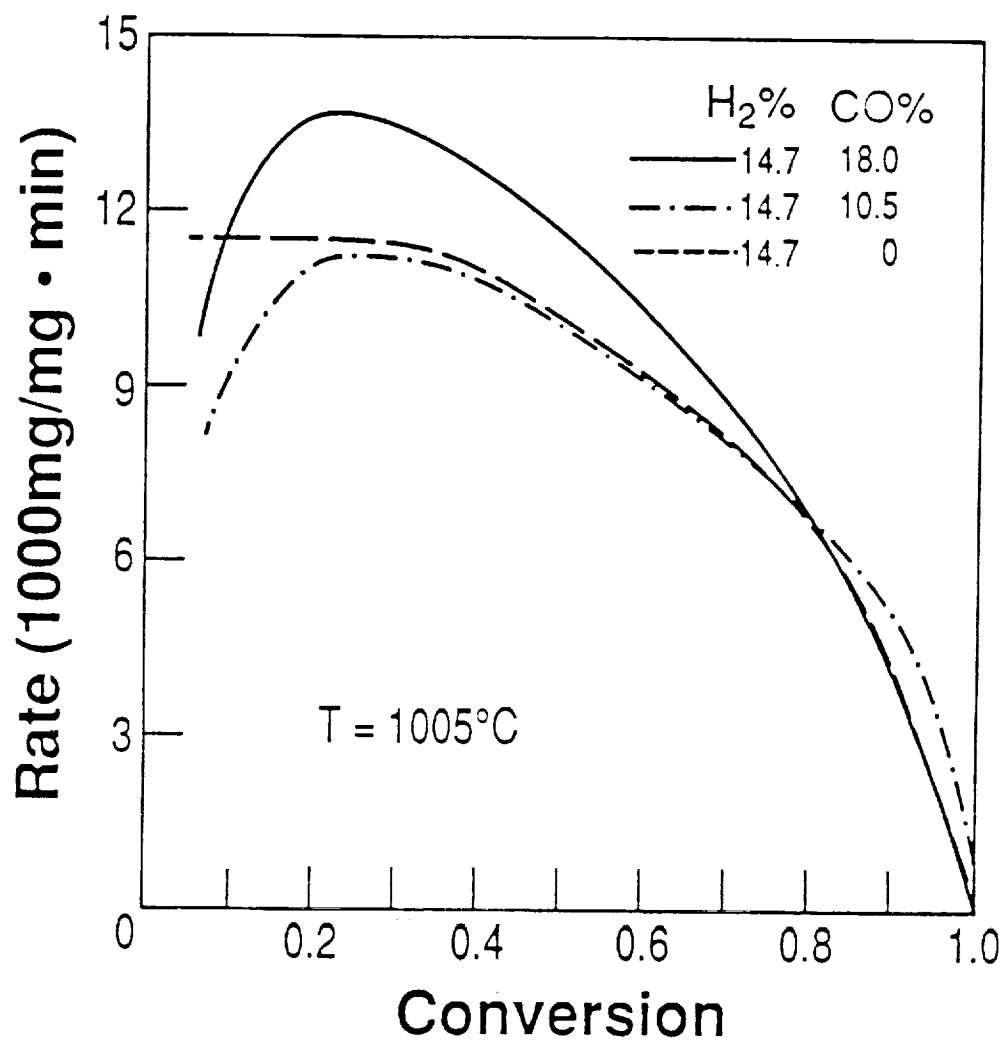


Figure 17 Effect of CO concentration on the reduction rate of ilmenite by a mixture of H_2/CO . $T=1005^{\circ}\text{C}$

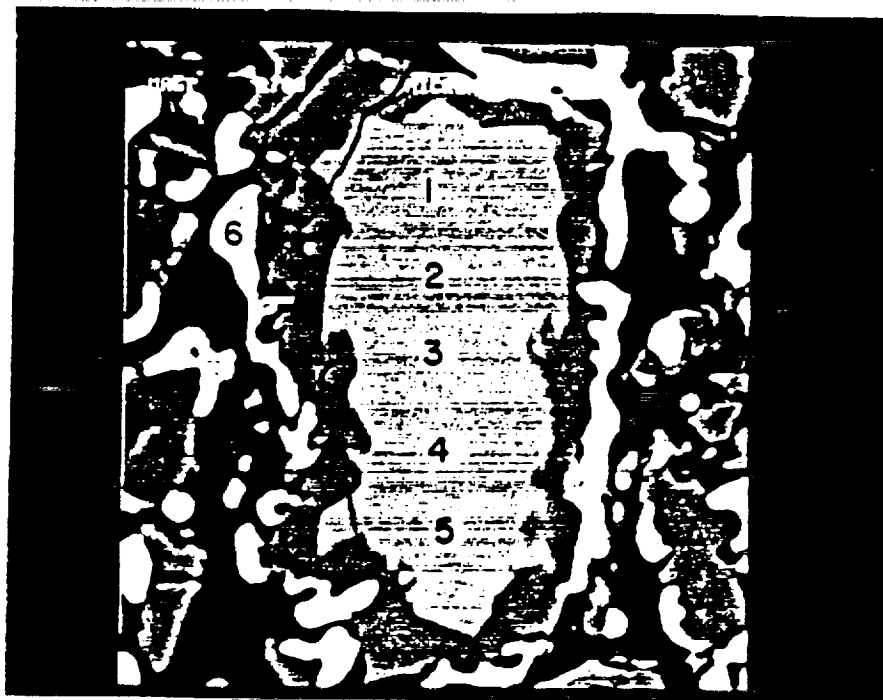


Figure 18a. Backscattered electron micrograph of the polished cross section of ilmenite flake after partial reduction, $T=1000^{\circ}\text{C}$, Magnification=2700X.

Point concentrations in atom% are:

Point	Ti	Fe
1	52	48
2	52	48
3	52	48
4	52	48
5	52	48
6	3	97
7	99	1



Figure 18b. Fe $K\alpha$ X-ray map of the cross section shown in 18a.

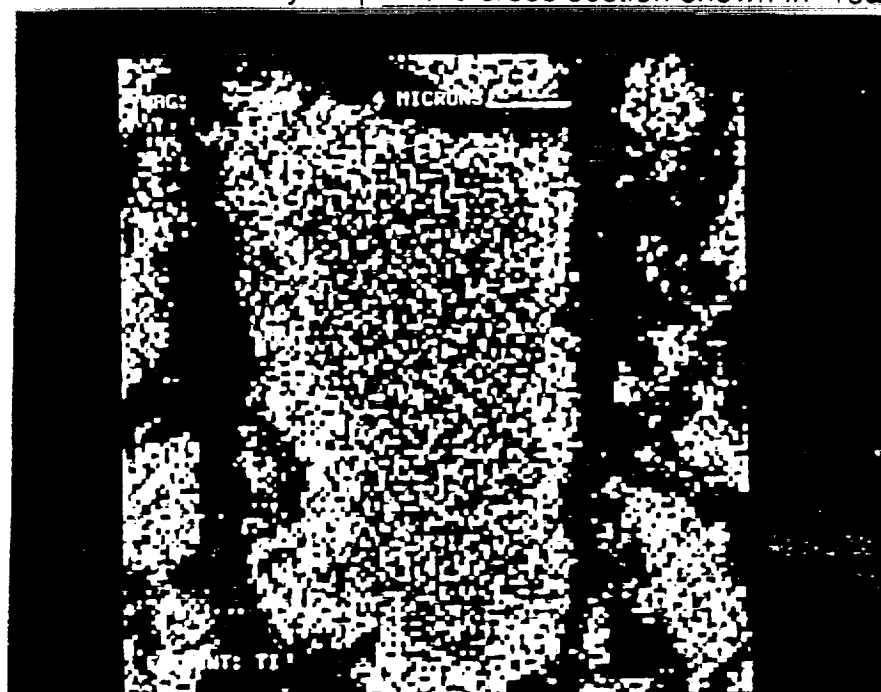


Figure 18c. Ti $K\alpha$ X-ray map of the cross section shown in 18a.

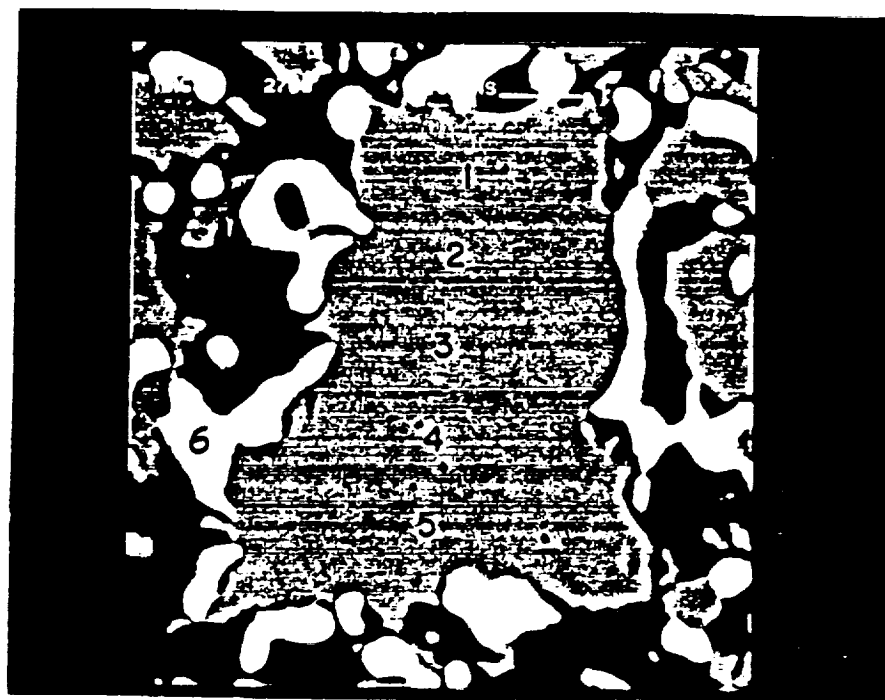


Figure 19a. Backscattered electron micrograph of the polished cross section of ilmenite flake after complete reduction, $T=1000^{\circ}\text{C}$, Magnification=2700X.

Point concentrations in atom% are:

Point	Ti	Fe
1	99	1
2	99	1
3	99	1
4	99	1
5	99	1
6	4	96

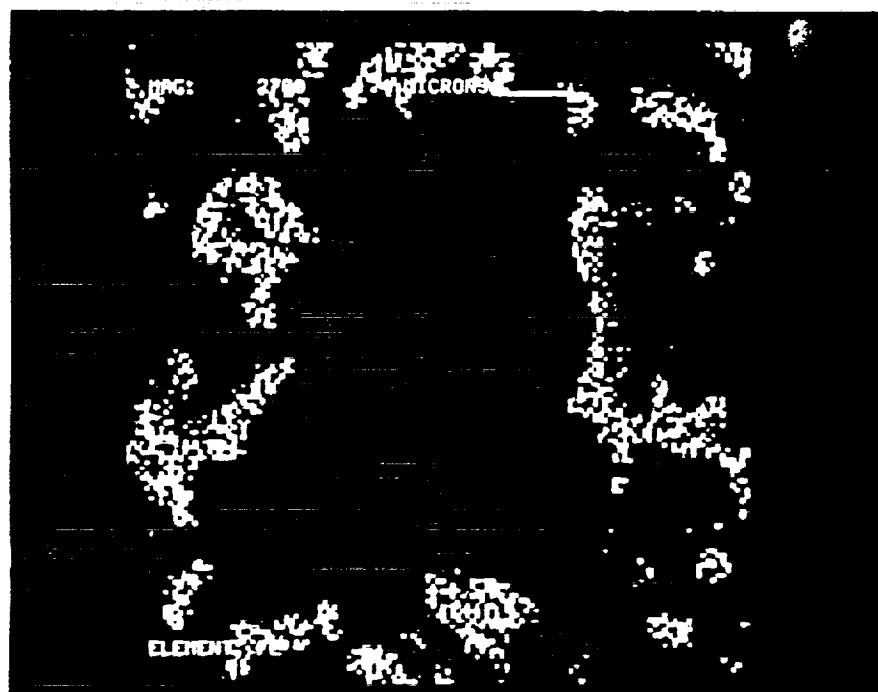


Figure 19b. Fe $K\alpha$ X-ray map of the cross section shown in 19a.



Figure 19c. Ti $K\alpha$ X-ray map of the cross section shown in 19a.

Non-slagging Carbothermal Reduction of Ilmenite

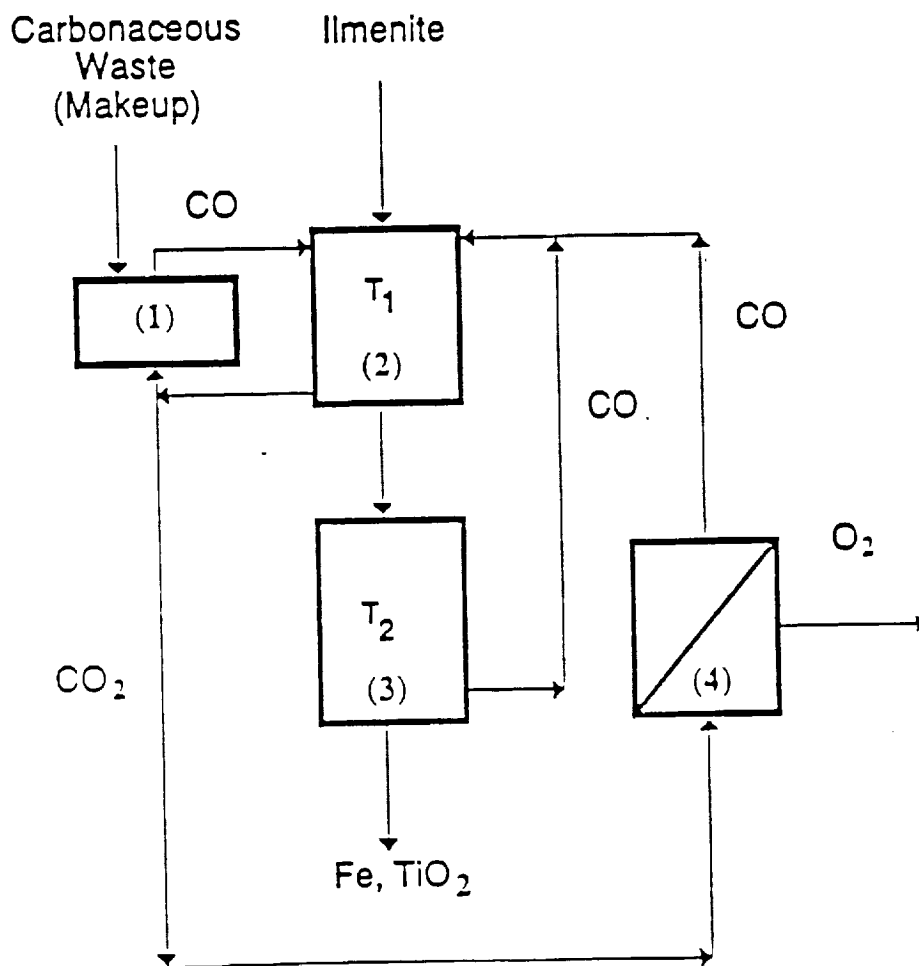


Figure 20 Flowsheet for carbothermal reduction of ilmenite using carbon deposited on the ilmenite

- (1) Carbonaceous waste converter
- (2) Carbon deposition reactor
- (3) Reduction reactor
- (4) Carbon dioxide electrolyser

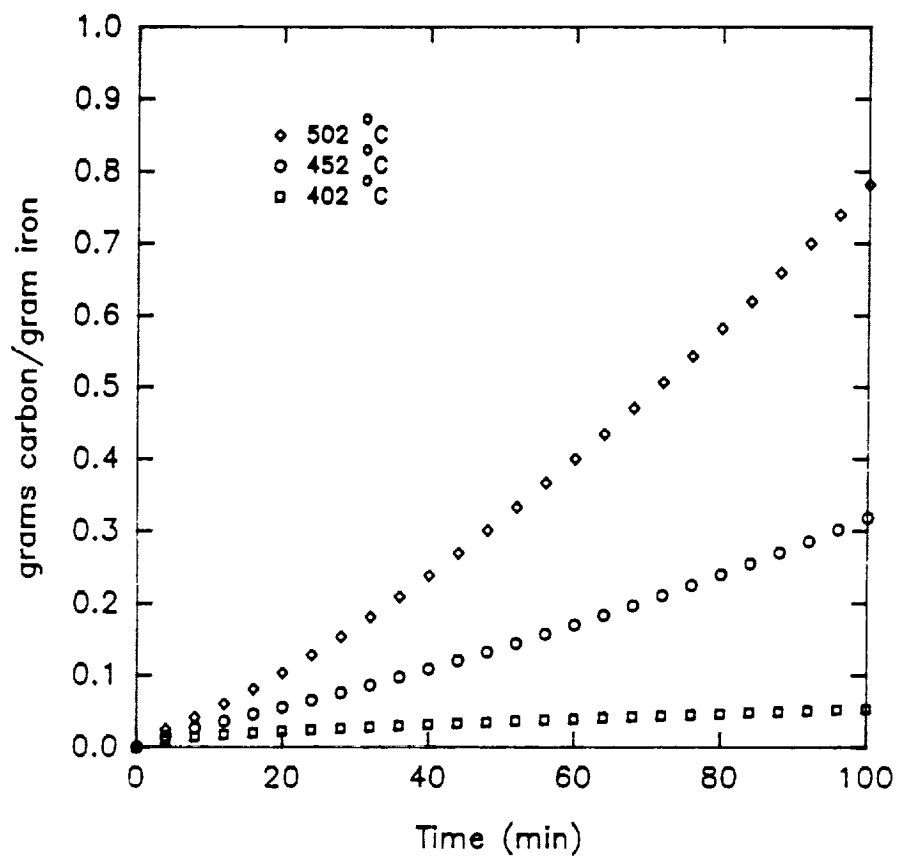


Figure 21 Deposition of carbon on iron in a mixture of 8.8% H₂ and 28% CO in N₂

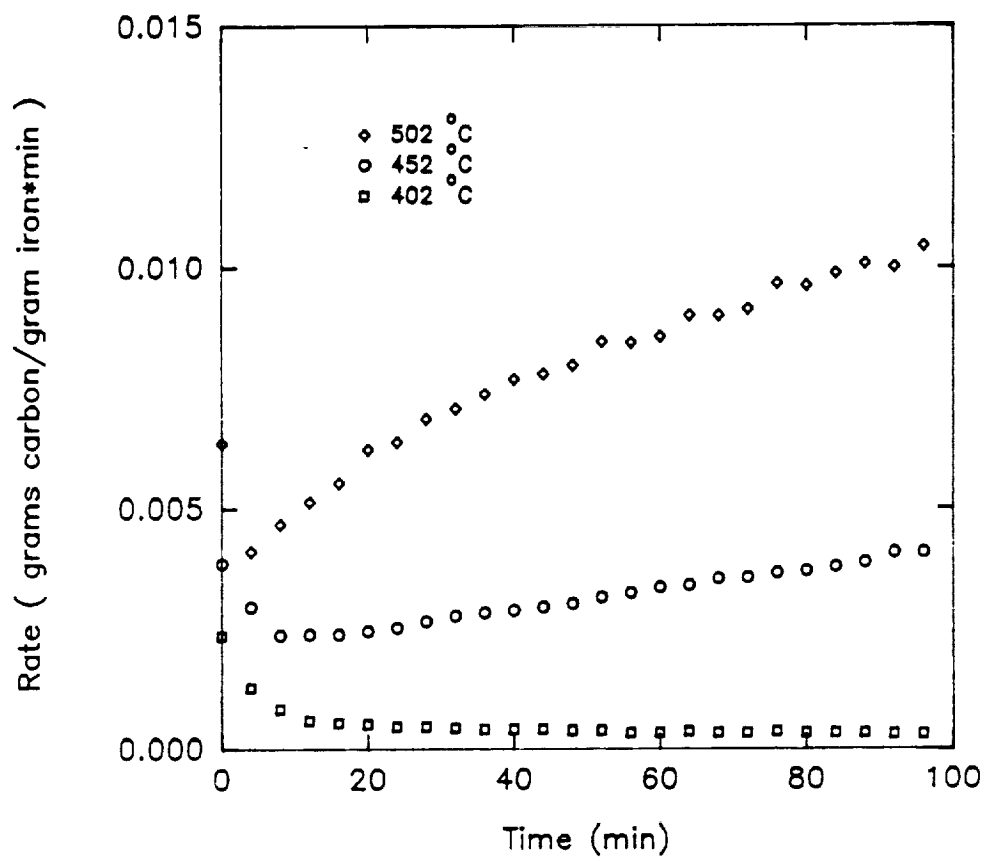


Figure 22 Rate of deposition of carbon on iron in a mixture of 8.8% H_2 and 28% CO in N_2

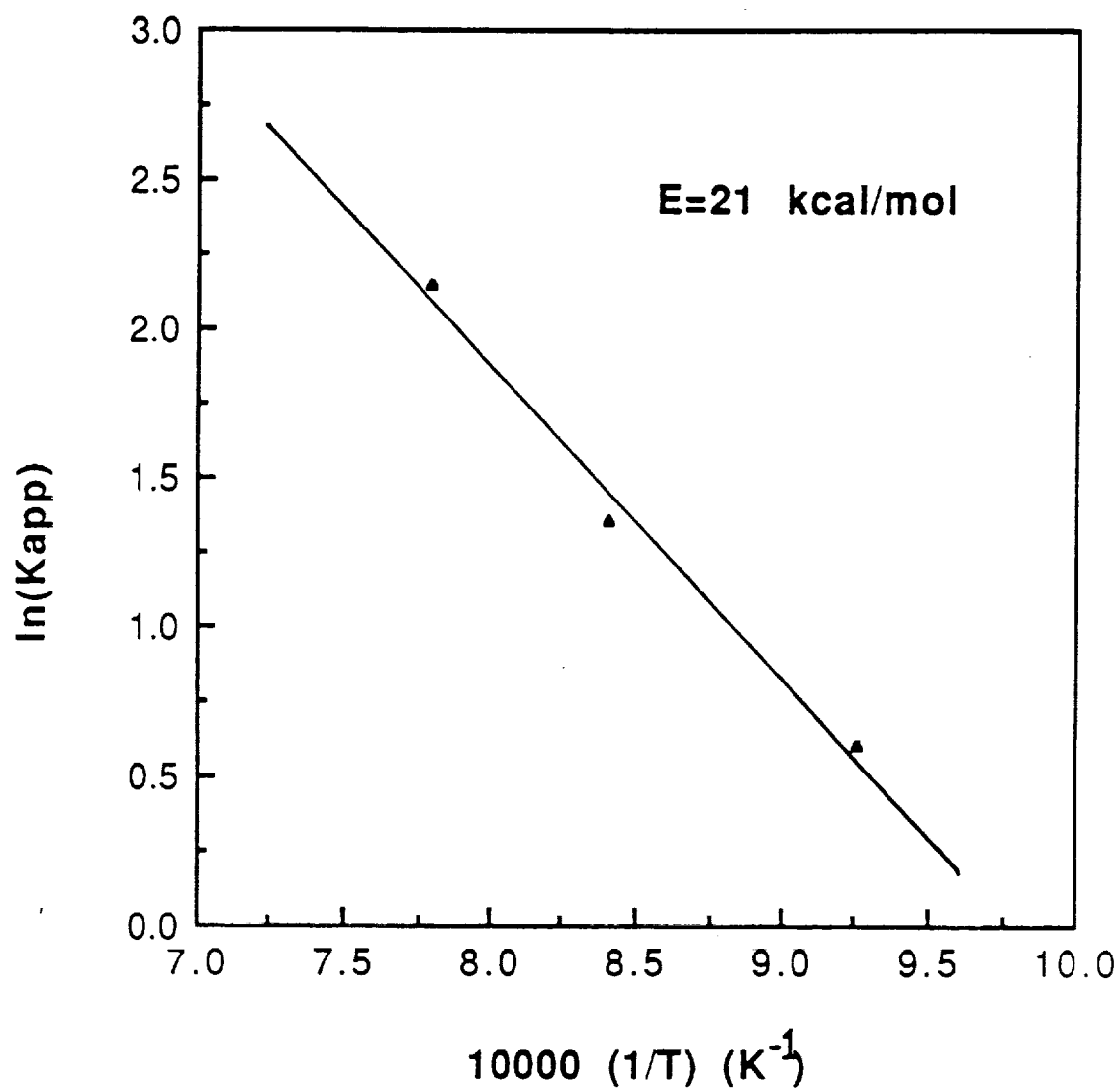


Figure 23 Temperature dependence of apparent rate coefficient

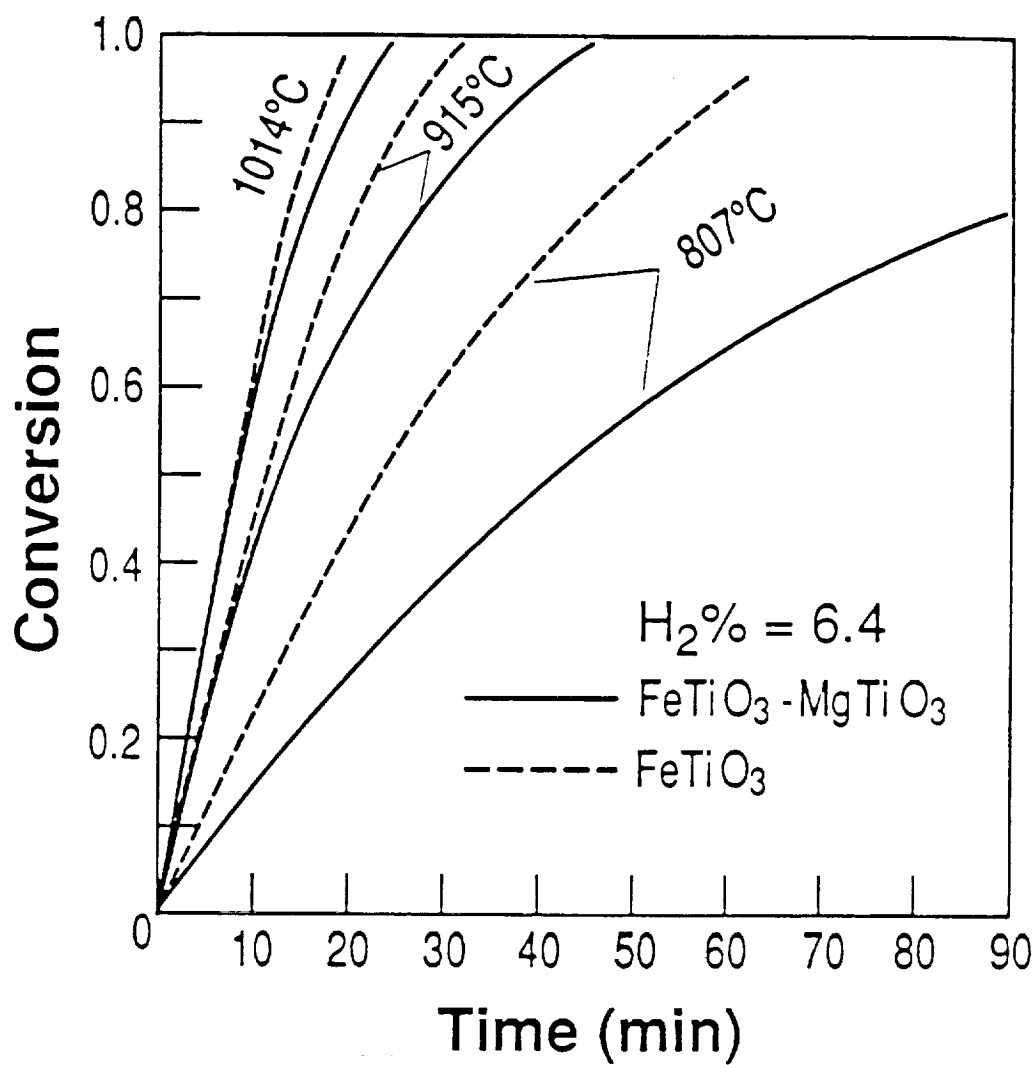


Figure 24 Effect of $MgTiO_3$ on the reduction of ilmenite.
 $MgTiO_3$ wt%=28.6, $H_2\%$ =6.4

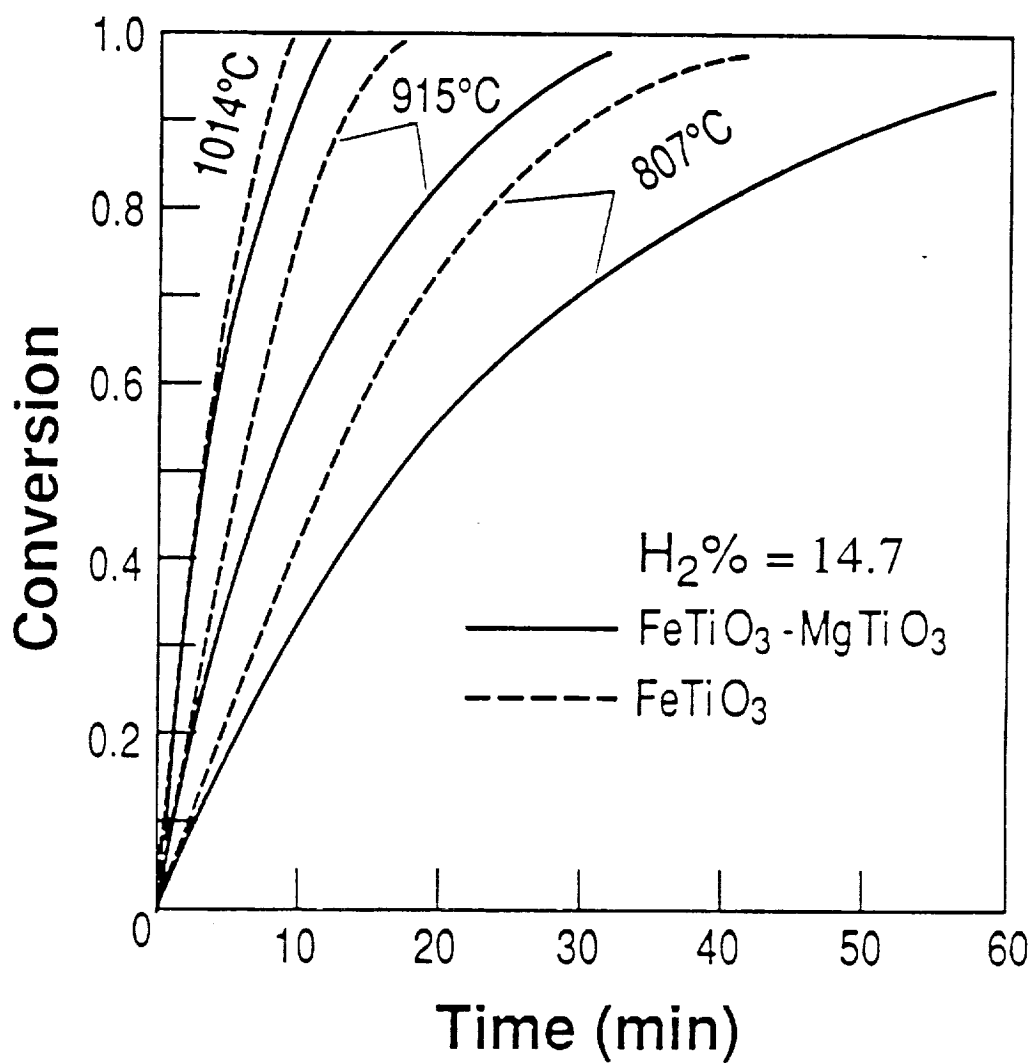


Figure 25 Effect of $MgTiO_3$ on the reduction of ilmenite.
 $MgTiO_3$ wt%=28.6, $H_2\%$ =14.7

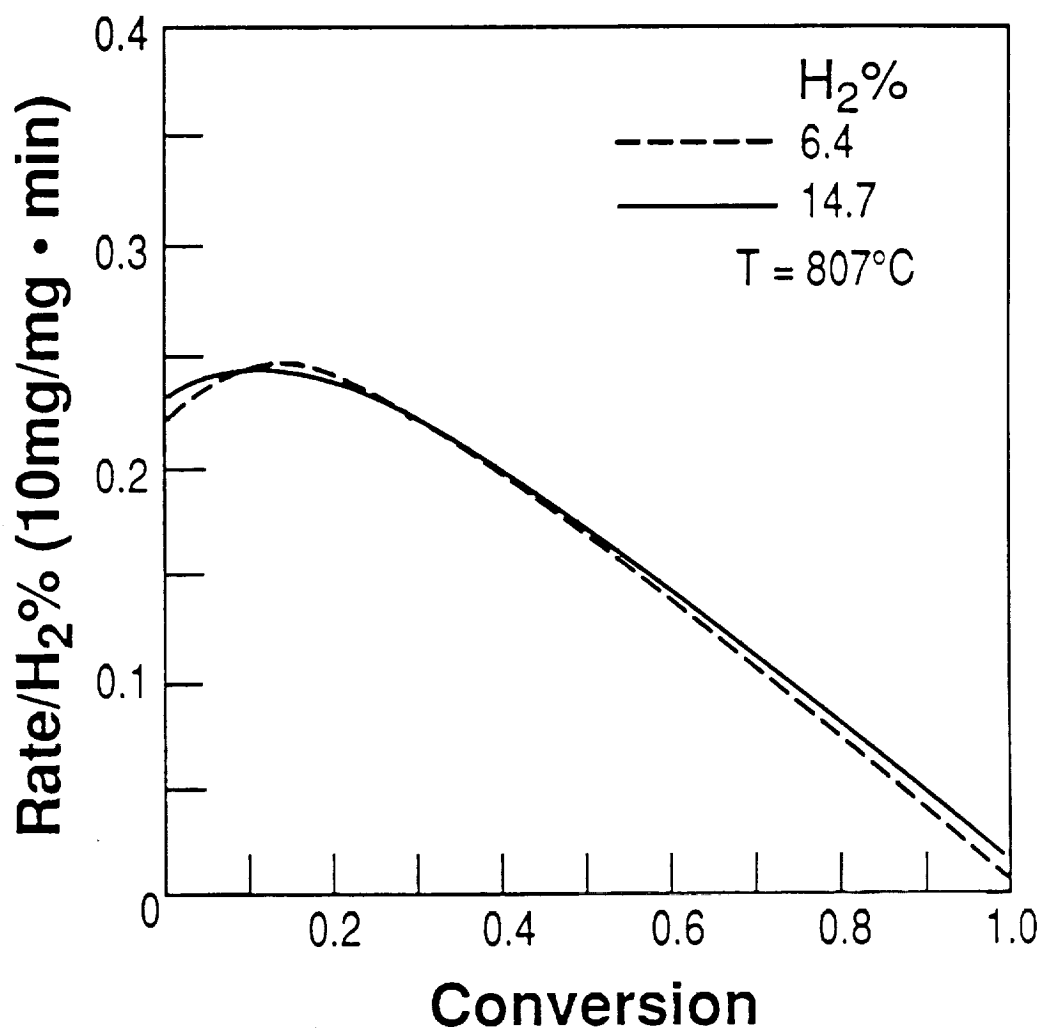


Figure 26 Effect of hydrogen concentration on the reduction rate of ilmenite.

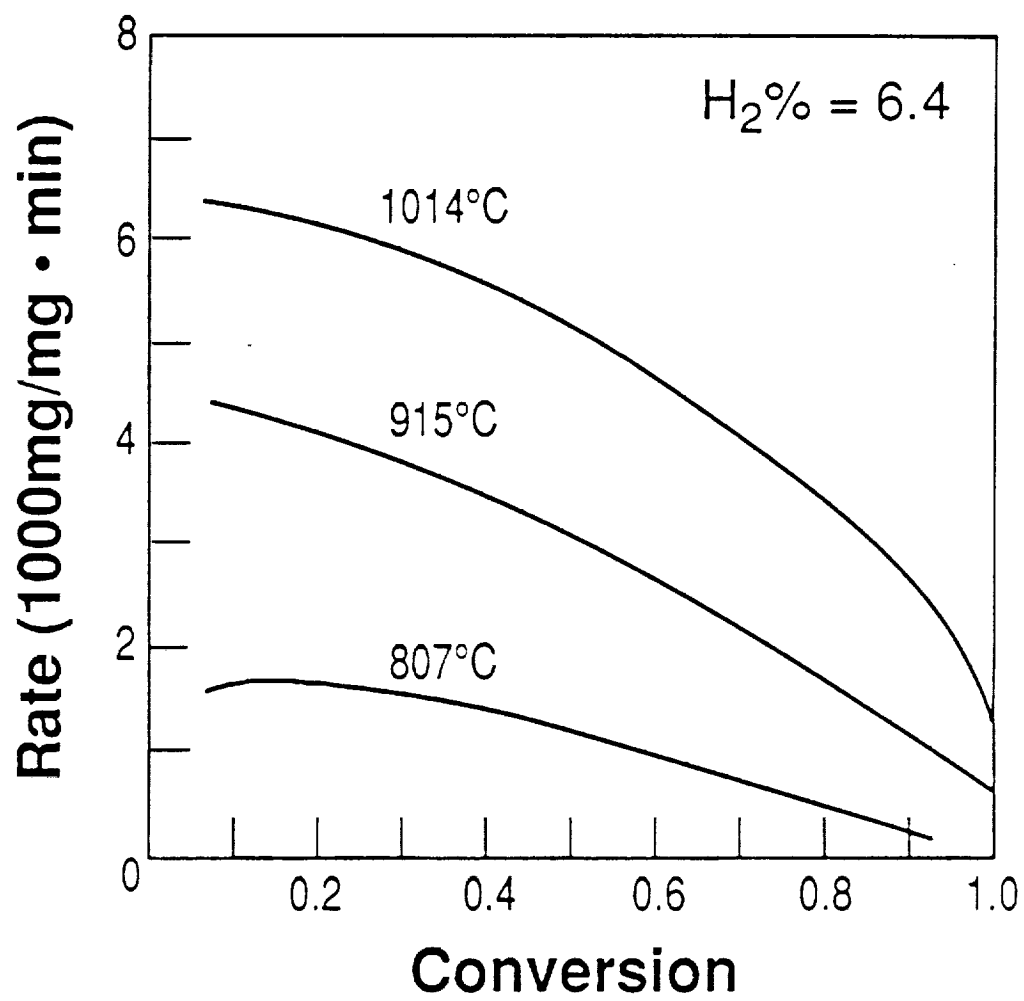


Figure 27 Effect of temperature on the reduction rate of ilmenite.

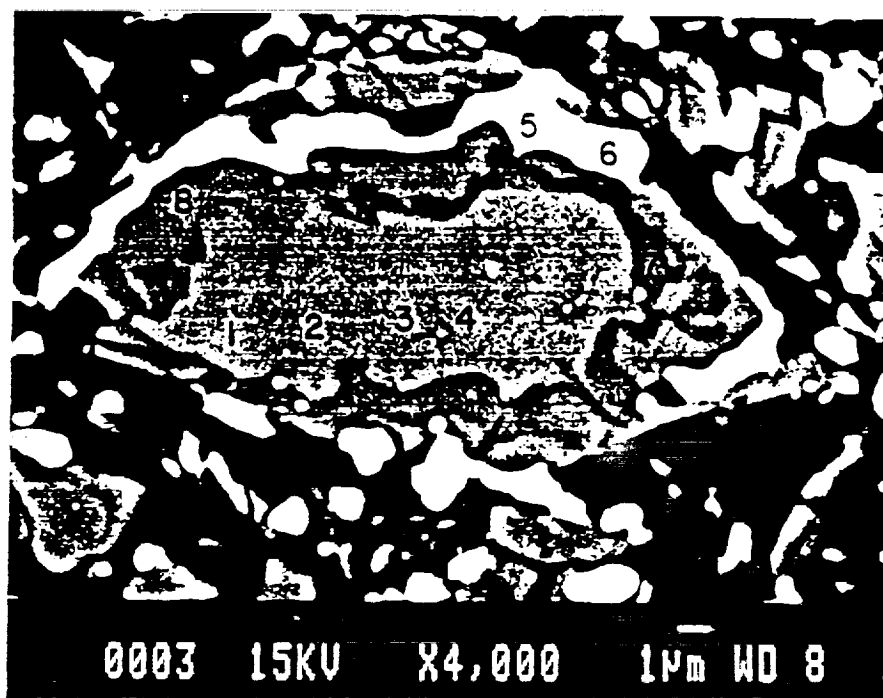


Figure 28a SEM backscattered electron micrograph of polished cross section of $\text{FeTiO}_3\text{-MgTiO}_3$ flake after partial reduction, $T=1000^\circ\text{C}$, Magnification=4000X. MgTiO_3 wt%=28.6

Point concentrations in atom% are:

Point	Ti	Fe	Mg
1	52	23	25
2	51	22	27
3	51	22	27
4	51	22	27
5	5	95	0
6	9	90	1
7	74	10	16
8	85	7	8

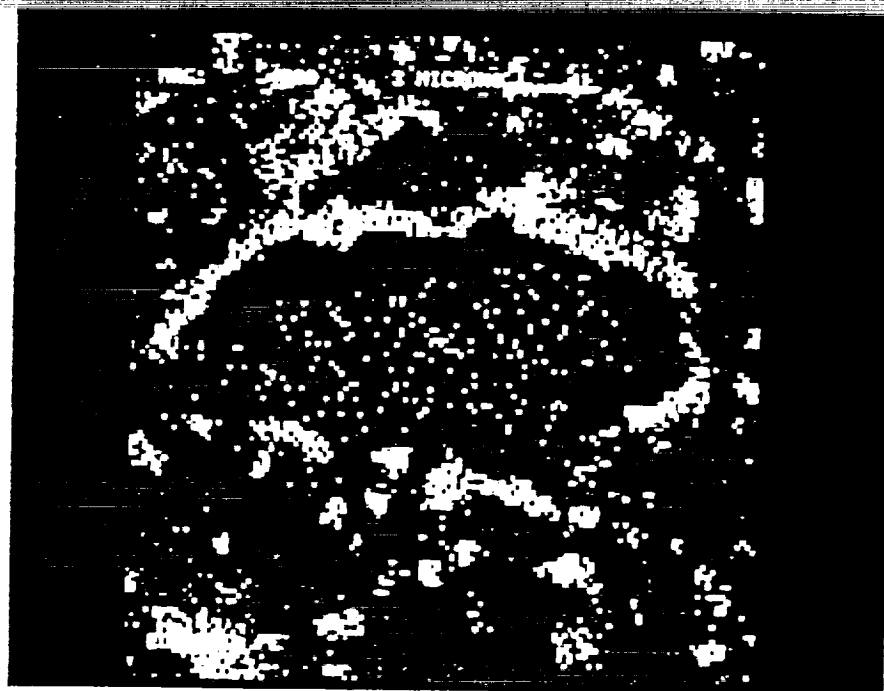


Figure 28b Fe K α X-ray map of the cross-section shown in 7.6a.



Figure 28c Ti K α X-ray map of the cross-section shown in 28a.

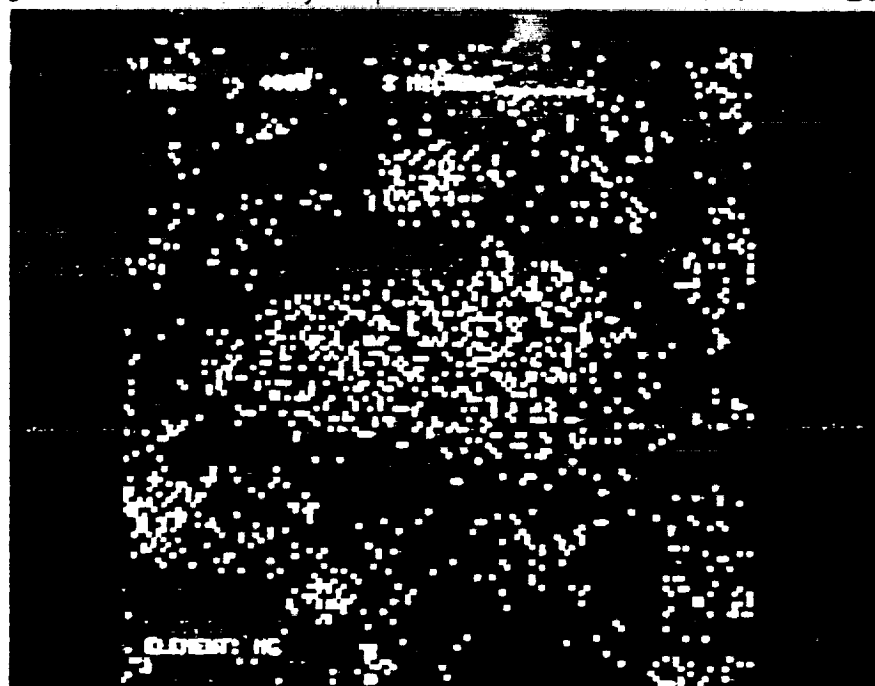


Figure 28d Mg K α X-ray map of the cross-section shown in 28a.

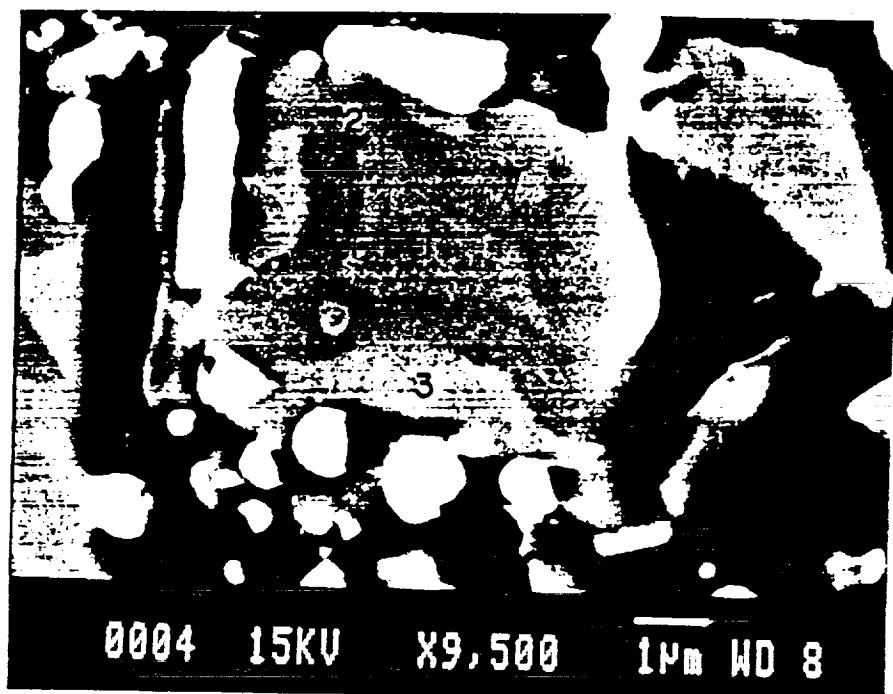


Figure 29a SEM backscattered electron micrograph of polished cross section of $\text{FeTiO}_3\text{-MgTiO}_3$ flake after partial reduction, $T=1000^\circ\text{C}$, Magnification=9500X. MgTiO_3 wt%=28.6

Point concentrations in atom% are:

Point	Ti	Fe	Mg
1	57	6	37
2	71	8	21
3	90	4	6

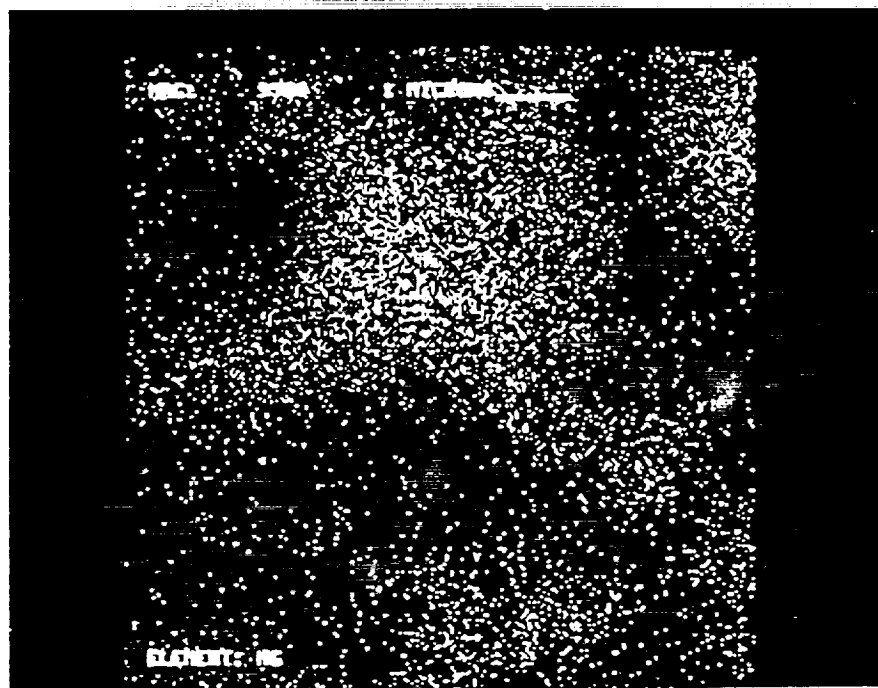


Figure 29b Mg K α X-ray map of the cross-section shown in 7.7a.



Figure 30a SEM backscattered electron micrograph of polished cross section of $\text{FeTiO}_3\text{-MgTiO}_3$ flake after partial reduction, $T=915^\circ\text{C}$, Magnification=8500X.
 MgTiO_3 wt%=28.6

Point concentrations in atom% are:

Point	Ti	Fe	Mg
1	51	7	42
2	52	7	41
3	50	7	43
4	50	8	42
5	4	95	1
6	97	2	1

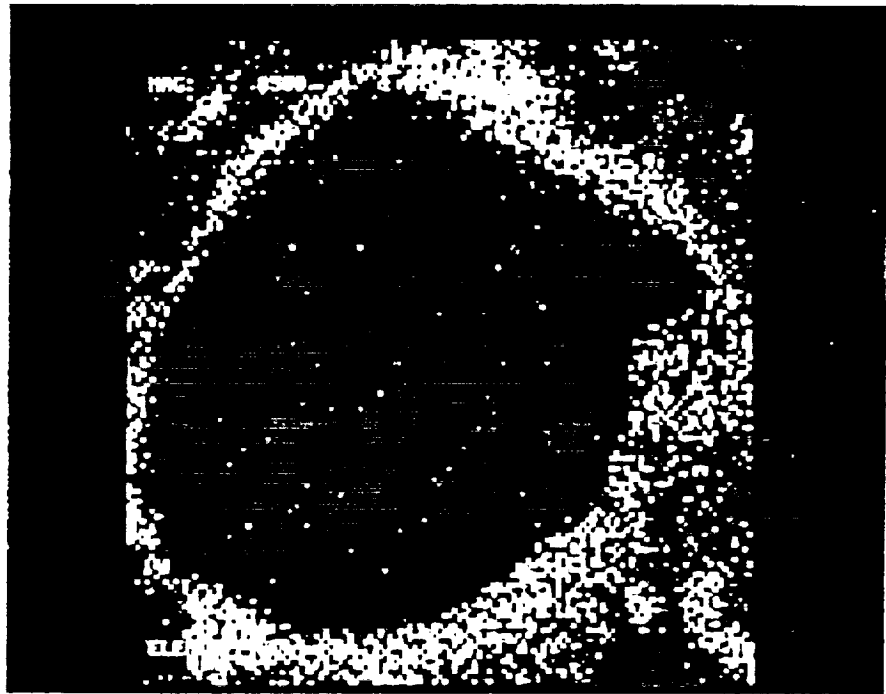


Figure 30b Fe K α X-ray map of the cross-section shown in 30a.

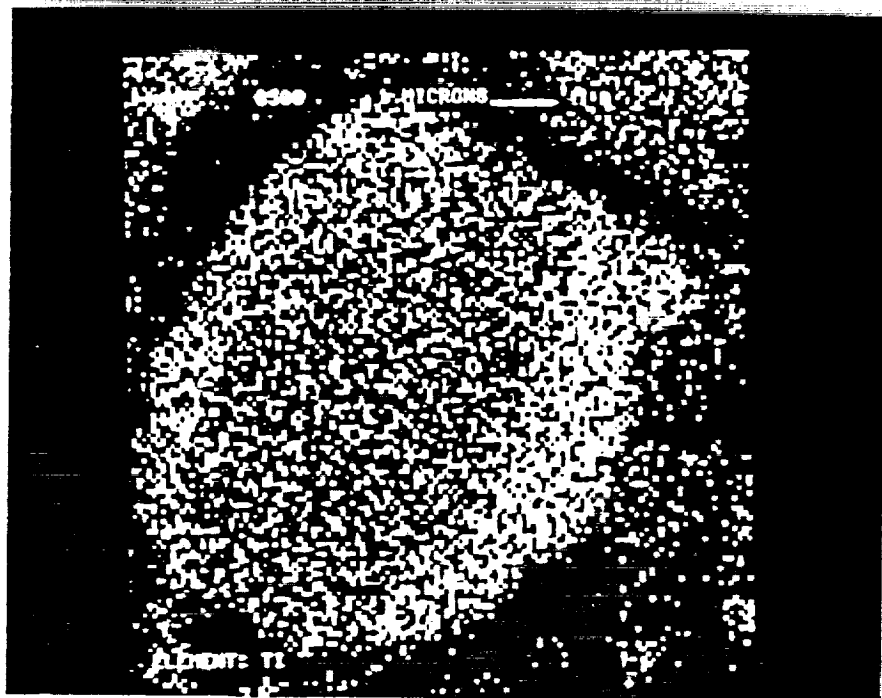


Figure 30c Ti K α X-ray map of the cross-section shown in 30a.

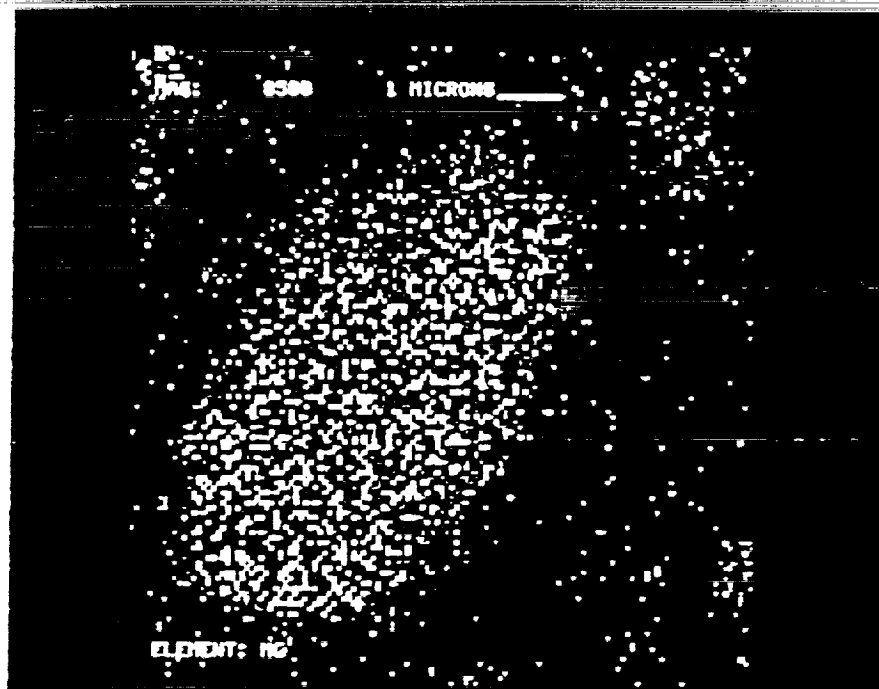


Figure 30d Mg K α X-ray map of the cross-section shown in 30a.

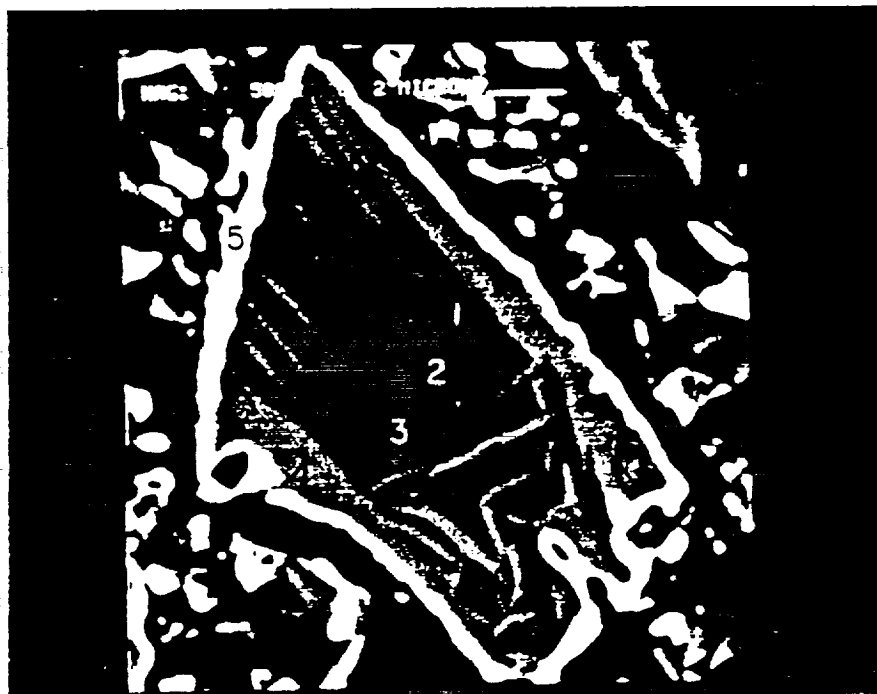


Figure 31a SEM backscattered electron micrograph of polished cross section of $\text{FeTiO}_3\text{-MgTiO}_3$ flake after partial reduction, $T=807^\circ\text{C}$, Magnification=5000X. MgTiO_3 wt%=28.6

Point concentrations in atom% are:

Point	Ti	Fe	Mg
1	50	8	42
2	51	7	42
3	50	6	44
4	94	4	2
5	7	91	2

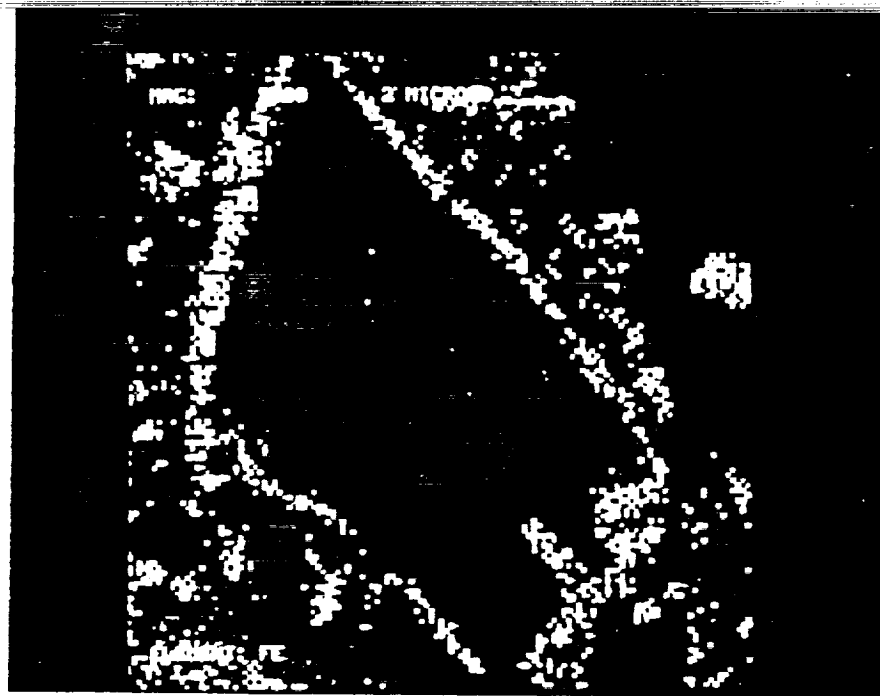


Figure 31b Fe K α X-ray map of the cross-section shown in 31a.

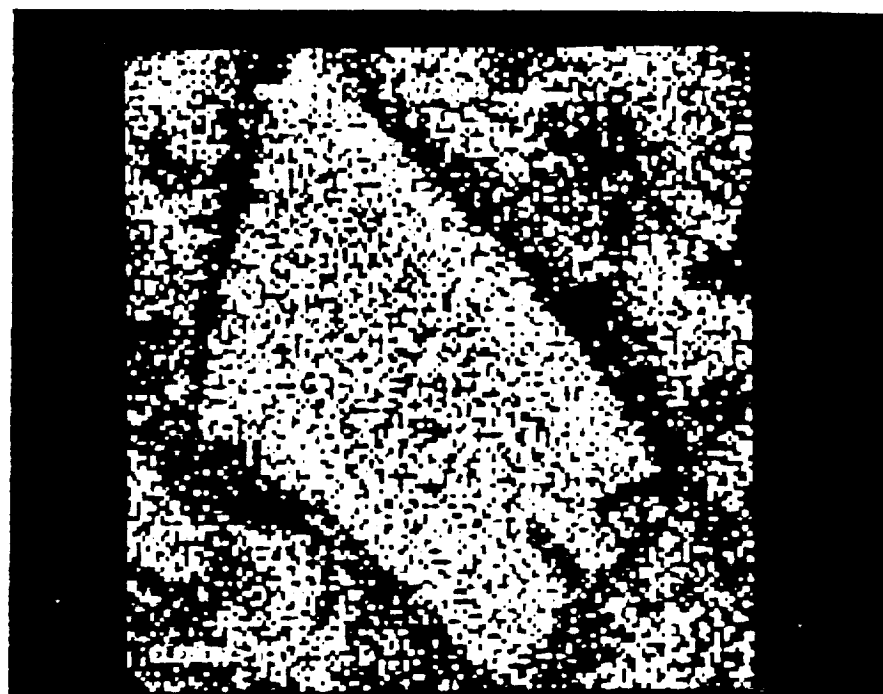


Figure 31c Ti K α X-ray map of the cross-section shown in 31a.

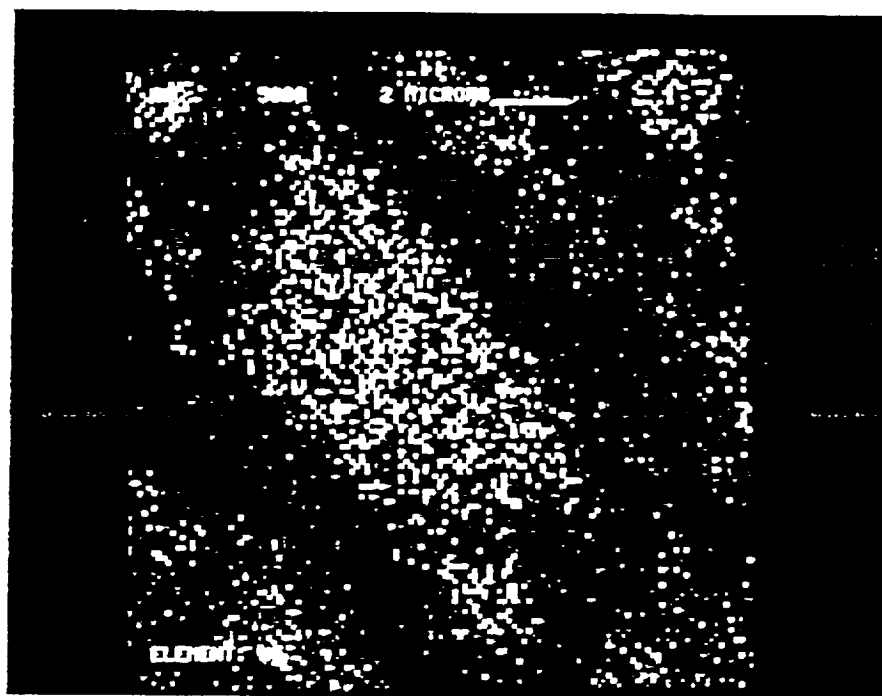


Figure 31d Mg K α X-ray map of the cross-section shown in 31a.

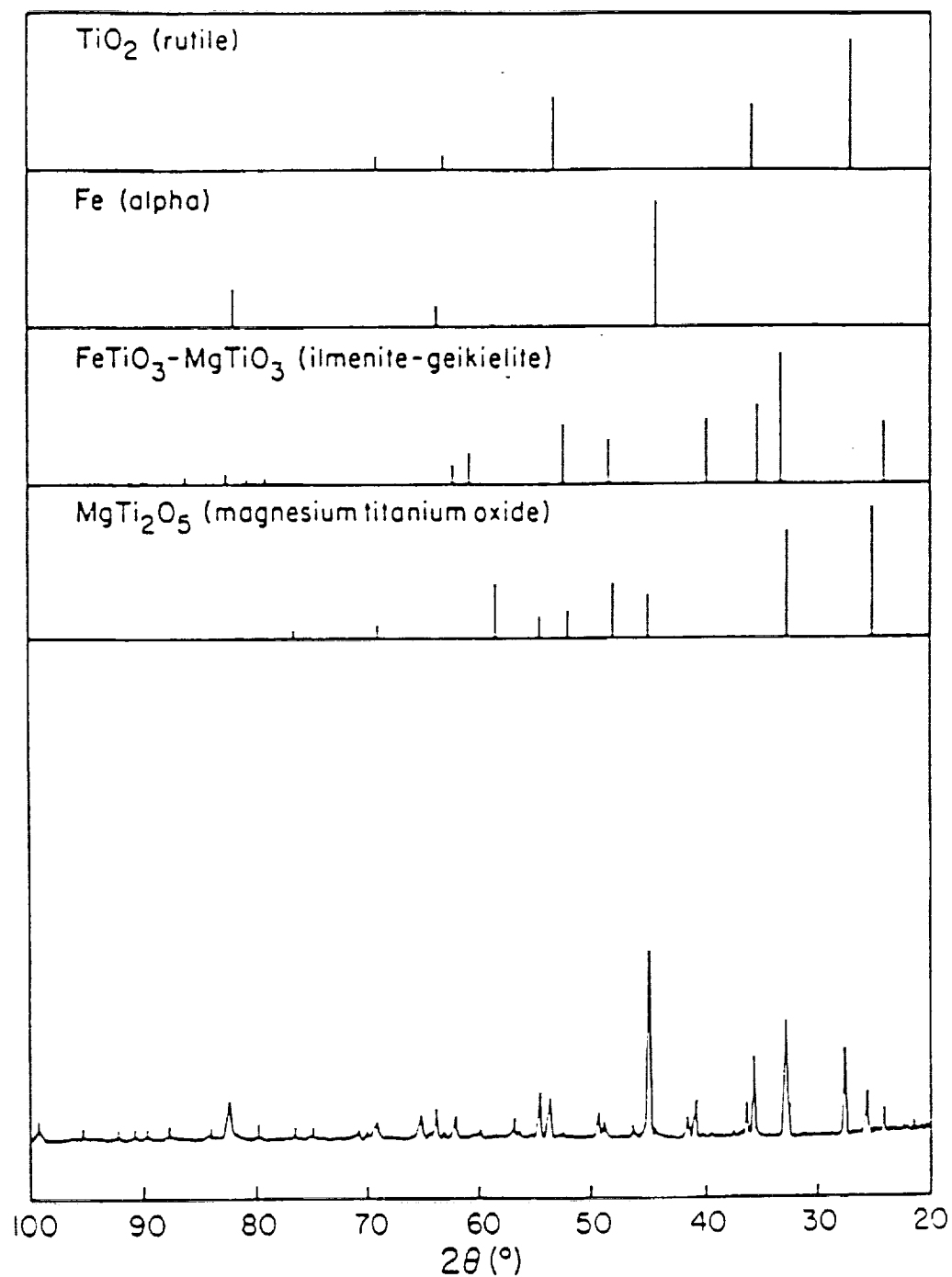


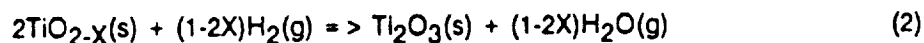
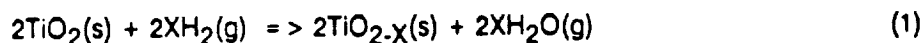
Figure 32 X-ray diffraction spectrum of FeTiO₃-MgTiO₃ flake after partial reduction, T=1000°C

Cold Plasma Processing of Local Planetary Ores
for
Oxygen and Metallurgical Important Metals

D. Bullard and D. C. Lynch
Department of Materials Science and Engineering
The University of Arizona

Abstract

Anatase has been reacted with hydrogen in a microwave induced plasma. A D. C. voltage regulator was used to provide an applied field within the plasma by which to accelerate electrons and ions for reaction with the solid specimen. The TiO_2 specimens were reacted at pressures ranging from 6 to 26 Torr, absorbed power levels of 0.4 to 1.4 KW, and applied field strengths of 0 to ± 65.6 V per cm. The anatase can be converted to Ti_2O_3 according to the reactions:

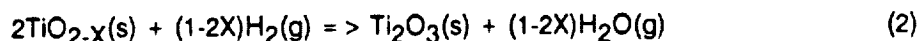
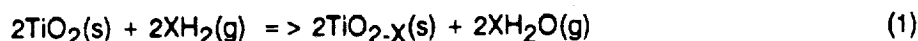


The applied field has a significant impact on the ability to promote the reaction. Without the applied field only reaction 1 occurs to any appreciable extent. With the applied field over 60 % of the TiO_2 can be converted to Ti_2O_3 with in 11 minutes.

Cold Plasma Processing of Local Planetary Ores
for
Oxygen and Metallurgical Important Metals

D. Bullard and D. C. Lynch
Department of Materials Science and Engineering
The University of Arizona

Anatase has been reacted with hydrogen in a microwave induced plasma. A D. C. voltage regulator was used to provide an applied field within the plasma by which to accelerate electrons and ions for reaction with the solid specimen. The TiO_2 specimens were reacted at pressures ranging from 6 to 26 Torr, absorbed power levels of 0.4 to 1.4 KW, and applied field strengths of 0 to ± 65.6 V per cm. The anatase can be converted to Ti_2O_3 according to the reactions:



The applied field has a significant impact on the ability to promote the reaction. Without the applied field only reaction 1 occurs to any appreciable extent. With the applied field over 60 % of the TiO_2 can be converted to Ti_2O_3 with in 11 minutes.

Introduction

This research program was initially funded by the Space Engineering Research Center (SERC), however during this past year the program has been funded entirely by the U.S. Bureau of Mines' Pyrometallurgy Center at the University of Missouri at Rolla (contract numbers MU-USDI-G1175129 and MU-USDI-G1105129). We wish to gratefully acknowledge their support.

Support from the Bureau of Mines has not altered our basic perspective, namely, to investigate the feasibility of using a "cold" or non-equilibrium plasma in the enhancement of reaction rates and in the biasing of the thermodynamics of reactions that would not proceed if conventional means were employed. There are many reasons to explore the potential of this new technology for both terrestrial and extraterrestrial applications. From an extraterrestrial view point the reduction of TiO_2 (or any oxide) with hydrogen will yield H_2O , which with electrolysis can be converted to O_2 and hydrogen for recycle.

Approach

In conventional processing reactants are heated until the chemical potential of the desired reaction is negative, and the temperature is high enough to ensure rapid reaction rates. In a cold plasma energy is used to produce radicals and heat. Radicals are produced by reducing the pressure,

such that electrons, responding to electromagnetic radiation, are accelerated until they have sufficient energy to liberate bound electrons, break bonds and excite both ions and neutral species upon impact. Radicals formed in this manner are available for reaction, provided they can get to the surface of the solid.

In a plasma, the specimen is bombarded by electrons, and as a result the specimen develops a negative charge. The charge builds up with time, eventually inhibiting further electron bombardment, but attracting positively charged ions. The positively charged ions form the Debye Sheath which surrounds the specimen. In order to promote reactions between ions produced in the plasma and a solid specimen, it is necessary to get the ion through the sheath so that it can contact the specimen. An applied field can be used to both draw ions and electrons to a solid specimen and accelerate those ions or electrons so that upon impact they may have sufficient energy to break bonds and thereby initiate reactions or enhance reaction rates.

Experimental

Energy Efficiency - The efficiency of energy utilization is an important issue in the development and design of a process for recovery of oxygen. Data have been collected to help evaluate the energy efficiency of a plasma. There are three issues which must be examined in order to evaluate the efficiency of a plasma reactor. Those issues are:

1. efficiency of converting electrical energy to microwaves at 2.45 GHz,
2. efficiency of absorption of microwaves by a plasma, and
3. effective utilization of the plasma in plasma - solid reactions.

The last item has been, and remains, the primary focus of this investigation. While advances are being made in understanding the fundamental problems involved in promoting plasma - solid reactions, measurements have also been made regarding the first two issues.

The efficiency of converting single phase electrical energy at 240 V and 60 Hz to microwaves can be estimated from the plot shown in Figure 1. In that figure the transmitted microwave power is plotted versus input power. The efficiency varies from 20% at lower transmitted power settings to 31% at 1.4 KW. Those efficiencies are well below the maximum of 65 to 70% reported by John Gerling of Gerling Brothers, a major manufacturer of microwave generators.

From Figure 1 it appears the efficiency is a function of scale. The absorbed power level is, as will be shown later, the output power level of the microwave unit. If Y in the equation in Figure 1 is assumed to be 3 KW (the maximum value for the unit) then the equation predicts an input power of 7.2 KW or an efficiency of approximately 42%.

Other issues which impact the efficiency of converting electrical energy to microwaves involves the choice of frequency. The frequency of 2.45 GHz is the standard choice for laboratory use. The efficiency of forming microwaves at that frequency is not as great as that which occurs with industrial equipment operated at a lower frequency. The choice of frequency is often dictated by the size of equipment, and the size of equipment is dependent on the wavelength of the radiation. At 2.45 GHz the wavelength is approximately 12 cm., small enough to produce bench scale equipment. A 900 MHz generator produces radiation with a wavelength of approximately 62 cm. A magnetron at that frequency is about 5 times as large ($62/12 \approx 5$) as that for a 2.45 GHz system.

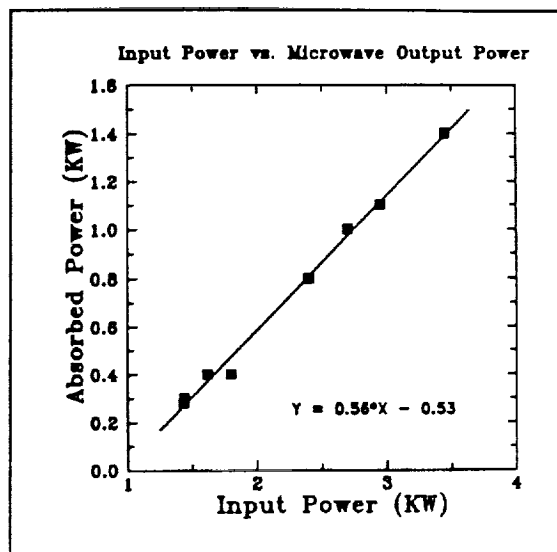


Fig. 1 - Indication of the power consumed to generate microwaves.

A plasma is an efficient absorber of microwaves. The microwave system being used in the experimental program is equipped with meters to detect both the forward and reflected power in the wave guide. From that information it is possible to determine the efficiency of power absorption by a plasma. The data in Figure 2 reveal that almost 100% of the microwave power is absorbed by the plasma at variable power settings, pressures, and gas flow rates. Additional data reveal that the effective absorption of microwaves by the plasma remains unchanged even at an applied power setting of 1.4 KW.

Chlorination Studies - In the last progress report we described our efforts to chlorinate TiO_2 . In that report we elaborated on problems we had in evaluating the data, the main problem being that a number of the intense peaks obtained with the mass spectrometer did not coincide with anticipated peaks for the Ti-O-Cl-Si system. In further evaluation of that data it was determined that a substantial portion of the mass spectrometer signal was due to Fe in addition to the other elements.

In those experiments in which TiCl_4 were formed a carbon steel rod was used to support the silica platform on which the TiO_2 specimen sat while being reacted in the plasma. The steel rod replaced an alumina rod. Both rods, when in use, are spun by a motorized chuck to ensure even heating of the specimen in the plasma. The alumina rod was replaced with the steel rod to see if the life expectancy of the O-rings used in the seal could be extended. The chuck, and the steel rod were grounded.

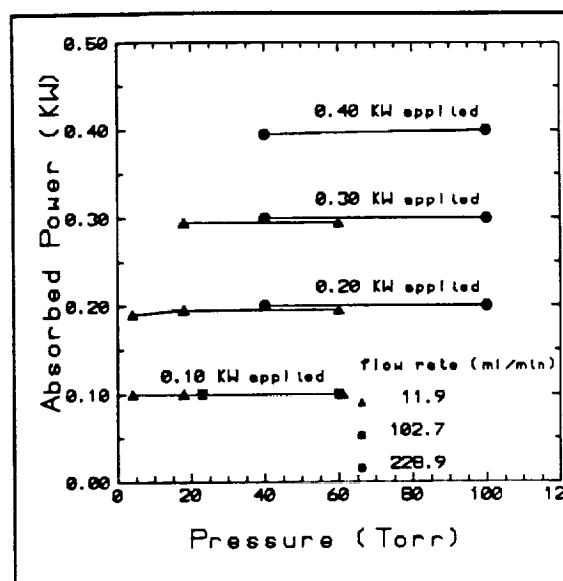


Fig. 2 - A plasma is an efficient absorber of microwave energy.

The position of the sampling tube for the mass spectrometer and the gas flow pattern should preclude any reaction between iron chlorides and the TiO_2 specimen. The position of the sampling tube and the gas flow pattern would, however, allow for reaction between titanium chlorides and iron chlorides in the gas phase and would not prevent their detection by the mass spectrometer.

The influence of the steel rod does not appear to be chemical. A plasma consists of ions, neutral species, and free electrons. The energy of the electrons follows a Maxwellian distribution. In that distribution there are a few electrons with very high kinetic energy levels, while the vast majority of electrons have a moderate or modest energy level. The steel rod, since it is grounded, provides a potential difference through which free electrons can be accelerated. An electron allowed to accelerate through a 2.5 voltage potential has enough kinetic energy to break a diatomic chlorine bond.

In reality, the electron will need additional energy to break a diatomic chlorine bond at the plasma- TiO_2 surface. The negative potential associated with the Debye Sheath is partially satisfied by the presence of positively charged ions. An electron impacting the surface of a non-conductor will have to overcome the residual potential that exists in the sheath.

Measurable chlorination of TiO_2 in a plasma without the aid of a reducing agent has been achieved only in the presence of the steel rod. The drop in potential with the grounded rod accelerates electrons toward the specimen with the resulting electron-specimen impact either breaking the

diatomic chlorine bond of adsorbed Cl_2 or damaging the TiO_2 structure. Both conditions raise the chemical potential of the reactants and thereby promotes an otherwise unfavorable reaction.

Hydrogen Reduction of TiO_2 - The use of hydrogen has several distinct advantages. Monatomic hydrogen, like monatomic chlorine, is highly reactive. Hydrogen, however, unlike chlorine, when reacted with a refractory oxide yields both solid and gaseous reaction products. The water vapor produced by the reaction can be continually flushed from the reactor with fresh gaseous reactant, thereby minimizing any back reaction.

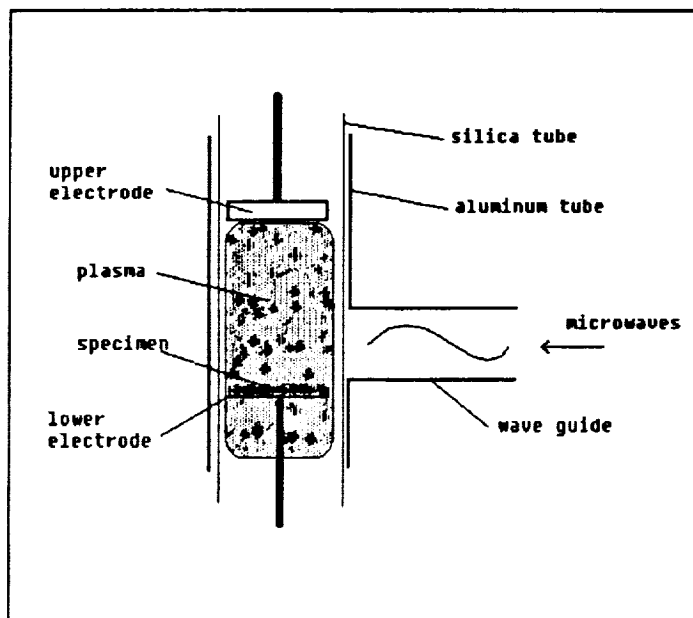


Fig. 3 - Apparatus

Powdered specimens of TiO_2 have been reacted in a microwave induced hydrogen plasma as shown in Figure 3. The specimen sits in a copper cup which also serves as an electrode. Above the specimen, 15.2 cm, is a second electrode which can be biased both positive or negative with respect to the electrode which contains the specimen. Specimens have been reacted at various pressures and power levels, plus at applied field strengths from 0 to ± 65.6 volts per cm.

During all experiments water vapor was evolved. The result of a typical experiment, as followed with the mass spectrometer, is shown in Figure 4. Initially we were concerned that the peak of water vapor detected at the beginning of an experiment may be due to adsorbed water. Differential thermal analysis (DTA) of an as stored specimen did yield one exothermic reaction peak. X-ray diffraction (XRD) analysis of the material revealed that the peak was due to transformation of the specimen from anatase to rutile. No peaks associated with water were detected with DTA. However, before beginning an experiment the powdered specimen was heated in dry air for 1 hour at a temperature of 550°C to ensure that any adsorbed water was removed.

Even after preheating each specimen, mass spectrometric analysis revealed the same results as that shown in Figure 4. During the first minute of reaction, the amount of water vapor evolved

peaked and then declined. After approximately 11 minutes a steady state rate was established for the evolution of water vapor. Visual analysis of the specimens revealed that a layer of the powdered specimen approximately 1/16 th to 1/8 th of an inch thick was converted from white to gray-black in color.

The plasma only contacts the surface of the specimen, it does not exist within the voids of the compact. While the microwave field can excite and accelerate electrons within voids, the mean free path of the electrons are restricted by the solid particles. That restriction

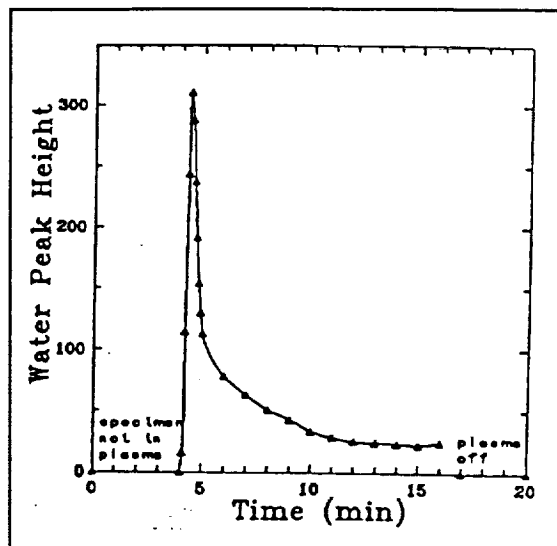


Fig. 4 - Water Vapor Evolved From TiO_2 Reacted in H_2 Plasma

leads to more electron-solid collisions than electron-gas molecule impacts. Gas-electron impacts are necessary to release additional electrons. Without those electrons the plasma can not be maintained. Because we are interested in what reactions can be achieved with a plasma, we have focused our attention on the surface where the plasma contacts the specimen. XRD analysis has been used to identify species and evaluate the extent to which they were formed.

In XRD analysis the X-rays penetrate the solid compact to a depth of approximately $25\mu\text{m}$. Since visual appearance indicates that the plasma reacts with the powdered specimen to a minimum depth of 1/16 th of an inch, the reacted portion of a specimen appears to be infinitely thick to XRD analysis. The external standards method has been used to provide quantitative XRD analysis.¹ This method requires X-ray analysis of the pure phases, which in this study are TiO_2 and Ti_2O_3 . The equation which is used to relate the volume fraction of a phase to the linear absorption coefficient of both phases (α and β) is presented below:

$$I_{\alpha} = \frac{K_1 C_{\alpha}}{C_{\alpha}(\mu_{\alpha} - \mu_{\beta}) + \mu_{\beta}} \quad (3)$$

where I_{α} is the integrated intensity, C_{α} is the volume of alpha phase and μ_i is linear absorption coefficient for the i th phase. K_1 is a constant. Now, if the intensity of a diffraction line of a mixture is compared to the same line of a pure sample equation 3 becomes:

$$\frac{I_{\alpha}}{I_{\alpha p}} = \frac{w_{\alpha} \frac{\mu_{\alpha}}{\rho_{\alpha}}}{w_{\alpha} \left(\frac{M_{\alpha}}{\rho_{\alpha}} - \frac{M_{\beta}}{\rho_{\beta}} \right) + \frac{M_{\beta}}{\rho_{\beta}}} \quad (4)$$

where w_i and ρ_i are the weight percent and density respectively of the i th phase. $I_{\alpha p}$ is the intensity of the diffraction peak for the pure specimen. This equation permits quantitative analysis of a two-phase mixture, provided that the mass absorption coefficients of each phase are known. If the absorption coefficients are not known a calibration curve must be made by using mixtures of known composition. Until such activities are completed a ball park analysis can be conducted by assuming that the absorption coefficients are equal, then equation 4 becomes:

$$\frac{I_{\alpha}}{I_{\alpha p}} = w_{\alpha} \quad (5)$$

Equation 5 has been used to obtain a first approximation to the extent of Ti_2O_3 formation. Specimens were reacted at a range of pressures and power settings using only a grounded specimen cup. The primary reaction product was a non stoichiometric and amorphous phase, TiO_{2-x} , which is gray to black in color as mentioned earlier. XRD analysis of the specimen reacted at 26 Torr and at a power level of 0.8 KW revealed formation of some Ti_2O_3 . The noted conditions, as a result of the formation Ti_2O_3 , were chosen for further study with an applied electric field.

Powdered specimens of TiO_2 were reacted in an electric field at strengths up to ± 65.6 V per cm. Field strengths of ± 6.56 V per cm produced the greatest extent of reaction. An entire series of experiments were conducted at that strength, the results of which are presented in Figure 5. Each point in the figure

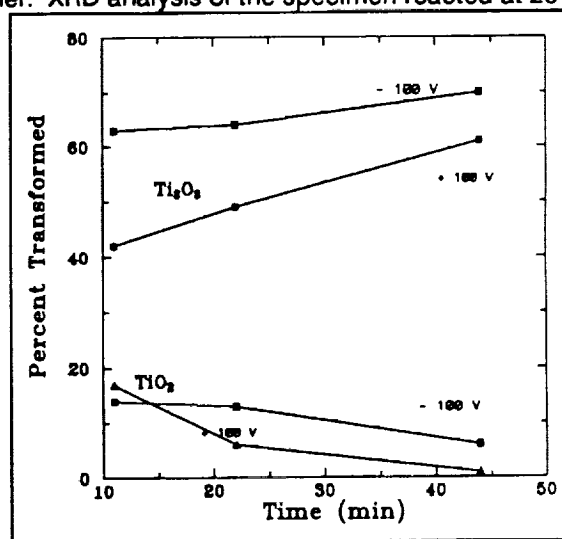


Fig. 5 - Experimental Results

represents a separate specimen reacted for the time indicated. The sign on the voltage indicates the polarity of the upper electrode with respect to the specimen cup. The greatest extent of Ti_2O_3 formation was observed at -100 V. At that condition, and after only 11 minutes, the resulting specimens were over 60 wt% Ti_2O_3 . Further formation of Ti_2O_3 increased only gradually with

additional reaction time. The experimental results presented in Figure 4 indicate that most of the reaction occurs within the first 11 minutes. That phenomena is most likely associated with the fact that the plasma reacts quickly with only a thin layer of the specimen. XRD results presented in the figure also indicate that the TiO_2 content of that layer was reduced to less than 20 wt% for all specimens reacted.

The percentages in Figure 5 do not add up to 100%. This is believed due to the simplifying assumption associated with equation 5 and the formation of TiO_{2-x} . TiO_{2-x} is amorphous and thus does not show up in XRD analysis as distinct peaks, accordingly, it could not be included in the analysis.

Student Participation

The experimental work presented in this report was conducted by Mr. Dan Bullard, a Ph. D. candidate in the Department of Materials Science and Engineering. Mr. Bullard has been supported during the past year by a grant from the U.S. Bureau of Mines' Pyrometallurgy Center at the University of Missouri at Rolla. Dan was initially recruited through funding provided by SERC.

Also assisting us in our work is Mr. Robert Ortega and Mr. Gary Thomas. Mr. Ortega has nearly completed his MS degree program. He has examined problems associated with using an optical pyrometer in obtaining temperature readings from a specimen in a plasma. Mr. Gary Thomas is a new MS candidate in the Department. Gary is designing both fluidized bed and spouted bed reactors for use with a non-equilibrium plasma.

Future Work

Our basic goal remains unchanged, namely, to investigate the feasibility of using a "cold" or non-equilibrium plasma in the enhancement of reaction rates and in the biasing of the thermodynamics of reactions that would not proceed if conventional means were employed. We will continue to look at both hydrogen reduction and chlorination of TiO_2 and ilmenite.

A new area under development involves the design of a fluidized and/or spouted bed reactor to utilize with the cold plasma. The experimental results presented above indicate that to recover oxygen from refractory oxides it will be necessary to achieve intimate contact between the refractory ore and the plasma.

References

1. B. D. Cullity, Elements of X-Ray Diffraction, 2nd ed., Addison Wesley, 1978.



Innovative Techniques for the Production of Energetic Radicals
for Lunar Materials Processing Including Photogeneration
Via Concentrated Solar Energy

D.E. Osborn and D.C. Lynch
Department of Materials Science and Engineering
and
Solar Energy Research Facility
University of Arizona

Abstract

The solar spectrum is a significant resource which is not yet fully appreciated. The spectrum, often viewed strictly as an energy source for heating of extraterrestrial ores, contains significant ultraviolet (UV) radiation that can be used to enhance reactions, and thereby reduce reactor mass and temperature of operation. In order to test the basic hypothesis that UV light can be used to enhance chemical reactions, iron has been chlorinated at 260 to 360 °C with and without UV radiation. The results confirm that the light significantly increases reaction rates.

Innovative Techniques for the Production of Energetic Radicals
for Lunar Materials Processing Including Photogeneration
Via Concentrated Solar Energy

D. E. Osborn and D. C. Lynch
Department of Materials Science and Engineering
and
Solar Energy Research Facility
University of Arizona

The solar spectrum is a significant resource which is not yet fully appreciated. The spectrum, often viewed strictly as an energy source for heating of extraterrestrial ores, contains significant ultraviolet (UV) radiation that can be used to enhance reactions, and thereby reduce reactor mass and temperature of operation. In order to test the basic hypothesis that UV light can be used to enhance chemical reactions, iron has been chlorinated at 260 to 360 °C with and without UV radiation. The results confirm that the light significantly increases reaction rates.

Introduction

The reduction of inorganic oxides is an energy intensive process whether accomplished terrestrially or extraterrestrially. From an extraterrestrial point of view the solar spectrum represents a potentially significant energy source. That claim does not involve the energy flux of the solar spectrum as much as it involves the makeup of that spectrum. The ultraviolet light of the solar spectrum can be used to break chemical bonds and thereby catalyze reactions. Catalyzing reactions can significantly reduce the size and mass of a reactor and allow for reactions to be conducted at lower temperatures. Ultraviolet light may be used to or as:

1. General Catalysis

The extraterrestrial solar spectrum begins at a wave length of less than 200 nm. and extends beyond 3000 nm. The UV portion of the spectrum can break a wide variety of bonds as indicated in Table I. UV light, with the ability to break chemical bonds, can serve as a catalyst. In subsequent sections of this report the effect of UV light on the chlorination of iron is discussed. Chlorination, however, is not the only area where the solar spectrum may be used to enhance reactions.

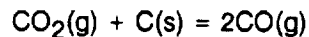
In another research project involving SERC carbon monoxide is being disproportionated on a catalyst to solid carbon and carbon dioxide. The effort is part of the program to build a pilot plant for the production of oxygen from the Martian atmosphere. To recycle the catalyst the carbon must be reacted with CO₂ at elevated temperatures. Experimentally it has been easy to disproportionate the carbon dioxide, but very difficult to oxidize the solid carbon with CO₂.

Oxidation of carbon by CO₂ involves a number of physical processes. The CO₂ must either contact the solid carbon or be adsorbed on to

Table I Dissociation Energies¹ For Chemical Bonds And Maximum Wavelength Which Can Break Bond

Bond	E(Kcal/mol) at 298 K	λ (nm) maximum
I-I	36.1	792
F-F	37.7	758
Br-Br	46.1	620
Cl-Cl	58.0	493
C-Cl	81	353
C-C	83	346
C-O	86	334
C-H	99	290
H-Cl	103	279
H-H	104	274
O-H	118	243
O-O	119	240
N-N	226	127

the surface of the catalyst. For the reaction



to occur both a C-O bond in the CO₂ molecule and a C-C bond in the solid carbon must be broken. Both bonds can be broken with the aid of UV light. If breaking of either the C-O or C-C is rate limiting then the solar spectrum can be used to enhance the rate of reaction.

2. Separate and Purify Metals from Complex Metal By-Products

In situ electrolysis of lunar regolith yields a complex residue consisting of alloyed metal and intermetallic compounds.² The material represents a significant investment of energy and a potential source of metals for construction. In order to utilize the material it is necessary to separate and purify metallic elements.

The task of separation and purification can be accomplished through chlorination. Most metal chlorides are volatile at relatively low temperatures, and as such, can be purified through distillation. The metals can be recovered either through hydrogen reduction or electrolysis. With the former electrolysis of the resulting HCl must be accomplished in order to recover both the hydrogen and the chlorine.

The chlorination of complex residues can be enhanced through utilization of UV light. The UV radiation can crack the Cl_2 molecule significantly raising the concentration of monatomic chlorine. Since the rate of chlorination of many metals is limited by the concentration of monatomic chlorine the UV light speeds the reaction.^{3&4}

3. Recovery of Iron from Reduced Ilmenite

In a similar manner as that mentioned in the previous example, iron can be recovered as a chloride from reduced ilmenite. Again, UV light can be used to speed the reaction and reduce reactor size. Chlorination can be achieved at temperatures below 300 °C. Subsequent processing of the chloride is necessary, as described previously, to reduce the iron and recover the chlorine.

While subsequent processing is undesirable in terms of mass and energy, it is not unusual. Recovery of iron by carbonyl processing suffers from similar problems. While carbonyl can be used to recover iron, it is known that there is extensive carbon carry-over in the process and that subsequent processing must be conducted to produce a pure iron.⁵ The secondary processing, given current technology, precludes using carbonyl as a means to both purify and provide for direct, final shape deposition of iron.

4. Carbo-Chlorination of TiO_2

The mining, beneficiation, and reduction of ilmenite ore represents a significant investment in energy and mass. Reduction of ilmenite with either carbon or hydrogen yields rutile, TiO_2 , as a waste material. Rutile has several potential uses; in aerobrakes, as a nucleating agent for glass ceramics, and as a potential source for oxygen and construction materials. Titanium is a light weight metal not subject to brittle failure as is high purity iron.

The energy expenditure required to recover oxygen from rutile must be balanced against both the need for construction materials and the energy required to mine, beneficiate, and reduce ilmenite for additional recovery of oxygen from the iron oxide portion of the mineral. From a purely thermodynamic view point TiO_2 can be readily chlorinated at temperatures below 500°C . Industrial practice, has determined that the rate of chlorination is not significant at temperatures below 1000°C . Barin and Schuler have shown that the rate of chlorination is dependent on the concentration of monatomic chlorine.⁶ At 500°C only an insignificant fraction of Cl_2 is thermally cracked. With UV light that situation is reversed, in which case it may be possible to chlorinate rutile in the presence of CO at significantly reduced temperatures. Oxygen can be recovered from the CO_2 produced and the chlorine recovered by electrolysis of the metal chloride.

Our ultimate objective is to determine how the solar spectrum can be used to enhance the rate of chemical reactions, with specific reference to production of oxygen and in the recovery of metal by-products from extraterrestrial resources.

Experimental Results

In our last report results of two experiments were presented which demonstrate the influence UV and near UV light can have on the chlorination of iron. The validity of those results depended on the actual specimen temperature and that recorded with a thermocouple. The experiments conducted since the last report have centered on continued chlorination studies of iron and verification that the specimen and thermocouple temperatures are approximately the same.

Temperature Experiments - An energy balance was conducted in order to estimate the influence of the UV radiation on the specimen temperature. A grey body approximation was assumed yielding the following equation,

$$h(T - T_g) + \epsilon \sigma (T^4 - T_w^4) = \alpha q$$

where h is the heat transfer coefficient, ϵ is the emissivity of the metal strip and the surroundings (the grey body approximation), σ is a constant, and α is the absorptivity of the metal specimen of the energy flux, q , incident upon the specimen. The temperatures T , T_g and T_w are the specimen, gas and wall temperatures respectively. Standard equations are available to calculate the heat transfer coefficient and q can be determined from knowledge of the intensity of the lamp source.

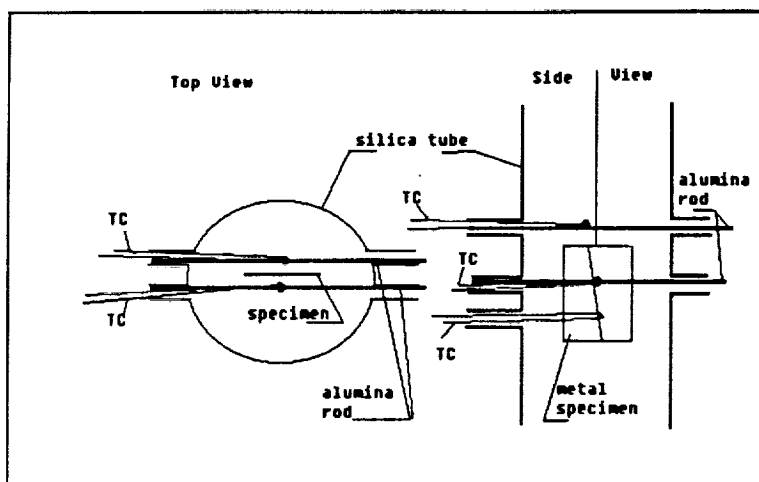


Fig. 1 - Apparatus For Evaluating Specimen Temperature

The wall temperature was measured. The heat balance is, thus, highly dependent on the values chosen for the emissivity and the absorptivity. The absorptivity was selected to have a value of one, the worst case condition. Several values of the emissivity were chosen and the equation solved for T assuming a specific value for T_g . The calculated value of T was found to

vary by a few degrees to 15 degrees depending on the choice of the emissivity. When the assumption of the grey body is removed the temperature variations become significantly larger. Since there is no reason to believe that the grey body assumption is valid and since without it small variations in the emissivities of the specimen and the surrounding wall have a significant impact (10s of degrees) on the calculated specimen temperature, a series of experiments were conducted to measure the specimen temperature with and without UV radiation.

In the first series of experiments a thermocouple was placed in contact with the specimen and then moved 1 to 2 mm away from the specimen. The specimen temperature and the gas temperature as measured with the thermocouple were found to vary by 2 to 4 °C (both positive and negative) with and with out the light source. The variation in the temperature between the specimen and the gas was found to be associated with the radial thermal variation associated with heat loss through the wall of the silica tube.

Another set of experiments were conducted whereby simultaneous measurement of the specimen and gas temperatures could be recorded. The reaction vessel was modified so that four thermocouples can be inserted into the reactor near the specimen as shown in Figure 1. The alumina rods shown in the figure were used to ensure that the distance between the specimen and the thermocouples used to measure the gas temperature is approximately constant. The alumina rods also allowed for permanent placement of the thermocouples for gas temperature measurement. During an experiment to measure the difference in the specimen and gas temperatures two thermocouples were placed along the alumina rods in front and back of the specimen as shown in Figure 1. A third thermocouple was placed above the specimen and the last thermocouple was crimped between a metal fold in the specimen. The temperature variation between the specimen

and gas was found to decrease with increasing gas flow. At the gas flow rates employed (in the previous experiments and in all subsequent experiments) the variation in the temperatures, as measured by the thermocouples, was found to be approximately 4 to 5 °C, with the specimen temperature being the higher. While turning the light source on raised the temperatures recorded by all the thermocouples, it did not alter the 4 to 5 °C variation between the thermocouples in contact with the specimen and those attached to the alumina rods.

These experimental results reveal that the light source, while it does raise the temperature of the specimen when on, does not alter the difference in the temperature between the specimen and that recorded with a thermocouple for the gas temperature. The results also reveal that the variation in the specimen and gas temperatures is due to radial heat loss.

Thermogravimetric Results - As a demonstration of the potential of photo enhanced reactions we have chlorinated iron metal with and without UV and near UV light. Our choice of iron is based on the fact that impure iron is a likely metal by-product associated with oxygen production as noted above.

During an experiment a metal specimen was positioned between the two alumina rods as shown in Figure 1. Only the thermocouple along the alumina rod between the specimen and the light source was used to monitor the gas temperature during an experiment. Numerous experiments have shown that the thermocouple is within 5 °C of the specimen temperature when no reaction is occurring. The actual temperature of the specimen can vary significantly as a result of the exothermic reaction.

Figure 2 and 3 constitute a summary of experiments conducted with Fe specimens. The temperatures reported with a bar over the value is an average temperature. During an experiment the temperature of the furnace was held constant, accordingly, the temperature variation recorded with the thermocouple (1 to 2 mm from the specimen) is

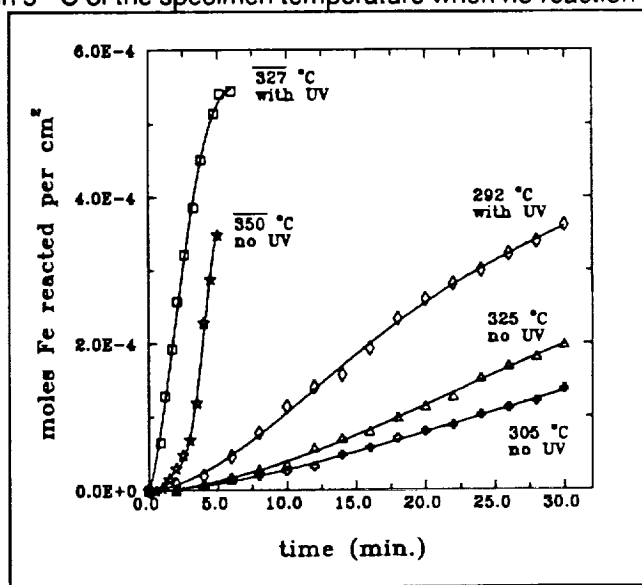


Fig. 2 - Experimental Results With Iron

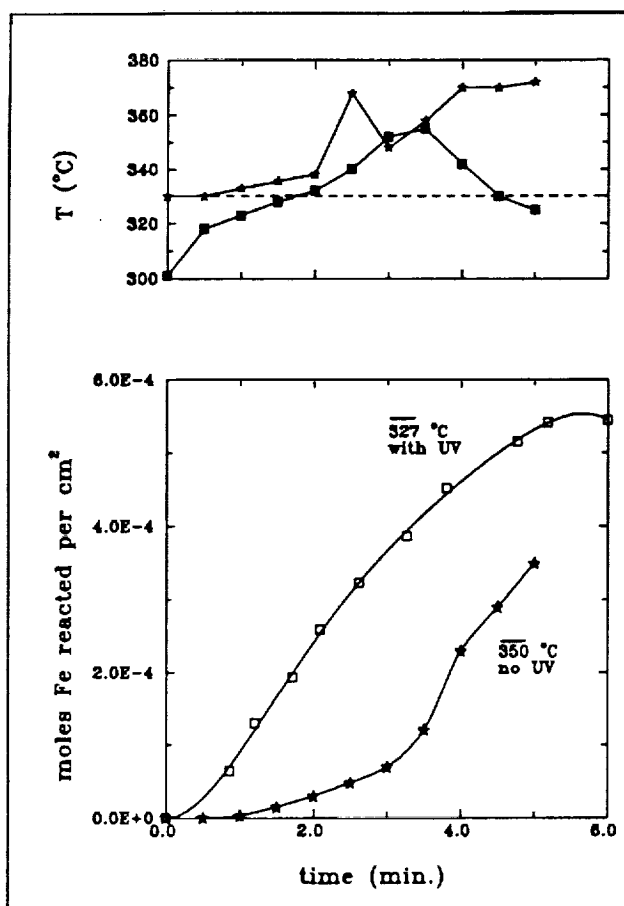


Fig. 3 - Thermogravimetric and Temperature Data
for Iron Specimens

associated with the heat of reaction. The chlorination of iron liberates 650 KJ per mole of Fe_2Cl_6 vapor produced. While during reaction the difference in the specimen temperature and the temperature indicated by the thermocouple is unknown, the combined knowledge of rate of weight change and the recorded temperature does give an indication as to the influence of heat transfer.

Those temperatures reported in Figure 2 without a bar over the top were, according to the thermocouple, conducted within ± 2 °C of the reported value. It is assumed that the specimen temperature and that recorded by the thermocouple during these experiments were always within the 5 °C noted when no reaction occurs.

The specimens identified as occurring at 350 and 327 °C in Figure 2 actually occurred over a broad temperature range as shown in Figure 3. The experiment identified as occurring at 350 °C with no UV in Figure 2 was initiated at 330 °C as shown in Figure 3. During this experiment the temperature of the furnace was maintained at a constant value. The experimental results presented in Figure 3 indicate that for the first minute little if any reaction occurred. During that period the temperature of the specimen (as indicated by the thermocouple) climbed by a few degrees. A near constant reaction rate was achieved during the second minute of the experiment, but the temperature of the specimen continued to rise. That rise in temperature initiates a thermal instability which, in turn, leads to a rapid rise in both reaction rate and specimen temperature.

The experimental run identified in Figure 2 as 327 °C with UV actually was begun at a temperature of 300 °C. The UV light reduced the induction period and increased reaction rates from the very beginning of the experiment. Again a thermocatalytic effect is observed.

A similar experiment involving the chlorination of iron was conducted at 260 °C. The results of that work are presented in Figure 4. The specimens were cut from the same sheet of material and were identical in size and weight. The induction period for the experiment conducted with UV radiation was substantially shorter than that which occurred with no UV. It is interesting to note, however, that the steady state rate for the reactions shown in Figure 4 are approximately the same. The steady state reaction rate for

the experiments conducted at 292 °C with UV was about twice as fast as the experiment conducted at 325 °C without UV radiation (see Figure 2).

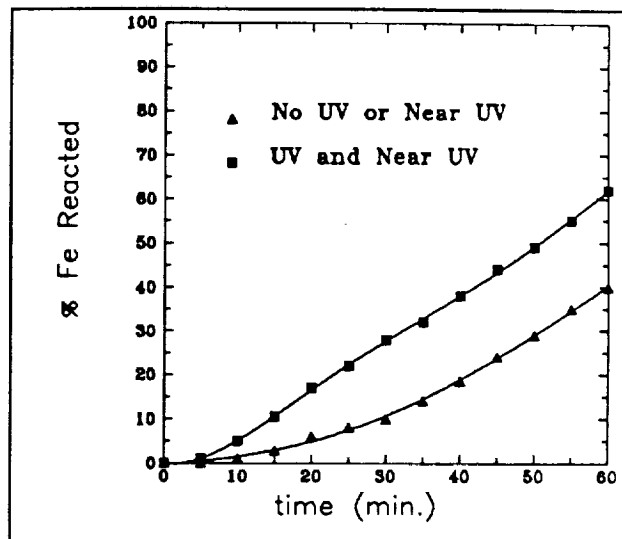


Fig. 4 - Experimental Results At 260 °C

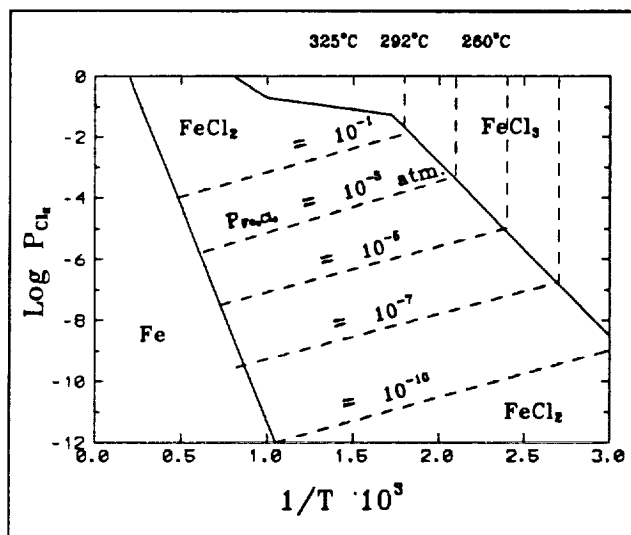


Fig. 5 - Fe-Cl Stability Diagram

The difference in the experimental results appears to be associated with formation of a protective chloride layer. The temperatures associated with each experiment are marked on the Fe-Cl stability diagram presented in Figure 5. At low temperatures, such as that used in this work, the primary iron chloride vapor species is Fe_2Cl_6 . At 260 °C the vapor pressure of Fe_2Cl_6 is less than 0.1 atm, while at 292 and 325 °C the vapor pressure of the chloride is greater than 0.1 atm. The specimens reacted at 292 and 325 °C always had ap-

proximately 50% of their surface area bare metal clear of any FeCl_3 which is dark brown in color. The specimens reacted at 260 °C were entirely covered in a brown coating of FeCl_3 .

Given the above results we have postulated that at 260 °C the UV and near UV light played an important role in forming nucleation sites for FeCl_3 formation. Since the equilibrium vapor pressure of Fe_2Cl_6 was less than 0.1 atm, the solid chloride did not readily vaporize, thereby leading to

complete coverage of the specimen by FeCl_3 . When the Fe specimen becomes completely covered by the solid chloride the rate limiting process can shift from chemical control to diffusion control. Transport control can negate the effect of the UV light.

All of these results reveal that UV radiation in the solar spectrum can be used as a unique resource to enhance chemical reactions. We will continue to explore how this resource can be utilized in the processing of extraterrestrial resources.

Student Participation

Don Osborn, a Ph D candidate in the Department of Materials Science and Engineering and also an employee of the Solar Energy Research Facility (SERF), has conducted the experimental work presented in this report. Together Don and Professor Lynch developed the concept that the UV portion of the solar spectrum could be used to enhance reactions. Support from SERC has allowed Don to devote 25% of his time to demonstrate the concept. State budget cuts have forced the termination of SERF effective December 31, 1991. Don is now allowed to devote 100% of his time to the project. Unfortunately, Don's financial constraints force him to seek new employment. It is unlikely Don will be able to complete his Ph D program.

Professor Lynch will use the funds requested for continued support of the project to recruit and support a new graduate student to continue the work.

Future Work

A time line for expected progress is presented in Figure 6. Our objectives are to complete our experimental work with the chlorination of iron by the end of the year and complete modeling of those results by June or July 1992. Much of the experimental work will be conducted at chlorine concentrations approximately one tenth that employed in the results presented in this report. The reduction in the chlorine concentration is to ensure that the effects of the UV radiation can be separated from the thermal instability experienced with the earlier results. After completing the experimental work, modeling of the results will commence. As the modeling progresses it is expected that some additional experimentation will be required.

By July we anticipate being in a position to explore the effects UV and near UV radiation have on the oxidation of solid carbon in the presence of CO_2 to form CO. That effort will be in support of Peter Nolan's work to explore ways to remove CO from the gas evolved from the electrochemical cell being used to produce oxygen from the Martian atmosphere. That experimental work is expected to continue through the remainder of the funding period.

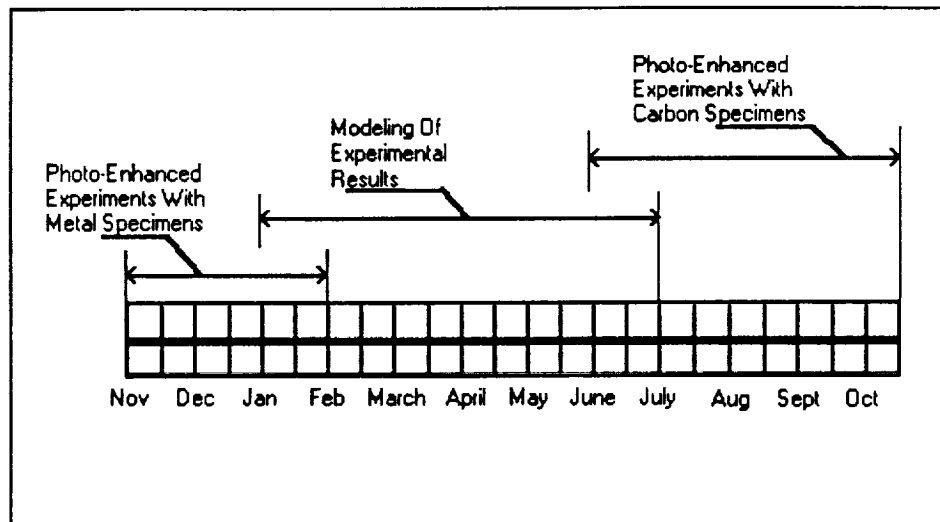


Fig. 6 - Time Line For Proposed Work

References

1. Ultraviolet Light Takes on CPI Role, R. W. Legan, Chem. Engr., January 1982.
2. Oxygen and Iron Production by Electrolytic Smelting of Lunar Soil, R.O. Colson and L.A. Haskin, in SERC's Annual Progress Report 1990-91, APR 91, pp. IA-52 to IA-62.
3. The Chlorination Kinetics of Tungsten, Molybdenum, and their Alloys, A. Landsberg, C.L. Hoatson, and F.E. Block, J. Electro. Chem. Soc., 118, pp. 1331-36, August 1971.
4. A Study of the Chlorination Kinetics of Germanium, Silicon, Iron, Tungsten, Molybdenum, Columbium, and Titanium, A. Landsberg and F. E. Block, USBM RI 6649, 1965.
5. High Purity Metals, J. H. Oxley, in Vapor Deposition, C.F. Powel, J.H. Oxley and J.M. Blocher, Jr. editors, pp. 452-483, John Wiley & Sons, New York, 1966.
6. On the Kinetics of the Chlorination of Titanium Dioxide in the Presence of Solid Carbon, I. Barin and W. Schuler, Metall. Trans. B, 11B, pp. 199-207, June 1980.

Oxygen and Iron Production by Electrolytic Smelting of Lunar Soil

R.O. Colson and L.A. Haskin

Dept. of Earth and Planetary Science and McDonnell Center for the Space Sciences

Washington University

Abstract

Our work of the past 8 months can be divided into 5 categories. These are 1) Continuation of theoretical calculations of steady-state electrolysis cell compositions, 2) Continuation of studies of metal solubilities in silicate melts, 3) Continuation of studies to identify the character and consequences of gas derived at the cathode during electrolysis, 4) General considerations of mineralizing processes on the Moon and the potential for existence of specialized lunar ores, 5) Reconnaissance experiments in preparation for a larger scale (30-90g) demonstration of the electrolysis process.

Oxygen and Iron Production by Electrolytic Smelting of Lunar Soil

R. O. Colson and L. A. Haskin

Dept of Earth and Planetary Science and McDonnell Center for the Space Sciences
Washington University

Our work of the past 8 months can be divided into 5 categories. These are 1) Continuation of theoretical calculations of steady-state electrolysis cell compositions, 2) Continuation of studies of metal solubilities in silicate melts, 3) Continuation of studies to identify the character and consequences of gas derived at the cathode during electrolysis, 4) General considerations of mineralizing processes on the Moon and the potential for existence of specialized lunar ores, 5) Reconnaissance experiments in preparation for a larger scale (30-90g) demonstration of the electrolysis process.

Theoretical calculations of steady state:

We have used information derived experimentally in our laboratory, published phase equilibria data, published melt viscosity data, and published compositions of lunar soils to model theoretically the progress of electrolysis. We have paid particular attention to the dependence of the energy required on the steady-state composition (related to viscosity, resistivity, and current efficiency of steady-state) and whether the refractory phase spinel (MgAl_2O_4) can be maintained in equilibrium with the steady-state melt. We have considered the relationships among feedstock composition, cell potential, and steady-state composition and whether known lunar soils are viable feedstocks. Two manuscripts included with this report (Colson and Haskin, 1992; Haskin and Colson, 1992) review and summarize our results.

We have also calculated expected energy loss in bus bars and electrodes as support for the calculations of energy required by the electrolysis itself. We find that energy loss due to resistive heating and electrodes be more important than resistive heating in the melt and of about the same magnitude as the total energy required by the electrolysis process (Haskin and Colson, 1992 and Fig. 1). In Fig. 1 acceptable ranges of Pt anode screen size (diameter of screen rods) are offered as rough guidelines. Actual dimensions will of course depend on how much energy loss to resistive heating is acceptable, composition of the anode (our calculations are for Pt), and details of the

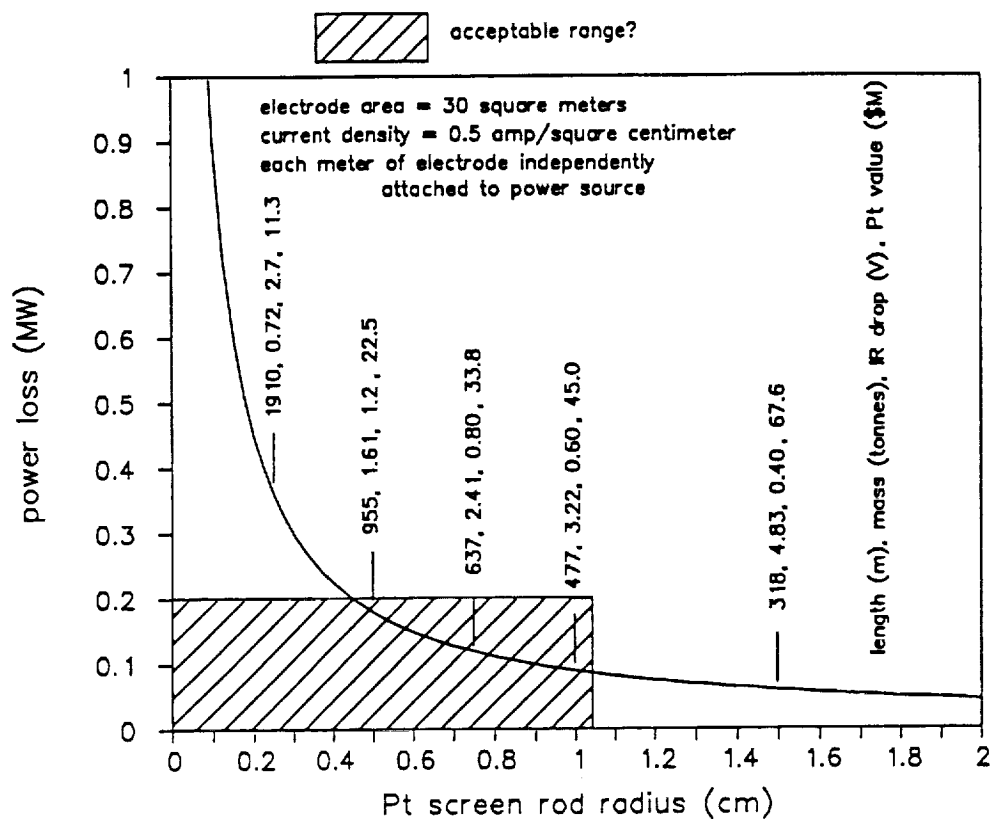


Fig. 1 Power loss in a Pt anode as a function of radius of the rods making up the Pt screen presuming that the screen is made up of a series of separate Pt rods each one meter long and attached independently to the power source. Given for reference at selected values of the rod radius are values of the total length of rods needed to achieve an electrode surface area of 30m², the mass of Pt needed, the IR drop in the Pt rods (in volts), and the approximate monetary value of the Pt (at the current rate) in millions of dollars. We offer a reasonable range of Pt rod radii. This range is selected such that the energy loss to resistive heating in the anode is less than the energy used by the electrolysis in the cell (including resistive heating of the melt). The power loss compares to a power required for the electrolysis itself (including resistive heating in the melt) of about 0.25MW.

actual cell design, which we don't know yet, but these constraints give us an idea of the mass and design that will be necessary.

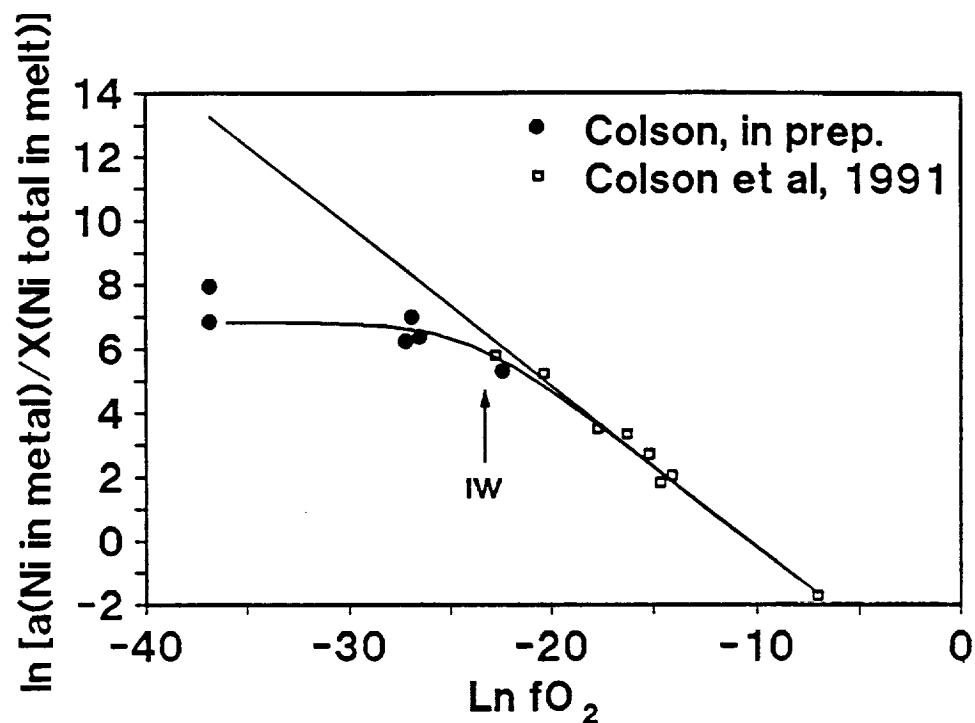
Metal solubilities in silicate melts:

We have demonstrated that nickel is soluble in silicate melts in the uncharged state (Colson, 1990 and Fig. 2). Nickel was used as an analog for iron because the oxygen fugacity required to do a similar measurement for iron could not be achieved in our experiments (an upper limit for Fe^0 solubility was determined and reported previously as $< \text{about } 0.2\text{wt}\%$). The solubility of Ni^0 obtained from Fig. 2 is about $0.1\text{wt}\%$. In commercial Al electrolysis, competing species at this concentration can substantially decrease current efficiency. However, because of the much higher concentration of the desired species (oxygen in silicate polymer) in silicate melt electrolysis than of Al in the commercial process, we suspect that solubility of Fe will not substantially affect current efficiency. We have determined that solubilities for Co are similar to those for Ni (Steele et al., 1991), suggesting that the transition metals may have similar solubilities and nickel may act as a good analog for iron.

We have also measured solubilities for Pt^0 and Ir^0 in silicate melts. These are shown in Fig. 3. These measurements may be important if Pt-group elements are used as anode materials. It is seen that Pt is substantially less soluble in the uncharged state than is Ir. As pointed out in Colson and Haskin (1992), these concentrations are sufficiently high that if equilibrium with slag is maintained, substantial loss of Pt or Ir will occur. Therefore, we need to determine how closely equilibrium is achieved in an actual electrolysis cell before we know whether this solubility is too high to permit use of Pt anodes. In our experiments of relatively short duration (30 minutes to 2 hrs), we have not observed any significant loss of Pt from the anode. We note that at the electron-poor anode, substantial Pt or Ir may be oxidized to a state that is even more soluble (Capobianco and Drake, 1990) and in fact we have reported Pt concentrations in the vicinity of the Pt anode to be as high as 100's of ppm (Colson and Haskin progress report 1990 to UA/NASA SERC), probably due to combined solubility in oxidized and reduced states.

Gas derivation at cathode:

In an attempt to determine the nature of the gas observed to form at the cathode during electrolysis, we did an electrochemical study to try to see if a reaction such as



$$K_a = \frac{X(\text{Ni, melt}) fO_2^{1/2}}{X(\text{Ni}^{2+}, \text{melt})}$$

$$K_b = \frac{a(\text{Ni, metal}) fO_2^{1/2}}{X(\text{Ni}^{2+}, \text{melt})}$$

$$\ln \frac{a(\text{Ni, metal})}{[X(\text{Ni}) + X(\text{Ni}^{2+})] (\text{melt})} = \ln K_b - \ln(fO_2^{1/2} + K_a)$$

Fig. 2 Variation of total nickel in silicate melt as a function of fO_2 . Filled circles are from Colson (1992 in prep) and filled squares are from Colson et al. (1991). The straight line indicates the trend expected if nearly all nickel were present as Ni^{2+} , the curve is a fit to the lower equation which expresses the relationship between fO_2 and total nickel ($\text{Ni}^{2+} + \text{Ni}^0$). (We measure total nickel in our experiments). At fO_2 values below the iron-wustite buffer (labeled IW), nickel concentrations in the melt become independent of fO_2 , demonstrating that Ni^0 becomes the dominant nickel species in the melt at these values of fO_2 .

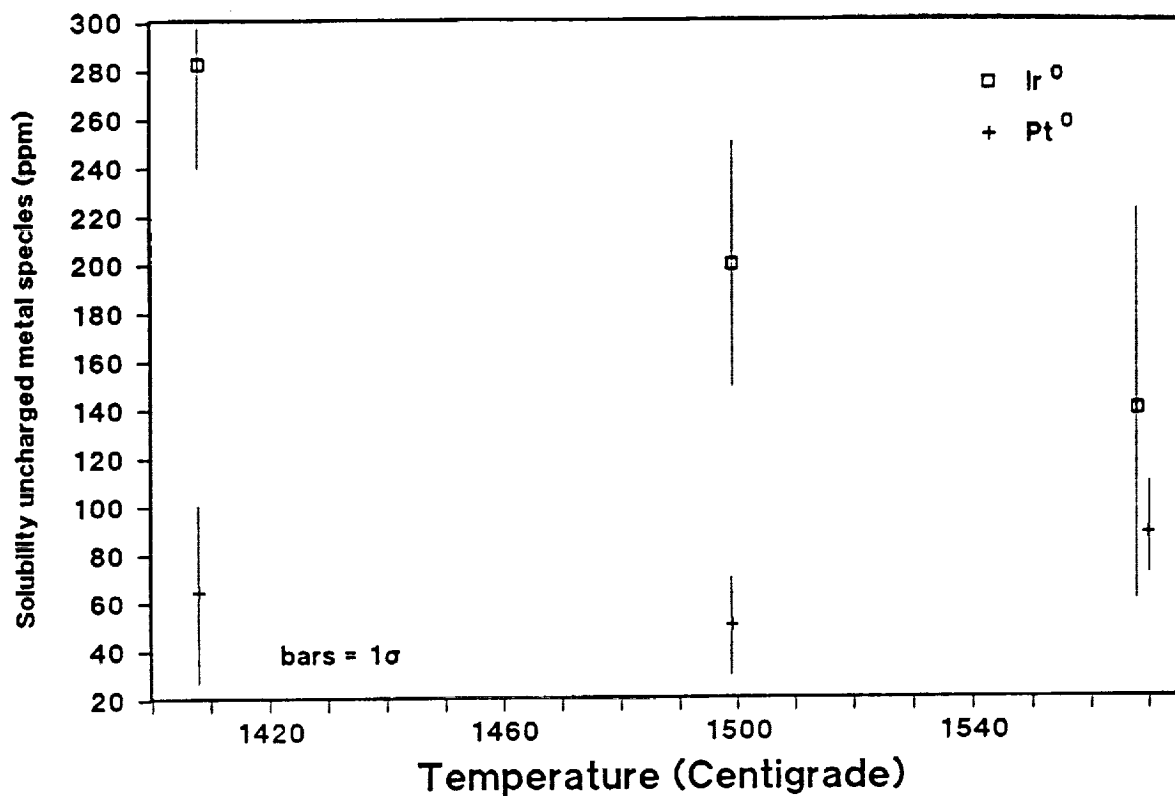
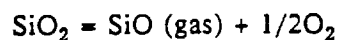


Fig. 3 Solubility of Pt⁰ and Ir⁰ as a function of temperature. No significant temperature dependence is demonstrated, but solubility of Ir is about a factor of 3 or 4 higher than Pt⁰ solubility. These measurements are at sufficiently low fO_2 such that virtually all Platinum and Iridium should be in the reduced (uncharged) state (see Fig. 3).



is occurring. We added a small amount of SiO_2 to Al_2O_3 -CaO or Al_2O_3 -CaO-MgO melts and did experiments of the type described in Semkow et al. (1982). Results were ambiguous. Although no evidence of the reaction above was found, any reduction of SiO_2 to produce SiO may have been masked by reduction of the Al_2O_3 -CaO-MgO electrolyte (Fig. 4). No reduction of Al_2O_3 (or less likely, CaO or MgO) was expected at these potentials, so our results suggest that the reaction dynamics at the cathode may be more complicated than we have previously realized. It is likely that during electrolysis, reduction of Al_2O_3 and perhaps other species, as well as Fe and Si, occurs. Species other than Fe and Si have not been observed in the metal phase in substantial quantities, possibly because the Al in the metal back-reacts with the melt to reduce Fe or Si in the melt. We have reported previously that Si in the metal backreacts with iron in the melt. The nature of the reduction in a CaO-MgO- Al_2O_3 -rich melt remains a subject of investigation.

Lunar ores and Lunar mineralization:

We have used the large database of published compositions of lunar rocks and soils to evaluate the compositional variations in known lunar materials and assess the potential for unsampled lunar ores. Concentrations of major elements (Si, Al, Mg, Fe, Ca, O) in the lunar rocks and soils vary substantially. These elements are common on the Moon and provide material for use there. Concentrations of rare or trace elements in lunar samples vary by several orders of magnitude, suggesting that geochemical processes operating on the Moon may have produced substantial concentrations that may be of use on the Moon. A copy of this manuscript (Haskin et al, 1992, submitted) is included with this report.

We have also done theoretical studies of the kind of mineralizing process that may have occurred on the Moon (Colson, 1992, submitted, and included with this report). We have considered the evidence for mobilization of metals (Fe, Ni, Zn) by chloride or carbonyl species and the conditions for precipitation and concentration as chlorides, sulfides, and metals. These theoretical studies provide the foundation for speculation concerning the existence of lunar ores that have not been sampled.

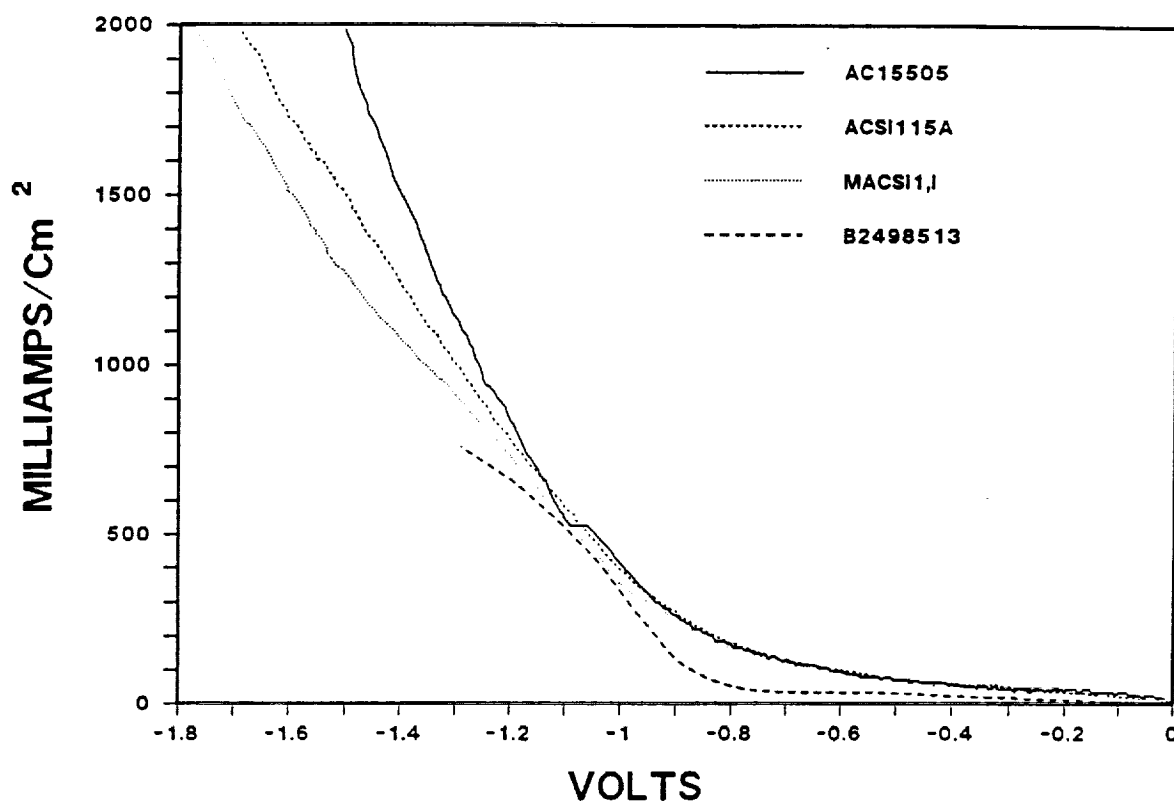


Fig. 4 Results of stationary electrode polarography experiments illustrating that any SiO_2 reduction peak is masked by reduction of the Al_2O_3 -CaO-MgO electrolyte. Compositions are as follows: AC15505 = (50wt% Al_2O_3 , 50%CaO); ACSi115A = (47% Al_2O_3 , 47%CaO, 6% SiO_2); MACSi1,1 = (49.5% Al_2O_3 , 42.2%CaO, 5.3%MgO, 3% SiO_2); B2498513 = (25.9%CaO, 18.5%MgO, 55.6% SiO_2). Temperatures are 1550°C except for B2498513 which is at 1498°C. Scan rate is 1200mV/sec. Current at potentials more negative than about -1.1 volts is probably affected by non-diffusional mass transport, however the fact that current is higher in the more SiO_2 -poor compositions might be due to the decrease in viscosity and increase in conductivity of low- SiO_2 melts.

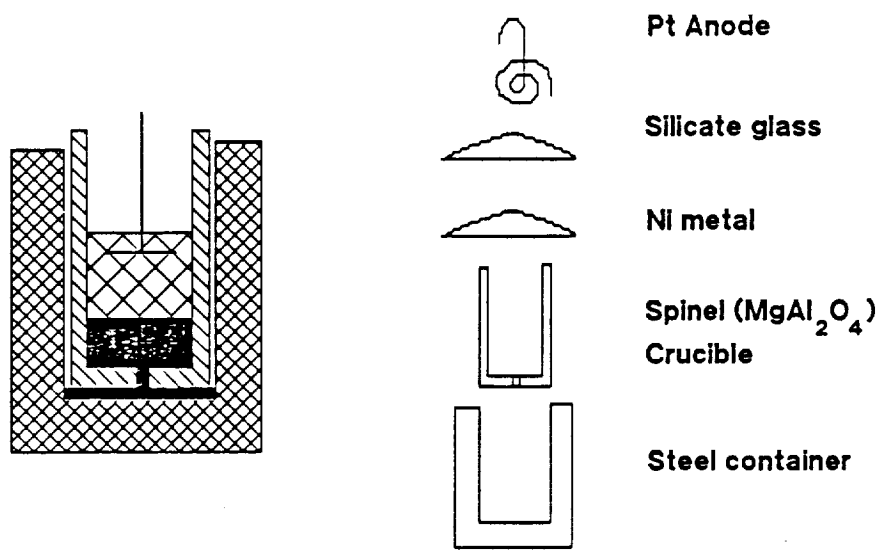


Fig. 5 Schematic illustration of experiments to demonstrate electrolysis. Spinel crucible sizes range from about 1 cm high to over 5 cm. Crucial parameters of these experiments such as cathode-anode distance, current density, melt composition, and cell potential are set in accordance with values determined from experimental work in smaller systems. We expect to be able to measure the amount and composition of metal produced, the energy used in resistive heating of the melt, and the amount of oxygen produced. Because these experiments are large enough such that the surface tension between the spinel crucible walls and the melt becomes a small part of the total system energy, we believe that these experiments are sufficiently scaled up to permit testing of many parameters of an actual working cell. (The constraint that the electrodes be on the order of 1 cm apart for the process to be energy efficient means that cm sized experiments are of nearly the dimensions of the ultimate working electrolysis cell.)

Electrolysis demonstration experiments:

We have begun a series of experiments to emulate more closely the workings of an electrolysis cell. These experiments use about 1 gram of silicate feedstock contained in a spinel (MgAl_2O_4) crucible, and a Pt wire coil used as the anode is placed 0.5cm from a pool of molten metal used as the cathode (Fig. 5). In these experiments, we measure continuously the current and cell resistance. We intend to scale up these experiments as we gain better understanding of them. We will use an oxygen getter to monitor continuously the production of oxygen from the experiments so that these experiments will constitute a better demonstration of the process than has been done to date.

So far, we have demonstrated that we can produce the desired configuration of melt plus anode above a metal pool in a spinel crucible. The crucible, placed within a metal jacket, has withstood the stress of heating and the corrosiveness of the melt. We have not yet succeeded in maintaining electrical connection with the cathode long enough for electrolysis.

References:

- Capobianco, C. J. and Drake M. J. (1990) Partitioning of ruthenium, rhodium, and palladium between spinel and silicate melt and implications for platinum group element fractionation trends, *Geochim. Cosmochim. Acta* 54, 869-874.
- Colson, R. O. (1990) Solubility of Ni^0 in silicate melts and implications for metal/melt and crystal/melt partitioning (abstract) *Geol. Soc. Am. annual meeting abstracts with programs* 22, A164.
- Colson, R. O. (1992) Mineralization on the Moon? : Theoretical considerations of Apollo 16 "rusty rocks", sulfide replacement in 67016, and surface-correlated volatiles on lunar volcanic glass, Submitted *Proc. 22nd Lunar and Planetary Sci. Conf.*
- Colson R. O. and Haskin L. A. (1990) Lunar oxygen and metal for use in near-earth space: Magma electrolysis, in *Engineering, Construction, and Operations in Space: Vol 1* (ed Johnson, S. W. and Wetzel, J. P.), ASCE New York.
- Colson, R. O. and Haskin, L. A. (1992) Producing oxygen by silicate melt electrolysis, in *Resources of Near-Earth Space* (in press).
- Colson, R. O., Haskin, L. A., and Crane, D. (1990) Electrochemistry of cations in diopsidic melt: Determining diffusion rates and redox potentials from voltammetric curves, *Geochim. Cosmochim. Acta* 54, 3353-3367.
- Haskin, L. A. and Colson, R. O. (1992) Steady state composition with low Fe^{2+} Concentrations for efficient O_2 production by "magma" electrolysis of lunar soils, submitted *Space* 92.

- Haskin, L. A., Colson R. O., Lindstrom, D. J., Lewis, R. H. and Semkow, K. W. (1991) Electrolytic smelting of lunar rock for oxygen, iron and silicon, in Lunar Bases and space Activities of the 21st Century (II), Mendell, W. W. (ed.), LPI, in press.
- Haskin, L. A., Colson, R. O., Vaniman, D. T., and Gillett, S. L. (1992) A geochemical assessment of possible lunar ore formation, in Resources of Near-Earth Space (in review).
- Semkow K. W., Rizzo R. A., Haskin L. A., and Lindstrom D. J. (1982) An electrochemical study of Ni^{2+} , Co^{2+} , and Zn^{2+} ions in melts of composition $\text{CAMGSi}_2\text{O}_6$. *Geochim. Cosmochim. Acta* 46, 1879-1889.
- Steele, A. M., Colson R. O., Korotev R. L., and Haskin L. A. (1992) Apollo 15 green glass: Compositional distribution and petrogenesis, submitted to *Geochim. Cosmochim. Acta*.

**EXPERIMENTAL STUDY OF THE ELECTROLYSIS OF
SILICATE MELTS
(MAGMAELECTROLYSIS OF INDIGENOUS SPACE RESOURCES)**

Rudolf Keller

EMEC Consultants
R.D. 3, Roundtop Road
Export, PA 15632

ABSTRACT

Electrolysis experiments with molten silicates were conducted at about 1425 °C. Currents of 2 A were applied to platinum anodes for periods up to 5 hours. Alumina crucibles dissolved into the melt slowly enough to permit their use as containers.

Platinum anodes in some cases corroded severely within less than an hour and necessitated early termination of the experiment. In other experiments, they showed no change in weight.

After carbon cathodes were found to react excessively with the iron oxide component of the melts, liquid metal cathodes were introduced. Copper and tin showed some weight losses, but silver seemed to be stable.

Positively identified cathode products represented only less than 10 percent of the faradaic current equivalent. The experimental arrangement permitted neither the identification and measurement of anodically evolved oxygen, nor the visual observation of gas evolution.

Questions regarding the conditions leading to long anode life and actual current efficiencies achieved remain open at this time.

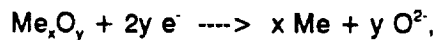
Progress Report to University of Arizona / SERC

6 September 1991

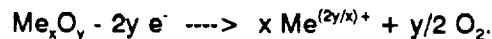
PRINCIPLES OF "MAGMA ELECTROLYSIS"

Raw materials readily available on the lunar surface are generally oxides. They contain copious amounts of oxygen for potential use as propellant or for life support. Elemental oxygen can be obtained by chemical oxidation or electrochemically. Melting available silicates and electrolyzing this melt appears particularly attractive because of its conceptual simplicity. This approach has been called "magma electrolysis". Its fundamentals have been studied in recent years at Washington University in St. Louis [1] [2].

Lunar raw materials for in-situ utilization include primarily silicates that contain various amounts of other oxides such as aluminum oxide, calcium oxide, magnesium oxide, iron (Fe) oxide, titanium oxide, etc. These silicates can be melted at temperatures of 1400 °C and higher, and electrolyzed to reduce metal components at the cathode,



and to oxidize oxides to oxygen at the anode,



When the electrolysis is conducted to produce oxygen as the product of primary interest, the melt can be partially electrolyzed and residual oxides discarded, possibly along with some metallic products. Reduction potentials and mass transport conditions determine which metals will be preferentially reduced.

The feasibility of "magma electrolysis" to produce lunar oxygen rests, we believe at this stage, upon the following key issues:

(1) Electrolyte Conductivity. To obtain acceptable production rates at reasonable space-time yields and energy efficiency, the specific conductance of the molten material must be high and remain high during the electrolysis.

(2) Current Efficiency. The process must have an acceptable faradaic yield. Low current

efficiencies may result from reoxidation of cathode products; metals often are soluble in molten electrolytes and solid metallic products may become dispersed in them, then react upon reaching anode products. Current efficiencies can also be affected by the oxidation of lower valent species to higher valent ones, as in the case of Fe^{II} to Fe^{III} . The presence of two- and three-valent iron may lead to electronic conductance of the electrolyte.

(3) Separation of Products. Products need to be removed from the system. This applies to the oxygen gas as well as to metals that form at the cathode.

(4) Stability of Electrode and Containment Materials. Because high temperatures and aggressive melts are involved, materials requirements are non-trivial.

ELECTROLYSIS EXPERIMENTS

Experimental Procedures

Electrolysis experiments were conducted in a DELTECH DT-28-6-STBL-B high-temperature furnace equipped with silicon carbide heating elements. Silicates or oxide mixtures were heated in glassy carbon or alumina crucibles and electrolyzed when molten. Tests of 5 to 6 hours of electrolysis were targeted, but experiments were often terminated prematurely when electrodes failed.

The experimental procedure (for experiments with liquid cathodes) was generally as follows. The oxide charge, 100 g or 200 g, was placed in an alumina crucible and melted under an argon atmosphere. The melt was kept at 1425 °C for an hour for outgassing; in some cases, the oxides were premelted in an alumina crucible, solidified, crushed and then used. Cathode host metal was placed in the crucible along with the oxide. The anode then was lowered into the melt. It was connected to the activated power supply to indicate the point where electrical contact was made, whereupon the anode was lowered precisely another centimeter. Constant electrolysis current of 2 A (1 A/cm^2) was passed until the end of the experiment or until the voltage increased excessively. When terminating the experiment, anodes were withdrawn and the cell cooled in the shut-down furnace. The cathode metal pool was then recovered and weighed. For analysis, the metal was remelted, a sample taken with a quartz tube, and sent to be analyzed by the Pittsburgh Applied Research Corporation at the University of Pittsburgh Applied Research Center.

Selection of Electrolytes

Three electrolyte compositions were used for the electrolysis experiments. They are given in Table I. Lunar Simulant, MLS-1 [3], was supplied by the University of Minnesota. The second composition represents one given by Haskin and coworkers as a representative lunar raw material [4] and was synthesized from purchased chemicals. A third composition corresponds to a partially electrolyzed, "steady-state" composition, with all the iron and titanium oxide as well as half of the silicon oxides electrolyzed and 10 percent of new feed added.

Table I. Electrolyte Compositions (in wt%)

	MLS -1	Haskin Example	All FeO,TiO ₂ 50% SiO ₂ red. 10% feed added
SiO ₂	43.86	46.2	41.24
TiO ₂	6.32	2.8	0.25
Al ₂ O ₃	13.68	12.6	21.35
FeO Fe ₂ O ₃	13.4 2.60	17.4	1.58
MgO	6.58	10.4	17.62
CaO	10.13	10.5	17.95
Na ₂ O	2.12		
K ₂ O	0.28		
P ₂ O ₅	0.20		
λ ohm ⁻¹ cm ⁻¹ at 1425 °C	0.304	0.320	0.313

Electrolysis with Glassy Carbon Crucibles

Two experiments were completed in glassy carbon crucibles. In one case, a graphite rod was used as cathode, in the other case, copper was placed in the crucible (while carbon walls remained exposed to the electrolyte).

Metal balls weighing 6.9 g were obtained in the case without host metal, also some small metallic particles dispersed in the electrolyte. After 80 minutes of electrolysis at 2 A, the amount of metal produced exceeded the amount that could have been reduced faradaically. The metal was analyzed to contain 91 wt% Fe, no Ti, and 0.16 wt% Al. Silicon and carbon may have been present, depressing the liquidus temperature enough that drops of metal formed. It appears that the carbon of the crucible and/or cathode reacted to reduce some metal oxides. This probably was also the case in the presence of copper which retained 6.6 wt% Fe, <0.01 wt% Ti, and 0.01 wt% Al at the end of the experiment (no analysis for silicon and carbon content conducted). The electrolysis time in this case was 3 hrs 10 min.

The platinum anode was in both cases in excellent condition according to visual inspection.

Experiments with Alumina-lined Graphite Crucibles

In order to increase the amount of electrolyte (to normally 200 g), the arrangement was changed to one used frequently in our molten salt experiments. As shown in Figure 1, a graphite crucible lined with an alumina crucible was the container. The material facing the molten silicates was not inert and dissolved into it, slowly increasing the alumina content of the melt in the process. Contact between the host metal of the cathode and the graphite crucible, which acted as a current collector, was made by a titanium diboride or carbon pin penetrating the alumina crucible through a hole.

Some difficulties occurred during electrolysis. Localized severe dissolution of the alumina liner and cracks in the sintered alumina led in some cases to reaction of the melt with carbon. Titanium diboride appeared to react and possibly formed a gas which could be trapped under the host metal and hamper electric contact.

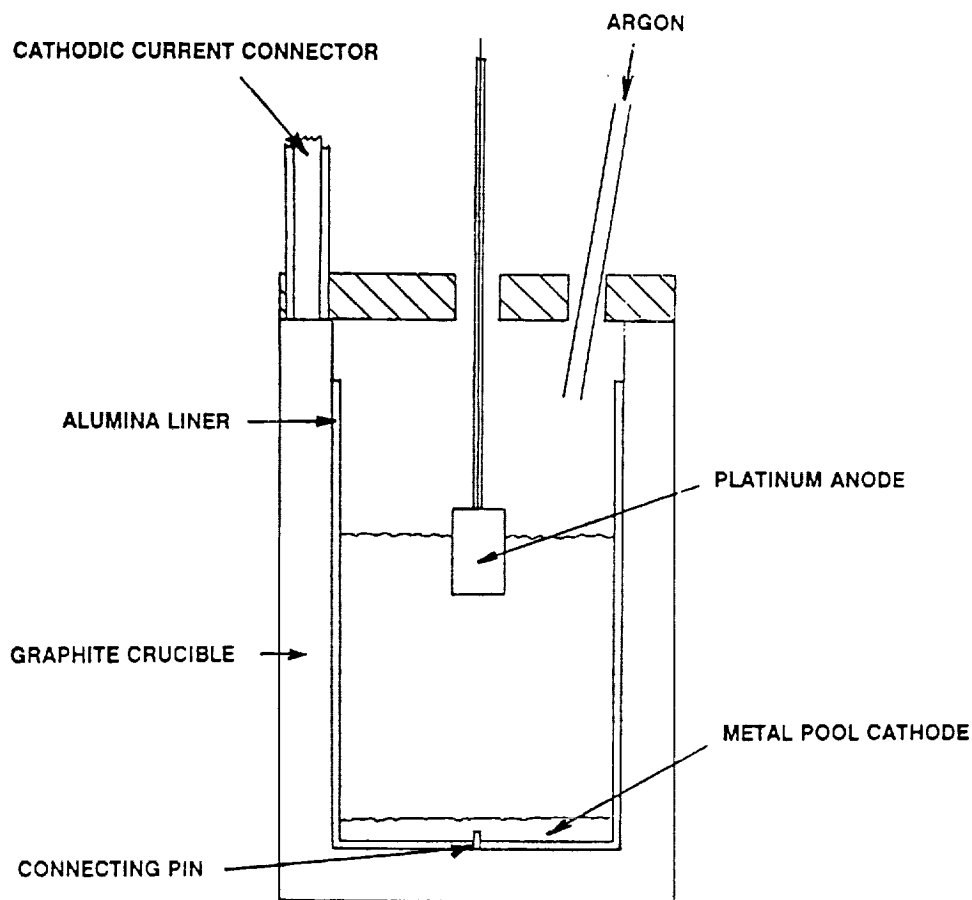


Figure 1 Electrolysis Arrangement with Host Metal Cathode

Electrolysis was conducted for periods of up to 5 hours. In some cases, the platinum anode was recovered in excellent condition after the experiment: the metal remained ductile, there were no measurable changes in dimensions or weight (estimating that weight losses exceeding 10 mg should have been detected, the platinum loss into the electrolyte was, thus, less than 50 ppm in reference to the electrolyte mass). In an other experiment, the width of the anode sheet decreased by 0.1 mm within 5 hours of electrolysis. Such good results were only obtained with high iron oxide contents in the melt.

Anode corrosion could be severe. In some cases, two thirds of the anode dissolved within 30-45 minutes.

Copper, silver, copper-silver alloy, or tin were employed as cathode host metal. Iron has a high solubility in copper (20 wt% at 1400 °C), but copper cathodes were found to lose considerable weight during the course of an experiment. Some weight loss was also observed with tin, which has a comparably high solubility for iron (20 wt% at 1400 °C). Iron, on the other hand, is only slightly soluble (0.26 wt% at 1400 °C) in silver, which was found to be reasonably stable in the melt.

Contents of reduced metals in the host metal, as determined by analysis after the experiment, were disappointing. Less than a gram of iron was found, while other elements were below or near detection limits. The iron content of the cathode metal typically represented a faradaic current efficiency of about 5 percent. The possibility exists that more iron was deposited but formed segregated lumps.

The experimental arrangement does not permit one to observe the anodes during electrolysis, to verify the evolution of anodic oxygen gas.

Titanium Diboride as Electrode or Container Material

Titanium diboride and a TiB_2 -AlN composite material were found to react with the molten silicates, possibly due to oxidation by iron oxide. Such a reaction seems to rule out the use of titanium diboride cathode elements, except perhaps if the electrolysis is carried out at potentials sufficiently negative to reduce aluminum.

CONCLUSIONS AND RECOMMENDATIONS

Within the time frame of 5-hour experiments, excellent stability of platinum anodes was found; the anode weight remained unchanged in one experiment and dimensional changes were minimal in another experiment. Good stability, however, was not achieved consistently, and the reason for the rapid deterioration of the platinum in some cases have not been identified. In all cases showing good anode performance, the iron oxide content of the melt was relatively high.

Current efficiencies based on collected and identified cathode products were low. Copper and tin metal cathodes lacked stability.

Focus of the experimental effort in the near future should be on achieving high cathodic current efficiencies, indicated by collected cathode products. If efforts prove futile, metal solubilities in the melts should be examined and electronic conductance of the melts considered. In addition, current efficiency may be determined by collecting the anodically produced oxygen, employing a sealed electrolysis system.

Regarding the stability of platinum anodes, pertinent information is expected to be forthcoming from an ongoing similar effort in molten fluorides [5]. It is recommended to await such results and to then examine their applicability to molten silicate systems.

REFERENCES

- [1] L. A. Haskin and R. O. Colson, "MISM Progress at Washington University", University of Arizona Workshop on Magmaelectrolysis of Indigenous Space Materials, August 1991.
- [2] R. O. Colson and L. A. Haskin, "Producing Oxygen by Silicate Melt Electrolysis", in Resources of Near-Earth Space, edited by J. S. Lewis, M. S. Matthews, K. Ramohalli, and T. Triffet, to be published.
- [3] P. W. Weiblen, sample supplied with analysis (1989).
- [4] L. A. Haskin, R. O. Colson, D. J. Lindstrom, R. H. Lewis, and K. W. Semkow, "Electrolytic Smelting of Lunar Rock for Oxygen, Iron and Silicon", Manuscript, December 1989.
- [5] EMEC Consultants, "Production of Oxygen by Electrolysis of Lunar Soil in Molten Salt", Contract NAS 9-18524, ongoing project.

B. REDUCTION OF CARBON DIOXIDE

ELECTROCHEMICAL SEPARATION OF OXYGEN FROM CARBON DIOXIDE

K. R. Sridhar* and P. Kaloupis**

Department of Aerospace and Mechanical Engineering
University of Arizona

There is considerable interest at the present time for in-situ propellant manufacturing on the Moon and Mars. One of the concepts for oxygen production that is actively being pursued is the processing of atmospheric carbon dioxide on Mars to produce oxygen by means of thermal decomposition and electrochemical separation. The key component of such a production facility is the electrochemical cell that separates the oxygen from the gas mixture of carbon dioxide, carbon monoxide, and oxygen. The objective of this investigation is the efficient design of an electrochemical separation cell and the selection of electrolyte and electrode materials of superior performance. A circular disk system has been developed for testing various electrolyte/electrode combinations. The electrolytes $\text{ZrO}_2\text{-Y}_2\text{O}_3$ 8% mole and $\text{CeO}_2\text{-CaO}$ 15% mole have been chosen for the initial investigations. The precious metals Platinum, Palladium, and Silver, as well as the perovskite Lanthanum Strontium Manganate (LSM), have been selected as the electrode materials. In addition to the disk configuration, a tube geometry system has been developed and tested. Commercially available $\text{ZrO}_2\text{-Y}_2\text{O}_3$ 8% mole tubes have been electroded in-house using precious metal electrodes and perovskite substrates. The results of these tests are presented here. The scale up capability of such a concept is also demonstrated. Electroded tubes have been purchased to scale up the tube configuration to a four tube cluster system. Preliminary results for the four tube cell are presented here. Further, a sixteen tube system using four clusters is currently being manifolded together and is near completion.

* Assistant Professor, Aerospace and Mechanical Engineering Department, University of Arizona

**Graduate Student, Aerospace and Mechanical Engineering Department, University of Arizona

ELECTROCHEMICAL SEPARATION OF OXYGEN FROM CARBON DIOXIDE

K. R. Sridhar and P. Kaloupis

Department of Aerospace and Mechanical Engineering
University of Arizona

There is considerable interest at the present time for in-situ propellant manufacturing on the Moon and Mars. One of the concepts for oxygen production that is actively being pursued is the processing of atmospheric carbon dioxide on Mars to produce oxygen by means of thermal decomposition and electrochemical separation. The key component of such a production facility is the electrochemical cell that separates the oxygen from the gas mixture of carbon dioxide, carbon monoxide, and oxygen. The objective of this investigation is the efficient design of an electrochemical separation cell and the selection of electrolyte and electrode materials of superior performance. A circular disk system has been developed for testing various electrolyte/electrode combinations. The electrolytes $\text{ZrO}_2\text{-Y}_2\text{O}_3$ 8% mole and $\text{CeO}_2\text{-CaO}$ 15% mole have been chosen for the initial investigations. The precious metals Platinum, Palladium, and Silver, as well as the perovskite Lanthanum Strontium Manganate (LSM), have been selected as the electrode materials. In addition to the disk configuration, a tube geometry system has been developed and tested. Commercially available $\text{ZrO}_2\text{-Y}_2\text{O}_3$ 8% mole tubes have been electroded in-house using precious metal electrodes and perovskite substrates. The results of these tests are presented here. The scale up capability of such a concept is also demonstrated. Electroded tubes have been purchased to scale up the tube configuration to a four tube cluster system. Preliminary results for the four tube cell are presented here. Further, a sixteen tube system using four clusters is currently being manifolded together and is near completion.

INTRODUCTION

In light of the The Report of the National Commission on Space [1] and the President's Space Exploration Initiative, it is expected that some sort of mission will be forthcoming for surface exploration or sample return from Mars. One way to reduce the overall weight requirements of such a mission, and hence its costs, is the use of in-situ propellant manufacturing [2]. Several concepts have been proposed for the manufacturing of oxygen from local Martian resources [3-5]. The production of oxygen alone would provide a tremendous advantage for sample return missions, in which oxygen is the primary propellant mass. The Martian atmosphere, with its known composition of 95.3% carbon dioxide, can provide an excellent source of oxygen. Since such a production plant would be independent of landing site, it is ideally suited for such a concept.

Although the design of a complete oxygen production plant involves many different compo-

nents, such as collection, separation, storage, and associated power systems, the main consideration here is the oxygen separation system. Carbon dioxide is thermally decomposed into carbon monoxide and oxygen by heating it to high temperatures. Oxygen is separated from the gas mixture using an electrochemical separation cell. With the design of the most efficient system possible, savings can be realized on the power requirements and weight characteristics of the overall plant.

The basic separation cell is shown schematically in Fig. 1. The oxygen separation capability of the system is due to the oxygen ion conduction of the electrolyte material selected. Oxygen vacancies exist in the crystal lattice of the electrolyte. These vacancies provide conduction sites for the transport of oxygen ions through the electrolyte. The driving force for the ions is a potential applied across the electrolyte material. CO_2 is heated so that it thermally dissociates into CO and O_2 . The gas mixture is then passed over the cell which consists of an electrolyte sandwiched between electronically conductive porous electrodes. The diatomic oxygen diffuses through the porous electrode to the electrolyte/electrode interface, and the O_2 molecule decomposes into oxygen ions with a negative charge of two. The applied potential supplies the electrons at the cathode, and provides the potential gradient to drive the oxygen ions through the crystal lattice structure. The oxygen ions move from vacancy to vacancy until they arrive at the electrolyte/electrode anode interface. Here they give up the excess electrons and reform O_2 , which then diffuses through the porous electrode. The pure diatomic oxygen can then be collected for use.

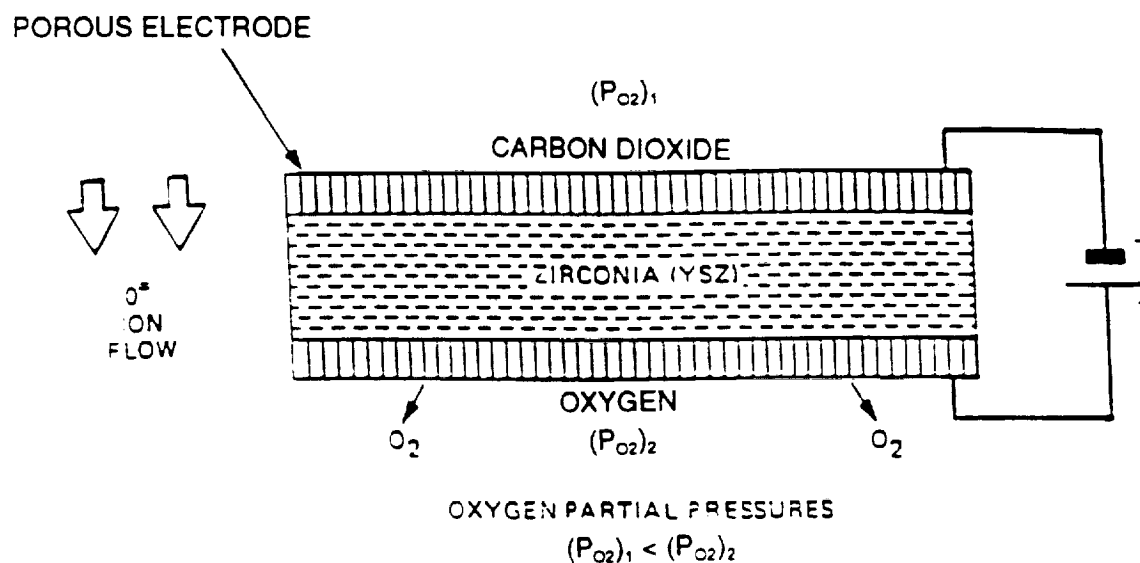


Fig. 1 Electrochemical Separation Cell

The properties of the electrolyte and the electrode are of paramount importance in determining the overall characteristics of the cell. For example, operation at a high temperature is desirable since this improves the oxygen ion conductivity through the lattice. Also, a porous electrode is preferred since the oxygen must be able to pass freely through it, however good electronic conductivity (which requires less porosity) is also necessary. Hence the proper selection of an electrolyte and electrode are critical to the success of the separation cell.

In order to facilitate the examination of many different electrolyte/electrode combinations, a circular disk cell has been designed. Two sides of a manifold are separated by a 2.86 cm diameter electrolyte/electrode sandwich. One side of the manifold represents the carbon dioxide supply side, and the other the oxygen collection side. The entire system is raised to the required operating temperature in order to thermally decompose the carbon dioxide and to increase the conductivity of the electrolyte material.

Also included in this phase of the study are tests conducted on zirconia tubes supplied by Ceramtec Inc. of Salt Lake City, Utah. These tests have been included since it is necessary to know the performance characteristics of these tubes, which are currently being used in another separate sequence of experiments. Some tubes have been electroded at the Space Engineering Research Center, and others have been electroded by Ceramtec.

In addition, a concurrent investigation involves the scale-up capability of the system. To this end, a cluster system of four tubes within a single manifold has been designed and tested. Further, four of these clusters are being manifolded together presently to form a sixteen tube system which would result in a higher production rate of oxygen.

ELECTROLYTE AND ELECTRODE SELECTION

The single most important element in the electrolytic separation of oxygen from carbon dioxide is the selection of the electrolyte. A substantial amount of work has been performed in this area by Sutor, et. al. [6], who have identified a search process based on certain criteria. It is desirable to select an electrolyte that has the highest possible conductivity at the lowest possible operating temperature, so as to reduce the overall mass and power requirements of an oxygen plant.

The most important consideration in selecting an electrolyte is the overall conductivity. It must have the maximum possible oxygen ion conduction with very little electron or secondary ion conduction. It must also be non-porous and have good micro-structural stability. The electrolyte must also be stable in chemistry and in phase during prolonged exposure to high temperatures and repeated cycling. In addition, it must resist cracking due to (a) mechanical stresses that arise due to differing thermal expansion coefficients of the electrode and casing, and (b) thermal cycling from periodic startup and shutdown. It must also be economical and relatively easy to fabricate.

Based on theoretical considerations [6,7] and some previous experimental evidence [8-11], Zirconia and Ceria have been selected as the electrolytes for this research. For the present study we investigated only $\text{ZrO}_2\text{-Y}_2\text{O}_3$ 8% mole and $\text{CeO}_2\text{-CaO}$ 15% mole to establish the fabrication

techniques required for the electrolyte. These molar percentages represent maximum conductivities based on past investigations [6,12].

The selection of the electrode and the technique used to apply it to the electrolyte surface is very important. The properties of the electrode and the electrolyte/electrode interface are critical to the overall performance of the cell. Typical electrode materials are precious metals and conducting oxides, doped with some impurity, as well as perovskites.

The most important considerations for the selection of an electrode material are its electronic conductivity, the thermal expansion coefficient, its porosity, oxidation resistance, and chemical and electrical stability. The thermal expansion coefficient must match that of the electrolyte as closely as possible, so that mechanical stresses do not arise at the interface. This could lead to cracking of the electrolyte during prolonged exposure to high temperature and thermal cycling. Also, it is necessary that the electrode be porous enough for the oxygen ions to move freely through it. However, a balance exists between good conductivity and free movement of oxygen ions. Another important consideration in selecting the electrode is the potential catalytic effect that it may have on the oxygen kinetic reactions, both on the cathode and the anode side of the cell [13]. The electrolyte/electrode interface is also of significance. If the electrolyte is very thin, then a significant portion of the ohmic losses will occur at the interfaces with the electrode [13]. Minimizing the losses at the point of contact could significantly change the performance of the cell.

For this study precious metals such as Silver, Palladium, and Platinum have been selected, based on past investigations [14,15]. Also considered is the perovskite Lanthanum Strontium Manganate (LSM). This has excellent properties with relation to the electrolytes, and it reduces thermal stresses that arise during thermal cycling.

THE DISK SYSTEM

The configuration of the disk system is shown schematically in Figure 2a and Figure 2b. There is a CO₂ supply tube and a CO + CO₂ exhaust tube on the cathode side, and an O₂ outlet tube on the anode side. The entire system can be raised to the required operating temperature of 800-1000 °C using a 300 W ceramic clam-shell heating element. The electrolyte/electrode sandwich is sealed to the alumina silicate manifold using a ceramic bonding agent, either Aremco's Ceramabond 569 or Saureisen's Product No. 8. The lead wires extend through the manifold and are connected to the Acopian power supply, which supplies the required 0.8-3.0 V for the tests.

ZrO₂ CELL DESIGN

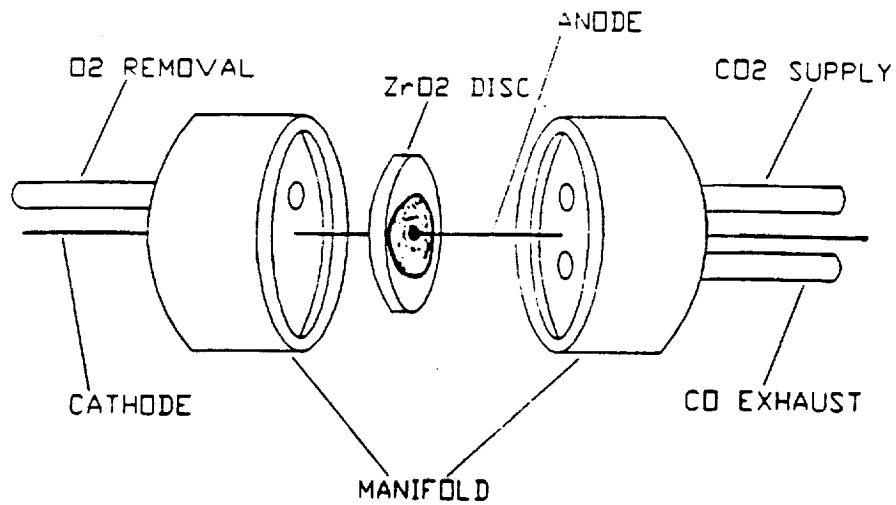


Fig. 2a Schematic of the Zirconia Disk and Manifold

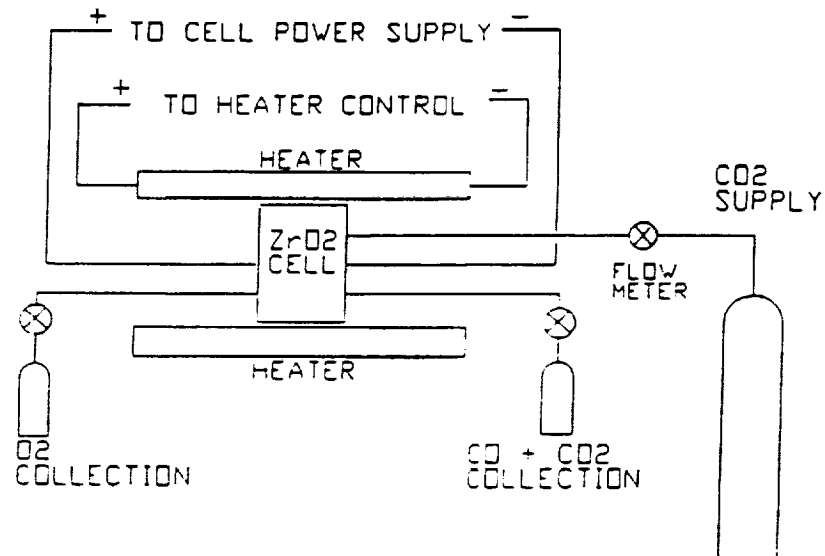


Fig. 2b Schematic of the Test Setup for the Disk Geometry

Fabrication of the Electrolyte

Two techniques have been used for fabricating the electrolyte. These are cold pressing and tape casting. Cold pressing involves a dry powder consisting of the ceramic powder and binder which is uniaxially pressed in a die to form the disk. Tape casting involves the use of a slurry that is prepared by mixing the ceramic powder, solvent, and binder and making a smooth paste. The slurry is then poured onto a flat surface, and a blade is drawn over it to cast the slurry into a uniformly thick layer. The end result is a flat, flexible layer of material from which any shape can be cut.

The Zirconia dry powder was prepared using TOSOH TZ-8Y, which is a commercially available $\text{ZrO}_2\text{-Y}_2\text{O}_3$ 8% mole powder. A 15% volume slurry was made from the dry powder by adding H_2O , and then 1.5% weight inorganic binder or 3% weight organic binder. The mixture was stirred for 20 minutes, and was then pan dried at 60 °C. The dried powder was sieved through a #45 sieve to ensure uniform particle size.

The Ceria dry powder was prepared by dry mixing appropriate quantities of Alfa Products CeO_2 (IV) and CaO corresponding to 15% mole, which was then ball milled in ethanol (ETOH) for 24 hours. The ETOH was boiled off by drying at 60 °C, and the powder was calcined at 1000 °C for 12 hours. The calcined powder was then ball milled for 12 hours, at which point 0.5% weight organic binder was added. This was then ball milled for an additional 4 hours. The wet powder was pan dried at 60 °C and sieved through a #45 sieve for uniformity.

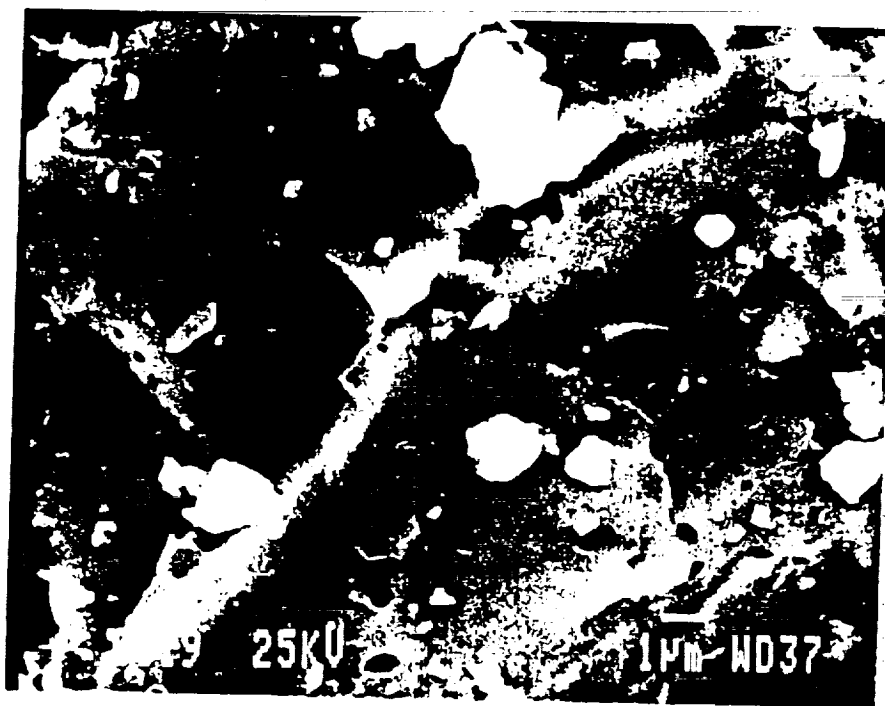
The slurry for the tape casting of the Zirconia was prepared by the author [Kaloupis] at the NASA Jet Propulsion Lab using the TOSOH TZ-8Y, and the TAM Products No. 73216 binder. Methyl Ethyl Ketone was added to the mixture, which was ball milled for 24 hours. The final product was 33% weight binder. The slurry was then drawn by a doctor blade into several thicknesses, ranging from 0.99 mm to 1.54 mm. There was a problem with rapid drying which resulted in cracking of the final tape casting, however several disks could be cut from areas that did not appear affected.

Green Zirconia disks of varying thicknesses resulting from the cold pressed technique were sintered at varying temperatures and heating rates. Many of these attempts resulted in uneven, wavy disks that could not be used. Sintering at 2 °C/minute to 1650 °C resulted in flat disks which were 2.86 cm in diameter. Flat disks obtained were 0.8-1.0 mm in thickness. Although many were obtained as thin as 0.1 mm thick, they could not be used. Weighting of the disks during the sintering process alleviated but did not remove the problem. The Ceria disks could not be fired flat within the temperature ranges and rates tested.

Disks which were cut from the tape casting also could not be fired flat. It is believed that this is because of possible cracks which may have been produced in the drying process which were not visible to the naked eye. In addition, these disks were very thin and warped readily, even at a relatively low sintering temperature of 1350 °C.

The Zirconia disks manufactured were examined using a Scanning Electron Microscope, and a representative image is shown in Figure 3. Small pores can clearly be seen in the sample, and a porosity test needs to be performed. The pores are approximately 0.3-0.5 microns in diameter

and do not appear to be interconnected. It is believed the disks are still sufficiently dense to perform the required experiments.



Disk

Fig. 3 Scanning Electron Microscope Image of Cold-Pressed Zirconia Disk

Electrode Application

The precious metal electrodes were applied directly to the surface of the disks. Commercially available Hereaus Products Silver, Platinum, and Palladium pastes were used. These were of varying consistencies, and were thinned with ETOH or Toluene. The electrode was applied using a brush or swab. The electrodes were then fired to set the paste at the manufacturers recommended temperature.

In addition, a Lanthanum Strontium Manganate (LSM) electrode paste was made using Trans Tech $\text{La}_{0.8}\text{Sr}_{0.2}\text{MnO}_3$ and an organic binder. The final product was 50% volume binder. Toluene

was added to this mixture, and the final product ranged from 10%-30% volume LSM as desired. This was degassed in vacuum, and then applied directly using a brush or swab. The LSM paste was fired at various temperatures ranging from 850-1150 °C.

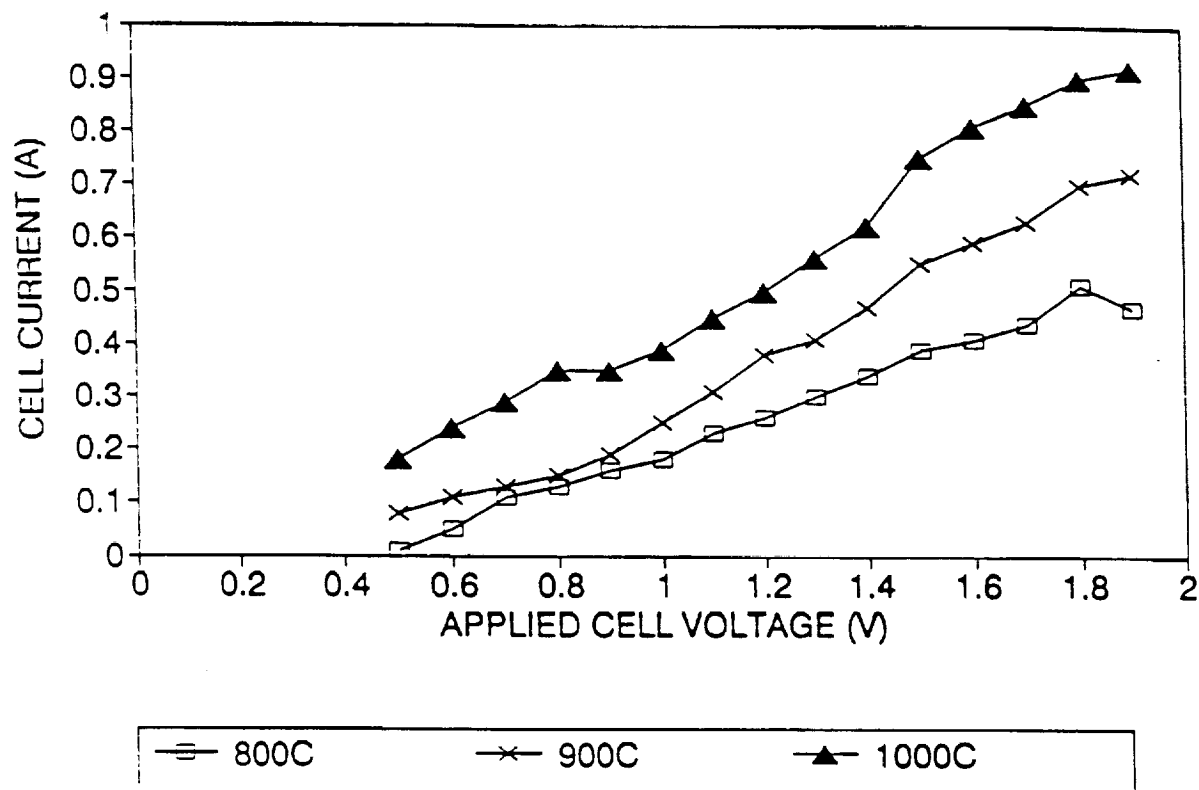


Fig. 4 Representative Results for a 1 cm Diameter Pt Electroded Disk

Results and Discussion

The electrode was applied over a circular surface area 1.0 cm in diameter on the cold pressed disks. Several electrodes were tested on the Zirconia disks, with current densities as high as 700 mA/cm², however there was some question with regards to the integrity of the seal. Figure 4 shows some representative results for a Pt electrode. The effect of a leak is evident in the zero crossing of the current. At this temperature range the voltage, which corresponds to the Nernst Voltage, should be approximately 0.798 V. It is possible that some of the current could be due to oxygen in

the air and not carbon dioxide. This would explain the shifting of the curve, since the zero crossing for air should read 0.0 V. Since these results were obtained, new methods of sealing the disk to the manifold have been developed. An examination of the failed seal revealed that the bonding agent withdrew from the surface of the Zirconia disk. With proper surface preparation, such as sand blasting the edge of the disk, a seal could most likely be obtained. The testing of these new, properly sealed systems is currently underway.

THE TUBE SYSTEM

The configuration of the tube system is shown schematically in Figure 5. It consists of a $\text{ZrO}_2\text{-Y}_2\text{O}_3$ 8% mole electrolyte with a 9 mm outside diameter and a wall thickness of 1.0 mm. The tube is sealed at one end and is 28 cm in length. It is isopressed as a single unit. These tubes are supplied by Ceramtec Inc. of Salt Lake City, Utah. The carbon dioxide is fed through an alumina tube into the Zirconia tube, and is then exhausted. The tube is sealed to the manifold in a cold seal, and this seal is therefore easy to attain. Various electrodes have been tested in the tube configuration.

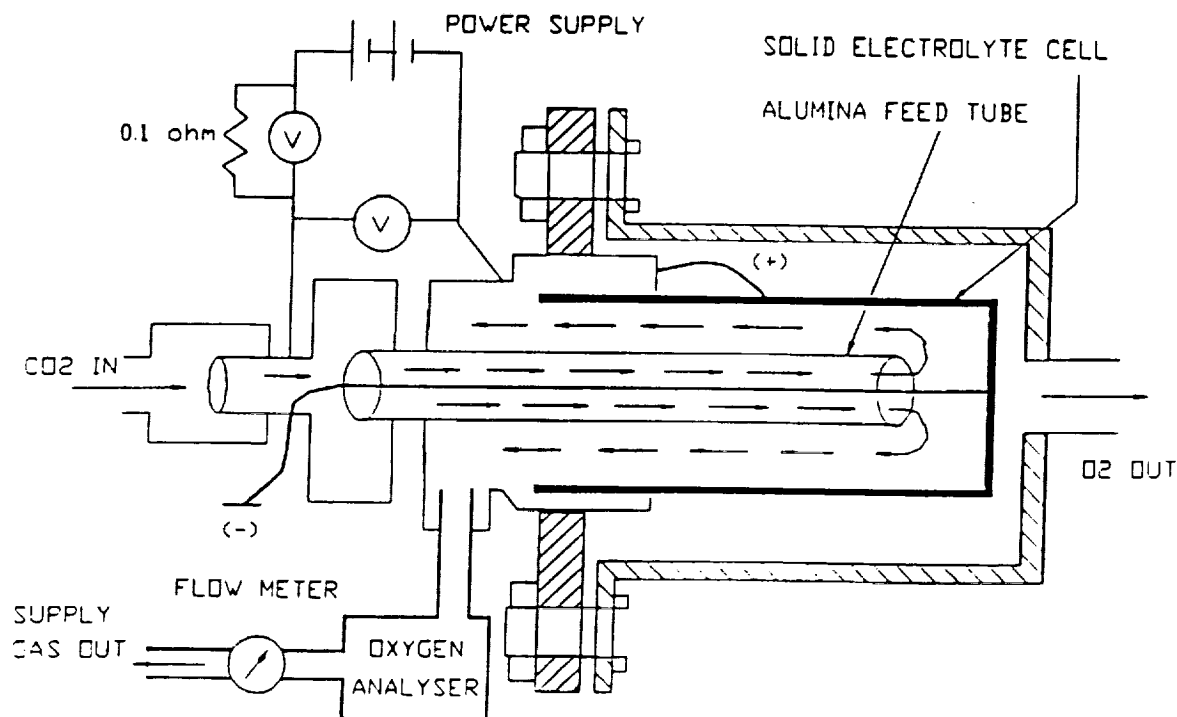


Fig. 5 Schematic of the Tube Geometry Cell and Testing Setup

It was necessary to conduct the tube tests because of the uncertainty in sealing the disk system. In addition, a scale up of the tube system is being concurrently performed, and the characteristics of the Ceramtec tubes are required for these alternate tests.

The exact composition of the electrolyte is proprietary to Ceramtec, but several electrodes have been tested with these tubes. Some of these were constructed in-house at SERC and others were supplied by Ceramtec. Typically, a given tube will have a perovskite substrate which acts as a catalyst, with a precious metal coating to act as the electron carrier.

Electrodes

Several electrode combinations were tried in-house. The tube was first coated with an LSM ink prepared as discussed in the preceding section, and then a Silver, Platinum, or Palladium coat was applied directly on top of this. The electroded area was 18 cm in length. The LSM was fired at various temperatures for varying lengths of time. It was discovered that the minimum firing temperature was 1100 °C, and that the minimum amount of LSM in the ink required is 20% volume. This suggests that the LSM is acting as a catalyst only when it is a current carrier. The high temperature is required for the LSM to sinter, and the minimum volume percent of LSM is required so that there is sufficient powder available for the particles to be drawn together.

Results and Discussion

The results of some in-house series of tests for Ag, Pt, and Pd electrodes are shown in Figure 6. It was noted that a difference in I-V characteristics could be measured depending on the thickness of the applied metal, particularly for the Ag electrode. It was also observed that for the Ag electrode the current measured was initially substantially higher than the steady-state current, by a factor of four or more sometimes. The current would drop off very quickly, almost exponentially. The current presented in Figure 6 for Ag is the current measured one minute after the voltage is applied. It is believed that these Ag coated cells are particularly good conductors of oxygen, but as the region next to the electrode is depleted of oxygen it becomes more and more difficult to pass more oxygen. The results for the Pt and Pd electroded tubes appeared to be steady. It can be seen that at lower temperatures the Ag coated tubes perform better. The actual flow rate of oxygen versus the theoretical flow rate expected corresponding to the measured current agreed very well, almost one-to-one.

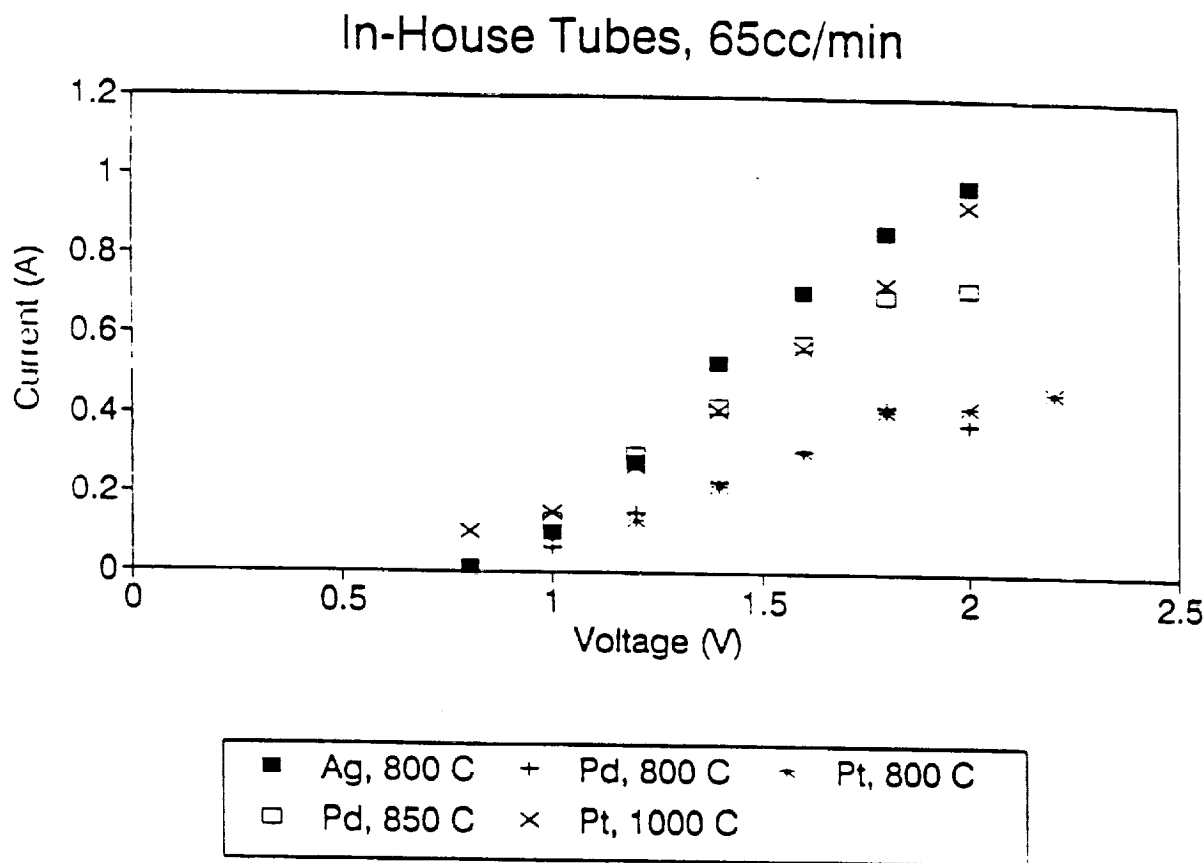


Fig. 6 Performance Characteristics of Tubes Electroded In-House

The results of the electroded tubes supplied by Ceramtec Inc. are presented in Figure 7. These tubes all have Ag coatings, but the perovskite substrates are LSCo, LSMnCo, LSM, and LSCoFe. Ceramtec would not make available information as to which perovskite was applied to which tube. It should be noted that a steady current was obtained from the onset. Several of these tubes were supplied with potentials as high as 3.8 V in some cases. Except for Tube #1, the results for the other tubes are very similar, and do not deviate from each other except at very high applied potentials. This may be above the breakdown voltage of the tubes. Above a certain potential, even though the current continues to increase, it is observed that the actual oxygen flow rate asymptotes to some limit. If the applied potential is increased beyond this the actual flow rate slowly increases. One representative curve is shown in Figure 8a, which shows the actual oxygen flow rate. Compare this to Figure 8b which shows the current vs. voltage. It is believed that this corresponds to the

Ceramatec Tubes, 825 C, 65cc/min

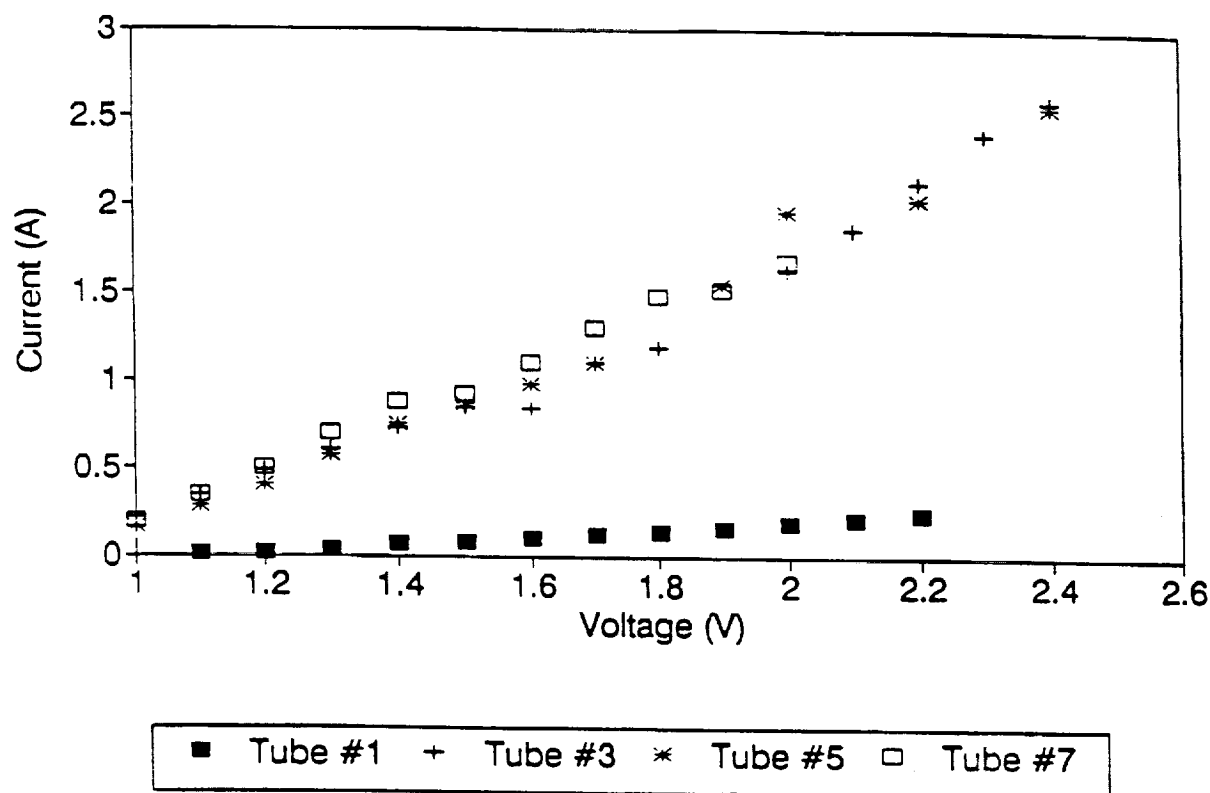


Fig. 7 Performance Characteristics of Pre-Electroded Tubes

"knee" of the I-V curve discussed by Richter [8], and that this may be the breakdown voltage of the Zirconia. It should be noted that there are differences in the performance characteristics of similarly electroded tubes that are made in the same batch. This is believed to be caused by the inherent uncertainties in the way the electrode is applied by brush. Variation in the thickness of the electrode could possibly affect the current distribution, and hence the production. Because of this a direct comparison cannot be made between different electrodes, since there is such a difference between similarly electroded tubes. It should be noted that in some cases a significant portion of the total current through these tubes is electronic, and that the actual oxygen production corresponding to the theoretical production based on the current can range from 65% to 95%, even below the "knee" of the curve. Ceramatec's preliminary results for their materials, tested using a disk system, are presented in the Appendix. These correspond to an electrode area of 3.2 cm². The results presented in the Appendix have not been independently verified at the University of Arizona, and the actual oxygen flow rates as compared to the corresponding current flow has not been measured.

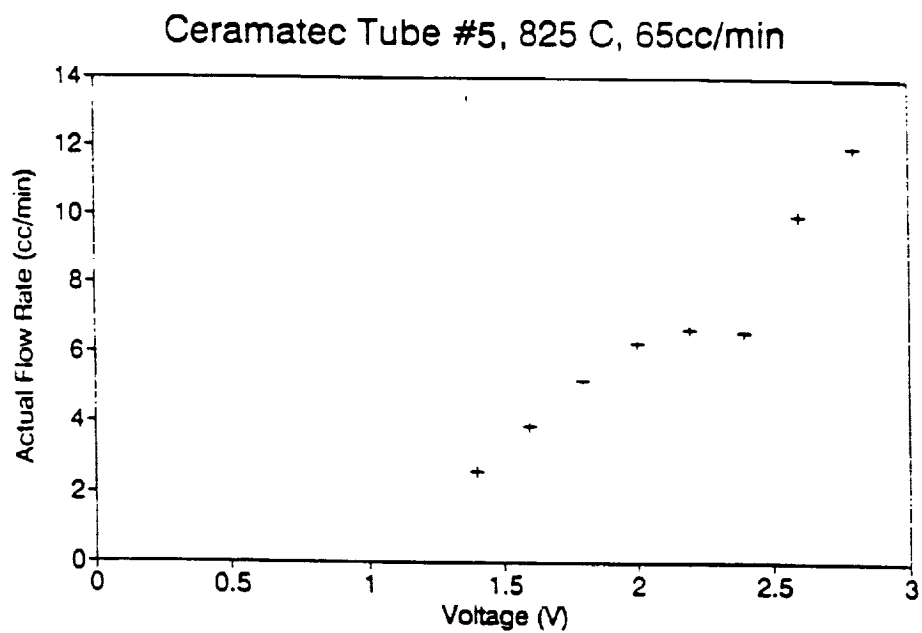


Fig. 8a Oxygen Flow Rate vs. Voltage for Tube Configuration

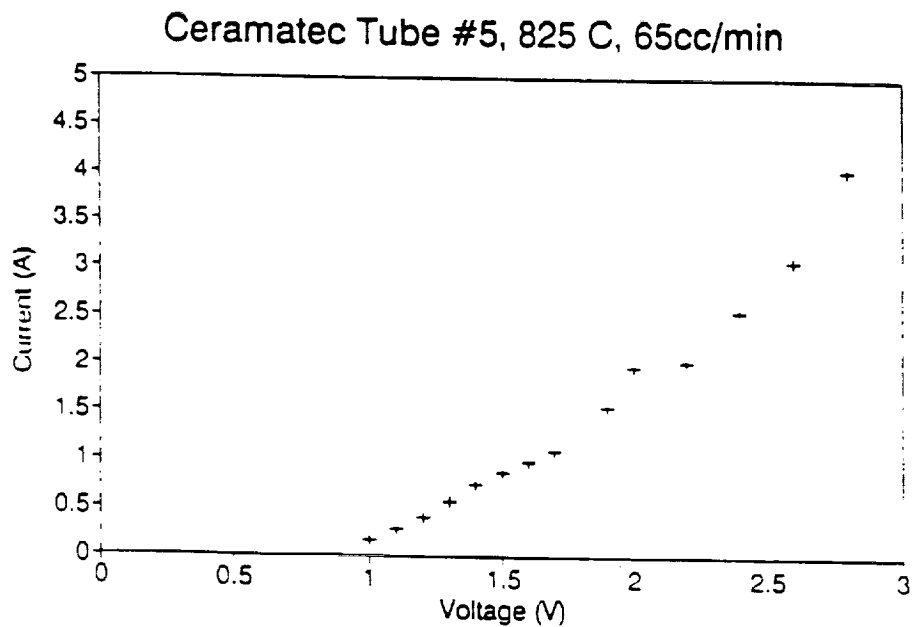


Fig. 8b Current vs. Voltage for Tube Configuration

Additional investigations on the tubes include complex impedance tests performed by the author [Kaloupis] at the Jet Propulsion Lab. These results can provide information on the resistance of the electrolyte and the contact resistance of the electrode [16,17]. Because of their preliminary nature they are not included here. Since those tests were conducted, the Space Engineering Research Center has acquired a Hewlett Packard Frequency Analyzer and future tests will be performed using this equipment to gather further necessary data. This will result in valuable information which can be used to develop better electroding techniques, thereby increasing the performance characteristics of the cell.

MULTIPLE TUBE SYSTEM*

In order to demonstrate the ability to scale up the electrochemical separation cell, a multiple tube system has been designed and built. This is shown schematically in Figure 9, and a photograph of the current system is shown in Figure 10. The unit consists of four tubes manifolded together as shown. Carbon dioxide is individually fed to each cell through an Alumina tube, but the oxygen is collected from all four through a single outlet. All four tubes are at the same temperature, and the applied voltage across each tube is the same. However, the current flow through each tube, and hence the oxygen production of each tube, can be individually monitored. It should be noted that for the multiple tube system the recorded temperature is the temperature of the oxygen gas, and not of the casing. Presently, this unit includes an active cooling system utilizing cold water so that the temperature of the cold seals can be maintained within the operating limits.

These four tube units can further be manifolded together into a single system consisting of sixteen tubes. Each cluster of four tubes may be individually monitored and controlled if desired, however all clusters are connected and operate as a single system. The construction of the sixteen tube system is currently nearing completion, and testing is expected to begin in the immediate future.

Results and Discussion

Some representative results of a single four tube cluster are presented in Figure 11. This figure shows the actual oxygen production flow rate. The tubes used in the four tube cluster are the best performing Ceramatec electroded tubes. The oxygen production of the four tubes manifolded together corresponds well to the sum of the oxygen production for the single tubes.

*Aerospace and Mechanical Engineering seniors Scott Miller, Doug Handley, and Brian Vaniman have designed, constructed, and tested the multiple tube system. The authors gratefully acknowledge their efforts.

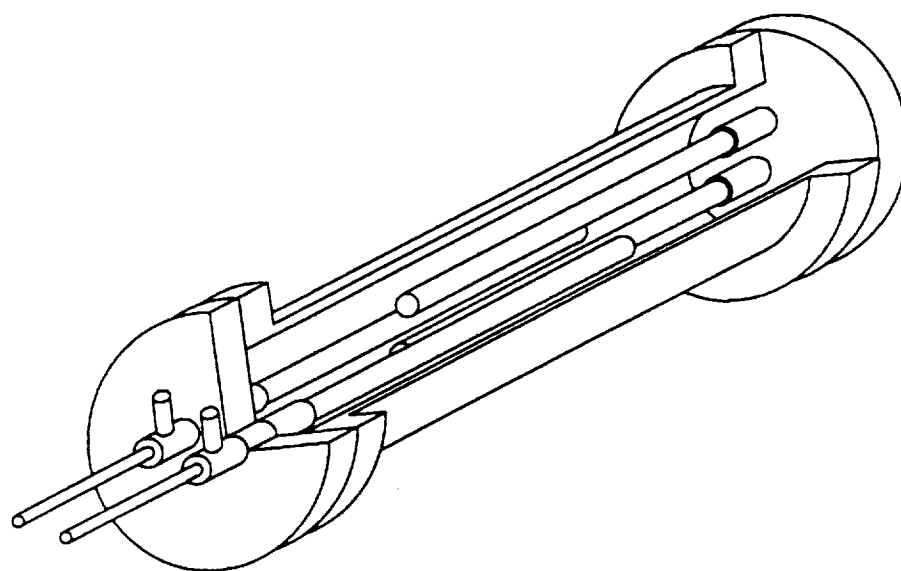
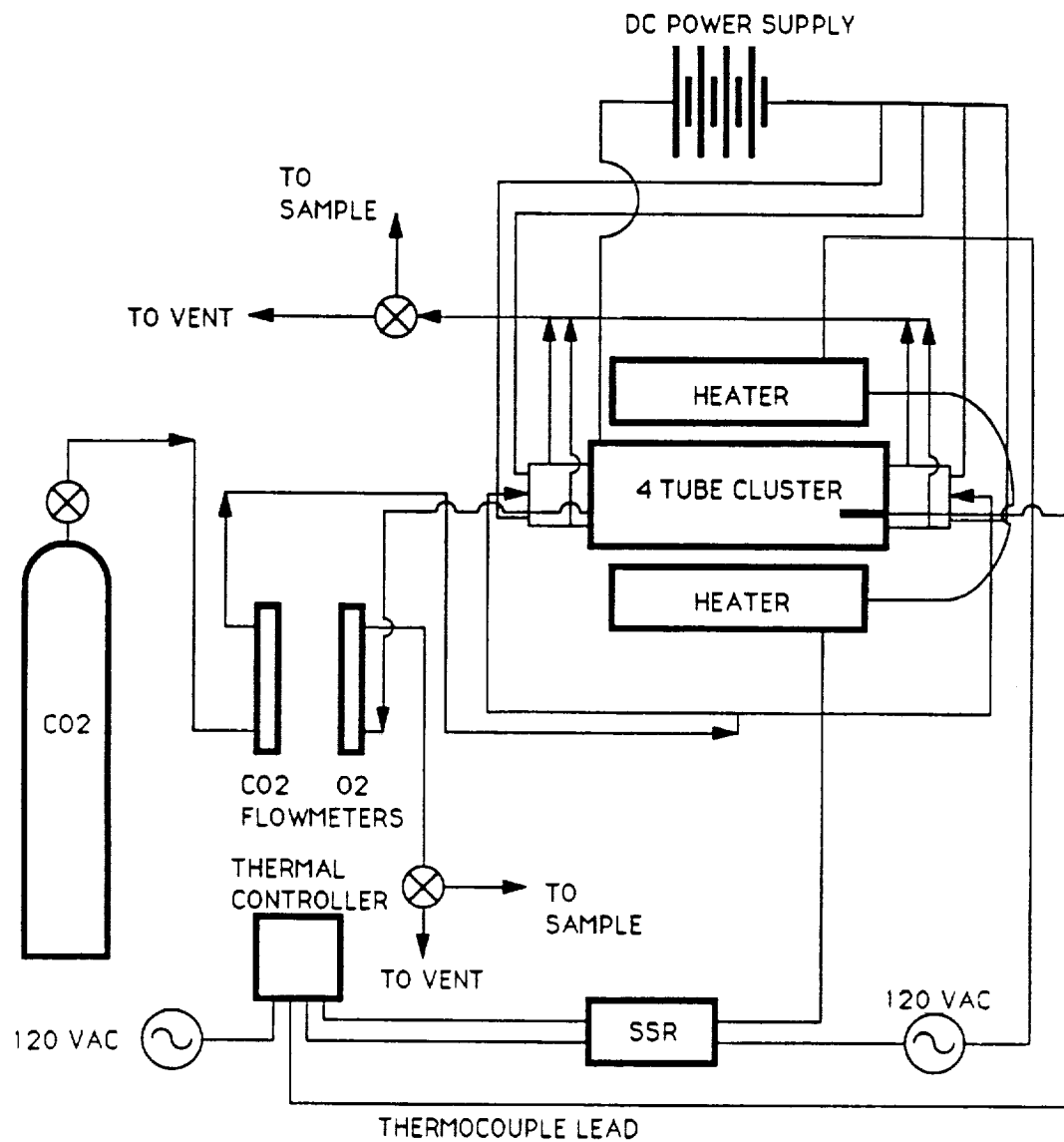


Fig. 9 Schematic of the Multiple Tube System Experimental Setup

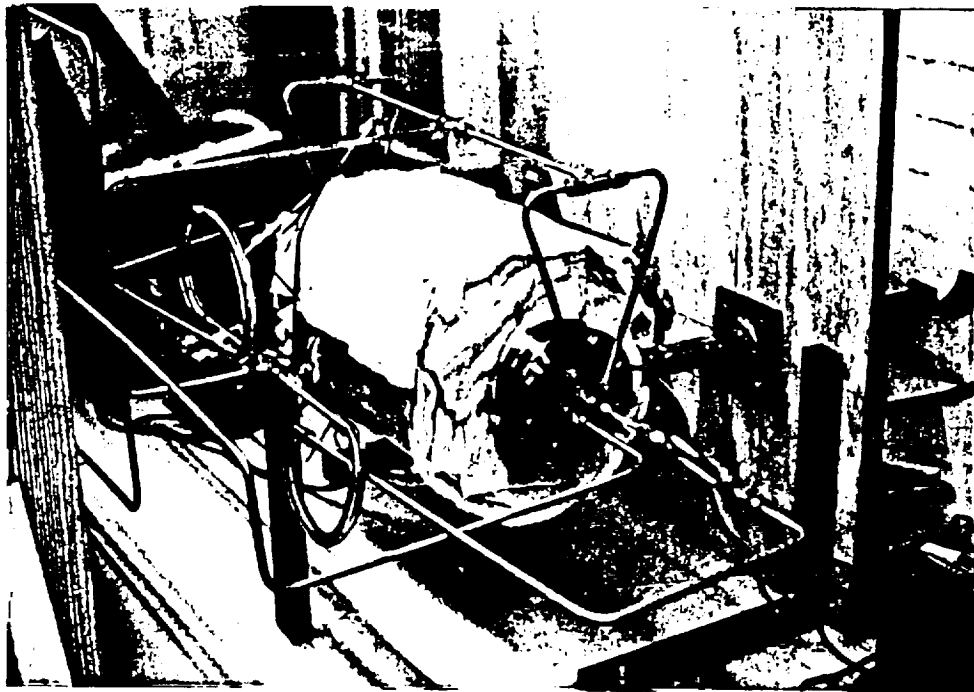


Fig. 10 Photograph of the Multiple Tube Experimental Setup

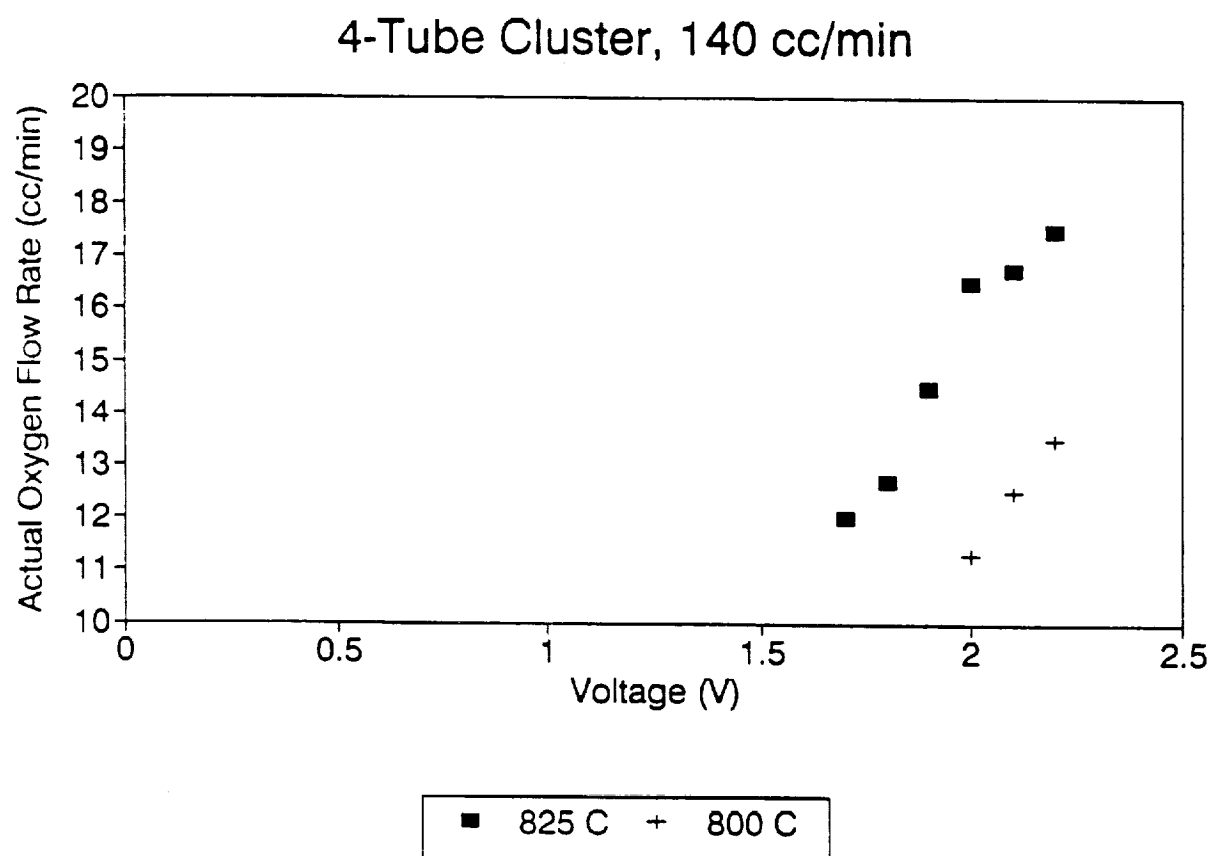


Fig. 11 Representative Results for the Multiple Tube System

REMARKS AND SUMMARY

Selection of the electrolyte and electrode materials have been made, based on previous investigations and concerns over reliability and ease of manufacturing. It is evident that the selection of the electrode is critical to the successful operation of the cell, and that an electrocatalytic electrode is necessary. More important than the precious metal coating which acts as the electron carrier is the perovskite substrate which acts as the catalyst.

A disk system has been built which can be used to readily test different electrolyte/electrode combinations, however a secure seal is still forthcoming. It is expected that a seal can be developed in the immediate future, and that the investigation of materials can begin in earnest. The disk system is preferred since it will be easier to operate. In addition, there is also some evidence to suggest that the disk geometry performs better than the tube geometry for the same electrolyte/electrode combination [18], possibly because of the electrode application technique.

Testing on the tube systems has continued while a seal is being developed, but it is apparent from the results that the application of the electrode is very important, and that the reaction kinetics at the surface of the cell still need to be better understood.

Successful testing of the multiple tube systems have demonstrated the scale-up capability of the concept. This permits the investigations on single cell units to continue with the confidence that any gains in production based on materials considerations can be applied to the larger system.

It is obvious that the most critical investigations that need to be performed in the future are with regards to the electrodes. It is believed that the application technique is very important. Also, the reaction kinetics need to be better understood so that a systematic search can be conducted for electrocatalytic materials, perovskites or otherwise.

ACKNOWLEDGEMENTS

The authors would like to acknowledge Dr. Jerry Suitor, Dr. Mark Underwood, Douglas Clark, and Bob Losey of the Jet Propulsion Lab who graciously permitted the use of their labs and equipment for the tape casting and complex impedance testing. In addition, the authors would like to extend their appreciation to Ceramatec Inc. for providing the electroded tubes used in the multiple tube system.

REFERENCES

1. The Report of the National Commission on Space, "Pioneering the Space Frontier," Bantam Publishing, New York, 1986.
2. Ash, R. L., Dowler, W. L., and Varsi, G., "Feasibility of Rocket Propellant Production on Mars," Acta Astronautica, Vol. 5, Sept. 1978, pp. 705-724.

3. Ash, R. L., Huang, J. K., and Johnson, P. B., "Elements of Oxygen Production Systems Using Martian Atmosphere," Paper No. AIAA-86-1586, AIAA/ASME/SAE/ASEE 22nd Joint Propulsion Conference, June 16-18, Huntsville AL, 1986.
4. Ash, R. L., Richter, R., Dowler, W. L., Hanson, J. A., and Uphoff, C. W., "Autonomous Oxygen Production for a Mars Return Vehicle," Paper No. IAF-82-210, 33rd Congress of the International Astronautical Federation, Paris, France, Oct. 1982.
5. Ramohalli, K., Lawton, E., and Ash, R. L., "Recent Concepts in Missions to Mars: Extraterrestrial Processes," J. of Propulsion and Power, Vol. 5, No. 2, March-April, 1989, pp. 181-187.
6. Suitor, J. W., Berdhal, C. M., Ferrall, J. F., Marner, W. J., Schroeder, J. E., and Shlichta, P. J., "Development of an Alternate Oxygen Production Source Using Zirconia Solid Electrolyte Membrane," Technical Progress Report for Fiscal Years 1986 and 1987, Report No. JPL-D-4320, May 1987.
7. Kaloupis, P., and Sridhar, K. R., "Issues on the Production and Electrochemical Separation of Oxygen from Carbon Dioxide," NASA Space Engineering Research Center Annual Progress Report 1990-91, APR-91, University of Arizona, Arizona, 1990, pp. IB-21 - IB-35.
8. Richter, R., "Basic Investigation into the Production of Oxygen in a Solid Electrolyte Process," Paper No. AIAA-81-1175, AIAA 16th Thermophysics Conference, June 23-25, Palo Alto CA, 1981.
9. Erstfeld, T. E., and Mullins Jr., O., "Carbon Dioxide Electrolysis Using a Ceramic Electrolyte," Paper No. AIAA-79-1375, Fourth Princeton/AIAA Conference on Space Manufacturing Facilities, May 14-17, Princeton NJ, 1979.
10. Dell, R. M., and Hooper, A., "Oxygen Ion Conductors," Solid Electrolytes, General Principles, Characterization, Materials, Applications, ed. Hagenmuller, P., and Van Gool, W., Academic Press, New York, 1978, pp. 291-312.
11. Miyayama, M., Nishi, T., and Yanagida, H., "Oxygen Ionic Conduction in Y_2O_3 Stabilized Bi_2O_3 and ZrO_2 Composites," J. of Materials Science, Vol. 22, 1987, pp. 2624-2628.
12. Subbarao, E. C., ed., Solid Electrolytes and their Applications, Plenum Press, New York, 1980.
13. Isaacs, H. S., Olmer, L. J., Schouler, E. J. L., and Yang, C. Y., "Electrode Reactions at Solid Oxide Electrolytes," Solid State Ionics, 1981, pp. 503-507.

14. Isaacs, H. S., and Olmer, L. J., "Comparison of Materials as Oxygen Catalytic Electrodes on a Zirconia Electrolyte," J. of the Electrochemical Society: Solid State Science and Technology, Feb. 1982, pp. 436-443.
15. Rohr, F. J., Eysel, H. H., and Kleinschmager, H., "Electronically Conducting Oxides as Cathodes of Interconnection Materials in High Temperature Fuel Cell Batteries," Fourth International Symposium on Fuel Cells, Antwerp, Belgium, Vol. 1, 1972.
16. Sasaki, J., Mizusaki, J., Yamauchi, S., and Fueki, K., "Studies on Electrode Processes of Stabilized Zirconia Cells by the Complex Impedance Method," Solid State Ionics, 1981, pp. 531-535.
17. Schouler, E. J., Mesahi, N., and Vitter, G., "In-Situ Study of the Sintering Process of Yttria Stabilized Zirconia by Impedance Spectroscopy," Solid State Ionics, 1983, pp. 989-996.
18. Dr. Meilin Liu, Research Scientist, Ceramtec Inc., Private Communication, Aug. 1991.

APPENDIX

This appendix contains data supplied by Ceramtec Inc. It has not been independently verified by the University of Arizona. Figure A-1 shows the results for a Silver electrode with various perovskite substrates at 700 °C and 800 °C. These tests were performed on a disk geometry system with an electroded area of 3.2 cm². There is a noticeable difference in the performance of the perovskites, which was not obvious with the tube geometry experiments of Figure 7. The corresponding oxygen production rates were not measured, and hence the ionic and electronic contributions to the total current are not known. Of the perovskites tested, LSMnCo appears to be the best performer.

In addition to these experiments, Ceramtec Inc. has investigated Ceria (CeO₂-CaO 15% mole) tubes with very limited success. The results of these tests are proprietary to Ceramtec, and are not presented here.

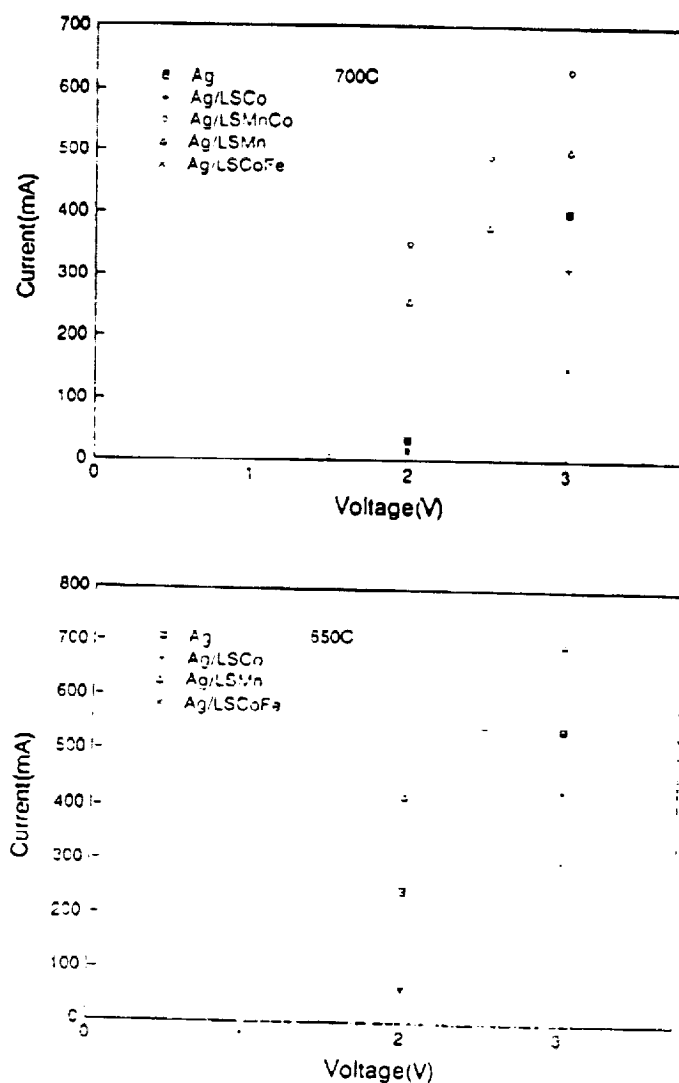


Fig. A-1 Results of Ceramtec Disk System Experiments for Various Perovskites

DESIGN AND OPTIMIZATION OF SUB-SYSTEMS IN THE MARTIAN OXYGEN PRODUCTION PLANT

K.R. Sridhar* and Venkatesh Iyer**
Department of Aerospace and Mechanical Engineering
University of Arizona, Tucson, AZ 85721

The objective of this research is to design the thermal components of the Mars Oxygen Production Plant. The design of the overall system and the selection and design of individual components is made with the objective of keeping the mass of the system, including the power supply, to a minimum. Based on analysis it was found that in spite of the added complexity, it is more efficient to recycle the unspent carbon dioxide back to the electrochemical cell for oxygen extraction rather than exhaust it. Though carbon dioxide is available in abundance on Mars, the cleaning and pressurizing of carbon dioxide in the system is energy intensive and requires bulky components. Hence a large saving in mass was obtained when the unspent CO_2 was recycled. A detailed look at the means of compressing the low pressure Martian carbon dioxide to higher pressures that exist in the production plant revealed that the optimal components for this process were a Roots pump with a dry (oil-free) backing pump.

*Assistant Professor
**Graduate Student

DESIGN AND OPTIMIZATION OF SUB-SYSTEMS IN THE MARTIAN OXYGEN PRODUCTION PLANT

K.R. Sridhar and Venkatesh Iyer
Department of Aerospace and Mechanical Engineering
University of Arizona, Tucson, AZ 85721

The objective of this research is to design the thermal components of the Mars Oxygen Production Plant. The design of the overall system and the selection and design of individual components is made with the objective of keeping the mass of the system, including the power supply, to a minimum. Based on analysis it was found that in spite of the added complexity, it is more efficient to recycle the unspent carbon dioxide back to the electrochemical cell for oxygen extraction rather than exhaust it. Though carbon dioxide is available in abundance on Mars, the cleaning and pressurizing of carbon dioxide in the system is energy intensive and requires bulky components. Hence a large saving in mass was obtained when the unspent CO_2 was recycled. A detailed look at the means of compressing the low pressure Martian carbon dioxide to higher pressures that exist in the production plant revealed that the optimal components for this process were a Roots pump with a dry (oil-free) backing pump.

Introduction:

Considerable progress has been made in the utilization of extraterrestrial resources since Ash, Dowler and Varsi [1] introduced the idea in 1978. Propellant production at locations remote from the Earth is vital for frequent, extended space exploration. In this report we focus on the manufacture of oxygen from the predominantly carbon dioxide atmosphere of Mars. Oxygen is produced by heating carbon dioxide to temperatures in the range of 800-1000°C and using an electrochemical cell to separate the oxygen. A schematic of the test bed is shown in Fig 1.

The test bed consists of the simulation sub-system for the Martian atmosphere, the carbon dioxide compression sub-system, the heating and separation sub-system, and the sub-system for recycling the spent gas. A brief description of each sub-system follows.

- The Martian atmosphere consists predominantly of carbon dioxide gas at 640 Pa and 200K. The simulation sub-system, consists of carbon dioxide supply and a cryo-vacuum chamber cooled by a cryo-cooler. It provides a supply of CO_2 at Martian ambient pressure and temperature. The minor atmospheric constituents, such as nitrogen and argon are not considered here. The issue of filtration of the dust in the Martian atmosphere will be the subject of a future study.
- The compression sub-system has the heaviest components in the test bed. It is necessary to pressurize the gas in order for the overall system to be of a reasonable size. At present, the operational characteristics of the electrochemical cell at subatmospheric pressures (< 0.1 MPa) are not known. This is a topic of future investigation at the UA/NASA Space Engineering Research Center. For this

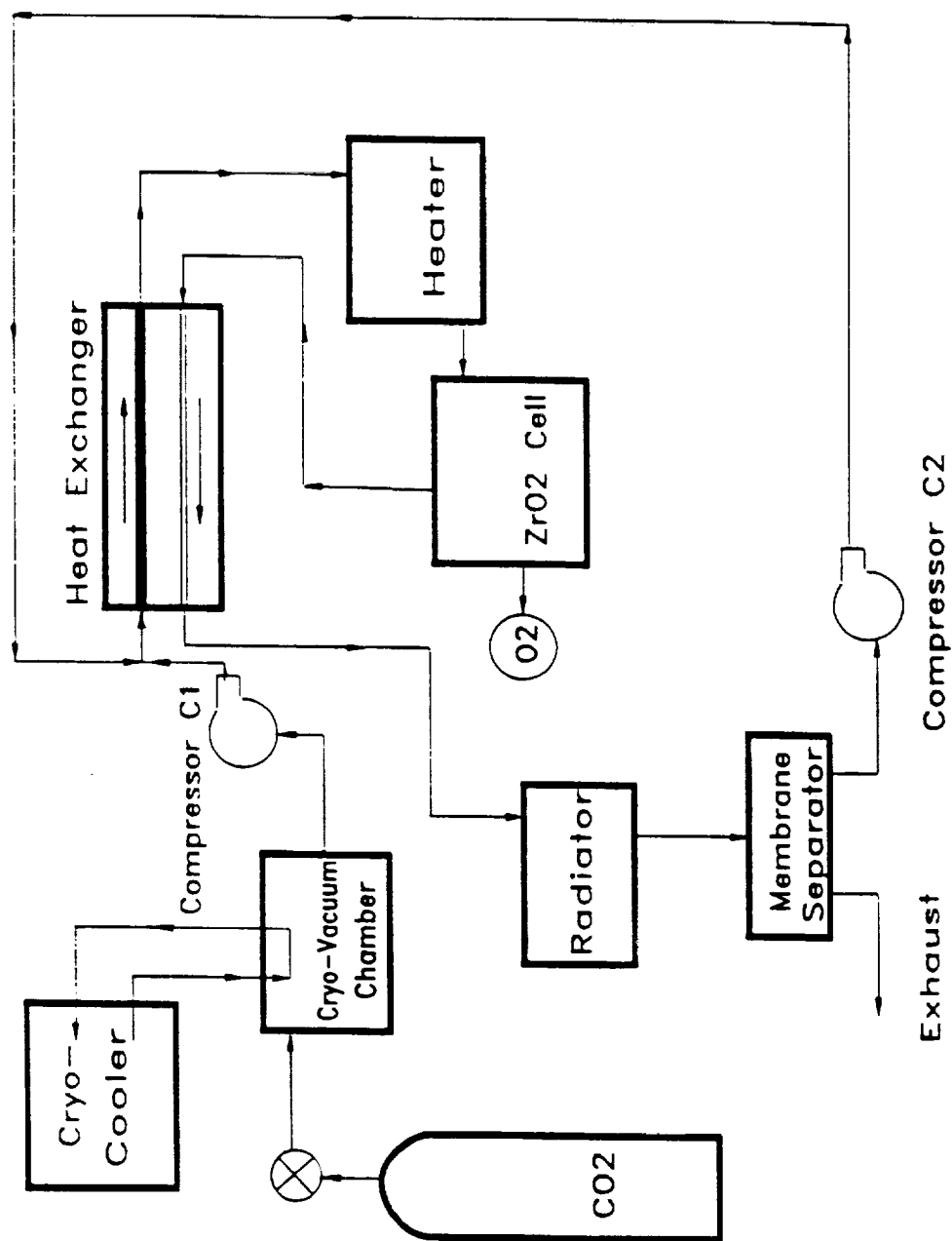


Figure 1: A Simplified Schematic of the Test Bed with Carbon Dioxide Recycling

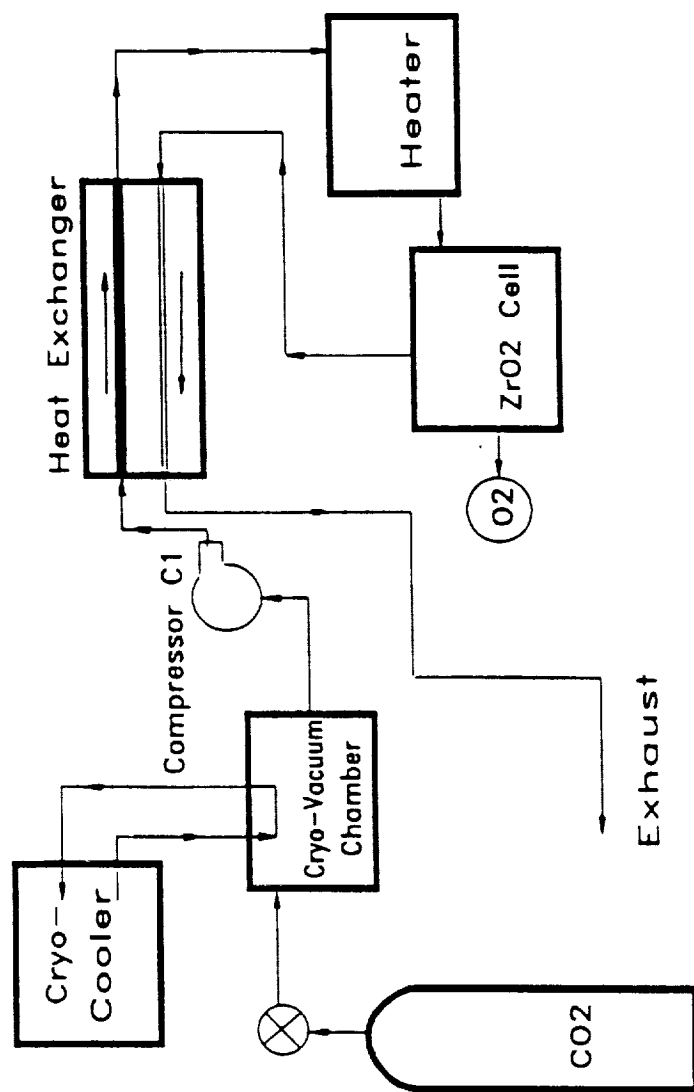


Figure 2: A Simplified Schematic of the Test Bed without Carbon Dioxide Recycling

reason and also for operational convenience in the laboratory, this study assumes that CO_2 will be compressed to 0.1 MPa (1 bar). The issue of the optimal compression pressure will be revisited when data is available on the operation of the electrochemical cell at subatmospheric pressures.

- The exhaust gases from the electrochemical cell are used to preheat the inlet CO_2 to the cell in a waste heat recovery heat exchanger. The CO_2 is further heated to the operating temperature of the electrochemical cell in a heater prior to entering the cell. Isothermality of the gases and the cell ensure that the cell is not subjected to sudden thermal loading. The separation of the oxygen from the gas mixture of CO_2 , CO and O_2 takes place in the electrochemical cell. The heat exchanger, heater and the electrochemical cell form the heating and separation sub-system.
- The recycling sub-system consists of the radiator, the membrane separator and the back-up compressor. The radiator is required because the polymeric membrane separator, which separates CO_2 from a mixture of CO_2 and CO, cannot withstand the high temperatures of the gases exhausting from the heat exchanger. At the present time, the temperature of the exhaust gases is kept above 700K in the heat exchanger because it is feared that in the range of 600-700K, carbon monoxide will oxidize to form carbon dioxide and deposit solid carbon in the heat exchanger tubes. The carbon dioxide separated by the membrane separator is compressed by the back-up compressor and merges with the intake gases upstream of the heat exchanger.

Fig 2 is a simplified schematic of the test bed that is similar to the one discussed above except for the recycling sub-system. In this once-through system, the unspent CO_2 from the electrochemical cell is exhausted to the atmosphere.

All the calculations in this report, unless stated otherwise, are based on an oxygen production rate of 10 kg/day, which corresponds to the production rate required for an unmanned Mars sample return mission [1]. The variation of the specific heats of the various gases over the temperature range is considerable, and therefore, has been taken into account in the calculations. The efficiency of the electrochemical cell, defined as the fraction of the theoretical maximum of the oxygen that is actually produced, has been taken to be 20% - the current level of performance of the cells in our laboratories.

Need for Recycling the Unreacted Carbon Dioxide:

The need for recycling the unreacted CO_2 has been discussed in detail in an earlier report [2]. The salient points are recapitulated here for completeness. Based on an electrochemical cell efficiency of 20%, and an oxygen production rate of 10 kg/day, the size of the pumps required to compress CO_2 from 640 Pa to 0.1 MPa for the cases with and without recycling was examined. For the case with recycling the inlet volumetric flow rate to the pump was $0.04682 \text{ m}^3/\text{s}$. It was found that Leybold's Model S160C [3], an oil-sealed mechanical rotary vane vacuum pump weighing 141 kg, with a power consumption of 5.5 kW, and a Leybold TRIVAC Rotary Vane Pump Model D2A as the back-up pump, weighing 19 kg, with a 0.25 kW power consumption, could handle the requirements with a minimum mass penalty. Fig 3 is a plot of the pump mass for various inlet volumetric flow rates at 640 Pa. The data points correspond to the mass of industrial pumps. Interpolating from this plot, the

mass of a pump for the $0.04682 \text{ m}^3/\text{s}$ flow rate is 130 kg. For the case without recycling, the inlet volumetric flow rate to the pump would be $0.1261 \text{ m}^3/\text{s}$, corresponding to a pump mass of 330 kg and a power consumption of about 11.4 kW.

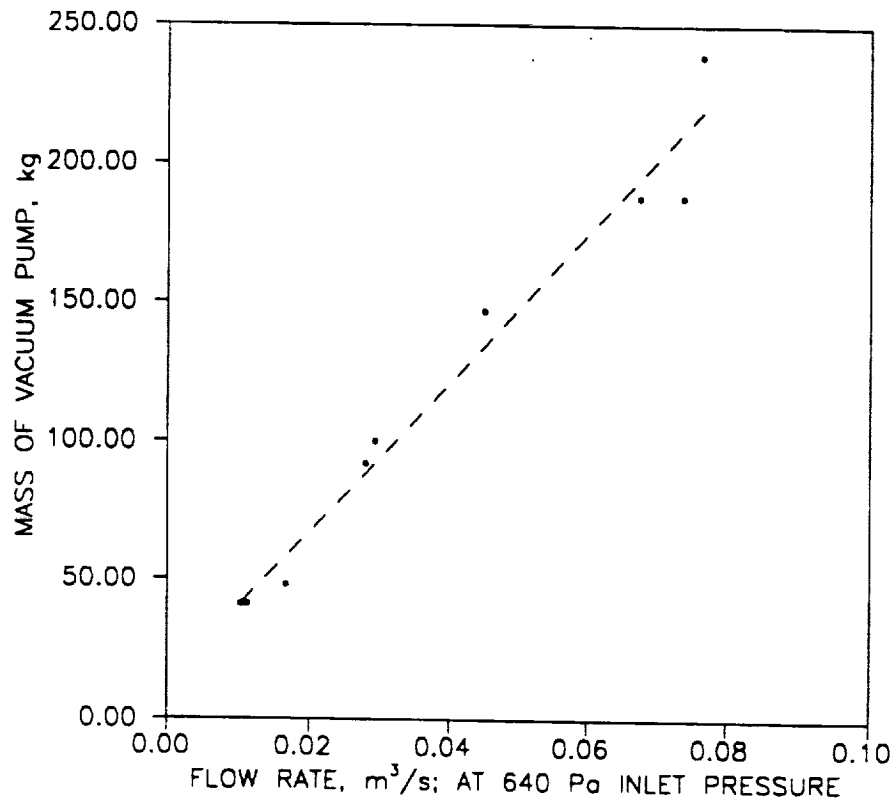


Figure 3: Variation of Industrial Vacuum Pump Mass with Flow Intake at 640 Pa

This simple exercise clearly demonstrated that the case with CO_2 recycling would be a better choice from the perspective of mass and power consumption, in spite of the added complexity due to the recycling equipment. It also emphasizes the usefulness of graphs generated from industrial data.

The Compression Sub-system:

The function of the compression sub-system is to increase the pressure of cleaned (filtered) Martian gases from 640 Pa to 0.1 MPa. Preliminary examination of the components, as seen in the previous discussion on recycling, suggested that the components of this sub-system would be massive and would consume more power in comparison with other sub-systems. Various means of compressing the CO_2 were considered in detail to identify the least mass and power penalty. This search was restricted to mechanical devices and did not include adsorption devices. Research on the adsorption compressors is being conducted independently at UA/NASA SERC by Prof D.C. Lynch and his students.

The various devices considered here were compared on the basis of a CO_2 flow rate of 1 scfm (standard cubic feet per minute). The mass and power consumption for the devices were obtained from industrial catalogs. Clearly, light-weight super-alloy materials would be used for the components in the actual mission. It is not necessary to account for this in this comparative study since the correction for the lower density of the materials applies across the board for all devices. It will, however, be considered when accounting for the mass of the device selected in the overall oxygen production plant system analysis.

Fig 3 shows the variation of vacuum pump mass with pump capacity at 640 Pa. The data points in this plot are from industrial catalogs [3,4,5,6,7,8]. Interpolating the data it can be seen that the mass of a pump with a capacity of 1 scfm (104 cfm (0.04682 m^3/s) at 640 Pa and 200K) is 136 kg.

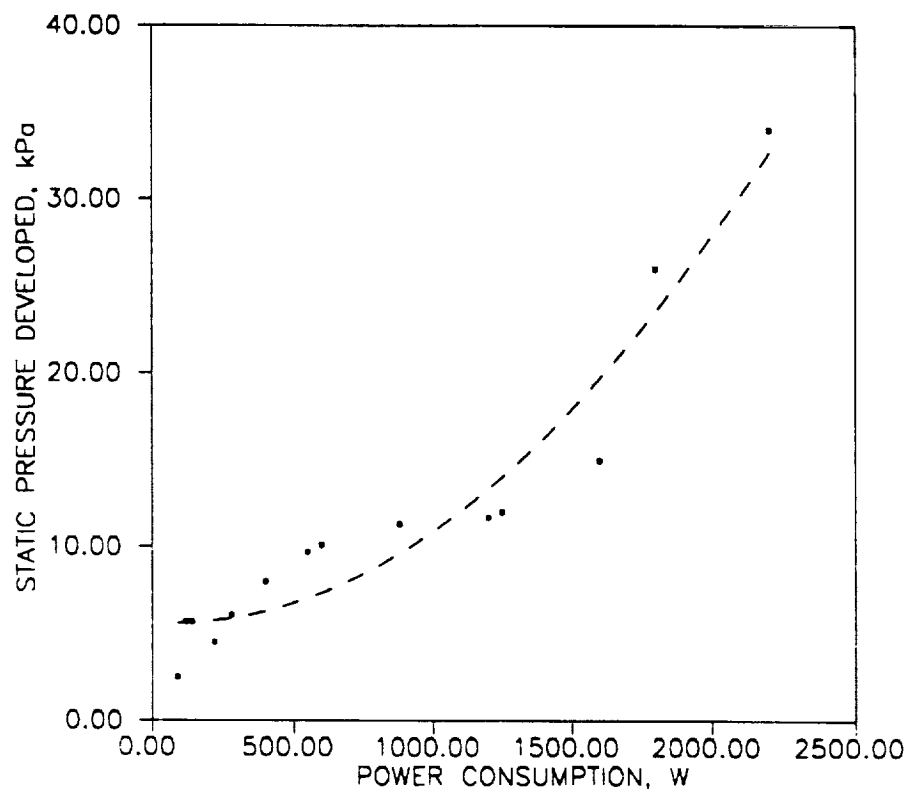


Figure 4: Variation of the Static Pressure Increase with Power Consumption for Various Industrial Blowers

An exercise was performed to determine the mass and power requirements for blowers to be used in series with back-up pumps. Fig 4 shows the static pressure increase plotted with the power consumption. It is to be noted that the blower data is valid only for an inlet pressure of 0.1 MPa (1 bar). The corrections for lower inlet pressures have been made using the Fan Laws [9].

These graphs are useful in determining the performance of a given combination of blowers and vacuum pumps, and in ascertaining whether it would be better to connect the devices in series, or in parallel, the overall objective being to minimize the mass and power requirements. There is a lot of flexibility in the choice of equipment used to compress CO_2 gas from 640 Pa at 200K to 0.1 MPa. The final temperature is not of great concern since the gases finally have to be heated to a temperature around 800-1000°C. Flexibility also exists in the choice of the thermodynamic compression cycle used, but since the gas temperature has to be increased, it is better to select a cycle as close to adiabatic compression as possible. This latitude in the selection of the device (or devices) used meant that various scenarios would have to be explored to show conclusively that a particular combination was best for the application at hand.

The use of a fan backed up by a compressor meant that the fan would have to operate at the low intake pressure of 640 Pa. Industrial data is available only for an intake pressure of about 0.1 MPa (atmospheric pressure). It was necessary to predict the performance characteristics and size of a fan operating at 640 Pa using the available information. The applicability of the Fan Laws [9], which express the relationships among the performance variables for any two fans that have similar flow conditions, is suspect when the variation in inlet pressures is so large. A perturbation analysis of the variables was carried out, yielding some very interesting information. The basis for the comparison, as mentioned earlier in this report, was a CO_2 flow rate of 1 scfm (0.0004502 m^3/s at standard conditions of 0.1 MPa and 300K).

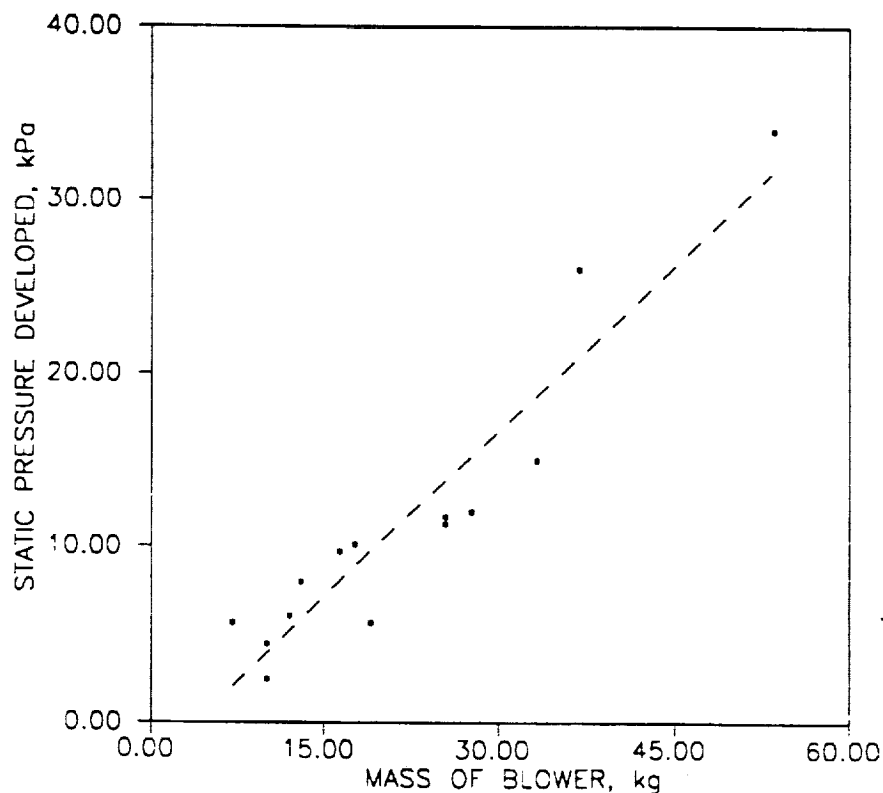


Figure 5: Variation of the Static Pressure Increase with the Mass of Industrial Blowers

At the intake conditions of 640 Pa and 200K, it corresponds to a flow rate of 104 cfm (0.04682 m³/s). The pertinent graph for this comparison is Fig 5, which has been developed from industrial data. Two cases were examined:

1. A fan capable of delivering a flow rate of 104 cfm at standard conditions has been found to weigh 37 kg and produces a total pressure rise of 27.6 kPa at 5500 rpm. This fan, the DR505R, manufactured by EG&G Rotron, has a diameter of 0.36 m. For a fixed static pressure increase, a decrease of 20% in the intake pressure and 10% in the intake temperature results in a diameter decrease of 3%, while the fan speed rise is 9%. This means that with a much lower intake pressure of 640 Pa, the speed will increase much more rapidly than the decrease in diameter, making the sub-system unviable. If the speed of the fan were kept constant at 5500 rpm, the diameter would increase considerably, thereby increasing the mass penalty.

2. Another fan which delivers 1 cfm (0.0004502 m³/s) at standard conditions weighs 6.8 kg and produced a 5.7 kPa total pressure rise at 3000 rpm. This is the DR083 manufactured by EG&G Rotron. It has a diameter of 0.19 m. A decrease of 20% in the intake pressure and 10% in the intake temperature resulted in a diameter increase of 5%, along with an increase in speed of 18%, the total pressure rise being kept constant.

From the two cases considered, it is clear that for a significant static pressure increase:

- a. If the fan size at intake conditions of 640 Pa and 200K lies in between the sizes of the DR083 and DR505R fans, then the speed of the fan would be orders of magnitude higher than the rated speed at 0.1 MPa. This configuration is not technically viable.
- b. If the speed of the fan were fixed at nominal levels, the fan required is so large that the mass and power penalties are unacceptable.

Hence the choice of a fan to pressurize CO₂ from the Martian intake conditions is not a viable option.

The Roots Pump and Backing Pump Combination:

Roots pumps have found wide application in the field of vacuum technology. They are used in pump combinations with backing pumps (sliding vane pumps, rotary piston pumps, trochoid pumps and others).

A Roots pump is a positive displacement rotary pump that can run at very high rotational speeds without mechanical wear. Since these pumps are not oil-sealed, they have an inherent internal leakage, resulting in comparatively low compression ratios. The compression ratio reaches a maximum at an intake pressure of about 100 Pa (1 mbar).

The selection of a Roots pump and backing pump combination was made with the aid of industrial catalogs and design curves. The procedure involves the use of a few terms which are defined below:

p_v - fore-pressure for the backing pump, Pa
 S_v - pumping speed of the backing pump, m^3/s
 S_{th} - theoretical maximum pumping speed of Roots pump, which is the product of the swept volume and the number of revolutions per unit time
 k_{th} - the gradation, or the ratio of S_{th} to S_v
 $k_o(p_v)$ - maximum compression ratio of the Roots pump
 η - volumetric efficiency of the Roots pump, $[k_o/(k_o+k_{th})]$, also $[S_{eff}/S_{th}]$
 S_{eff} - effective pumping speed of Roots pump, the product of η and S_{th}
 p_s - intake pressure of the Roots pump, $[(p_v S_v)/S_{eff}]$, Pa

In the design, a Roots pump and backing pump combination which can handle the intake flow rate of $0.04682 \text{ m}^3/\text{s}$ at 640 Pa and 200K is selected. The combination is then verified. A sample calculation is shown below.

The selected combination is a WS/WSU 251/D25D/BCS pumping system manufactured by Leybold Inc. The Roots pump, which is a WS/WSU 251, has a theoretical pumping speed (S_{th}) of $0.07 \text{ m}^3/\text{s}$. The backing pump, D25B/BCS, has an S_v of $0.00694 \text{ m}^3/\text{s}$. The effective pumping speed (S_{eff}) required is $0.04682 \text{ m}^3/\text{s}$. The intake pressure p_s is 640 Pa. The gradation k_{th} is calculated, knowing S_{th} and S_v , to be 10.04. Volumetric efficiency of the Roots pump is determined as the ratio of S_{eff} to S_{th} and is 0.67. The maximum compression ratio k_o is then found to be 20.53, from η and k_{th} . The fore-vacuum pressure p_v is calculated using p_s , S_v and S_{eff} to be 4334 Pa. The backing pump selected can handle this intake pressure and delivers the gas at the system pressure of 0.1 MPa (1 bar). The mass of the Roots pump and backing pump combination is 123 kg and it consumes about 2.2 kW.

Power-mass penalty represents the mass of the power supply unit required to provide a certain requirement. In this report, a penalty of 30 kg/kW has been used. This figure is reasonable when compared with the power-mass penalties of the SP-100 nuclear power (26.9 kg/kW) and photovoltaic power (30.3 kg/kW) supplies [10]. Using this figure, the mass of the compression sub-system is found to be about 190 kg.

The above discussion clearly indicates that the Roots pump and backing pump combination is best for the application in consideration, and that the use of other devices would be more massive, bulkier and consume more power.

References:

1. Ash, R.L., Dowler, W.L. and Varsi, G., "Feasibility of Rocket Propellant Production on Mars", *Acta Astronautica*, Vol 5, 1078, pp 705-724
2. Iyer, V.A. and Sridhar, K.R., "Thermal Analysis, Optimization and Design of a Mars Oxygen Production Plant", NASA/SERC Annual Progress Report, Apr. 1991, The University of Arizona, Tucson, pp 1B9-1B20
3. Leybold Inc., "Product and Vacuum Technology Reference Book", San Jose, CA, 1990
4. Varian Associates Inc., "Price List Catalog", Lexington, MA, 1990
5. Atlas Copco AB, "Atlas Copco Manual", Stockholm, Sweden, 1978

6. KNF Neuberger Inc., "Vacuum Pump and Compressor Catalog", Princeton, NJ, 1990
7. Kinney Vacuum Company, "Guide to the Selection of Vacuum Pumps", Canton, MA, 1990
8. EG&G Rotron, "Rotron Regenerative Blowers", Saugerties, NY, 1990
9. Jorgensen, R., "Fan Engineering" Buffalo Forge Co., Buffalo, NY, 1986
10. Drolen, B., "Heat-Pump Augmented Radiator for High Power Spacecraft Thermal Control", AIAA 89-0077, presented at the 27th Aerospace Sciences Meeting, Reno, Nevada, Jan 9-12, 1989



FULL SYSTEM ENGINEERING DESIGN AND OPERATION OF AN OXYGEN PLANT

James Colvin, Paul Schallhorn and Kumar Ramohalli

UA/NASA Space Engineering Research Center

Aerospace and Mechanical Engineering

University of Arizona, Tucson, Arizona 85712

ABSTRACT

This section describes the SERC centerpiece project whose general aim is to produce oxygen from carbon dioxide. After discussing briefly the project's background, the case for indigenous material utilization, and the benefits in terms of lower overall cost (through the reduction in launch mass), specific experimental details of the electrolytic cells are presented. At the heart of the oxygen production system is a bank of solid zirconia electrolytic cells that will electrochemically separate oxygen from a high temperature stream of carbon dioxide. Experimental results are discussed. The parameters varied include: the cell operating temperature, the carbon dioxide flow rate, and the voltage applied across the cell. The results confirm our theoretical expectations. At the time of this report (September 1991) two one-hundred hour runs have been completed and the extensive data are being carefully analyzed.

I. INTRODUCTION

BACKGROUND

A primary concern for any venture into space must be how much energy will the mission require. As we plan to visit local extraterrestrial bodies more frequently, or as we plan to venture further into space, an important consideration has to be, should we continue to bring all propellants with us from earth, or should we take advantage of the many resources that are available to us once we reach our destination? With this idea in mind and wishing to expand on the success of the Martian Viking program, Ash, Dowler, and Varsi¹ in the late seventies envisioned an in-situ propellant plant which would make use of the Martian atmosphere to produce an oxygen and methane propellant.

At the heart of this system would be an array of zirconia solid electrolyte cells. These cells have the ability to selectively transport oxygen ions thus allowing the production of pure oxygen. The oxygen plant has undergone many changes since it was first envisioned by Ash et al. Lawton and Frisbee, at the Jet Propulsion Laboratory (JPL), have done extensive work on improving the overall system^{2,3,4}, reducing the total system mass and increasing the total system reliability.

Their improved system would have the Martian atmosphere drawn in through an electrostatic dust filter which is necessary as there are numerous long term dust storms on the Martian surface. The atmosphere, which consists of approximately 95% carbon dioxide, will be drawn into the system by a CO₂ adsorption compressor. Present plans³ require the atmosphere to be compressed from the ambient pressure of 6.8 mb to a pressure of 1 bar for delivery to the cathode side of the electrolyte. Before entering the zirconia array, the flow will pass through a heat exchanger which will raise the temperature from the CO₂ compressor's exit of 600 K to approximately 1000 K. The source of the heat for the heat exchanger is the exhaust flow from the array. Once the flow has entered the zirconia array, it will be further heated to a temperature of 1273 K. This temperature is sufficient to partially dissociate the carbon dioxide into carbon monoxide and diatomic oxygen.

It is the O₂ that the cell will selectively transport to the anode side of the cell where the pressure of the O₂ will be increased to 4 bar. The cell's exhaust will consist of mostly CO₂ with some CO also present. The O₂ at the anode will now pass through a radiator where it will be cooled from 1270 K to 250 K at 3.8 bar. The O₂ flow will next pass through an O₂ adsorption compressor where the

pressure will be increased to 28 bar and its temperature to 400 K. After passing through one more radiator, where the flow will be cooled to 230 K, the O_2 will be finally cooled to 100 K by a molecular adsorption cryo-cooler refrigerator and stored for its final use. This use could initially be the oxidizer for the propellant necessary to return a Martian sample to earth, and then eventually, life support for a manned Martian mission.

YTTRIA STABILIZED ZIRCONIA SOLID ELECTROLYTE

In Lawton's work³, he lists development risk factors for components. In his option III, the oxygen cell is the only component still listed as risk factor 4 meaning "there are still serious problems that must be addressed as well as some intensive development required." This is an area of current research being conducted at the NASA sponsored University of Arizona Space Engineering Research Center (NASA/UA SERC). Further details were worked out in reference 5.

Since the Martian atmosphere is predominantly CO_2 , the remainder of this report will consider the atmosphere as CO_2 . The CO_2 , when it enters the cell array, will be heated to 1273 K. At this temperature, the CO_2 will begin to partially dissociate into CO and O_2 . The zirconia electrolyte is sandwiched between two porous platinum electrodes. This dissociation will occur on the cathode side with the O_2 entering the electrode and moving towards the electrode-electrolyte interface.

The driving potential for this movement is the partial pressure gradient developed by the electrolyte removing oxygen from the interface area. Once the O_2 reaches the interface, it is further reduced to monatomic oxygen. This oxygen receives two electrons from the negative electrode and becomes an oxygen ion and begins to migrate through the electrolyte towards the anode. Upon reaching the anode, the ion will release its two electrons to the positive electrode and then recombine with another oxygen atom to form the O_2 molecule. Qualitatively, this is how the oxygen separation process occurs. Figure 1 shows this process schematically.

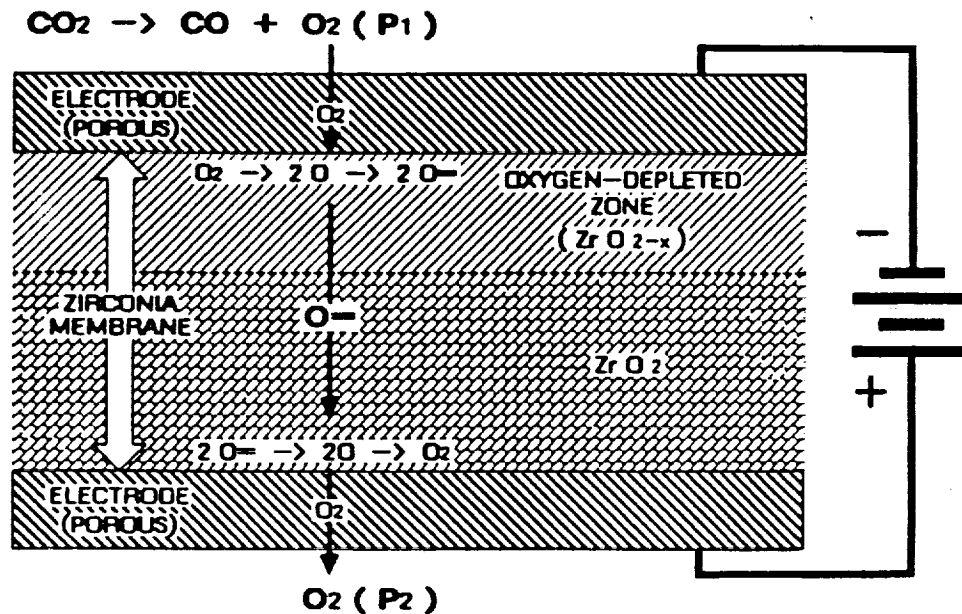


Figure 1: Oxygen Migration Through the ZrO₂ Cell⁴

Richter, at JPL, performed the initial intensive testing of this electrochemical process with the aim of quantifying this physical procedure⁶. His work was performed using a tubular zirconia cell. He developed the basic thermodynamic and electrochemical models for the reduction of CO₂ and the subsequent production of O₂. A few years later at JPL, Suitor continued the investigation.⁷ In his experiments, he used the disk geometry for his cells. Additionally, he investigated the use of different electrode materials.

In the work being conducted at SERC, we are using cells of the tubular geometry. Our aim is to investigate various cell efficiencies by varying several of the controlling parameters. These parameters are: a) the potential applied across the electrolyte; b) the electrolyte operating temperature; and c) the incoming CO₂ flow rate. We would like to know the O₂ production rate as a function of these parameters. The various efficiencies include: a) the cell's over potential (Nernst efficiency), and b) the system efficiency. The definitions of these efficiencies will be developed in this report.

II. SINGLE ZIRCONIA CELL TEST BED

The single zirconia cell test bed is currently in place at the NASA/UA Space Engineering Center.

The test bed consists of the following:

- 1) One tubular zirconia cell
- 2) One low voltage DC power supply
- 3) Two digital multimeters
- 4) Two clam shell type heaters surrounding the cell
- 5) One Watlow heater controller
- 6) Kaowool type ceramic insulation
- 7) One oxygen pressure transducer
(measuring in absolute pressure, 0-500 psia)
- 8) One carbon dioxide pressure transducer
(measuring in absolute pressure, 0-500 psia)
- 9) One oxygen flow meter (0-50 ISCCM)
- 10) One carbon dioxide flow meter (0-5000 ISCCM)
- 11) Three K-type thermocouples
- 12) Anaerobic carbon dioxide
- 13) One 386 based PC for data acquisition
- 14) Gas Chromatograph

To simulate the Martian atmosphere, which contains approximately 95% CO₂ and only 0.13% O₂, Coleman grade CO₂ was used to feed the test bed. This grade contains less than 20 ppm O₂. The flow was maintained at slightly above local atmospheric pressure (13.7 psia) at a temperature of 75 degrees F. The flow rates were varied between 37.5 sccm and 1475 sccm. Flow would enter the zirconia tube through a 1/8 inch alumina tube and then pass to the far end of the zirconia chamber (see figure 2).

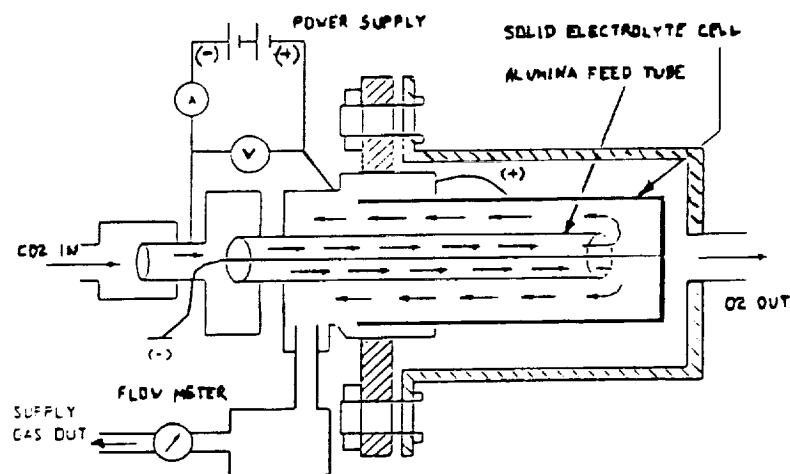


Figure 2. Zirconia Tubular Device

The clam shell heaters are centered about the middle 7 inches of the zirconia device. This means flow heating will begin in the alumina tube. Exiting the alumina tube, the flow reverses direction, continues to be heated, and flows across the cathode of the electrolyte. The CO_2 begins dissociating at the cathode. The stream is now a mixture of CO_2 , CO , and O_2 . O_2 is then electrochemically passed through the zirconia to the anode while the CO_2 and CO exhaust pass out through the exit. The CO_2 flow rate is controlled by a metering valve in this exhaust flow. O_2 flow passes through a volumetric flow meter and then can be directed to a water bubbling device, a sample cylinder, or directed to the gas chromatograph for analyzing. The exhaust flow can also be directed to the gas chromatograph for analyzing. The zirconia, and its electrode, have an upper temperature limit of 1200°C . A critical voltage limit of 2.23 VDC was assumed in accordance with Frisbee⁴. With these material limits in mind, a self imposed limit of 1100°C , and 2.0 VDC was used during all testing.

III. SINGLE CELL TEST RESULTS

FUNDAMENTAL RESULTS

A series of tests were conducted to attempt to characterize the effects of temperature, cell potential, and carbon dioxide flow rate on the production rate of oxygen. During the testing temperature was varied from 800°C to 1100°C in increments of 25 degrees. Cell potential varied from the zero O_2 production voltage to 2.0 Volts in increments of 0.1 VDC. The CO_2 flow rate varied from 37.5 cc/min to 1475 cc/min. The following figures show the results of this testing. Figure 5 is a characteristic curve of the production rate of O_2 vs the applied cell potential for a variety of CO_2 flow rates at a temperature of 1000°C , while figure 6 displays the production for four temperatures at a CO_2 flow rate of 137.5 cc/min. Note, on both figures 5 and 6, the second order dependence of oxygen production on the applied cell voltage.

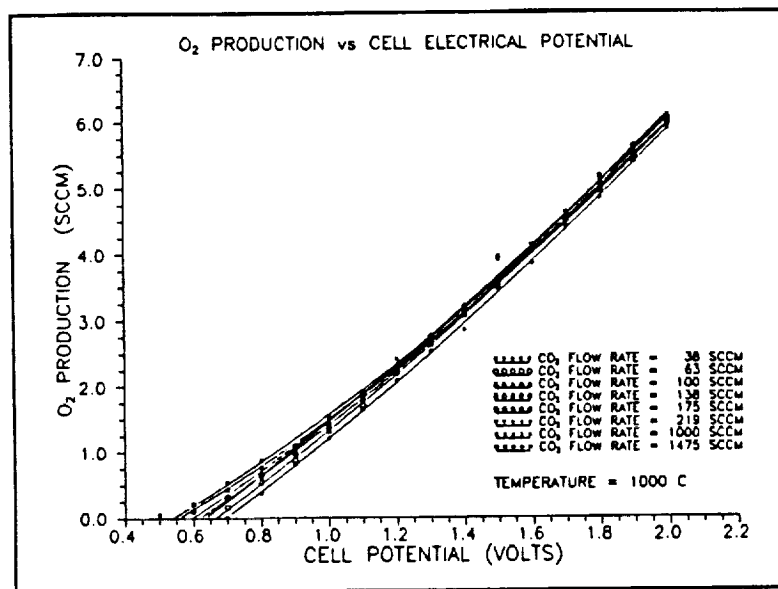


Figure 3: Oxygen Production vs Cell Voltage

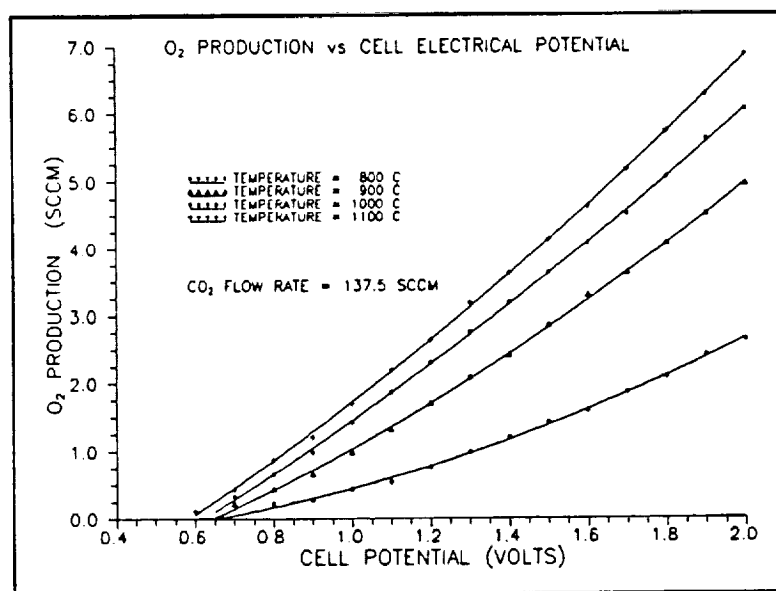


Figure 4: Oxygen Production vs Cell Voltage

Figure 5 demonstrates the dependence the oxygen production has on temperature of the cell, for an applied cell potential of 2.0 VDC. Notice the weak dependence the oxygen production has on the carbon dioxide flow rate. Figure 6 presents the oxygen production vs cell temperature at a carbon dioxide flow rate of 137.5 cc/min for various flow rates. Figure 6 clearly depicts the

dependence of voltage on the oxygen production.

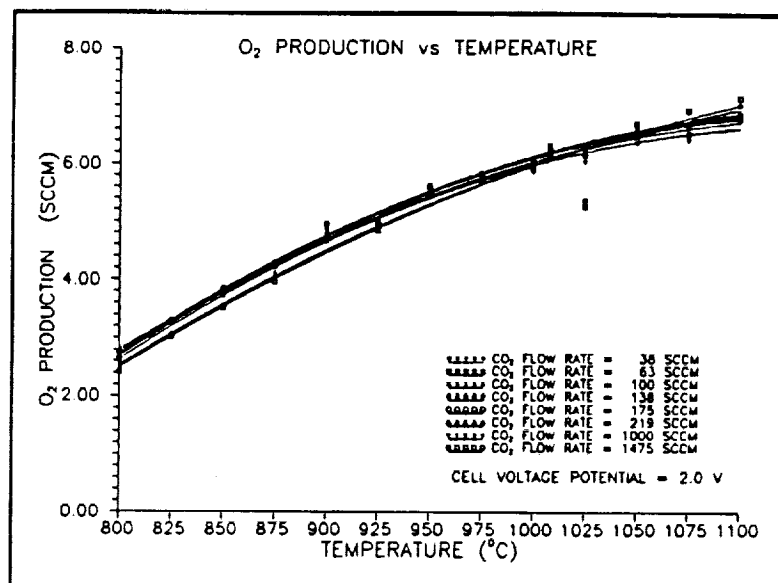


Figure 5: Oxygen Production vs Temperature

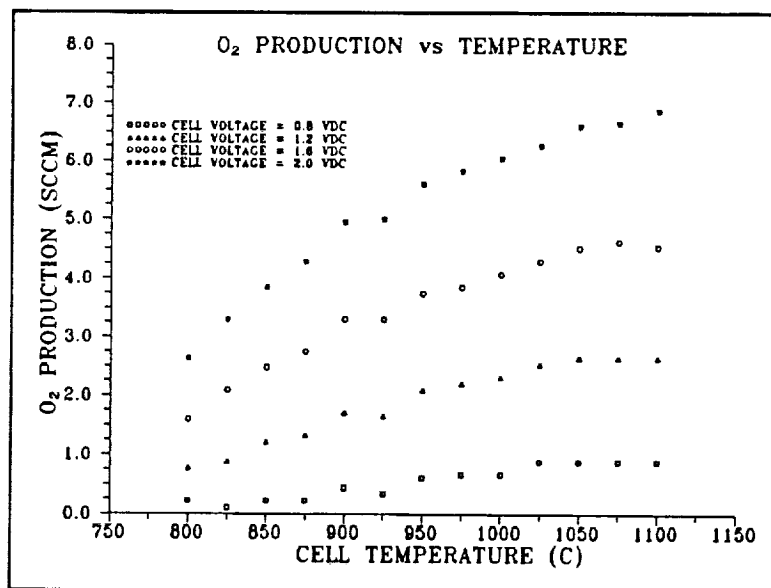


Figure 6: Oxygen Production vs Temperature

Figure 7 presents the O₂ production dependence on CO₂ flow rate, for an applied cell potential of 2.0 VDC. This is the most graphic illustration of the lack of dependence of the carbon dioxide flow

rate on the oxygen production, especially for CO_2 flow rates greater than 200 SCCM. It, like previous graphs, shows the temperature dependence on the O_2 production.

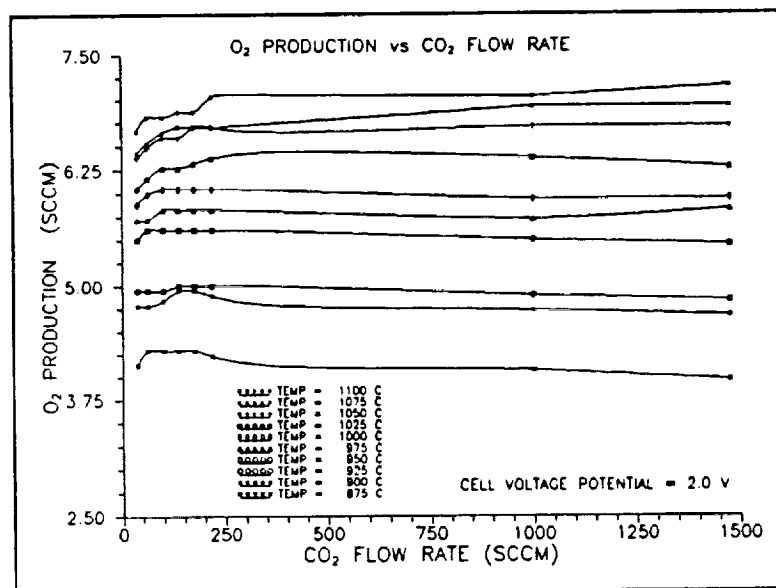


Figure 7: Oxygen Production vs CO₂ Flow Rate

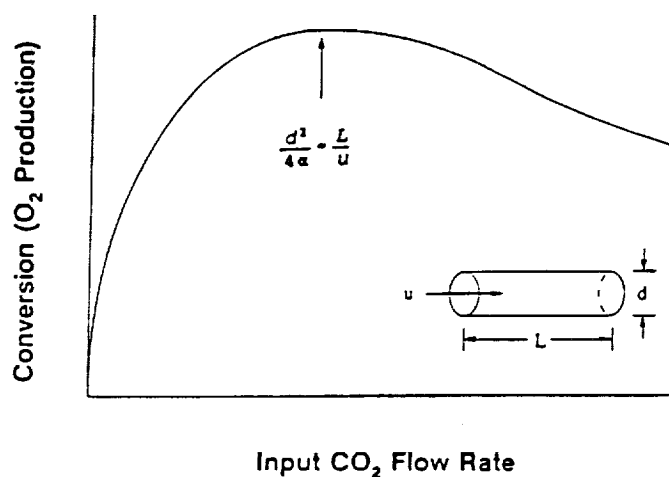
INTERPRETATION OF THE RESULTS

The four important results are: flow rate effects, cell voltage effects, cell temperature effects, and chemical effects. The latter refers to phenomena such as carbon formation, zirconia cell breakdown, local "hot-spot" effects, etc.

The flow rate effects are the easiest to interpret. The basic schematic is shown in figure 8. It was initially found that the oxygen yield rate (production rate) increased as the CO_2 flow rate increased, but only up to a certain point, after which increased flow rate actually resulted in the decrease of the yield of oxygen. This was observed while other parameters such as cell voltage and cell temperature was held constant. It was suspected that the carbon dioxide may not have had sufficient residence time within the heated cell to achieve the required temperature at the high flow rates. To verify this hypothesis, a simple thermal diffusivity analysis was performed, after confirming

characteristic time for heat transfer within the tube is given by $(d/2)^2/\alpha$, where d is the cell inside diameter and α is the thermal diffusivity ($k/\rho c_p$) of the carbon dioxide at high temperatures. As can be seen in figure 8, the peak occurs almost precisely where the two times become equal. It is thus clear that up to the point where the residence time is sufficient to bring the carbon dioxide to the requisite temperature, the production rate of the oxygen increases with the flow rate, but beyond this point the production rate falls off. It would be instructive to measure the actual gas temperature, and not merely the cell wall temperature as is done in the experiments reported here.

EXPLANATION OF FLOW-RATE EFFECT



[α is the thermal diffusivity of CO₂ at 1000°C]

Figure 8: Thermal Diffusivity vs Residence Time

The mass flow ratio (the rate of mass of O₂ produced divided by the CO₂ mass flow rate) would probably be of much interest. This is due to other constraints within scaled-up systems such as the primary carbon dioxide compressor, the heat exchanger, and the radiators. For these reasons figures 9 and 10 plot the mass flow ratio vs CO₂ flow rate (figure 9) and temperature (figure 10).

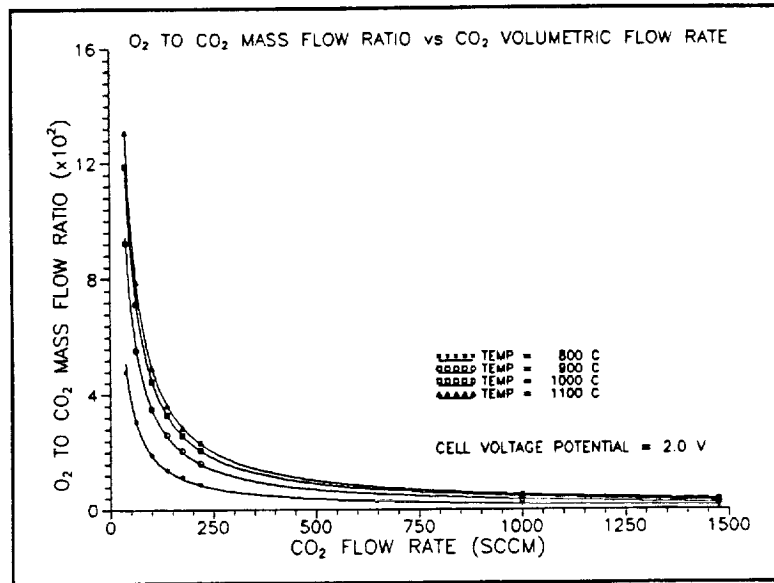


Figure 9: O₂ - CO₂ Mass Flow Ratio vs CO₂ Flow Rate

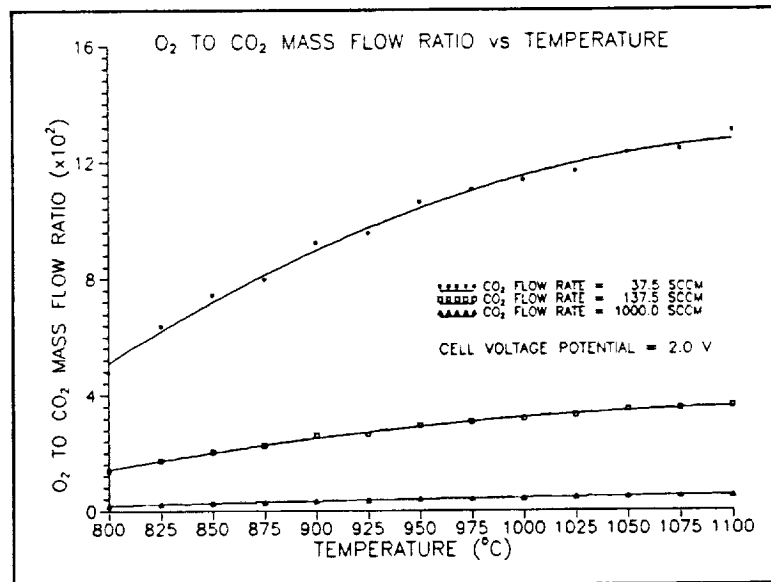


Figure 10: O₂ - CO₂ Mass Flow Ratio vs Temperature

In previous studies of the propellant production plant, the emphasis was placed on sizing of the system^{2,3,4}. For these studies, oxygen conversion efficiencies of 25%-30% was used when

considering the estimated surface area needed to produce a required amount of oxygen per day. The use of these efficiencies were necessary to minimize the oxygen plant mass. However, when considering the operation of the zirconia cell alone, figure 11 shows the complete range of oxygen conversion efficiencies.

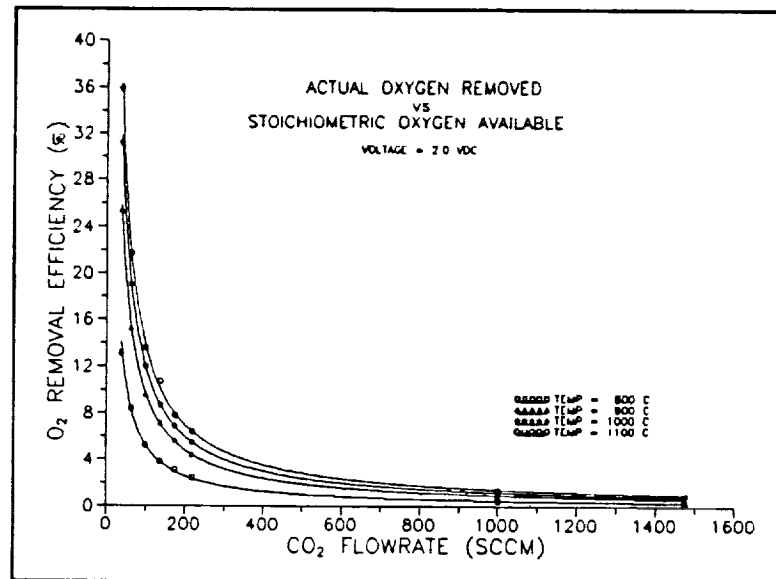


Figure 11: Oxygen Conversion Rate

As the concern of this report is the complete characterization of the zirconia electrolytic cell, all conversion efficiencies must be investigated. Richter, in his early work⁶ on the reduction of CO₂, began with the basic Nernst relation:

$$E_N = \frac{RT}{zF} \ln [P_2 / X_{O_2} P_1] .$$

Here, E_N is the nernst voltage, T is the temperature (K), z is charge/mole ($z=4$), R is the universal gas constant, and F is the Faraday constant. Additionally, P_2 is the pressure at the anode of the cell while $X_{O_2} P_1$ is the partial pressure of the oxygen in the incoming CO₂ flow stream at the cathode. Richter then continued with his model and developed an instantaneous Nernst potential:

$$E_{Ni} = \frac{RT}{zF} \ln \left[\frac{P_2}{\left(\frac{K(1-n)}{n} \right)^2} \right] .$$

In this equation, K is the normal equilibrium constant and n is the mole fraction of CO₂ reduced to CO. The value n can be calculated from this equation:

$$n = C \frac{I}{\dot{V}_{CO_2}} .$$

The value C is a constant from Richter's work (C=6.969), I is the current produced across the cell, and \dot{V}_{CO_2} is the volumetric flow rate of the incoming CO₂ stream. The current (A) was measured experimentally, as well as the volumetric flow rate of the CO₂ (SCCM). The cell temperature was measured by a k-type thermocouple positioned at the outside of the cell wall (K), and the pressure of the O₂ collection side of the cell was assumed to be one atmosphere. Using the proper values for the equilibrium constant K⁸, there is now enough information available to calculate the instantaneous Nernst voltage. Richter cautions the use of this equation by stating it is valid only if the critical voltage over the cell is not reached. This can be defined as the potential which will be just sufficient to begin driving oxygen from the lattice of the zirconia. This process will be apparent from an "elbow" being observed in the O₂ production vs potential plot. Figure 3 shows this potential has not been reached in this work. It is evident that this potential is now a function of the operating temperature and the actual amount of O₂ removed and not the partial pressure of the O₂ at the cathode.⁶ The Nernst potential is used in defining the Nernst efficiency.

$$\eta_N = \frac{E_{Ni}}{E_{act}} .$$

This equation shows the Nernst efficiency is the ratio of the theoretical potential divided by the actual potential (E_{act}). What this indicates is the instantaneous amount of cell overpotential. Figure 12 shows the results of this analysis.

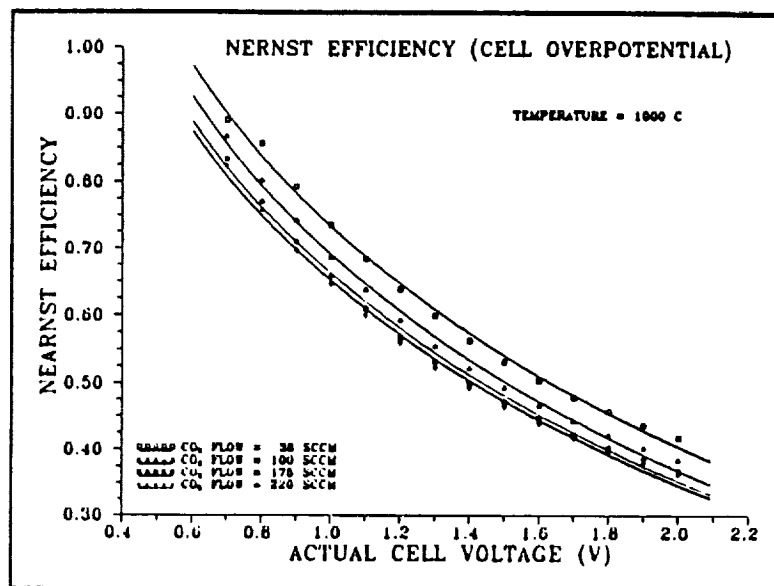


Figure 12: Nernst Efficiency vs Cell Voltage

It is apparent from this figure that the amount of cell overpotential rises as the actual cell potential rises. One source of this overpotential could be the pressure drop through the porous electrode. It is important to remember that from figure 3, the rise in O_2 production is almost directly proportional to the potential applied to the cell. Ash⁹ et al, point out that experiments have shown that as the O_2 production rate rises, there is an increase in the pressure drop across the negative electrode which can approach the partial pressure of the oxygen in the CO_2 stream resulting in an ever increasing pumping power requirement. Another possible source of the overpotential is slow diffusion, adsorption, or dissociation processes near the electrode-electrolyte interface of the cell resulting in concentration overpotential¹⁰. They also state the possibility of a transition overpotential due to slow electrochemical reaction. The sources of overpotential can not be experimentally determined with this system as currently constructed, but any future characterization of the zirconia electrolyte should definitely keep in mind these processes.

With the Nernst efficiency established, it was next desired to arrive at a system efficiency. The control volume is taken around the entire cell system. The useful work inside the control volume is divided into two parts. The first being the rate of thermodynamic energy being used to dissociate the CO_2 . The second being the work required to electrochemically conduct the oxygen ions through the zirconia. The power passing into the control volume is also divided into two components. The first being the power delivered to the ceramic heaters and the second being the

power delivered to the electrolyte. The energy required to thermally dissociate the CO_2 is given by the equation:

$$\dot{Q}_{TH} = \sum_p N_j (\Delta h_f^\circ + h_T - h_{298})_j - \sum_r N_j (\Delta h_f^\circ + h_T - h_{298})_j.$$

Here, Q_{TH} is the thermodynamic power input with the calculation showing the normal enthalpy of reaction equation with the enthalpy of formation and sensible enthalpies. The subscripts i and j represent the products and reactants respectively. The coefficient N represents the molar flow rate of each respective constituent. This value and the other power values give the following definition for the system efficiency:

$$\eta_{sys} = \frac{E_N I_{cell} + \dot{Q}_{TH}}{E_{cell} I_{cell} + E_{heat} I_{heat}}.$$

In this equation, the subscript heat refers to observed conditions on the ceramic heater and the subscript cell refers to observed conditions with the electrolyte, E being the potential (V) and I being the current (I). Figure 13 displays the results of this analysis.

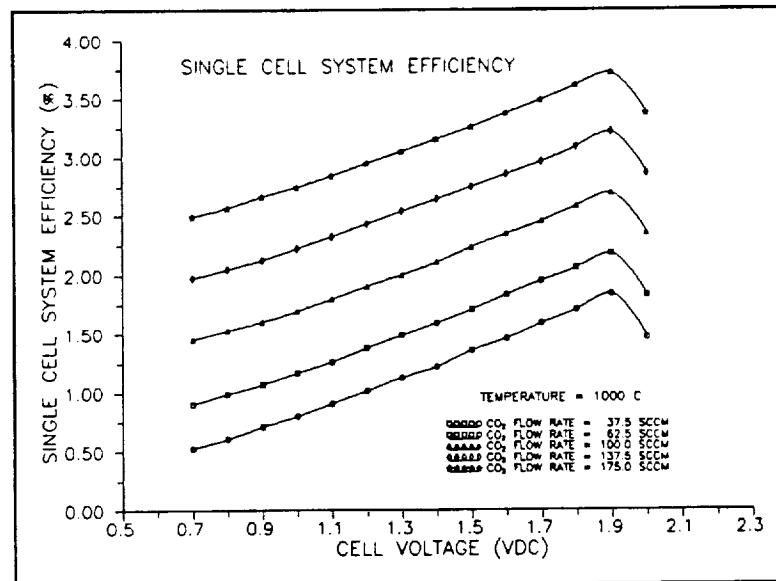


Figure 13: Single Cell System Efficiency

HUNDRED-HOUR RUNS

Two tests were run in the completely automated mode (see the section by Schooley & Celier in this report for automation details). The plant was started with helium flow at room temperature. The cell was next brought to operational temperature (while still under helium flow). Next, the gas flow was changed to an authentically procured Martian atmosphere simulant (anaerobic CO₂ including nitrogen). Finally, the cell voltage was applied. The shut down procedure was exactly in the reverse order. The helium purge during shut down ensured that no contaminates would occur from atmospheric air in the laboratory while the cell was still at a high temperature. Very detailed diagnostic tests were conducted including SEM, EDAX and BET measurements of the post-test cell surface (cut and exposed) and contrasted with an unused cell. Two typical plates are shown here in figures 14 and 15. More data will be published soon.

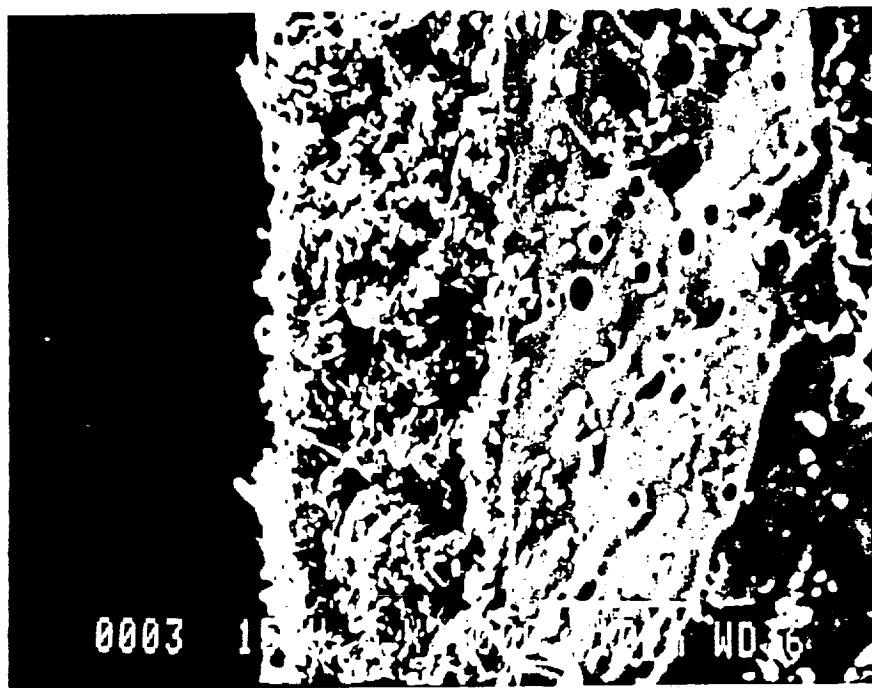


Figure 14: Post 100 Hr Test (2000X)

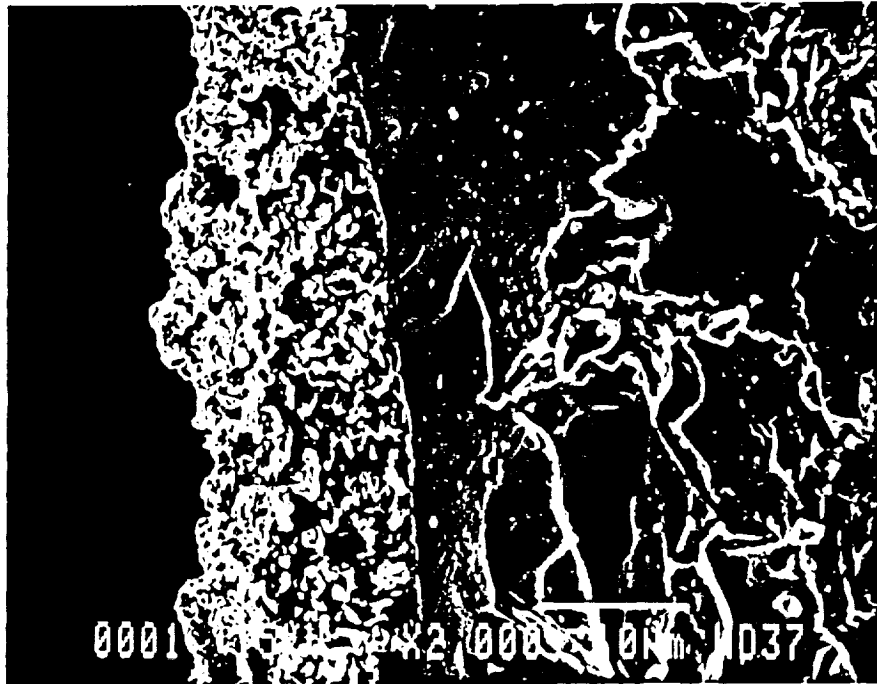


Figure 15: Unused Cell (2000X)

V. SUMMARY

This paper has presented results from the first phase of a well planned multi-phase research program aimed at significantly reducing costs of future space missions; terrestrial applications are always kept in mind. This proof of concept study has realistically used full system hardware, realistic solid electrolytic cell material, realistic operating temperatures, full cell voltages, full scale flow rates, and most important, realistic long-duration operation. These features distinguish our experiments from the usually understood test-tube demonstrations, where the conditions are substantially different from the real life counterpart. The only feature that is not duplicated here is

the overall energy input. The carbon dioxide flow rate, cell voltage, cell temperature and the duration of operation are all varied parametrically. A simple heat transfer theory explains the flow rate effects. The voltage effects are in good agreement with the manufacturer's specifications. The one hundred-hour runs were made with a cell made in-house. The extensive data from these runs are currently being analyzed. These thorough characterizations of the component performance parameters naturally lead us to the next step of scale-up and full system demonstration with active controls. Creative solutions to these engineering designs indicate that future space missions could realize substantial cost savings through the use of local (in-space) resources.

REFERENCES

1. Ash, R. L.; Dowler, W. L.; Varsi, G.: "Feasibility of Rocket Propellant Production on Mars." Acta Astronautica, Vol. 5, pp. 705-724. (1978)
2. Lawton, A. L.; Frisbee, R. H.: "A New Look at Oxygen Production on Mars ISPP." JPL D-2661, September 1985
3. Lawton, A. L.: "Risk Factors in the Development of Zirconia Cell Technology for the Production of Oxygen from the Martian Atmosphere." JPL D-3546, August 1986
4. Frisbee, R. H.: "Mass and Power Estimates for Martian In-Situ Propellant Production Systems." JPL D-3648, October 1986
5. Ramohalli, K.; Lawton, E.; Ash, R.: "Recent Concepts in Mission to Mars: Extraterrestrial Processes." AIAA Journal of Propulsion and Power, Vol. 5, No. 2, pp 181-187. Mar-Apr 1989
6. Richter, R.: "Basic Investigation into the Production of Oxygen in a Solid Electrolyte." AIAA-81-1175, June 1981
7. Suitor, J.W.; Berdahl, C.M.; Ferrall, J.F.; Marner, W.J.; Schroder, J.E.; Shichta, P.J.: "Development of an Alternate Oxygen Production Source Using a Zirconia Solid Electrolyte Membrane." JPL D-4320, May 1987
8. Wark, K.: Thermodynamics. Third ed. p. 840. McGraw-Hill, Inc. 1977
9. Ash, R. L.; Richter R.; Dowler, J. A.; Hanson and Uphoff, C. W.: "Autonomous Oxygen for a Mars Return Vehicle". IAF-82-210 1982
10. Etsell, T. H.; Flengas, S. N.: "Overpotential Behavior of Stabilized Zirconia Fuel Cells." Journal of the Electrochemical Society. Vol. 118, No. 12, pp 1890-1900. Dec. 1971

It is a pleasure to acknowledge the helpful comments from the advisory committee and by Dr. Sanders D. Rosenberg in particular. Mario Rascon's help in the reporting is much appreciated.

Carbon Monoxide Removal From Electrochemical Cell Discharge Gas

Peter Nolan, A. H. Cutler and D. C. Lynch

Department of Materials Science and Engineering
and
Space Engineering Research Center
The University of Arizona

Abstract

Design specifications for an electrochemical cell for recovery of oxygen call for a production rate of 10 kg of O_2 per day and for compression of 50 times that mass of CO_2 from the Martian atmosphere. Those specifications require a compression rate of over 770 cfm at standard Martian temperature and pressure (SMTP). Much of the CO_2 being compressed represents waste unless it can be recycled. Recycle can reduce the volume of gas that must be compressed to 40 cfm at SMTP. That volume reduction represents significant mass savings in the compressor, heating equipment, filters and energy source. Successful recycle of the gas requires separation of CO (produced in the electrochemical cell) from CO_2 , N_2 and Ar found in the Martian atmosphere. CO separation has been the focus of our work during the past year.

A number of materials, ceramic and metal, have been tested as a catalyst for the disproportionation of CO to produce solid carbon and CO_2 . Attention has been primarily focussed on ruthenium. The disproportionation reaction with ruthenium catalyst has been examined at temperatures between 200 to 600 °C utilizing a CO_2 - 10% CO gas mixture. At 260 °C and above the disproportionation reaction on ruthenium catalyst is fast, with 100% of the CO reacted at a gas flow rate of 28.6 cc per min. After approximately 20 minutes the ruthenium is saturated at 0.15 grams of carbon per gram of ruthenium and the rate of disproportionation decreases significantly. The carbon monoxide continues to disproportionate for an extended period but at a much reduced rate. Temperature appears to affect the reduced rate, it is faster at lower temperatures. This phenomenon may be due to thermodynamic equilibrium conditions which favor disproportionation at lower temperatures.

A critical aspect associated with the removal of CO from the gas evolved from the electrochemical cell involves burnout of the solid carbon from the catalyst after it has been disproportionated. Burnout of carbon from ruthenium, a metal which is not only known to catalyze the disproportionation reaction but also the oxidation of carbon when it is oxidized in the presence of oxygen, has been tested. On Mars, unfortunately, the luxury of using oxygen to burn carbon will not be available. Instead CO_2 must be used to accomplish the task. To date several experiments have been conducted in order to burn off carbon deposited on ruthenium catalyst with CO_2 , very little success has been achieved. Regeneration of the catalyst by removal of the solid carbon with CO_2 appears to be major problem, one we will continue to examine.

Introduction

The Space Engineering Research Center (SERC) at the University of Arizona is in the progress of designing and building a prototype system for production of O₂ from CO₂. While SERC is currently addressing conditions typical of the Martian atmosphere, the technology being developed is applicable wherever CO₂ is produced and can be used as a raw material.

Recycle of the gas leaving the electrochemical cell has a distinct advantage of reducing the volume of the Martian atmosphere that must be compressed. Successful recycle, however, requires separation of the CO produced in the cell from the remainder of the compressed atmosphere. Carbon dioxide and carbon monoxide are not easily separated as both have the same approximate kinetic diameters since both molecules are linear. That fact precludes the use of zeolites for the separation of CO from CO₂. Polymeric membranes are used to separate CO₂ from CO. Since the gas stream under consideration consists primarily of CO₂ an extensive membrane surface area would be required. In addition the membranes are susceptible to failure at elevated temperatures. Cooling the gas leaving the electrochemical cell to a temperature where polymeric membranes could be used to separate CO₂ from CO could result in carbon deposition. That deposition, if not controlled, could lead to failure of the entire system.

Thermodynamic analysis of the exit gas, as proposed, has revealed that carbon deposition is possible at temperatures below 600 °C. the reaction involved,



is referred to as the disproportionation reaction. At temperatures below 600 °C the reaction is sluggish, but is known to be catalyzed by ruthenium and ferrous metals.¹⁻⁵

At temperatures above 600 °C the gas evolved from the electrochemical cell or CO₂ compressed from the Martian atmosphere can be used to burn off the deposited carbon. The chemical reaction involved is the reverse of that presented in reaction 1. A useable catalyst must not only promote the diproportionation reaction, it must also be easily regenerated by burning off the carbon with CO₂. This second issue does appear to be a significant problem.

Approach

The basic approach to the experimental program involves:

1. testing the effectiveness materials to catalyze the disproportionation reaction in a weak CO stream,
2. regeneration of the catalyst by burning off the deposited carbon with CO₂, and
3. repeating steps 1 and 2 to evaluate both the impact repeated use of the catalyst has on its ability to promote the disproportionation reaction and to evaluate any structural changes in the catalyst.

Through a search of the literature a number of potential catalyst were identified. Since most previous work in the area has involved gas streams with CO concentrations well in excess of that used in the present work, some of the materials were tested. However, before reviewing the results, it is beneficial to understand what constitutes an effective catalyst.

Choosing A Catalyst

A potential catalyst comes in contact with a gas stream super saturated with CO. The extent of the saturation can be represented by plotting the equilibrium condition for reaction 1 as has been done in Figure 1. All the conditions to the left of the equilibrium line for the reaction constitute the super saturated condition. A line drawn horizontally at 90% CO₂ represents the composition of the gas evolved from the electrochemical cell.

Many elements react in a CO₂ - CO atmosphere, forming oxides, carbides, carbonates, and carbonyls. Iron on its own, is not an effective catalyst. One can begin to understand why Fe does not act as

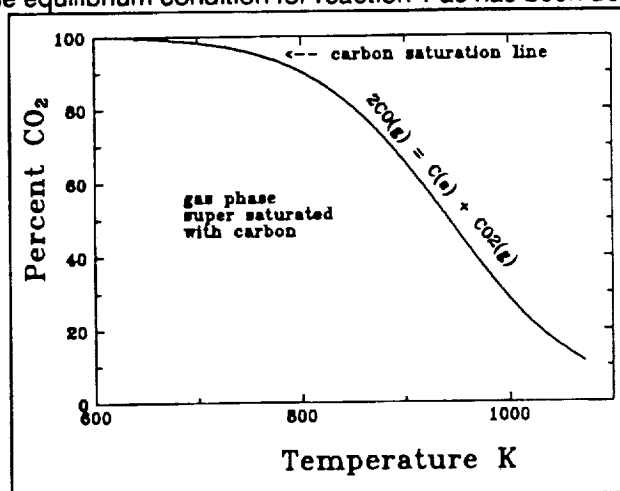


Fig. 1 - Carbon saturation line for CO-CO₂ Gases

a catalyst (except under strict constraints) by plotting the equilibrium conditions for iron and its oxides and carbide as has been done in Figure 2. For iron to catalyze the disproportionation reaction it is necessary for bare metal surface to exist.² Examination of Figure 2 reveals only a narrow range of temperatures and gas composition can be utilized and still have metallic iron on the CO super saturated side of the equilibrium for reaction 1. this condition can be altered by alloying the metal or by including H₂ in the gas stream.⁶ While it is uncertain what effect H₂ has on the stability

regions in Figure 2, hydrogen has a significant impact on the ability of iron to catalyze the disproportionation reaction.

Since H_2 has a detrimental impact on metal at elevated temperatures, temperatures such as that employed in the electrochemical cell, it is unlikely that hydrogen can be used to assist in the disproportionation reaction. Examination of Figure 2 reveals that an ideal metal for catalysis of the disproportionation reaction must be one that does not form carbides or oxides. Such a metal would be able to maintain its metallic state over a range of temperatures at both highly oxidizing and carburizing conditions.

Ruthenium meets nearly all of the above requirements. Ruthenium does not form carbides and only under extreme oxidizing conditions does it form a solid oxide. If Ru is substituted for Fe in Figure 2 the resulting diagram appears as shown in

Figure 3. Ruthenium appears to be an ideal candidate for disproportionation of CO.

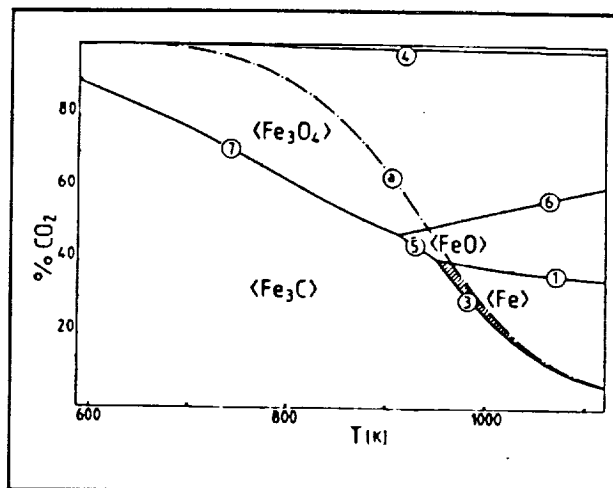


Fig. 2 - Fe - C - O Stability Diagram²

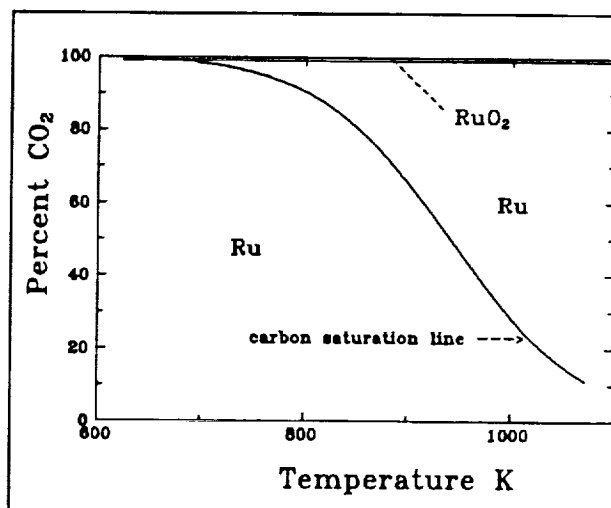


Fig. 3 - Ru - C - O Stability Diagram

In selecting a material to act as a catalyst there are two other significant considerations. The catalyst must not hinder the oxidation of the deposited carbon when regenerating the catalyst. Ruthenium is known to also catalyze the oxidation of solid carbon in the presence of oxygen.

The second issue involves the structural integrity of the catalyst after repeated usage. Carbon when deposited on a metal catalyst usually forms filaments. A filament grows by separating a small piece of the metal from the catalyst, and that material becomes the active center for the growth of the fiber. Carbon super saturates the exposed surface of metal piece as shown in Figure 4. The dissolved carbon then diffuses through the small piece of metal and precipitates as

indicated in the figure. The result is a carbon filament, which at its tip is a small piece of the metal catalyst. This process renders the catalyst friable and degrades its continued use.

Growth of filaments on ruthenium does not always follow the procedure described above. The filament growth is as described

above, but when the deposited carbon is oxidized, the growth mechanism is reversed. The metal piece at the tip of the filament is returned to its original position and is again available for reaction.^{7&8} This phenomenon has not been observed with Fe, Co, or Ni.

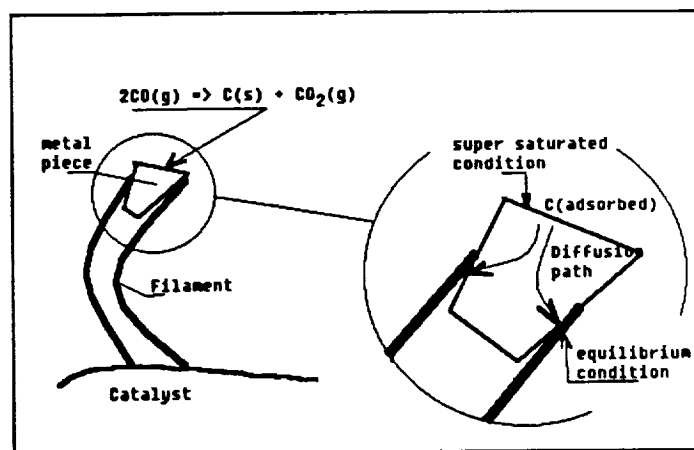


Fig. 4 - Filament Growth Mechanism

Experimental Results

Disproportionation of CO On Ruthenium - Several experiments were conducted at temperatures between 200 and 600 °C. Some of those results are presented in Figures 5 and 6. All the experiments were conducted with a gas mixture consisting of CO₂ with 10 % CO and at gas flow rates

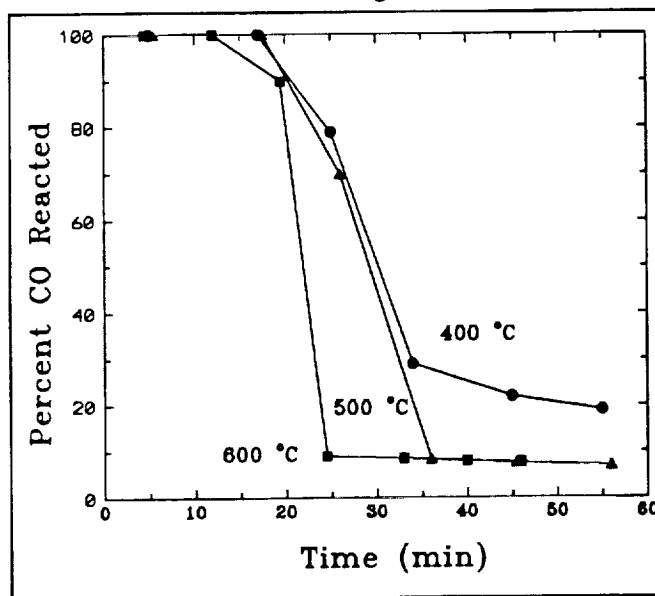


Fig. 5 - Experimental Results

of 28.6 cc per min. At temperatures of 260 °C and above the initial disproportionation reaction is fast with all the CO reacting during the first 20 minutes as shown in Figure 5. In that figure it can be observed that after 20 minutes the fraction of CO reacted in the gas drops to 20% at 400 °C to 10% at 500 and 600 °C. The experimental results in Figure 5 indicate that at least two physical mechanisms are involved. It has been postulated that the initial fast rate is associated with filament growth. That rate mechanism is slowed when either the

active metal particles become covered by carbon or the compact of filaments physically prevents further growth. Once filament growth ceases, further deposition of carbon must occur on the all

ready deposited carbon. The latter is known to be slow.¹⁻⁵ Visual and optical microscopy has not provided evidence as to how the carbon is deposited. Additional evaluation with scanning electron microscopy is required before a final conclusion can be reached. The area under the curves in Figures 5 and 6 correspond to the amount of carbon deposited during an experiment.. The amount of carbon deposited during the initial fast rate mechanism was the same for all specimens reacted at 260 °C and

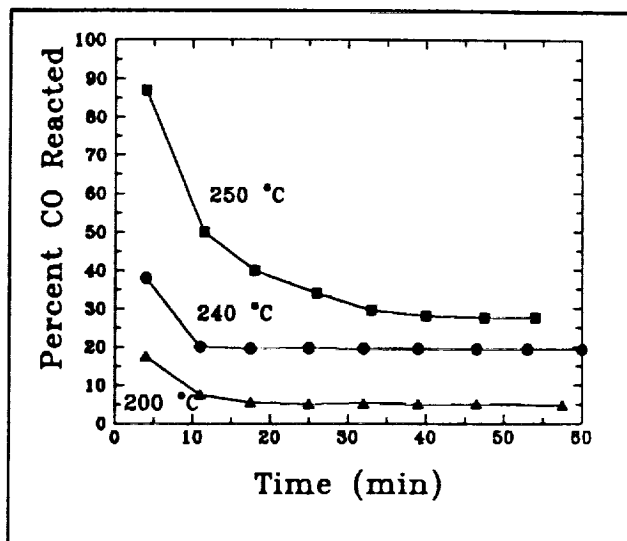


Fig. 6 - Experimental Results

above. Approximately 0.15 g of carbon deposited per gram of ruthenium. Based on that value, 25 Kg of ruthenium catalyst (this does not include the mass of catalytic carrier) would be required to meet the design specification for 10 Kg of O₂ produced per day. That mass can be reduced if the catalyst can be regenerated more than once per day.

The results from the experimental runs presented in Figure 6 were conducted in order to gain insight into the initial rate associated with filament growth. While we are still analyzing this data, the preliminary results indicate that the initial mechanism may itself involve two processes. It is anticipated that those results will yield a rate constant or constants that can be used in design specifications.

Regeneration of Catalyst - Catalyst regeneration must be achieved for continuous removal of CO. Carbon dioxide is readily available in the Martian atmosphere and has been proposed for burning off the carbon from the catalyst. The extent of reaction which can be achieved can be estimated by examining Figure 1. Carbon dioxide reacted with solid carbon at 700 °C should yield a product gas consisting of CO₂ and CO, the latter at a concentration of 62% if thermodynamic equilibrium is approached. Attempts to burn the carbon off with CO₂ at temperatures of 500 to 800 °C have not worked. Only on one occasion has any CO been detected with the gas chromatography, and then only in very minute quantities.

Carbon monoxide was disproportionated on several specimen at 500 °C. Those specimens were in turn reacted with CO₂ in an effort to regenerate the catalyst. After attempting to regenerate the catalyst the specimens were again exposed to the CO₂ - CO gas mixture and the amount of CO

disproportionated followed by analysis of the exit gas with the gas chromatography. The results of those experiments are presented in Figure 7. Experiment 1 in the figure corresponds to a specimen not previously treated and then reacted with the CO_2 - CO gas mixture. That curve is identical to the results presented in Figure 5 and is a basis for comparison.

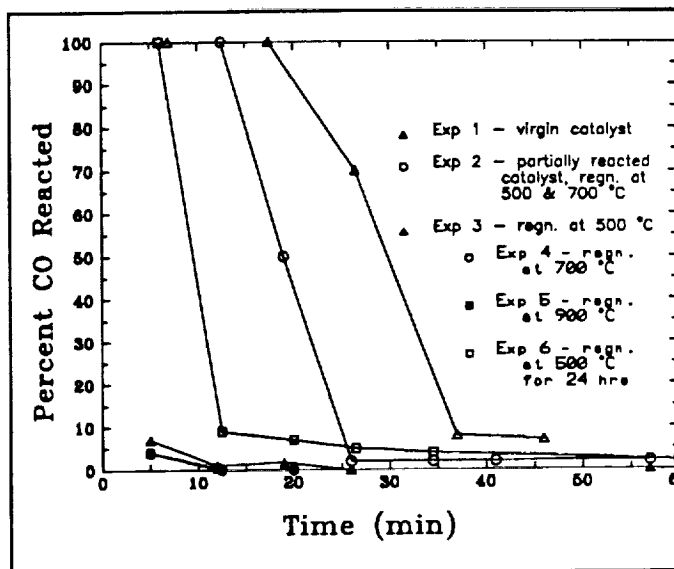


Fig. 7 - Comparison of Reactivity of Regenerated Catalyst to Virgin Catalyst

The second experiment in Figure 7 involves a specimen reacted with the

CO_2 - CO gas for 9 minutes, approximately half the time required to achieve saturation in the first experiment. The specimen was then exposed to a CO_2 atmosphere at 500 °C for two hours and then at 700 °C for 30 minutes. No CO was detected during the regeneration process. Again the specimen was exposed to the CO_2 - CO atmosphere at 500 °C. The extent of disproportionation during the second cycle was approximately that which would be expected if the specimen had been allowed to react to completion during the first cycle.

Experiment 3 in Figure 7 refers to a specimen completely saturated with carbon and the regenerated at 500 °C in CO_2 for 14 hours. Again there was no indication that CO was evolved during the regeneration process. Exposing the regenerated catalyst to the CO_2 - CO results in very little further disproportionation of CO. Similar results were achieved with specimens regenerated in CO_2 at 700 and 900 °C as shown in the figure.

The only experiment which suggests that some regeneration of the catalyst occurred was that regenerated in CO_2 at 500 °C for 24 hours. Again no CO was detected in the off gas during regeneration. The contradiction appears to be due to a change in the structure of the catalyst. X - ray analysis of the unreacted catalyst suggests an amorphous structure for the ruthenium. While X - ray analysis of the reacted and regenerated specimen reveals a strong crystal pattern for the ruthenium.

In order to evaluate the effect of crystal structure on the disproportionation reaction, two specimen fully saturated with carbon at 500 °C, were soaked in ultra high purity N₂ at 500 °C for 4 hours and at 250 °C for 4 days. X-ray diffraction of the specimen soaked for 4 days revealed that the ruthenium had crystallized. Again the crystallized specimen resulted in further disproportionation of CO as shown in Figure 8.

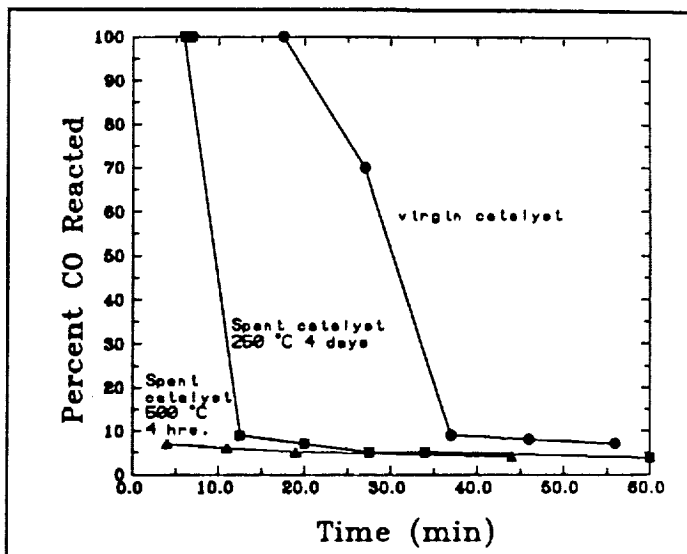


Fig. 8 - Spent catalyst heated in N₂ is reactivated as a result of crystallization of the Ru.

These results reveal that the regeneration process with CO₂ may be more difficult than catalyzing the disproportionation reaction. The experimental results also reveal that crystal structure can play a significant role in the amount of carbon that can be deposited on the catalyst.

Student Participation

Peter Nolan, a M. S. candidate in the Department of Materials Science and Engineering, has conducted the experimental work reported in this document. Support from SERC was essential in allowing the Department to recruit Peter.

Future Work

A time line for expected progress is presented in Figure 9. Our objectives are to continue analysis of the physico-chemical processes involved in the burn out of deposited carbon from the catalyst. The extent of time required to achieve this goal is uncertain but we anticipate devoting six months to the project. At the same time we will test other catalyst to see if they suffer from the same regeneration problem. When we are able to regenerate the catalyst, several experiments will be conducted to test long term effects of recycling the catalyst on its power to promote the disproportionation reaction as well as the catalyst ability to retain its structural integrity. After completing those experiments we will complete our final design calculations.

Another area we hope to evaluate this year involves pressure swing adsorption (PSA) of CO on copper chlorides. We are in the process of recruiting an undergraduate to begin these experi-

ments. If the early results warrant additional effort, and we have continued problems with the regeneration of the catalyst, additional efforts will be taken to develop PSA as a means for CO removal. Adsorption of CO on copper chlorides has been used in ORSAT analysis and recently by the Japanese to recover CO from iron blast furnace off gas.⁹

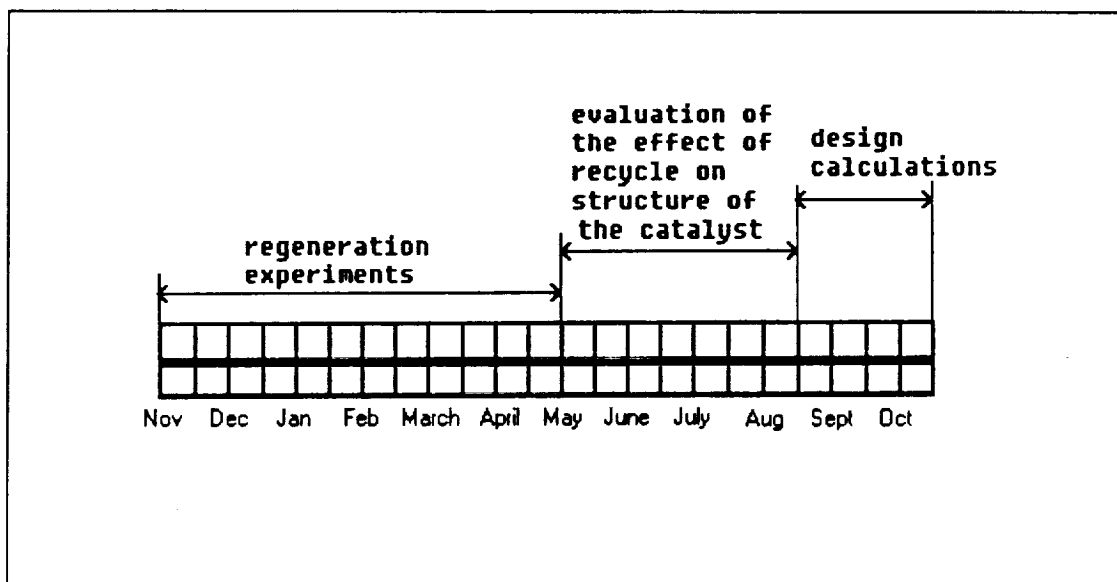


Fig. 9 - Time Line For proposed Work

References

1. Kinetics and Microscopic Aspects of Catalytic Carbon Growth, M. Audier and M. Coulon, *Carbon*, 23, pp. 317-23, 1985.
2. Disproportionation of CO on Iron-Cobalt Alloys -I, Thermodynamic Study, M. Audier, M. Coulon, and L. Bonnetian, *Carbon*, 21, pp. 93-98, 1983.
3. Disproportionation of CO on Iron-Cobalt Alloys -II, Kinetic Study on Iron-Cobalt Alloys of Different Composition, M. Audier, M. Coulon, and L. Bonnetian, *Carbon*, 21, pp. 99-104, 1983.
4. Disproportionation of CO on Iron-Cobalt Alloys -III, Kinetic Laws of the Carbon Growth and Catalyst Fragmentation, M. Audier, M. Coulon, and L. Bonnetian, *Carbon*, 21, pp. 105-110, 1983.
5. Metal Catalyzed Gasification of Graphite, R. T. K. Baker, in *Carbon and Coal Gasification Science and Technology*, edited by J. L. Figueiredo and J. A. Moulijn, Martinus Nijhoff, Boston 1986, pp. 231-271.

6. Carbon Deposition and Filament Growth on Fe, Co, and Ni Foils using $\text{CH}_4\text{-H}_2\text{-H}_2\text{O-CO-CO}_2$ gas Mixtures, A. Sacco, Jr., W.A.H. Geurts, G. A. Jablonski, S. Lee, and R.A. Gatley, J. Catal., 115, pp. 322-341, 1989.
7. In-Situ Electron Microscopy Studies of the Behavior of Supported Ruthenium Particles. 1. The Catalytic Influence on Graphite Gasification Reactions, R.T.K. Baker and J.J. Chludzinski, Jr., J. Phys. Chem., 90, pp.4730-4734, 1986.
8. In-Situ Electron Microscopy Studies of the Behavior of Supported Ruthenium Particles. 2. Carbon Deposition from Catalyzed Decomposition of Acetylene, R.T.K. Baker and J.J. Chludzinski, Jr., J. Phys. Chem., 90, pp.4734-4738, 1986.
9. High-Purity CO Gas Separation System by Pressure Swing Adsorption Method, J. Yokoe, K. Taki, T. Tsuji, T. Aokata, M. Kida, and F. Kasuya, in Gas Separation Technology, edited by E.F. Vansant and R. Dewolfs, Elsevier Science, Amsterdam, pp. 343-50.

C. REDUCTION OF CARBONACEOUS MATERIALS



MODAL ABUNDANCE AND DEHYDRATION KINETICS OF VOLATILE BEARING PHASES
IN CARBONACEOUS CHONDRITES

Kunal Bose and J. Ganguly

Department of Geosciences

The University of Arizona

Abstract

We present results of calculations, which have been carried out in collaboration with Professor S. K. Saxena, on the modal abundance of volatile bearing phases in C2 carbonaceous chondrites, and experimental data on the dehydration kinetics of talc. Also experimental studies are currently in progress in our laboratory to determine the dehydration boundary of talc over a large pressure range, which would provide a very important set of phase equilibrium data to refine the equation of state of water.

The results on the dehydration kinetics of talc (grain size 0.7-1 micron) in the temperature range 875-975°C at 1 bar can be treated in terms of a second order rate equation with an activation energy of 376 kJ. Work is currently in progress to study the effect of finer grain size on the dehydration kinetics.

Introduction

Carbonaceous chondrites are usually believed to be the primary constituents of near-Earth asteroids and Phobos and Deimos, and are potential resources of fuels that may be exploited for future planetary missions. The most volatile-rich members of this class of meteorite are known as C1 (or CI) and C2 (or CM) classes. Our group has been involved in an integrated study on the thermodynamics and kinetics of reactions of the volatile-bearing phases that are likely to be present in carbonaceous chondrites. The results will provide important constraints on the fundamental aspects concerning nature, abundance, and time scale of formation of volatile-bearing phases in the solar nebula, and the closely related practical problem of the feasibility of extraction of volatiles for fuels from carbonaceous chondrites. Some insight into the latter problem can be gained from the results of step-wise heating experiments of meteorite samples, and analyzing the released gas in an on-line mass spectrometer (e.g. Hashimoto et al., 1979). Our objective is to develop a more general and operationally much simpler approach in which the pattern of volatile release during controlled heating of a meteorite can be depicted into a computer terminal through numerical experiments if one feeds in the data on heating rate, range of temperature of interest and bulk composition of the sample. A preliminary report of this numerical experiment at 1 bar in the temperature range 400 -800°C has been published earlier (Ganguly and Saxena, 1989), in which it is assumed that the equilibrium volatile release is obtained at each heating step. The bulk composition chosen are those corresponding to the average compositions of Orgueil (C1) and Murchison (C2) meteorites. The results of volatile release pattern for Murchison are found to be broadly similar to those of step-wise heating experiments by Hashimoto et al. (1979).

Our on-going project involves determination of thermochemical properties and devolatilization kinetics of minerals which are potential components of carbonaceous chondrites, refinement of the numerical experiments by incorporating these data. The latter part of the project has been carried out in collaboration with Professor Surendra Saxena (Brooklyn College, New York and University of Uppsala, Sweden). The results obtained during the current funding period (March 1, 1991-Oct 31,1991) are reported below.

Modal Abundance of Minerals in C2 Chondrites

We have expanded on our earlier work (Ganguly and Saxena, 1989) on the calculation of modal abundance of minerals in the C2 bulk composition by incorporating the thermochemical properties of minerals that have become available recently. The results of calculation at in the temperature range 200 -800 K at 200 bars are illustrated in Fig. 1. The major volatile bearing mineral phases predicted by these calculations are epsomite, talc, antigorite, brucite, magnesite,

pyrite and pyrrhotite. These predictions are in very good agreement with the known mineralogy of C2 chondrites.

Dehydration Kinetics of Talc and Anthophyllite

We have reported earlier (Ganguly and Bose, 1990) the results of dehydration kinetics of talc in the temperature range 775-985°C. The results were based on thermogravimetric record of dehydration of crushed samples from a natural talc at 1 bar. The composition of the material was $(\text{Mg}_{.98}\text{Fe}_{.01})_3\text{Si}_4\text{O}_{10}(\text{OH})_2$, which had been crushed to a grain size of 1-0.7 micron. It was reported that the data up to 50-60% dehydration can be fitted by a rate expression of the form $\alpha = \exp(-kt^n)$, where α is the weight fraction of talc remaining, k is a rate constant and n is a numerical constant for a given temperature. For a set of isothermal data, we reported a major change in the value of n for larger dehydration.

We have recently modified our apparatus to improve its stability, and repeated the experiments on dehydration kinetics of talc. The results show that the reported change in the value of n is an artifact of small but significant instrumental noise in the initial stage of the earlier experiments following the introduction of the sample into the hot spot of a preheated furnace. The revised data can be fitted nicely over the entire range of dehydration by a second order rate expression, viz.

$$-d\alpha/dt = k\alpha^2 \quad (1)$$

or the equivalent integrated form

$$1/\alpha = 1/\alpha_0 + kt. \quad (2)$$

The results at 950°C are illustrated in Fig. 2. The Arrhenian plot of the rate constant in the range of 875-975°C is shown in Fig. 3. The least square regression of the data yields

$$k = 3.23(10^{14})\exp(-Q/RT) \text{ min}^{-1} \quad (3)$$

where the activation energy $Q = 376 (\pm 20 \text{ kJ})$, the error bar representing 1σ uncertainty.

We have also begun a study of the effect of grain size on the dehydration kinetics of talc. The typical grain size reported from carbonaceous chondrites is around 100 angstrom. Earlier study by Gregg and Razuk (1949) on the dehydration kinetics of brucite showed a maximum in the dependence of reaction rate on grain size. The typical grain size of phyllosilicates reported from carbonaceous chondrites is around 100 angstrom (i.e. 0.01 micron). Although it is practically impossible to crush a sample of mineral and separate such a small grain size, it is hoped that one should be able to determine a trend on the dependence of dehydration kinetics on grain size and extrapolate the kinetics to this range. We have developed the technique of grain size separation up to 0.1 micron by repeated ultracentrifuging of particles suspended in a liquid medium. This is a very tedious process with a small yield of very fine separates. It may be necessary to perform the thermogravimetric experiments with the sub-micron samples in a more sensitive instrument (e.g. a model marketed by Du Pont) than ours requiring much smaller amount of sample than is

needed in our apparatus.

Equilibrium Dehydration of Talc at High Pressure

Professor S. K. Saxena, who is our collaborator in this project, has recently calculated the equilibrium dehydration boundary of talc ($\text{Talc} = \text{Enstatite} + \text{SiO}_2 + \text{H}_2\text{O}$) in the range of 1 to 60 kb on the basis of available internally consistent thermochemical data (Fig. 4). The equilibrium dehydration boundary shows a strong curvature changing from a positive to negative P-T slope due to the transformation of α -quartz to coesite, and the compression of H_2O with increasing pressure. Precise experimental determination of this dehydration boundary affords a means of refining the equation of state of water. Work is currently in progress in this direction. We have synthesized the required starting materials, which will be used to make high pressure runs in the piston-cylinder apparatus to determine the P-T stability field of talc over a large range of pressure.

References

- Ganguly, J. and Saxena, S.K. (1989) Theoretical predictions of volatile abundances and volatile bearing phases in carbonaceous chondrites. In Space Manufacturing 7: Space Resources to Improve Life on Earth. Proceedings of the ninth Princeton/AIAA/SSI Conference, 1989. American Institute of Aeronautics and Astronautics, Washington D.C..
- Gregg, S.J. and Razouk, R.I. (1949) The kinetics of the thermal decomposition of magnesium hydroxide. J. Chem. Soc., part V, 536-544.
- Hashimoto, A., Kumazawa, M. and Onuma, N. (1979) Evaporation of primitive dust material in the early solar nebula. Earth and Planetary Science Letters, 43, 13-21.

Fig. 1: Calculated modal abundances of minerals in the C2 bulk composition. The total amount of a Fe-Mg phase is the summation of Fe and Mg end-member components.

Fig. 2: (a) Plot of isothermal dehydration of talc at 950°C, 1 Bar. Alpha is the weight fraction of talc remaining. (b) Illustration of the data in (a) in terms $1/\alpha$ vs time. The linear dependence $1/\alpha$ versus time indicates that the dehydration of talc follows a second order rate law (see text).

Fig. 3: Arrhenius relation of dehydration rate constant between 875 and 975°C at 1 bar. The activation energy is 376 kJ/mol.

Fig. 4: Calculated equilibrium dehydration boundary of talc ($\text{Talc} = \text{Enstatite} + \text{SiO}_2 + \text{H}_2\text{O}$) in the range of 1 to 60 kb on the basis of available internally consistent thermochemical data.

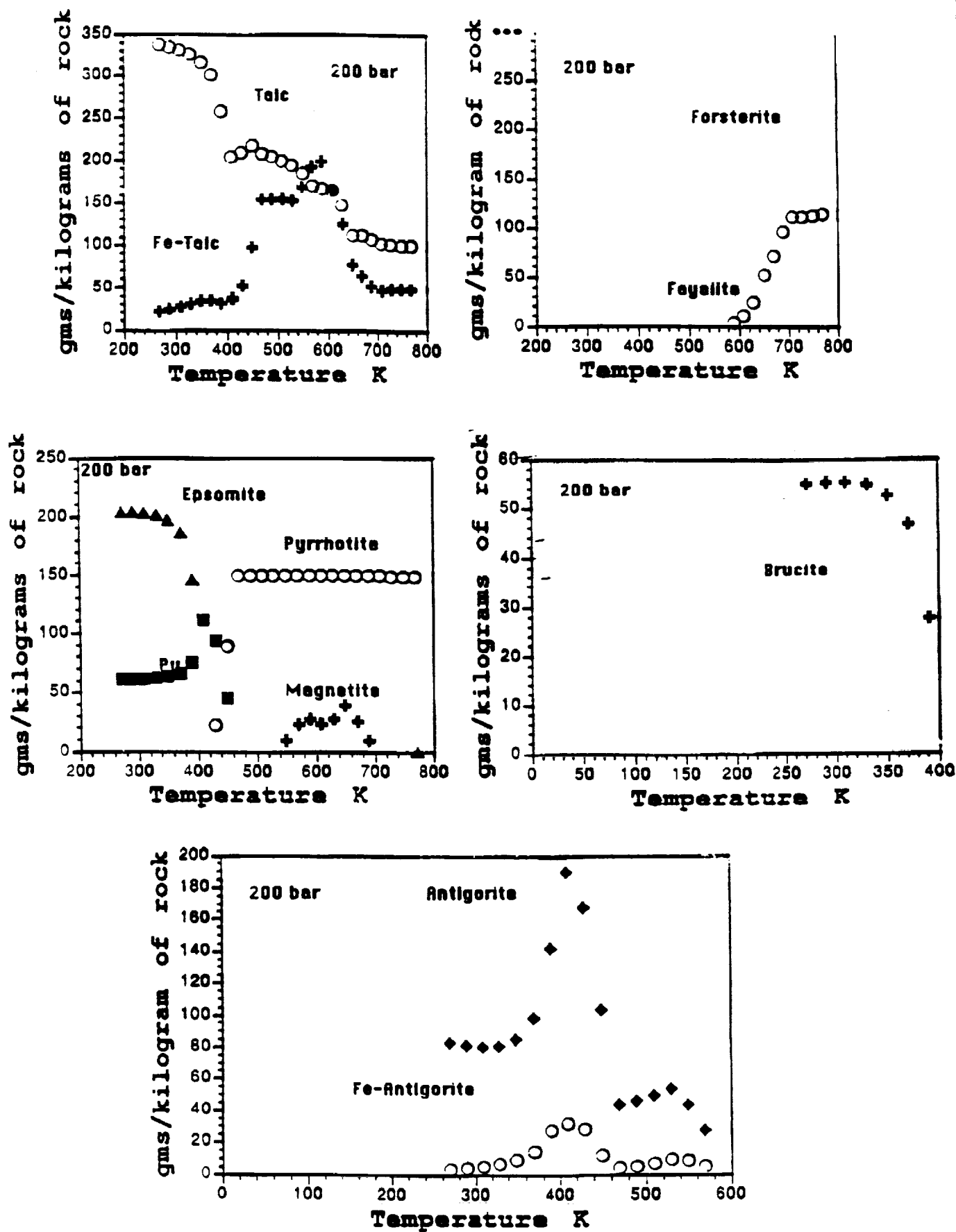


Fig. 1: Calculated modal abundances of minerals in the C2 bulk composition. The total amount of a Fe-Mg phase is the summation of Fe and Mg end-member components.

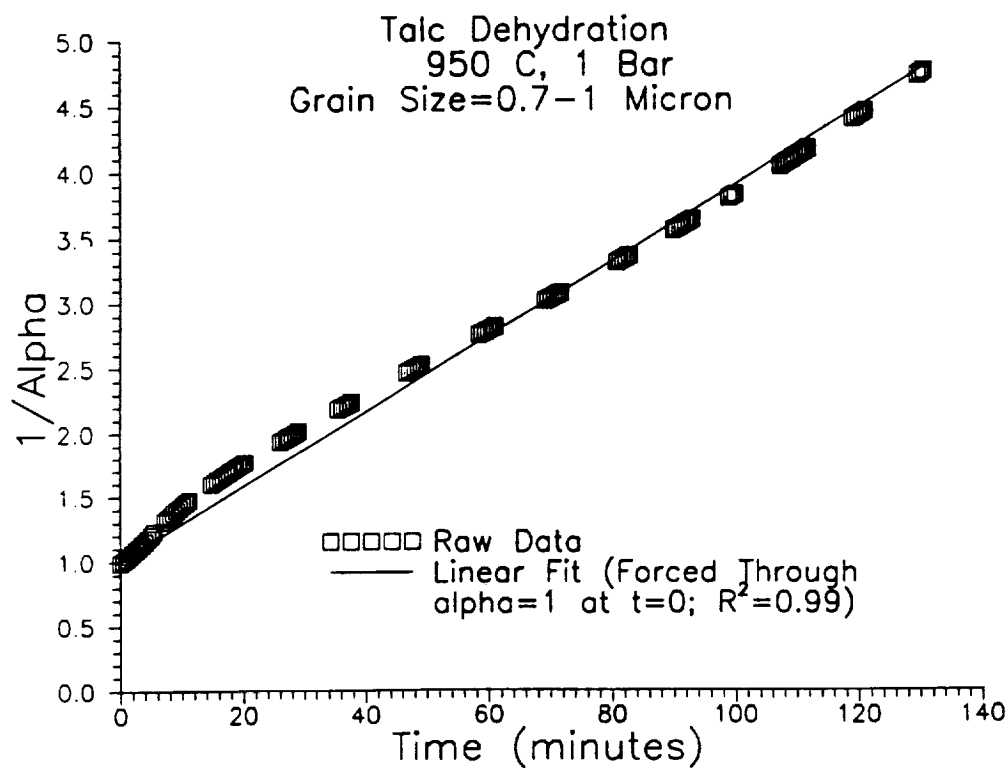
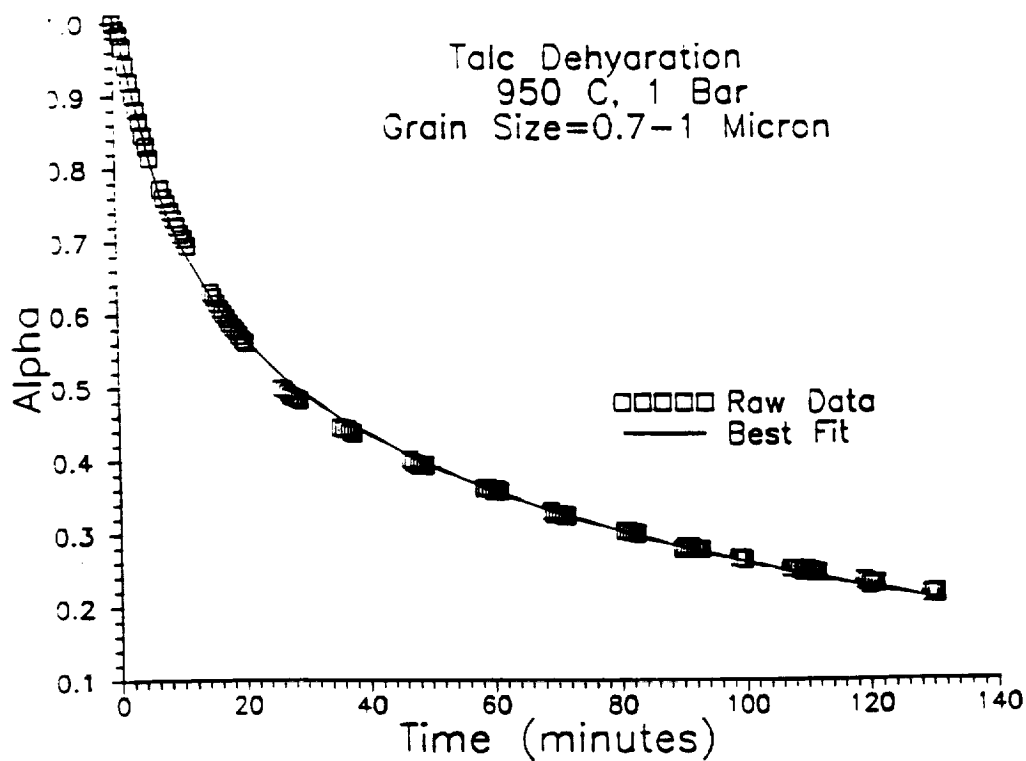


Fig. 2: (a) Plot of isothermal dehydration of talc at 950°C, 1 Bar. Alpha is the weight fraction of talc remaining. (b) Illustration of the data in (a) in terms $1/\alpha$ vs time. The linear dependence $1/\alpha$ versus time indicates that the dehydration of talc follows a second order rate law (see text).

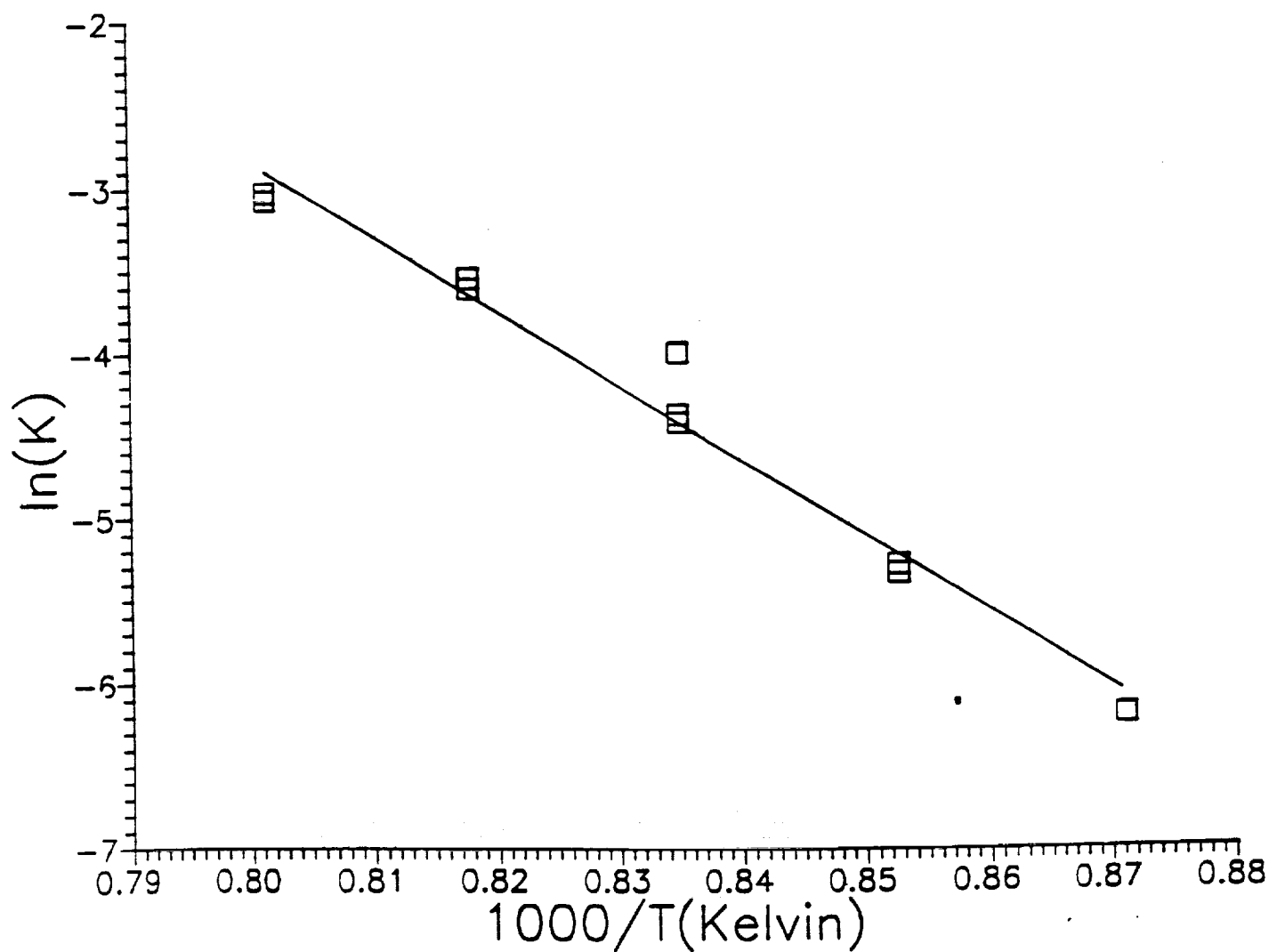


Fig. 3: Arrhenius relation of dehydration rate constant between 875 and 975°C at 1 bar. The activation energy is 376 kJ/mol.

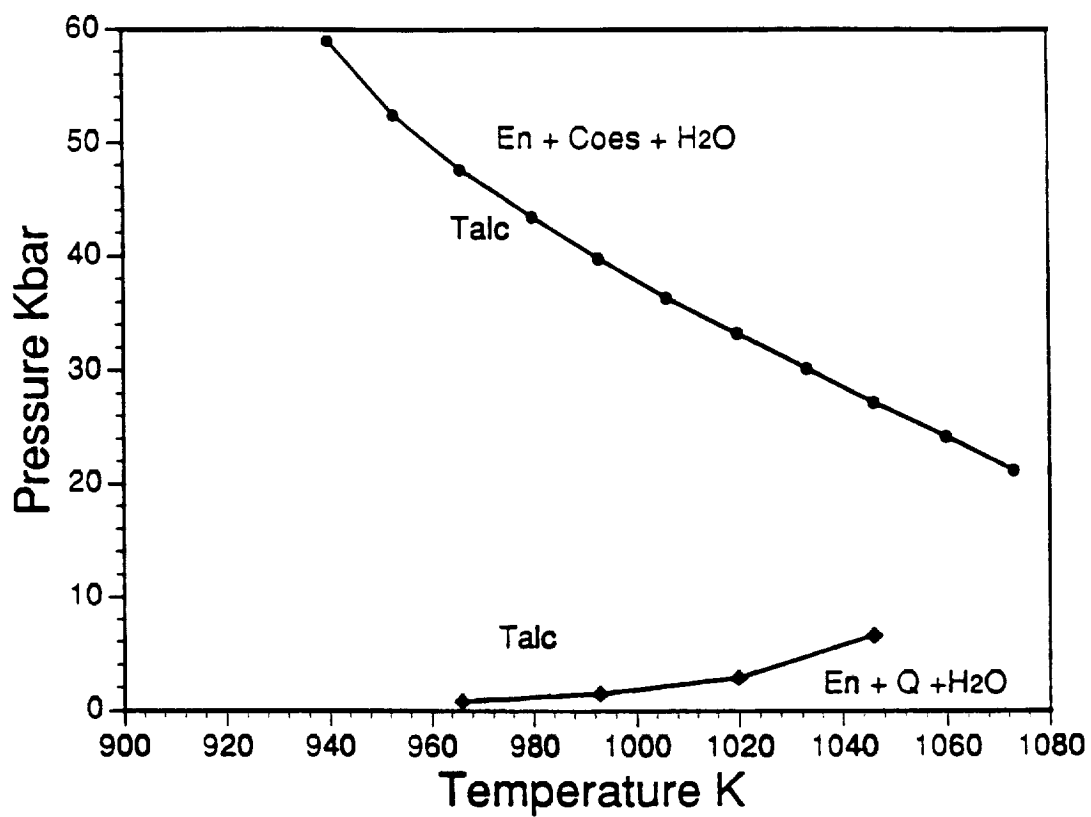


Fig. 4: Calculated equilibrium dehydration boundary of talc (Talc = Enstatite + SiO₂ + H₂O) in the range of 1 to 60 kb on the basis of available internally consistent thermochemical data.



II. PRODUCTION OF STRUCTURAL AND REFRACTORY MATERIALS



Processing of Glass-Ceramics from Lunar Resources

B. D. Fabes, W. H. Poisl, and D. Allen
Department of Materials Science and Engineering
The University of Arizona

Abstract

The goal of this project is to fabricate strong ceramic materials, suitable for structural and thermal applications, using the by-products of lunar oxygen production processes. Previously, glass-ceramics, which are polycrystalline ceramics made from the controlled crystallization of homogeneous glasses, were selected as the material to study for these applications. In the past year we continued our studies of the thermodynamics and kinetics of crystallization of simulated lunar glasses. We also formed large glass monoliths, subjected these to a variety of heat treatments to produce polycrystalline, fine-grained ceramics, and examined the mechanical properties of these materials. Strengths were found to vary with the inverse square root of the crystal grain size, as expected if the strength-limiting flaws originate at the crystal grain boundaries. For materials with the smallest grains tensile strengths greater than 300 MPa were obtained.

Introduction

In evaluating the attractiveness of the different process which have been proposed for producing oxygen from lunar resources it is important to consider what can be done with the by-products. By-products which can be used for structural (e.g., in shelters, buildings, roadways, tubes, pipes, etc.) or thermal (e.g., in building insulation, furnace bricks, and heat shields) applications are clearly desirable. The goal of this research program is to apply basic concepts of materials science to developing such materials from lunar resources. Since it is likely that production of oxygen will provide the main impetus for in-situ materials use on the moon, a further goal of this research is to develop processes which use the by-products of oxygen production schemes as starting materials.

Our initial investigation showed that ilmenite-extracted regolith – a by-product of lunar oxygen production via reduction of ilmenite – is a promising candidate for a starting material from which glass-ceramics could be made. Glass-ceramics are not only strong, but also are abrasion resistant, are extremely stable (both chemically and thermally), are resistant to thermal shock, and possess a variety of other attractive properties. In addition, it is relatively easy to make glass-ceramics in complicated shapes, since their shape is formed using standard glass-forming processes. Thus, glass-ceramics made from ilmenite-extracted regolith were selected for study.

As described in our previous reports, the key to fabricating glass-ceramics with desirable properties is to control the sequence of crystal nucleation and growth. Such control is obtained by understanding the effect of composition and heat treatment on the physical properties (most importantly viscosity) of the homogeneous glass. This program therefore has two foci. The first emphasis is on understanding the effects of composition, especially iron oxide, titania, and alkali impurities, on the crystallization and, hence, properties of glass-ceramics made from lunar resources. The second focus is on developing a set of heat treatment schedules which result in optimized microstructures and, hence, properties for a limited number of compositions. Thus, we are developing both the "science and engineering" of producing glass-ceramics from lunar resources. By optimizing the processing of a few, selected compositions we will develop a knowledge base for processing glass-ceramics, and by understanding the underlying scientific issues we will be able to expand our processing skills to develop processes which are robust, with respect especially to variations in the composition of the starting materials.

Progress

In the first year of this program we set up facilities for melting and casting small samples of simulated lunar glasses and began to examine the effects of Fe_2O_3 , TiO_2 , and alkali impurity content on the viscosity of the simulated lunar glasses listed in Table I. The effects of most of these constituents were as expected. For example, alkali impurities tended to decrease the viscosity of a glass and enhance crystallization at low temperatures. Such impurities need to be minimized, therefore, since they make glass-formation of large samples extremely difficult. Progress over the past year and plans for the future are summarized in the following sections.

1. Thermodynamics and Kinetics of Crystallization

This past year we began to study the effects on composition on the thermodynamics of crystallization of the glasses in Table I. Differential thermal analysis (DTA) was used to determine the temperature at which crystallization occurred for each composition. Small changes in composition were found to produce large changes in crystallization behavior. For example, some compositions, such as sample B12 (Figure 1) exhibited only one crystallization peak, while other compositions, such as A12 (Figure 2) showed two distinct crystallization peaks. The effects of these variations on the microstructure and properties of the final glass-ceramics remain unexplored. Clearly, samples which exhibit different crystallization peaks will require different heat treatments to optimize their mechanical or thermal properties. Exactly how sensitive the final properties are to the variations in composition will depend on the phases which are crystallizing and the different microstructure which are produced. We are in the process of determining the crystallization products using x-ray diffraction, and are characterizing the microstructures using electron microscopy.

Table I: Composition (in wt%) of lunar simulants studied in the past year

	A12	A17	B12	B17	MLS-2*	MLS-4
SiO_2	46.7	46.8	50.2	49.4	54.0	51.8
Al_2O_3	13.6	14.7	14.6	15.5	14.6	14.0
CaO	10.5	12.6	11.4	12.3	13.4	12.9
MgO	9.8	11.0	10.5	11.6	7.6	7.3
TiO_2	5.0	5.0	5.4	5.3	0.9	5.0
Fe_2O_3	14.4	9.9	8.0	5.0	9.3	8.9

*MLS-2 also contained a small amount (≈ 2 wt%) of alkali and other impurities.

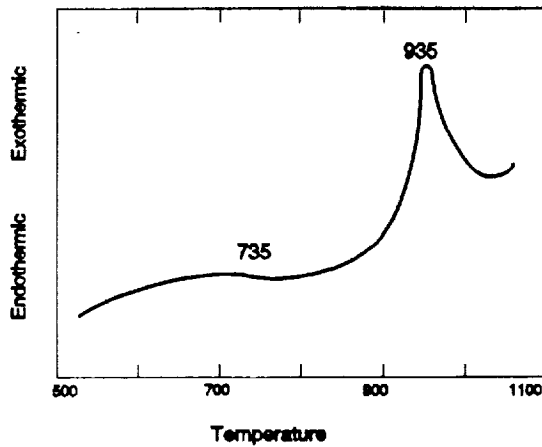


Figure 1: DTA Trace of Sample B12, a simulated lunar glass which exhibits only one distinct crystallization peak.

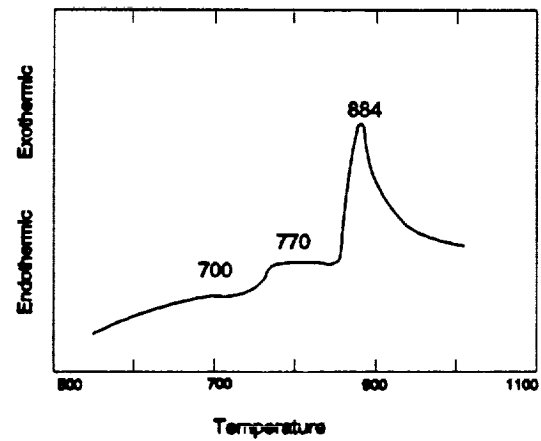


Figure 2: DTA Trace of Sample A12, a simulated lunar glass which exhibits two distinct crystallization peaks.

2. Mechanical Properties of Simulated Lunar Glass-Ceramics

Having established in qualitative terms the impact of compositional variations on the viscosity of the glass, our main focus on the engineering side during the past year has been to examine the mechanical properties of some compositions with higher viscosity (i.e., those for which large glass monoliths can be made and for which crystallization should be most easily controlled.) In addition, a new, larger copper mold for casting glass monoliths was fabricated. This mold, and a solidified glass "puck" produced in it, are shown in Figure 3. Pucks weighing up to 300 g and measuring approximately 7 cm in diameter and 3 cm in thickness have been fabricated with no indication of undesirable crystallization. Up to this point, the sizes of the glass monoliths which we can produce are limited by amount of melted glass which our Pt crucible can hold, and not by parasitic crystallization of the glass.

To examine the mechanical properties of our glass-ceramics the DTA trace of sample B12 (Figure 1) was used to develop a "semi-controlled" crystallization schedule. After casting a large, homogeneous glass puck, the amorphous sample was heated to 720 °C (well below the crystallization temperature) for nucleation. After one hour at 720 °C, crystal growth was carried out by heating the sample to 940 °C and holding at that temperature for three hours.

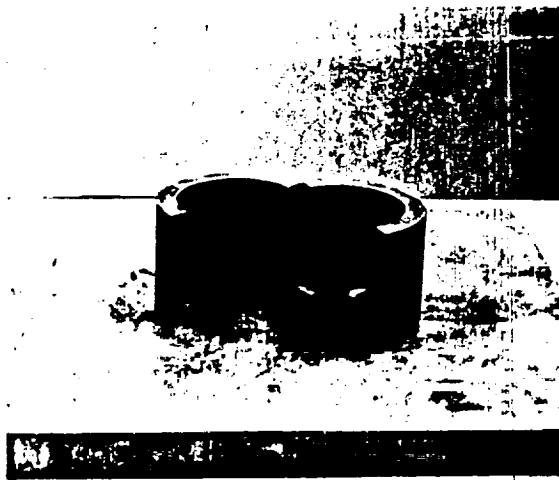


Figure 3: New, large copper clamshell mold and simulated lunar glass "puck" produced in the mold.

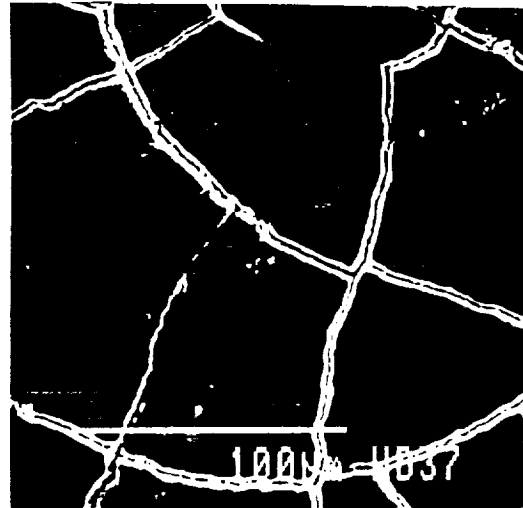


Figure 4: SEM micrograph of polished and etched glass-ceramic formed by crystallization of Sample B12.

The resulting glass-ceramic microstructure, after polishing and HF etching, is shown in the SEM micrograph in Figure 4. The material is pore-free and homogeneous. The crystal grains range in size from roughly 50 to 100 μm and are separated from one another by a thin ($\approx 300 \text{ nm}$) glass phase. (The glass phase appears black in the micrograph as a result of the HF etching.) There is no evidence of columnar, spherulitic, or incomplete grain growth, in this sample.

Four samples of the uncrystallized glass and four samples of the crystallized glass-ceramic were polished to a 15 μm finish and broken using a ball-on-ring bend test jig to measure their tensile strengths. The results are shown in Table II. The strength of the glass-ceramic is almost twice that of the uncrystallized glass.

These procedures were repeated for two other glass compositions, resulting in samples with different crystal phases and microstructures. For all samples the strength of the glass was relatively insensitive to changes in composition. This was not surprising, since the strength of inorganic glasses is controlled almost entirely by the state of the surface (i.e., amount and size of flaws) and not by composition. The strength of the crystallized samples, on the other hand, was quite variable. As shown in Figure 5, the strength of the glass ceramics varied roughly linearly with the inverse square root of the grain size, which indicates that the strength limiting flaws for the glass-ceramics originate at the crystal grain boundaries, and not on the surface. The sample with the smallest grain size exhibited the largest tensile strength, greater than 300 MPa. As far as we are aware this is the highest value reported for the strength of simulated lunar ceramics.

Table II: Mechanical Properties (in MPa) of glass B12 and crystallized glass-ceramic

	<u>Parent Glass</u>	<u>Glass-Ceramic</u>
Tensile Strength	125	215
Standard Deviation	1.8	40.2

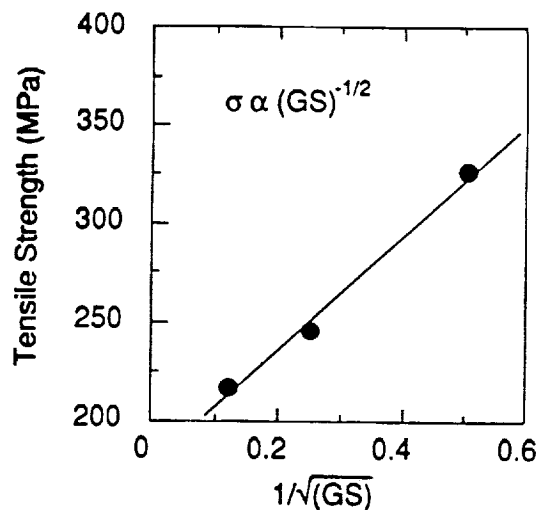


Figure 5: Variation in tensile strength with grain size for simulated lunar glass-ceramics.

Future Work

In the coming year we plan to continue our "two tier" (science and engineering) approach. We will continue to study the effect of composition on the crystallization sequence of simulated lunar glasses, using x-ray diffraction and scanning electron microscopy to characterize the crystallization products. Our goal will be to determine ranges of compositions which are removed from line compounds, which promote crystallization. By developing compositions which are removed from such compounds, the crystallization should be controlled by bulk diffusion, which will enhance our ability to control microstructure development.

In this work we will pay special attention to the effects of the oxidation state of iron (Fe_2O_3 , as found on Earth) vs. FeO , which is the predominant species on the Moon. Cukierman et al have shown that the oxidation state of iron has a significant effect on the viscosity (and, by implication, on the crystallization kinetics) of lunar glasses with high iron contents. For this work we have already purchased and set up a controlled atmosphere furnace and viscometer, and arrangements have been made with NASA Johnson Space Center to use their Raman spectroscopy facilities to characterize the oxidation state and coordination of iron in various glasses.

We will also pay special attention to the effects TiO_2 on crystallization. TiO_2 is commonly added to glasses as a nucleating agent for terrestrial-produced glass-ceramics. While the mechanism of nucleation remains an issue of debate, it is an effective nucleating agent, and is likely to be abundant on the moon as the by-product of oxygen production from ilmenite reduction. Hence, we will use TiO_2 as a nucleating agent for our simulated lunar glass-ceramics,

and we will examine the effects of additions of TiO_2 to the crystallization, microstructure, and properties of simulated lunar glass-ceramics..

On the engineering side we will measure the effects of water (or, more precisely, the lack of water) on the strength of simulated lunar glasses. The literature contains many references to the increase in strength of glasses which should result from lack of water in the lunar environment. While it is true that the strength should be somewhat higher, for everyday use we have calculated that this increase should be no more than a factor of two. We will make measurements to test these calculations.

We will also continue to optimize the heat treatment schedules for a limited number of (high viscosity) samples to probe the limits of strength which we can obtain. And finally, for the materials with the highest strengths, we will use the glass-ceramics as a matrix material for ceramic matrix composite. By adding silicon carbide fibers to the glass melt, we will try to make a material that is not only strong (a result of the strength of the glass-ceramic matrix) but also is tough (a result of the fiber reinforcements).



DESIGN OF HIGH TEMPERATURE SEALS
K. R. Sridhar* M. Yalcintas and G. Honea****
Department of Aerospace and Mechanical Engineering
University of Arizona

ABSTRACT

Design and fabrication of high temperature seals between ceramics and metals in oxidizing environments is one of the key technologies that has to be developed for the Mars Oxygen Production Plant. In order to design a compact, efficient and reliable electrochemical cell it is necessary to seal the ceramic electrolyte (Partially Stabilized Zirconia) to a metal or ceramic manifold. A computational model is being developed to analyse the stresses in the seal due to thermal loading and gas pressure. This effort will help identify the optimal shape of the seal for a given application. The progress is summarized. Equipment has been designed, fabricated and tested for the testing of high temperature seals. Direct brazing with stress mitigation bellows and adhesives have been used to form seals. The procedure used for these processes are reported.

* Assistant Professor, Aerospace and Mechanical Engineering Department, University of Arizona.

** Graduate Students, Aerospace and Mechanical Engineering Department, University of Arizona.

DESIGN OF HIGH TEMPERATURE SEALS

K. R. Sridhar

Department of Aerospace and Mechanical Engineering

University of Arizona

Design and fabrication of high temperature seals between ceramics and metals in oxidizing environments is one of the key technologies that has to be developed for the Mars Oxygen Production Plant. In order to design a compact, efficient and reliable electrochemical cell it is necessary to seal the ceramic electrolyte (Partially Stabilized Zirconia) to a metal or ceramic manifold. A computational model is being developed to analyse the stresses in the seal due to thermal loading and gas pressure. This effort will help to identify the optimal shape of the seal for a given application. The progress is summarized. Equipment has been designed, fabricated and tested for the testing of high temperature seals. Direct brazing with stress mitigating bellows and adhesives have been used to form seals. The procedure used for these processes are reported.

INTRODUCTION

The key component of the Mars oxygen production plant is the electrochemical cell unit that separates oxygen from a gas mixture of carbon dioxide, carbon monoxide, and oxygen. Before a Mars mission can be committed to in-situ resource utilization involving the oxygen production plant it is necessary to ensure that an extremely efficient and reliable electrochemical cell can be designed and developed. Research on the optimal performance of the electrochemical cell has shown that the design of a seal between the Zirconia electrolyte and the manifold (made of metal or ceramics) that can withstand (1) the high operating temperatures of the cell (800-900 C) (2) the oxidizing environment in the cell and (3) the thermal cycling from start-up and shutdown, is essential. The design of such a seal is necessary for both the tubular and flat disk configurations of the electrochemical cell currently under consideration. This report summarizes the theoretical and experimental programs that are currently underway to develop effective seals for such high temperature applications.

PROBLEM DEFINITION

A simplified model of the tubular configuration of the electrochemical cell consists of two concentric cylinders of finite length with the annulus closed by seals at both ends. The inner tube is the electrochemical cell made of partially stabilized Zirconia and the outer tube is made of Haynes 214 alloy (nickel based super alloy). During operation, the two tubes, seals and the gases inside would be at temperatures ranging from 800 - 900 C. The annular region contained by seals would be filled with

oxygen. The pressure of oxygen in this chamber would depend on the oxygen bleed pressure and the voltage applied across the cell. While current experiments are conducted with oxygen pressure at 0.11 MPa, future tests will explore the possibility of operating the cell at oxygen pressures of upto 2 MPa.

The disk configuration of the electrochemical cell has been described in detail in another paper by the author and Kaloupis in this report. For such a configuration it is essential to develop a seal between the electrochemical disk and the manifolds. Since ceramic disks have low tensile strength, the oxygen side will not be pressurized. For this reason the stresses due to gas pressure will not be significant for the seals in the disk configuration.

Research is in progress to computationally analyze the stresses in the seals using the Finite Element Method and to develop procedures to make the seals, and test them in the laboratory. The current status of the work is described in the following sections.

1. COMPUTATIONAL STRESS ANALYSIS

Graduate Student: Melek Yalcintas*

The stresses induced in a seal due to variable thermal expansion coefficients and gas pressures have to be analyzed to arrive at an optimal shape for a seal between two surfaces. The ultimate objective of the code being developed will be to compute the stresses at joints and seals between any two surfaces due to thermal and other loads. Presently, the code is being developed for seals between concentric tubes, since the tubular configuration is being adopted currently for the scale up of the oxygen production plant. It will be adopted for the disk configuration in the near future.

The approach taken for the stress analysis is to consider the tube set up as a simply supported beam. Stresses on the tubes and seals are caused by both gas pressures and variable thermal expansion coefficients. This approach permits us to predict the stresses on the whole device although our main interest lies in the prediction of the stresses on the seals. To arrive at an optimal seal geometry stresses on the seals can be calculated for various geometries (and materials) until the minimum stress case is found. The approach taken here is to start with a very simple model and add on the complexities as we proceed. The FEM analyses are verified against theoretical values for the simple cases.

* Professor E. Madenci, AME Department, is a co-advisor of M. Yalcintas and contributes to the FEM analysis of the seal.

1. 1 Theoretical stress calculation

Theoretical calculations of the stresses for the simplified model of the tube configuration described earlier are performed using the methodology given in [1]. The properties and dimensions used in the analysis are listed in Table 1.1 , the tubular device is shown in Fig.1.1. The calculations are performed in the radial coordinate system.

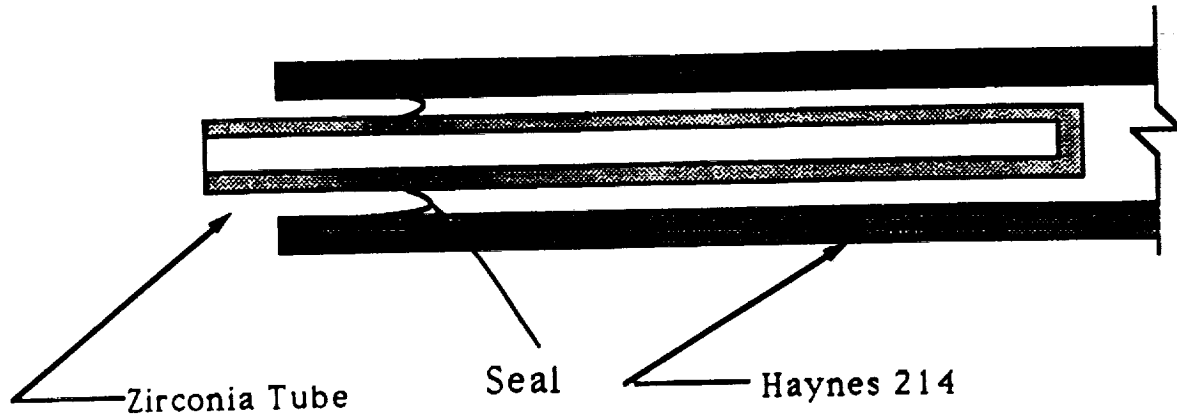


Fig. 1 .1 Ceramic tubular device

Quantity	Notation	Unit	Ceramic tube	Metal tube	Seal
Poisson's ratio	Pr	-	0.2	0.3	0.3
Young's modulus	E	Pa	152e9	193e9	193e9
Integral gas pressure	Pi	Pa	5000	5000	5000
Inner diameter	Di	Pa	8	18	12
Outer diameter	Do	mm	12	22	18
Thickness	t	mm	2	2	2
Length	l	mm	250	250	—

Table 1. 1 Parameters for the tubular configuration.

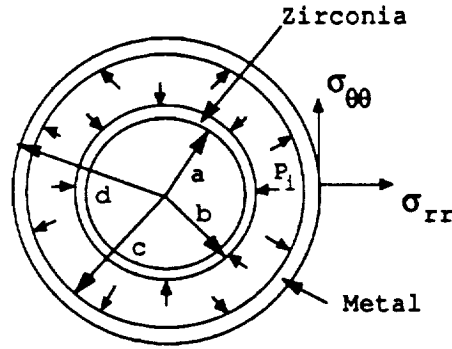


Fig. 1.2 Tubular device cross section.

The stresses on ceramic and metal tubes due to applied pressure shown in Fig.1.2 are:

$$\sigma_{rr}^{(1)} = k_1 - \frac{k_2}{r^2} \quad \sigma_{\theta\theta}^{(1)} = k_1 + \frac{k_2}{r^2} \quad (1)$$

and

$$\sigma_{rr}^{(2)} = k_3 - \frac{k_4}{r^2} \quad \sigma_{\theta\theta}^{(2)} = k_3 + \frac{k_4}{r^2} \quad (2)$$

respectively where k_1 , k_2 , k_3 , and k_4 will be determined by applying boundary conditions. The boundary conditions are:

$$\sigma_{rr}^{(1)}(r=b) = -P_i \quad \text{and} \quad \sigma_{rr}^{(1)}(r=a) = 0 \quad (3)$$

for the ceramic tube and

$$\sigma_{rr}^{(2)}(r=c) = -P_i \quad \text{and} \quad \sigma_{rr}^{(2)}(r=d) = 0 \quad (4)$$

for the metal tube.

Applying the boundary conditions (3) and (4) in (1) and (2), and writing the parameters listed in Table 1, the resultant stresses are:

$$\sigma_{rr}^{(1)} = -920.29 \times 10^3 + \frac{14.73}{r^2} \quad (5)$$

$$\sigma_{\theta\theta}^{(1)} = -920.29 \times 10^3 - \frac{14.73}{r^2} \quad (6)$$

$$\sigma_{rr}^{(2)} = 1.0354 \times 10^6 - \frac{125.27}{r^2} \quad (7)$$

$$\sigma_{\theta\theta}^{(2)} = 1.0354 \times 10^6 + \frac{125.27}{r^2} \quad (8)$$

The numerical values of the theoretical calculations are compared to the corresponding values obtained using the FEM in section 1.3.

1.2. FEM Codes

The four FEM codes used in this research are Ingrid, Nike3d, Taurus and Topaz which were all developed at Lawrence Livermore National Laboratory. A brief description of the codes are as follows:

1.2.1 INGRID

It is a three dimensional mesh generator for modelling nonlinear systems. Ingrid generates a complete input file for Nike3d. Geometries are described primarily using index space concepts. Complicated meshes can be generated, exact surface equations and surface intersections can be introduced and, 30 000 element meshes can be generated. Boundary conditions, loads, material properties required by nonlinear mechanics problems can be applied.

1.2.2 NIKE3D

It is a fully implicit three-dimensional finite element code for analyzing the finite strain, static and dynamic response of inelastic solids, shells and beams. A contact-impact algorithm permits gaps and sliding along material interface. By customizing this algorithm, those interfaces can be made to admit variable zoning without the need for a transition region.

1.2.3 TAURUS

It is a post processor program that reads the binary plot files generated by Nike3d. It plots contours, time histories and deformed shapes. Contours of a large number of quantities may be plotted on meshes consisting of plate, shell and solid type elements. It can compute a variety of strain measured reaction forces along constrained boundaries.

1.2.4 TOPAZ3D

It is a three dimensional implicit finite element heat transfer analysis code. Topaz3d can be used to solve for the steady state and transient temperature field on three dimensional geometries. Material properties may be temperature dependent and either isotropic or orthotropic. A variety of time and

temperature dependent boundary conditions can be specified including temperature, flux, convection and radiation. By implementing the user subroutine feature, users can model chemical reaction kinetics and allow for any type of functional representation of boundary conditions and heat generation. Topaz3d can solve problems of diffuse and specular band radiation in an enclosure coupled with conduction in the material surrounding the enclosures. Additional features include thermal contact resistance across an interface, bulk fluids, phase change and energy balances. Thermal stresses can be calculated using the solid mechanics code Nike3d which reads the temperature state data calculated by Topaz3d.

Topaz3d has no general mesh generation capability. Rows of evenly spaced nodes and rows of sequential elements may be generated. For complex zoning the mesh generating code and processor Ingrid should be used. The Taurus interactive post-processor can be used to provide temperature contour, temperature-time history and various geometry plots.

1.3. Mesh Generation and FEM Results for the Model

Mesher for the model are generated using Ingrid. Since the main interest is in the stresses on the seal, finer meshes are generated at seals and its surroundings.

First the FEM analysis of the simplified model is carried out where only the pressure effects are considered. Stresses on the seal in x, y, z - direction are shown in Fig. 1.3 a, b, c and stresses on metal tube and ceramic tube in x - direction are shown in Fig. 1.4 a, b. It is observed that, due to the symmetry of the model, stresses in x and y directions are equal.

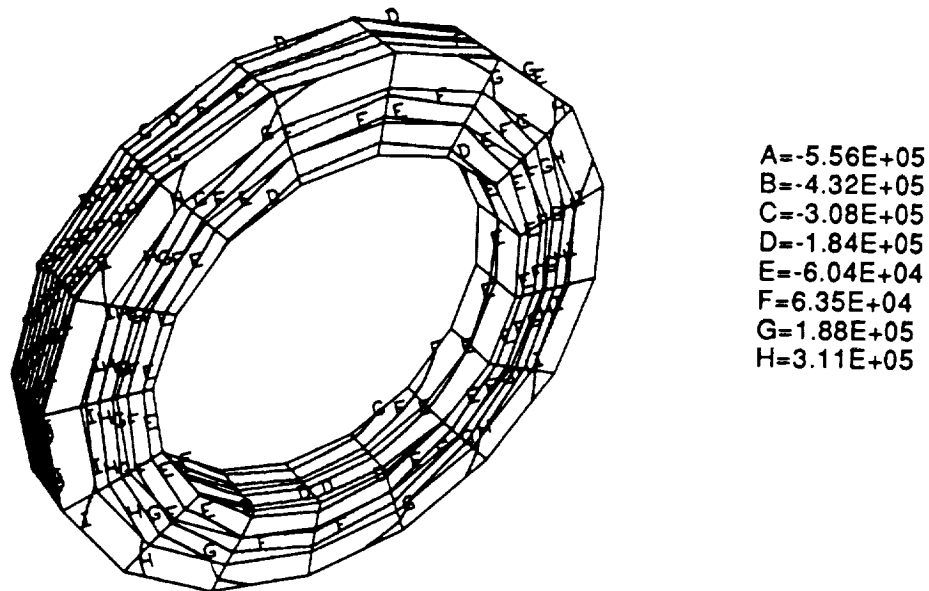
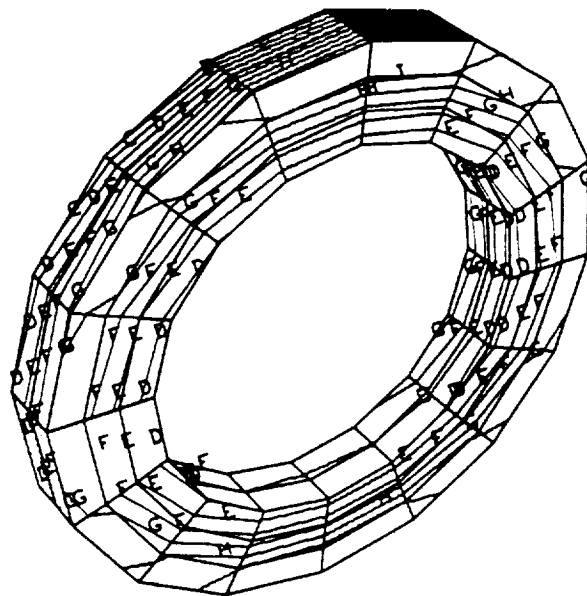
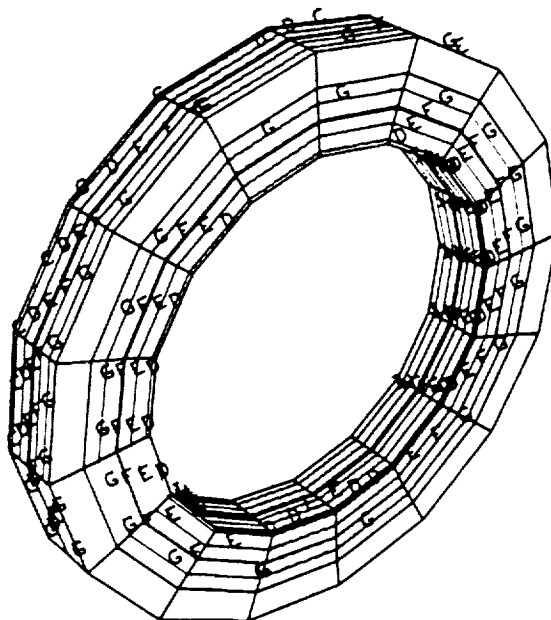


Fig 3.a Stress contours of seal in x-direction (in Pa).



$A = -5.56E+05$
 $B = -4.32E+05$
 $C = -3.08E+05$
 $D = -1.84E+05$
 $E = -6.04E+04$
 $F = 6.35E+04$
 $G = 1.88E+05$
 $H = 3.11E+05$
 $I = 4.35E+05$

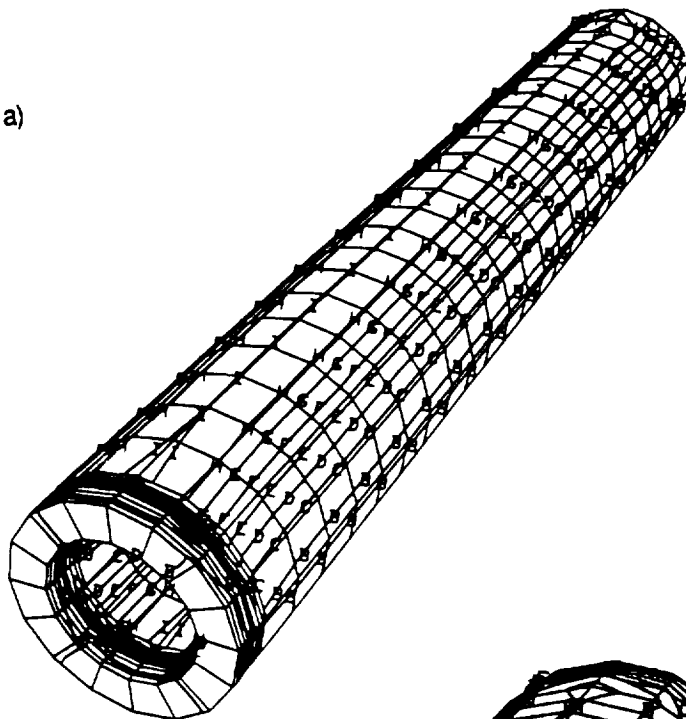
Fig 3.b Stress contours of seal in y-direction (in Pa).



$A = -4.68E+05$
 $B = -4.12E+05$
 $C = -3.56E+05$
 $D = -3.00E+05$
 $E = -2.45E+05$
 $F = -1.89E+05$
 $G = -1.33E+05$
 $H = -7.70E+04$
 $I = -2.12E+04$

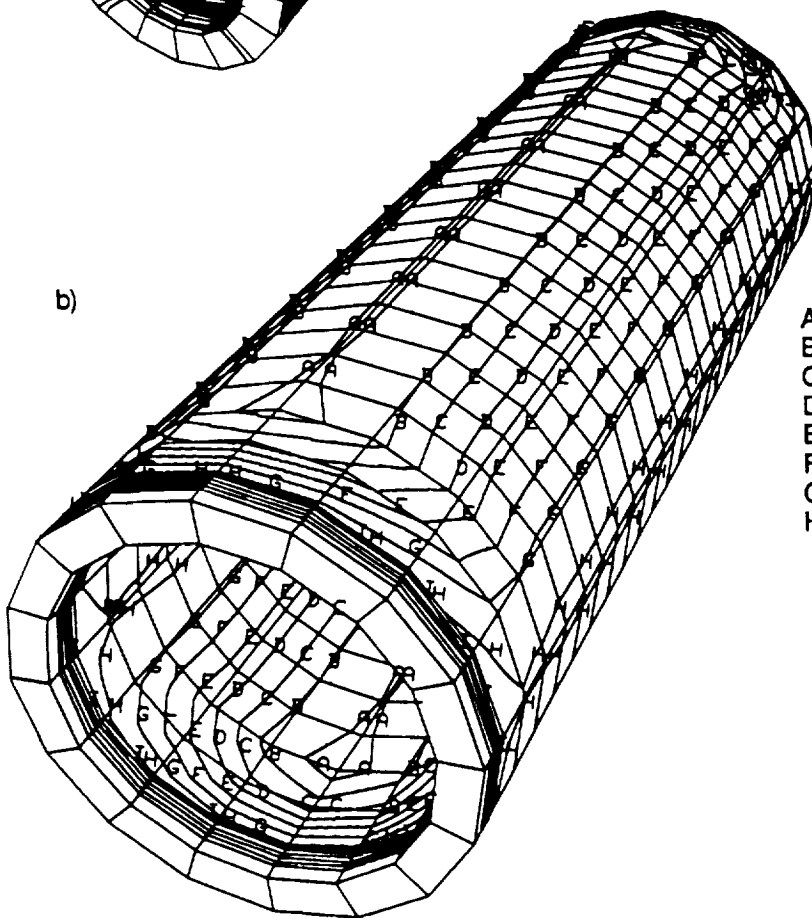
Fig 3.c Stress contours of seal in z-direction (in Pa).

a)



A=5.905E+05
B=-1.084E+05
C=1.142E+05
D=4.16E+05
E=7.20E+05
F=1.02E+06
G=1.32E+06
H=1.63E+06
I=1.93E+06

b)



A=-2.67E+06
B=-2.35E+06
C=-2.04E+06
D=-1.73E+06
E=-1.42E+06
F=-1.10E+06
G=-7.92E+05
H=-4.80E+05
I=-1.67E+05

Fig. 1.4 a,b Stress contours of ceramic tube and metal tube in x-direction (in Pa).

1.4 Comparison of Theoretical and FEM results:

The theoretical stresses on ceramic and metal tubes are calculated as described in section 1.1. Stress resultants in radial coordinates are transferred into cartesian coordinates and the maximum stresses are compared with corresponding stresses calculated by FEM codes. The results are:

	THEORETICAL	FEM
Metal tube	$\sigma_{xx\max} = \sigma_{yy\max} = -2.582 \times 10^6 \text{ Pa}$	$\sigma_{xx\max} = \sigma_{yy\max} = -2.67 \times 10^6 \text{ Pa}$
Ceramic tube	$\sigma_{xx\max} = \sigma_{yy\max} = -1.840 \times 10^6 \text{ Pa}$	$\sigma_{xx\max} = \sigma_{yy\max} = -1.93 \times 10^6 \text{ Pa}$

The orders are close each other in both results. In theoretical analysis the effects of pressure acting on seal is not considered. The slight difference at maximum stress values are due to this consideration.

1.5 Temperature Analysis

The temperature distribution in the metal tube, the annulus, ceramic tube and inside the ceramic tube need to be calculated. The temperature analysis can be done either theoretically or by using the FEM code Topaz3d. In order to check the accuracy both methods are pursued. Later these temperature distributions will be used to calculate thermal stresses in the seals.

Heat is transferred from the outer wall of metal tube to the inside of ceramic tube by conduction, convection and radiation. The transfer through the wall of the metal tube is by conduction, in the annulus between the metal tube and ceramic tube by radiation and convection, through the wall of the ceramic tube by conduction and inside the ceramic tube by convection and radiation. Temperature distribution in all these regions are calculated by formulating them separately and applying the thermal boundary conditions. Fig. 1.5 illustrates the heat transfer through the media.

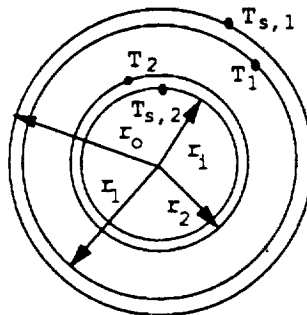


Fig. 1.5 Heat transfer through ceramic tube and metal tube

1.5.1 HEAT TRANSFER BY CONDUCTION ON THE METAL TUBE WALL

For steady state condition, with no heat generation the differential equation is:

$$\frac{1}{r} \frac{d}{dr} \left(kr \frac{dT}{dr} \right) = 0 \quad (9)$$

where boundary conditions are:

$$T(r_0) = T_{s,1} \quad (10)$$

$$T(r_1) = T_1 \quad (11)$$

solving the differential equation by applying the boundary conditions, temperature distribution through metal tube wall becomes:

$$T(r) = \frac{T_{s,1} - T_1}{\ln r_0 / r_1} \ln r / r_1 + T_1 \quad (12)$$

and heat transferred through the metal tube wall is:

$$q_r = -k(2\pi l) \frac{T_{s,1} - T_1}{\ln r_0 / r_1} \quad (13)$$

1.5.2 RADIATION HEAT TRANSFER ON THE ANNULUS

The formulation for this case is derived in reference[2]. For infinite long cylinders:

$$\psi = \frac{\psi_b}{[(D_1 / D_2)E_2 + E_1]\psi_b + 1} \quad (14)$$

$$\phi(r) = \frac{\phi_b(r) + E_2(D_1 / D_2)\psi_b}{[(D_1 / D_2)E_2 + E_1]\psi_b + 1} \quad (15)$$

where

D_1 and D_2 are inside and outside diameters of the annulus.

$$E_N = (1 - \epsilon_N) / \epsilon_N$$

$$\psi = Q_1 / A_1 \sigma (T_1^4 - T_2^4)$$

$$\psi_b = Q_{1b} / A_1 \sigma (T_1^4 - T_2^4)$$

ψ_b , ϕ_b are given in reference [4,5].

with the boundary conditions :

$$T(r_1) = T_1 \quad (16)$$

$$T(r_2) = T_2 \quad (17)$$

the temperature distribution:

$$T^4(r) = \phi(r)(T_1^4 - T_2^4) + T_1^4 \quad (18)$$

and the radiative heat transfer:

$$q_{rad} = \psi \sigma (T_1^4 - T_2^4) \quad (19)$$

1.5.3 CONDUCTION HEAT TRANSFER OVER THE CERAMIC TUBE WALL

For steady state condition, with no heat generation the differential equation is given in eqn. (9).

The boundary conditions for this case are:

$$T(r_2) = T_2 \quad (20)$$

$$T(r_1) = T_{s,2} \quad (21)$$

Solving the differential equation by applying the boundary conditions, temperature distribution through ceramic tube wall becomes:

$$T(r) = \frac{T_2 - T_{s,1}}{\ln r_2 / r_1} \ln r / r_2 + T_2 \quad (22)$$

and heat transferred through the ceramic tube wall is:

$$q_r = -k(2\pi l) \frac{T_2 - T_{s,1}}{\ln r_2 / r_1} \quad (23)$$

1.5.4 HEAT TRANSFER TO CARBONDIOXIDE INSIDE THE CERAMIC TUBE

Heat transfer inside the ceramic tube is analyzed using the method developed by Thomas H. Enstein [3]. A two-dimensional analysis is presented for determining the heat transfer to a gray uniformly

absorbing gas enclosed in a black circular pipe under the combined influence of radiation , gas flow through the pipe, and thermal distribution in the gas. The analysis also takes into account the presence of distributed energy source in gas.

In this analysis, the axial component of conduction is neglected.

The heat balance on an infinitesimal volume of gas dv located at position r in the interior of the pipe is:

$$4k\sigma T^4(r_0) + Gc_p \left. \frac{\partial T(r)}{\partial x} \right|_{r=r_0} - \frac{\lambda}{\rho} \frac{\partial}{\partial \rho} \left[\rho \frac{\partial T(r)}{\partial \rho} \right]_{r=r_0} \\ = k \iiint \sigma T^4(r) f(r - r_0) dv + k \iint \sigma T^4(r) g(r - r_0) dA + q''(r_0) \quad (23)$$

where

$q''(r_0)$	heat generation in the gas per unit volume at r_0
$4k\sigma T^4(r_0)$	radiant energy emitted per unit volume at $r=r_0$
$Gc_p \left. \frac{\partial T(r)}{\partial x} \right _{r=r_0}$	rate of enthalpy increase of the flowing gas at $r=r_0$
$\frac{\lambda}{\rho} \frac{\partial}{\partial \rho} \left[\rho \frac{\partial T(r)}{\partial \rho} \right]_{r=r_0}$	net conduction heat transfer per unit volume at $r=r_0$
$k \iiint \sigma T^4(r) f(r - r_0) dv$	radiation absorbed per unit volume r_0 from emission given off the rest of the gas in the cylinder.
$k \iint \sigma T^4(r) g(r - r_0) dA$	radiation absorbed per unit volume at r_0 from emission of pipe wall and end surfaces.

To solve above equation for cylindrical geometry, the interior of cylinder is divided into finite number of zones. The resulting two-dimensional integro-differential equation is approximated by a system of algebraic equations. Computations are being performed and the results will be reported in the near future.

1.6 Future Work

The calculation of the FEM analysis will be verified against theoretical values for the simplified cases. The next step is to use the FEM analysis to consider thermal stresses. Then the geometry for the seal in tubular device will be optimized. Later the code being developed will be applied to compute the thermal stresses at joints and seals between any two surfaces due to thermal and pressure loads and to optimize seal shapes.

1.7 References

- 1-John Wiley and Son, Introduction to Aerospace Structural Analysis, 1985.
- 2-Siegel, Robert, Howell John R., Thermal Radiation Heat Transfer, 1981.
- 3- Einstein B. Thomas, 'Radiant Heat Transfer to Absorbing Gases in a Circular Pipe with Conduction, Gas Flow, and Internal Heat Generation, National Aeronautics and Space Administrations, Technical Report, r-156, 1963.
- 4- Perimitter, M., and Hovell, J.R., Radiant heat Transfer Throuhg a Gray Gas between Concrete Cylinders Using Monte Carlo, J. Heat Transfer Vol. 86. no 2. pp 169-179, 1964.
- 5- Grief Ralph, and Gean P. Clapper: Radiant Heat Transfer between Concentric Cylinders, Appl. Sci., Sec. A, Vol. 15, pp 469-479, 1966.

2. LABORATORY TESTING

Graduate Student: Gary Honea

The design of both the tubular and disk configurations of the electrochemical cells revealed the need for the design of high temperature seals between the ceramic cell and the metal manifolds. A modest program has been started to develop the seals. Presently seals are being developed between Haynes 214 alloy and Zirconia that can withstand upto 900 C in an oxidizing atmosphere. The choice of Haynes 214 for the manifold is due to its excellent oxidation resistance at elevated temperatures. Haynes 241 is a nickel based super alloy with chromium, iron and aluminum. It has an Young's modulus of 1.37×10^{11} Pa and a coefficient of thermal expansion of $7 \times 10^{-6} \text{ K}^{-1}$. The yttria stabilized Zirconia has a Young's modulus of 1.52×10^{11} Pa and a coefficient of thermal expansion of $20 \times 10^{-6} \text{ K}^{-1}$.

The techniques being investigated for the seals are: direct brazing, indirect brazing and adhesive cements.

2.1 Direct Brazing:

In this joining process, a filler material that has a lower melting point than the base materials melts, flows and fills the gap between the base materials. The success of the brazing depends on the ability of the filler material to wet the base materials. The wettability as given by the contact angle is dependent on the interfacial tension between the solid, liquid and vapor. The relationship is given by the well known Young's equation. The surface tension value depends on the cleanliness, porosity and surface smoothness of the base material and these values are not readily available. It was found that one had to essentially depend on the expertise of the specialists in the field to suggest from prior experience, the possible filler materials.

The initial seal was for the tube-in-tube configuration. After several considerations it was decided that some type of stress-mitigating-bellow (SMB) was needed due to the wide difference in the Coefficient of Thermal Expansion (CTE). The SMB was machined out of 316 stainless steel as shown in fig.2.1.

The vacuum brazing sequence that followed was to first braze the SMB to the Haynes with AMS 4776 filler material at 1175 C. The next braze was at the SMB to PSZ interface using a copper ABA filler material. The secondary braze did not hold on the first run, but on the second run it held pressure. Braze temperature on the second run was between 1040 and 1065 C. The choice of these braze FMs was made due to the known ability to wet the parent materials. These FMs are also available commercially. The braze will be tested in the 750-850 C range.

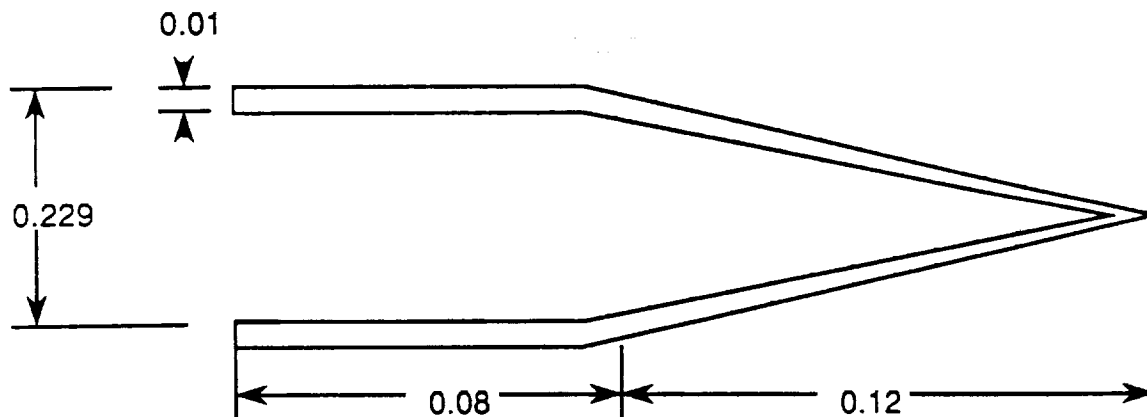


Fig. 2.1 Stress Mitigating Bellow

2.2 Adhesives

After an exhaustive search of adhesive products for high temperature applications two products were selected for testing. Aremco paste # 569 was used to form a seal between a Zirconia disk and a Haynes tube. The Haynes tubes was cleaned with acetone and the Zirconia disk roughened with a silica

abrasive prior to bonding. A thin layer of the paste was applied and allowed to cure for 24 hours at room temperature.

Based on discussions with Dr Akbar Ali at Hughes Aircraft company Sauereisen # 8 adhesive was used to obtain a seal for the disk system. The procedure for bonding is listed in the appendix. Seals were also made at the university using a layering of different adhesive (that has different CTEs). The layering was made out to Sauereisen # 360,31,29 from the Haynes tube to the Zirconia disk, in that order as shown in figure 2.2 and 2.3.

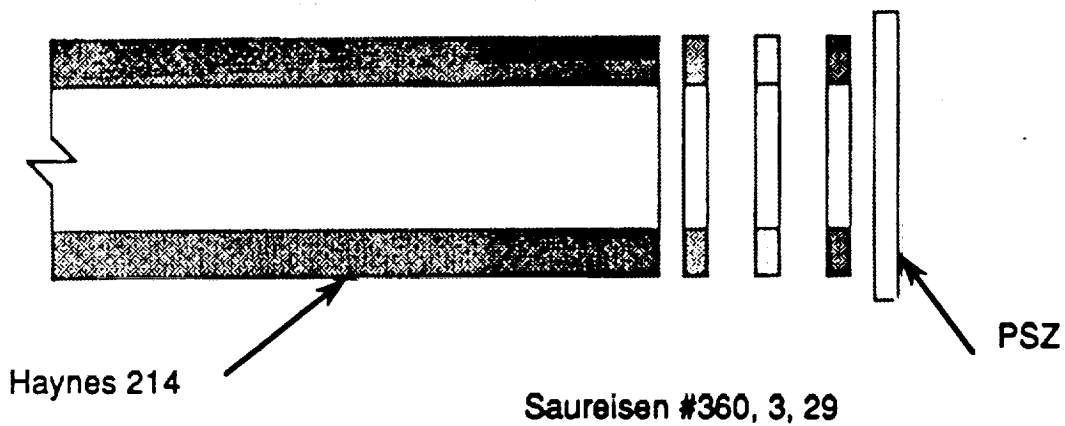


Fig. 2.2 Schematic of the adhesive seal for the disk configuration.

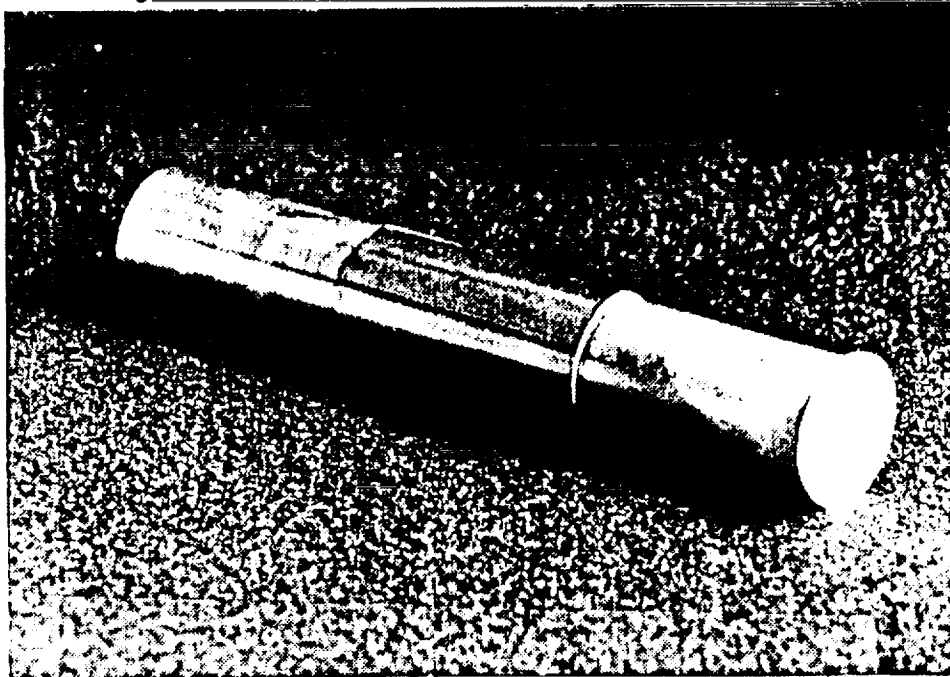


Fig. 2.3 High-temperature seal for a disk configuration.

2.3 Testing Procedure

A simplified schematic of the setup used to test the seals is shown in Figure 2.4. Oxygen gas can be filled into the test chamber at a predetermined pressure and the seal and the test chamber can be ramped to a desired temperature and maintained at that temperature. The present will permit the temperatures up to 1200 C.

A very sensitive differential pressure transducer is used to detect even minute leaks in the seal. The temperature of the test chamber is ramped at a specified rate during start up, shutdown and thermal cycling. The test setup has been constructed and has been leak tested and calibrated. The next step is to test the seals. This effort is forthcoming.

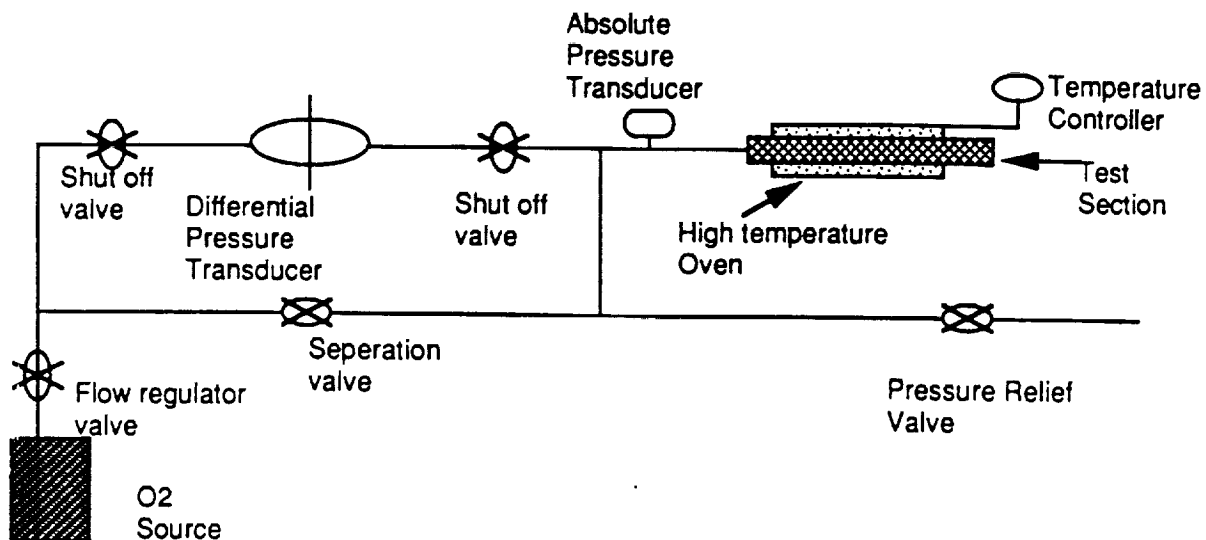


Fig. 2.4 Schematic of the apparatus for high-temperature seal testing.

2.4Appendix

SEALING PROCEDURE

These are the procedures followed in the seal preparation . They were recommended by Dr. M. Ali at Hughes Aircraft Company.

1. Vacuum degrease the Zirconia disk and the steel tube.
2. Alumina grit blast the bonding areas of the disk and the tube.
3. Ultrasonically clean both parts followed by a second vacuum degreasing.
4. Mix 5.0 grams of Sauereisen cement #8 in 0.5 grams of deionized water
5. Apply the paste to the sand blasted surfaces of the tube and the disk using a spatula.
6. Gently press the disk to squeeze out the excess paste, avoid smearing the cement paste on the steel.

7. Let the cemented parts set over night for air drying, make sure the disk is face up.
8. Oven dry the parts in air at 70 C for 72 hours in an oven.
9. Sinter the parts in an electric furnace.
10. To prevent possible damage to the steel curing at a temp of 900 C (controlling the heating/cooling rate to 3 C) will help attain the necessary bond.
- 11 The preferred sealing schedule is as follows:
 - 11.1 Room temperature to 500 C at 3 C/min.
 - 11.2 Hold for 1/2 hour at 500 C for binder to burn up.
 - 11.3 500 C to about 50 C above usage temperature hold here for 15 mins.
 - 11.4 Cool the sealed unit at 3 C/min.

Acknowledgements

The author would like to express his thanks to the following people for their suggestions and advice:

Jim Costello	Aremco,
R.S. Kirby	Los Alamos National Labs,
S. Sicar	Lockheed Engineering and Science Co.,
M. Akbar Ali	Hughes Electro-Optical Group and Data System Group,
Carl Schalansky	Vacuum Process Engineering,
Howard Mizuhara and Harry Kerr	G.T.E. Wesgo Materials Division,
Rick Yoon	I.J. Research,
Glenn Whiteside	Arizona State University (summer intern)

Special thanks are due to the Allied Signal Aerospace Company for their support under a seed project program.

RECOVERY OF PRECIOUS METALS FROM SPACE

Professor Henry Freiser, Director
Dr. S. Muralidharan, Senior Scientist
Strategic Metals Recovery Research Facility
Department of Chemistry
University of Arizona
Tucson, Arizona 85721

ABSTRACT

Our major overall objective in this project is to develop efficient and economical large scale separation and recovery methods for the metals of the platinum group and other precious metals that are suitable for use in space. Our analysis of the problem has led us to the use of multistage separation processes involving two liquid phases as the optimum direction to pursue. The relatively novel separation technique known as Centrifugal Partition Chromatography(CPC), has been selected as the most promising of the various types of chromatography, particularly from the point of view of scale up, as well as the strong scientific support provided by analogies of solvent extraction, an area of great strength in our group.

In work to date, we have focussed our efforts on finding optimal solution to problems of reagent systems affording great selectivity and sufficiently rapid kinetics to eliminate threats to separation efficiency. First, we developed a CPC procedure which served to separate Pd(II) from the rest of the platinum group metals(PGM). We used our experience here to uncover the **chemical** factors limiting selectivity and efficiency of separation because we learned that, for many metal separation systems, these outweighed the **mass transfer** factors governing most multistage separations. This study led us to an investigation of the chemical kinetics of extractable complex formation and dissociation reactions and the testing and evaluation of appropriate new systems. This past project period, we have been successful in separating Pd(II) and Pt(II) from each other and from the remaining PGM. Our current research is directed towards applying the principles we have discovered to the separation and recovery of all of the individual members of PGM and scaling up the best of the systems we find. Finally, we will address the problems of adapting our processes to conditions in space. Before the end of this project period, we expect to apply the separation and recovery schemes to the production of fractions of the individual PGM from the CO- treated residue of iron meteorite sample(s) to be made available to us by Dr. John Lewis.

INTRODUCTION

Centrifugal Partition Chromatography (CPC), a recently introduced countercurrent liquid-liquid distribution technique, has been used mainly for the separation of a broad spectrum of organic compounds, has now begun only to be applied to the separations of metal ions (1,2). We were the first to demonstrate the efficient separation by CPC of adjacent lanthanides including the separation of both light and heavy lanthanides in a single run using gradient pH elution (3). With NASA support, we were the first to achieve the separation of palladium(II) from the other PGM with CPC using a mixed complex, $\text{Pd}(\text{TOPO})_2\text{Cl}_2$ (4).

These studies revealed that, under comparable conditions, CPC efficiencies for metal ions separations were significantly lower, by a factor of 4-5, than those regularly seen for organic compounds. Another anomaly that occurs with metal ion separations is the dependence of column efficiency on the distribution ratio of a given metal species, unlike experience with organic compounds. Although not commented on in the literature, similarly low efficiencies and their dependence on the distribution ratios of the extracted metal species can also be observed in the separation of metals by derivatized solid supports.

Generally, in chromatography the column efficiency is constant for a given set of operating conditions, exhibiting no dependence on the distribution ratios of the species being separated. Possibly, because separations of metal ions by CPC involve formation and dissociation of extractable complexes using suitable ligands, chemical factors may be responsible for the differences. During the last project period we undertook systematic investigation to determine whether, and in what manner, chemical factors, in contrast to simple solvation and desolvation as well as mass transfer factors, were responsible for the differences in CPC efficiencies for metals and organic separations. CPC studies coupled with solution kinetic studies using stopped flow has allowed us to clearly establish the influence of chemical kinetics on CPC column efficiencies and correlate them to the half-lives of the chemical reaction responsible for the lowered chromatographic efficiencies.

EXPERIMENTAL SECTION

Apparatus. We have already described the CPC used in our earlier work(3,4). The Schoeffel UV-VIS detector (0.1 mL cell volume and 8 mm pathlength) was set at 238 nm and 255 nm for Pd(II) and 3-picoline experiments, respectively. Data was acquired every 10 seconds using an IBM/PC interfaced to the detector and a DASH-8 program

(Metabyte Co., USA).

A HI-TECH Scientific Stopped Flow SHU spectrophotometer was used for the kinetic study of the formation and dissociation of Pd(II) and TOPO complex. Data acquisition and treatment were accomplished with the associated Hi-Tech software. Pd(II) and TOPO as well as chloride (NaCl) were dissolved in aqueous solutions of various concentrations of surfactant (0.7-4% Triton X-100). The kinetics experiments were monitored at 420 nm.

The viscosities of heptane solutions of TOPO were measured using an Ostwald viscometer.

Reagents. Trioctylphosphine oxide, TOPO, was recrystallized from acetone (M.P. = 53-54 °C). All other reagents were of analytical grade. Metal-free heptane and water solutions were equilibrated overnight before use. Palladium stock solutions (10^{-2} M) were prepared by dissolving a weighed quantity of palladium(II) chloride (59.9% Pd, Alfa Products) in 0.10 M HCl solution. 3-Picoline (Eastman Kodak Co.) was purified by distillation before use. The stock solution of 10^{-2} M 3-picoline was prepared in water. Succinic acid buffer of pH = 6.10 (3.88×10^{-3} M succinic acid and 6.94×10^{-3} NaOH) was prepared using Perrin's method (6). Deionized-distilled water was used throughout this study.

Procedure. All CPC, kinetic and viscosity measurements were performed at 25° C. CPC experiments were conducted with 0.1-0.5 M TOPO in heptane as the stationary phase and an aqueous phase at pH 3 and appropriate chloride concentration (using NaCl) as the mobile phase, pumped in the descending mode. Equilibration of the two phases at 800 rpm resulted in 20 mL of heptane and 100 mL of water. One mL of palladium stock solution (10^{-3} M) was injected into the CPC for each run. Flow rates between 0.5 and 4.0 mL/min. were used in these experiments.

The experimental configuration for 3-picoline experiment was identical to that for palladium except that the detection wavelength was set at 255 nm. The mobile phase was adjusted to pH 6.10 using succinic acid buffer before injecting 1 mL of 10^{-3} M 3-picoline.

RESULTS AND DISCUSSION

CPC Studies. We have completely characterized the extraction equilibria of Pd(II) by TOPO by batch extraction and CPC. It was established that Pd(II) was extracted as the $\text{PdCl}_2(\text{TOPO})_2$ complex. In accordance with prediction from equilibrium considerations, the distribution ratio increased with [TOPO] and decreased with [Cr].

To characterize the separation efficiency of CPC, we define the term CETP, channel

equivalent of a theoretical plate (2400/N). The dependence of CETF on flow rates for Pd(II) and 3-picoline were compared in the heptane:water system. The peak widths are significantly greater for palladium than for 3-picoline under comparable conditions, which reveals an abnormally lower efficiency for Pd(II). Not only is the CETF for Pd is higher than that for 3-picoline, but it exhibits a far greater sensitivity to flow rate.

Chromatographic efficiency is typically limited by various types of diffusion processes which are operating for both 3-picoline and Pd(II). Simple diffusion alone can not account for the significantly lower efficiency for Pd(II), however, even when the effect of TOPO on increasing the viscosity, η , of heptane solution is taken into account. The CETF values of 3-picoline at the viscosities of TOPO solutions in heptane were calculated from the CETF value in pure heptane assuming a linear relationship between CETF and $\eta^{0.5}$, given the narrow range of viscosities, as indicated by Knox equation (7). As seen from Table I, the viscosity of TOPO solution in heptane and the CETF values for 3-picoline and Pd(II) increase with the concentration of TOPO. The CETF values for Pd remain distinctly higher indicating that viscosity alone does not account for the increase in CETF for Pd with increasing TOPO concentration. It is also evident from this table that the CETF values for Pd(II) are dependent on its distribution ratio. The CETF values are larger at higher distribution ratios indicating poorer column efficiencies at higher D values. The additional peak broadening in the case of Pd(II) compared to 3-picoline under identical conditions and at the higher distribution ratios of Pd(II) must arise from chemical kinetic factors. Approximately 50% of the 3-picoline molecules are protonated at pH = 6.1 ($pK_a = 6$) at which its CPC chromatograms were obtained. The deprotonation reaction will not cause CPC band broadening in the case of 3-picoline as it is very rapid and indeed is termed diffusion controlled. In the manner of the Van Deemter and Knox equations in which the reduced plate height is seen as a sum of contributions from various factors we can express the observed CETF for Pd ($CETP_{obs}$) as a sum of contributions from diffusion ($CETP_{dif}$) and chemical kinetics ($CETP_{ck}$):

$$CETP_{obs} = CETP_{dif} + CETP_{ck} \quad (1)$$

We can isolate the contribution due to the chemical kinetics to the observed CETF for Pd(II) by subtracting the CETF values for 3-picoline at the appropriate TOPO

concentrations. We shall show that the $CETP_{ck}$ is related to the half-life for the kinetics of back extraction of the $PdCl_2(TOPO)_2$ complex.

A further examination of the involvement of chemical kinetic factors in the CPC efficiency for Pd(II) was obtained by studying the dependence of CETP on the concentration of chloride in the aqueous phase and the concentration of TOPO in the heptane stationary phase. It is evident from equation 2 that the distribution ratio of Pd(II) should depend on the chloride and TOPO concentrations, with D being directly proportional to $[TOPO]^2$ and inversely proportional to $[Cr]^2$. It is not obvious, however, that CETP should depend on these concentrations as well. It was found that increasing $[Cr]$ and decreasing $[TOPO]$ provided better CPC efficiencies for Pd(II) (Figures 3 and 4). As may be seen, CETP is directly proportional to $[TOPO]$ and inversely proportional to $[Cr]$. These observations are consistent with the hypothesis that the kinetics of the back extraction reaction, equation 2, is the major factor in affecting the CPC efficiency for Pd(II).



Study of the Back Extraction of $PdCl_2(TOPO)_2$ Complex using Stopped Flow.

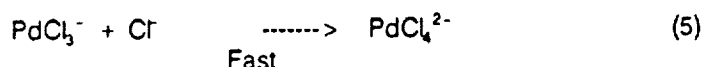
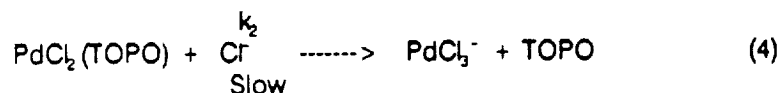
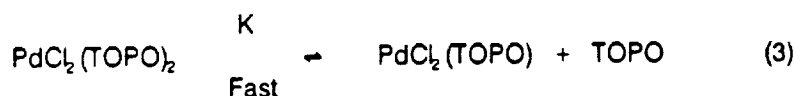
Since the CPC results indicated the involvement of slow chemical kinetics, a systematic study of the kinetics of the process of extraction and back extraction of Pd(II) seemed in order. We learned from preliminary experiments of extraction and back extraction of Pd(II) by TOPO in heptane-water system using the microporous teflon phase separator (MTPS)(11), that these kinetics were too fast to be measured by this system which can measure half-lives 5 s and longer.

Stopped Flow Kinetic Studies. In order to understand the influence of the kinetics of formation and dissociation of $PdCl_2(TOPO)_2$ on CETP, we resorted to stopped-flow and examined the kinetics in the presence of micelles, which we have demonstrated earlier, provide excellent models for extraction systems (12). The micellar system containing up to 4% Triton X-100, a neutral surfactant, to solubilize TOPO was chosen to compare the formation and dissociation rates of $PdCl_2(TOPO)_2$. The formation of $PdCl_2(TOPO)_2$ under a variety of conditions was too fast even for the stopped flow apparatus (limit of $t_{1/2} = 0.4$ ms). The dissociation kinetics of $PdCl_2(TOPO)_2$ could be followed by stopped flow.

The $PdCl_2(TOPO)_2$ complex was formed in the Triton X-100 system using 10^{-3} M Pd(II).

The dissociation of this complex under pseudo first order conditions in $[Cr]$, was monitored as a function of $[Triton\ X-100]$, $[Cr]$ and $[TOPO]$. The observed pseudo first order rate constant was independent of the Triton X-100 concentration (Table II), indicating that the dissociation of $PdCl_2(TOPO)_2$ occurred essentially in the bulk aqueous phase. This also indicated that no appreciable dissociation occurred in the micellar phase and that mass transfer of $PdCl_2(TOPO)_2$ between the bulk aqueous and the bulk micellar phases was rapid.

The value of k_{obs} increased with increasing $[Cr]$ at constant $[TOPO]$ and decreased with increasing $[TOPO]$ at constant $[Cr]$. These observations can be rationalized based on the mechanism in equations (3)-(5) for the decomposition of $PdCl_2(TOPO)_2$.



The rapid preequilibrium step, equation 3 and the rate limiting step, equation 4, yield the following expression, equation 6, for k_{obs} under pseudo first order condition in $[Cr]$.

$$k_{obs} = \frac{k_2 K}{K + [TOPO]} [Cr] \quad (6)$$

Equation 6 can be rewritten as:

$$\frac{[Cr]}{k_{obs}} = \frac{1}{k_2} + \frac{1}{Kk_2} [TOPO] \quad (7)$$

The plot of $[Cr]/k_{obs}$ as a function of $[TOPO]$ yielded a straight line. The k_2 and K values derived from the intercept and slope of this plot are $168 \pm 8\ M^{-1}s^{-1}$ and $0.004 \pm 0.0002\ M$, respectively. Equation 6 indicates two limiting cases, $K \gg [TOPO]$ and $K \ll [TOPO]$ (Equations 8 and 9). Equation 8 is encountered in stopped flow experiments at $10^{-4}\ M$ TOPO where k_{obs} is linear in $[Cr]$, Table II.

$$k_{obs} = k_2 [Cr] \quad (8)$$

These observed rate constants yield a k_2 value of $158 \pm 4\ M^{-1}s^{-1}$ which is in excellent

agreement with the value from equation 7.

$$k_{bs} = \frac{k_2 K}{[TOPO]} [Cr] \quad (9)$$

Equation 9 indicates that $t_{1/2} \propto [TOPO]/[Cr]$ ($t_{1/2} = \ln 2/k_{bs}$). It is evident from Table I and Figures 3 and 4 that CETP has a similar relationship to $[TOPO]$ and $[Cr]$.

Plotting the difference in the CETP for Pd and 3-picoline to eliminate the contribution from viscosity changes (equation 1), at constant $[Cr]$ as a function of $t_{1/2}$ yielded a straight line with slope 6.4 ± 0.2 . A similar plot at constant $[TOPO]$ yielded a straight line with slope 5.9 ± 0.3 . The CETP determined chromatographically, is thus a measure of the half-life for the kinetics of back extraction of $PdCl_2(TOPO)_2$. It is also evident that the dependence of CETP on $[TOPO]$ and $[Cr]$ is different from the dependence of the D value of Pd(II) on these concentrations (equation 2). Interestingly, we find that CETP is directly proportional to $D^{0.5}$, Table I. Such a relation is not obvious from the basic chromatographic equations used to calculate the D value from retention volume and the efficiency from the retention volume and the peak width. The relationship between CETP and $t_{1/2}$ and CETP and D have become evident through the independent elucidation of the mechanism of the kinetics of back extraction of $PdCl_2(TOPO)_2$ using the stopped flow technique.

This analysis of chromatographic efficiency in separations involving the distribution of metal complexes clearly reveals the influence of the kinetics of complex formation and dissociation on the chromatographic efficiencies and affords a semi-quantitative description of the relevant kinetic parameters.

CONCLUSIONS

The differences in the CETP values for the Pd(II) and 3-picoline systems at a given flow rate can be explained by the slow kinetics of back extraction of the $PdCl_2(TOPO)_2$ complex. The CETP for the Pd(II) system is directly proportional to the half-life, $t_{1/2}$, for the kinetics of back extraction of the $PdCl_2(TOPO)_2$ complex. Hence, the band broadening in the Pd(II) system arises from the slow kinetics of dissociation of the extracted Pd complex. Thus CPC provides not only provides useful clues as to the chemical kinetics of extraction and back extraction but also clarifies the correlation of column efficiencies with independently measured chemical kinetic parameters. Further, the kinetic information obtained from the correlation of column efficiencies with distribution ratios, as demonstrated here, can be

used to improve the CPC efficiency.

The customary screening of extraction reactions involving single-stage equilibrations serve not only to determine D values, but to enable one to discard reactions which are too slow to be chromatographically useful. Even when these experiments indicate that extraction reactions are too fast to be measured by ordinary means, the sensitivity of CPC and related chromatographic techniques to reaction rates are dramatically greater. Slow reactions that have half lives of even c.a. 1 s will begin to adversely affect the observed column efficiency. Conversely, observation of efficiencies lower than otherwise expected, provides a qualitative index of slow reaction kinetics. Although our study is focused on extraction reactions involving metal complexation, these will apply to any process in which the transferring species is formed (and dissociated) by slow kinetics.

Work Currently Under Way. On the basis of principles revealed in our work, we are now designing procedures in which increased separation efficiencies should enable us to deal effectively with the other members of the PGM. Preliminary experiments have been carried which look very promising. We hope to be able to provide a demonstration of the efficacy of our methodology by separating and recovering quantitatively all the individual PGM contained in an iron meteorite sample following carbon monoxide treatment to remove iron and nickel.

LITERATURE CITED

- (1) Araki, T.; Okazawa, Y.; Asai, H.; Ando, J. *J. Liq. Chromatogr.* **1988**, *11*, 2487-2506.
- (2) Akiba, K.; Swai, S.; Nakamura, S.; Murayama, W. *J. Liq. Chromatogr.* **1988**, *11*, 2517-2536.
- (3) Muralidharan, S.; Cal, R.; Freiser, H. *J. Liq. Chromatogr.* **1990**, *13*, 3651-3672.
- (4) Surakitbanharn, Y.; Muralidharan, S.; Freiser, H. *Solv. Extr. Ion Exch.* **1991**, *9*, 45-59.
- (5) Braun, T.; Ghersini, G. *Extraction Chromatography*, Elsevier: New York, 1975.
- (6) Perrin, D.D. *Australian J. Chem.* **1963**, *16*, 572-578.
- (7) Knox, J.H. *J. Chromatogr. Sci.* **1980**, *18*, 453.
- (8) Watarai, H.; Cunningham, L.; Freiser, H. *Anal. Chem.* **1982**, *54*, 2390-2392.
- (9) Muralidharan, S.; Yu, W.; Tagashira, S.; Freiser, H. *Langmuir* **1990**, *6*, 1190-1196.
- (10) Y. Surakitbanharn, S. Muralidharan^{*} and H. Freiser, *Anal. Chem.* **1991**, in press.

Table I. CETP and D values for 3-picoline and Pd(II) at different TOPO and chloride concentrations at a flow rate of 2.00 mL/min.

[TOPO],M	η ,cp	3-Picoline			Pd(II)		
		CETP	D	[Cr]	CETP	$t_{1/2}$,s	D
0.0	0.386	3.2	0.9	-	-	-	-
0.2	0.485	3.6	-	0.1	10	2.2	0.4
0.3	0.556	3.9	-	0.1	17	3.3	0.9
0.4	0.643	4.2	-	0.1	25	4.4	1.4
0.5	0.738	4.4	-	0.1	33	5.5	2.8
0.5	0.738	4.4	-	0.05	68	11.0	8.3
0.5	0.738	4.4	-	0.20	13	2.7	0.6
0.5	0.738	4.4	-	0.30	11	1.1	0.4

Table II. Variation of k_{obs} with Triton X-100, Chloride and TOPO concentrations.

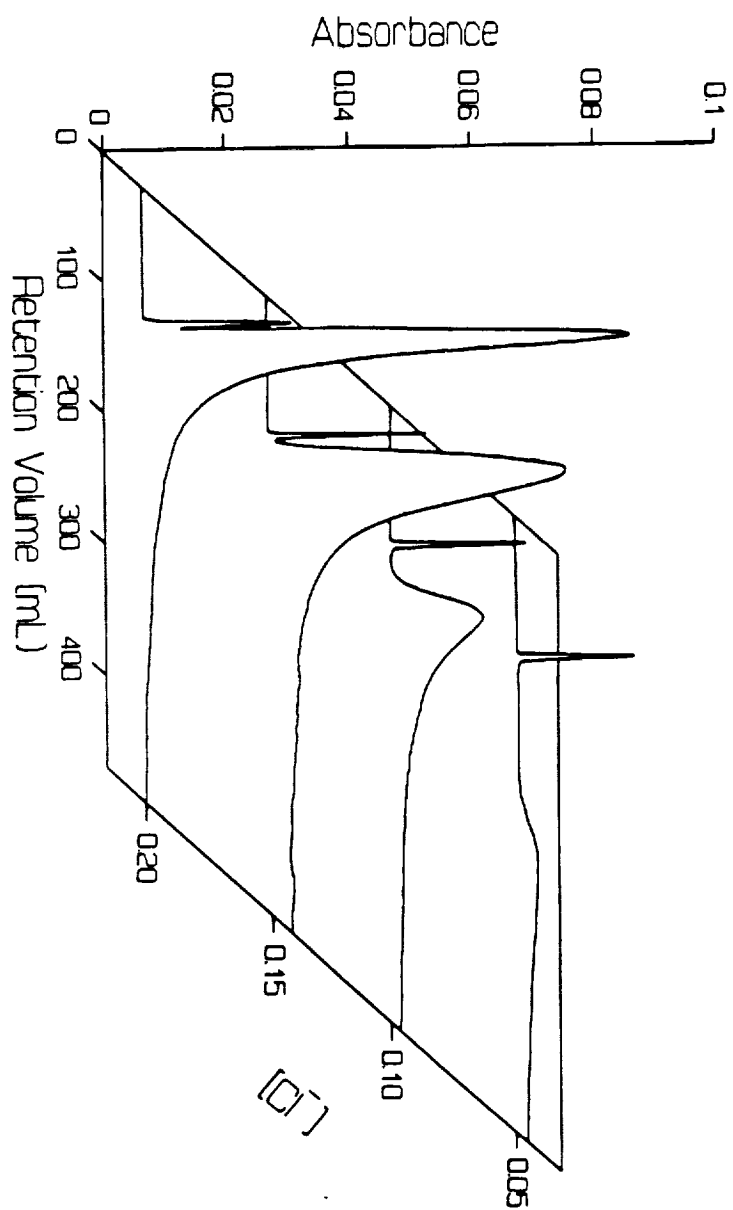
[Triton X-100],M	[Cr],M	[TOPO] $\times 10^4$,M	k_{obs} ,s ⁻¹
0.011	0.1	1	15.99
0.016	0.1	1	17.05
0.032	0.1	1	17.97
0.064	0.1	1	16.49
0.016	0.05	1	7.90
0.016	0.2	1	32.18
0.016	0.3	1	46.59
0.016	0.4	1	61.36
0.016	0.5	1	80.64
0.016	0.6	1	96.54
0.016	0.5	5	75.00
0.016	0.5	10	66.72
0.016	0.5	20	56.50
0.016	0.5	30	47.52

FIGURE CAPTIONS

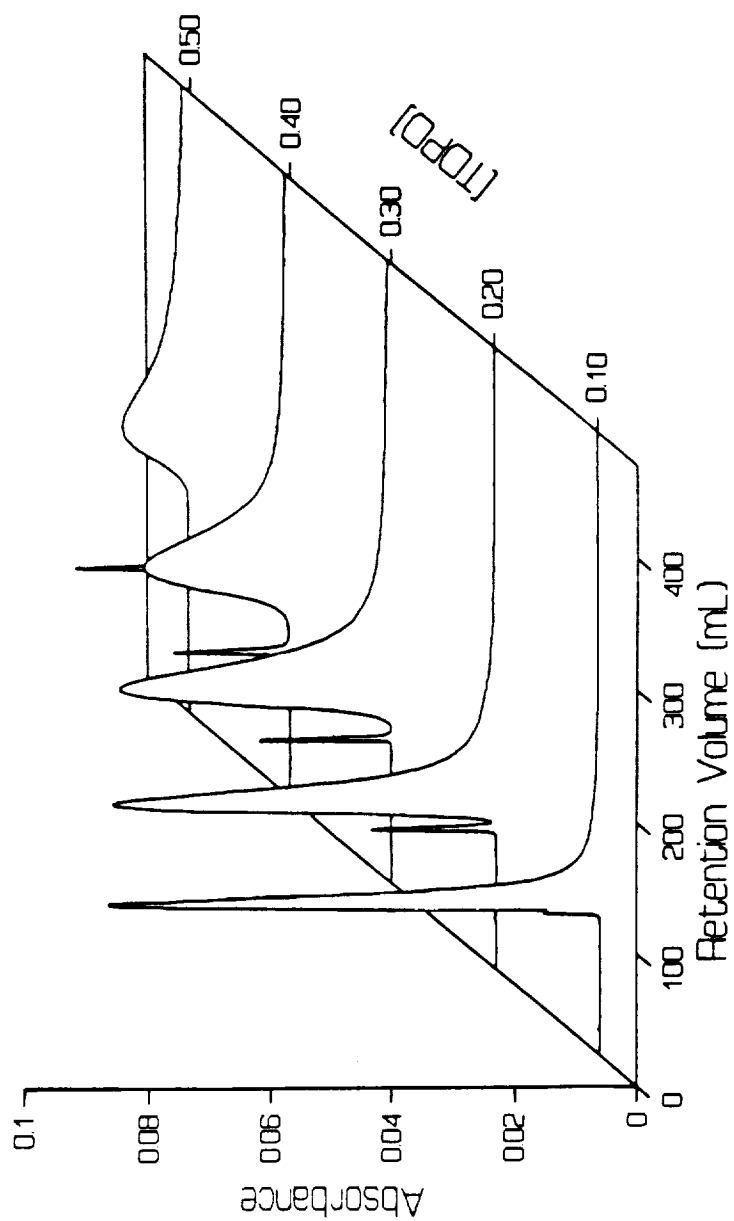
Figure 1. The CPC chromatograms for Pd (10^{-3} M) at 0.5 M TOPO and $[Cl^-] = 0.05-0.2$ M.

Figure 2. The CPC chromatograms for Pd (10^{-3} M) at 0.05 M chloride and $[TOPO] = 0.1-0.5$ M

**EFFECT OF $[Cl^-]$ ON RETENTION VOLUME AND
EFFICIENCY (CETP) OF Pd(II) SEPARATION**



**EFFECT OF [TOPO] ON RETENTION VOLUME AND
EFFICIENCY (CETP) OF Pd(II) SEPARATION**



1

2

3

4

5

6

7

8

9

10

11

12

13

14

15

16

17

18

19

20

DEVELOPMENT AND MECHANICAL PROPERTIES OF STRUCTURAL MATERIALS FROM LUNAR SIMULANT

Chandra S. Desai

**Department of Civil Engineering and Engineering Mechanics
The University of Arizona**

Abstract

Development of versatile engineering materials from locally available materials in space is an important step toward establishment of outposts such as on the Moon and Mars. Here development of the technologies for manufacture of structural and construction materials on the Moon, utilizing local lunar soil (regolith), without the use of water, is an important element for habitats and explorations in space. It is also vital that the mechanical behavior such as strength and flexural properties, fracture toughness, ductility, tensile properties, and deformation characteristics are defined toward establishment of the ranges of engineering applications of the materials developed.

The objectives here include two areas: (1) thermal "liquefaction" of lunar simulant with different additives (fibers, powders, sulphur, iron, pyrite, etc.) and (2) development and use of a new triaxial test device in which lunar simulants are first compacted under cycles of loading, and then tested with different vacuums and initial confining or insitu stress. The second area has been described in previous progress reports and publications^{1,5,6}; since the presently available device allows vacuum levels up to only 10^{-4} torr, it is recommended that newly acquired (by SERC Center) vacuum pump that can allow higher levels of vacuum be utilized.

DEVELOPMENT AND MECHANICAL PROPERTIES OF STRUCTURAL MATERIALS FROM LUNAR SIMULANT

Chandra S. Desai

**Department of Civil Engineering and Engineering Mechanics
The University of Arizona**

Introduction and Results to Date

The development of new construction materials through liquefaction of lunar simulants with various admixtures, and determination of mechanical properties using various laboratory testing devices to perform bending, cylindrical triaxial, and three-dimensional multiaxial tests are the main objectives in this progress report.

The lunar simulant used, called Arizona Lunar Simulant, has been developed locally from a basaltic rock found near Hanford, WA. This material has a mineralogical composition similar to that of the lunar mare soil. The rock is ground so that its grain size distribution falls well within that of the distribution envelopes for the samples of the lunar regolith brought to earth by Apollo missions, Fig. 1.

In order to achieve various engineering properties such as flexure, compressive, tensile and fracture strengths, deformation characteristics, and ductility, the lunar simulant is combined with various powders and fibers. These include steel, stainless steel, aluminum, and fiberglass. The simulant itself, and with various percentages of powders or fibers, is liquefied in a furnace with a temperature capacity of 1700°C. The material is placed and compacted in molds made of graphite and titanium so that appropriately sized specimens for various tests can be obtained (see Table 1). Diagrams of three types of samples with loading conditions are shown in Figure 2.

Table 1. Various specimens

SHAPE	SIZE	TEST	STATUS
Rectangular	1.0 x 2.5 x 25 cm	Bending	Current
Cylindrical	5.5 cm diam. x 15 cm ht.	Triaxial	Future
Cubical	10 cm x 10 cm x 10 cm	Multiaxial	Future
Plate	7 cm x 100 cm x 1 cm	Tensile	Future

In the thermal liquefaction, the simulant melts at about 1100°C and forms a matrix that can be made into various specimen sizes and shapes. The resulting intermediate ceramic, formed solely by the simulant, is relatively brittle. With addition of a powder or fiber, the liquefaction may involve melting of the admixture at a lower or higher temperature than that for the soil simulant. Thus the powder/fiber melts before the heated soil particles or vice versa, resulting in a "ceramic composite". Such composites can possess a wide range of the aforementioned mechanical properties.

An objective of the research is to perform a parametric study in which the ratio of simulant to powder/fiber is varied, together with different levels of temperature and cycles of temperature, the latter is expected to add "prestressing" due to residual expansion of the powder/fiber. It has been noted that such powders and fibers can be manufactured from the lunar regolith. Table 2 shows details of samples tested.

Table 2. Beam samples prepared to date

1. Lunar Simulant Only			
<u>Sample</u>	<u>p.gm/cc</u>		
1 -	2.43		
2 -	2.44		
2. <u>Fibers</u>	<u>% By Weight</u>	<u>% Volume</u>	<u>Matrix p. gm/cc</u>
Steel	15.0	4.65	2.17
Steel	30.0	10.95	2.26
Stainless	7.5	2.32	2.39
Stainless	15.0	4.54	2.20
AL	7.5	7.27	2.61
AL	15.0	--	--
AL shavs	10.0	--	--

- 20 samples have been made so far.
- Each of these is cut into 1-3 beams for testing.
- All batches were heated at the same cycle. Heat of 1100C was held for 1 hour, then cooled over an eight hour period.
- AL = Aluminum

Specimens of the material combinations thus developed will be tested for bending, fracture, ductility, and stress-strain-strength properties using laboratory testing methods as described previously. This is a vital step toward potential engineering applications of the materials developed, because based on the parameters and constants determined, the ranges and type of application of the materials developed for space construction can be established.

The current research so far has included: 1. Acquisition of the furnace, 2. development of a beam bending device as per the ASTM standard, 3. production of a number of beam specimens with varying admixture content (Table 2), and 4. testing of a number of beam and compression specimens for their load-displacement and stress-strain-strength behavior. Typical test results for bending and compression tests are shown in Figures 3 and 4. It can be seen that the load-carrying capacity, stress-strain-strength response and ductility are influenced by different additives.

Figure 3 shows the load vs. displacement curves for beam specimens with no fiber, with 7.5% Al, and with 15% stainless steel. As can be seen from these curves, the addition of aluminum fibers significantly increased the ultimate strength; and the addition of stainless steel fibers increased both the ultimate strength as well as the deflection at failure. Figure 4 shows the stress-strain curve for a typical compression test. The specimen had 15% by weight carbon steel fibers.

Development of cylindrical and multiaxial specimens and specimens for tension testing will be the subjects of future research. The multiaxial specimens will be tested in unique three-dimensional devices (Figure 5) that allow application of three independent principal stresses, different paths of loading, and static and cyclic loading. Future work will also involve use of the Arizona simulant and the simulant developed at the University of Minnesota to include determination of the effect of agglutinates in this type of research. Agglutinate is a small glass-welded aggregate of rock, mineral, and glass fragments formed during micrometeorite impacts into the regolith. Also considered will be acquisition and use of a pump with higher vacuum levels and testing of specimens under higher levels of vacuum, about 10^{-12} torr. This will also be used to continue the study using the new vacuum triaxial device.

Initial results have been obtained through liquefaction of the simulant with sulphur and iron; here the liquefaction temperatures range from about 200 to 500°F. The percentage of sulphur is intended to be as low as possible as it is not readily available on the moon. However, it is felt that an optimum combination of iron and sulphur can be found that will lead to viable structural materials with the use of relatively low temperatures. In the subsequent research, this approach will be continued in which the specimens of 'concrete' with iron and sulphur will be

tested, results compared with those obtained with fibers, and the range of application of the resulting materials will be studied based on their mechanical properties.

The final objective of the research is to develop a methodology by which structural materials can be produced on the Moon using locally available and derived (fibers, powders, iron, sulphur, etc.) materials, formed into useful shapes by thermal solar energy and compaction. In addition to the development of materials, attention must be given to the determination of the mechanical properties necessary for structural design so that the material can be used in a wide range of engineering applications such as roads, foundations, blocks, walls, floors, buildings, support systems, and shields. The research results are expected to represent a significant contribution towards construction of facilities on the Moon.

References

1. C.S. Desai, K. Girdner, H. Saadatmanesh, and T. Allen, "Mechanical Properties of Structural Materials from Lunar Simulants," Proc. Conf. on Resources of Near-Earth Space, Univ. of Arizona, 7-11 January, 1991.
2. K. Girdner, "Development and Mechanical Properties of Construction Materials from Lunar Simulants," The SERC Newsletter, Vol. 2, No. 1, Dec. 1990.
3. K. Girdner and C.S. Desai, "Development and Mechanical Properties of Structural Materials from Lunar Simulants by Thermal Liquefaction," Report to NASA SERC Center, Tucson, AZ, 1991.
4. C.S. Desai, K. Girdner, and G. Frantziskonis, "Development of Construction Materials Like Concrete from Lunar Soil Without Water," Annual Progress Report, NASA Space Eng. Res. Ctr., Univ. of Arizona, 1988-89, pp. 11-14.
5. C.S. Desai, H. Saadatmanesh and T. Allen, "Effect of Vacuum on Density and Stress-Strain-Strength Behavior of Compacted Lunar Soil Simulant," Report to NASA Space Eng. Res. Ctr., CEEM Department, 1990.
6. C.S. Desai, H. Saadatmanesh and T. Allen, "Behavior of Compacted Lunar Simulants Using New Vacuum Triaxial Device," J. Aerospace Eng. Div., American Society of Civil Engineers, under publication, 1991.

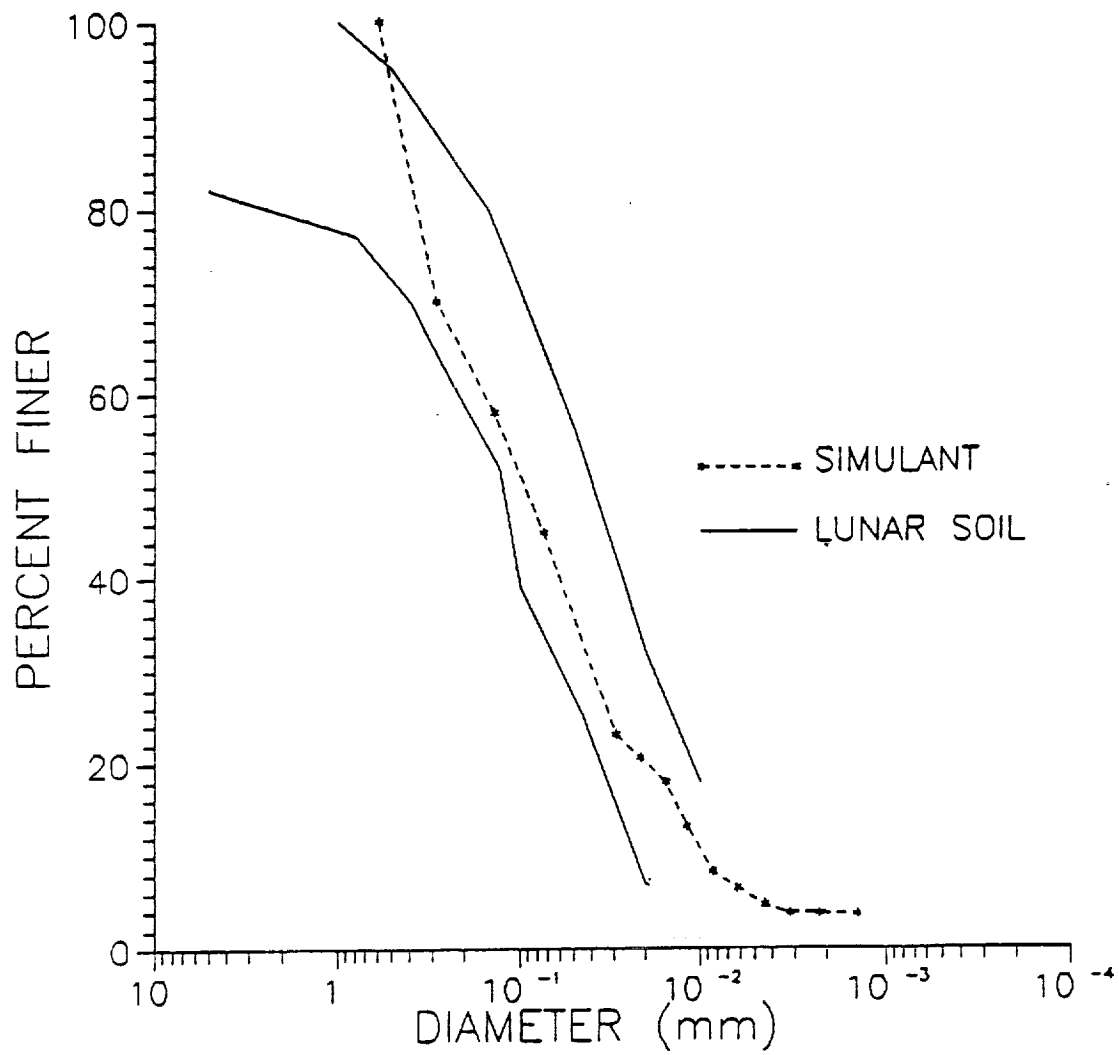
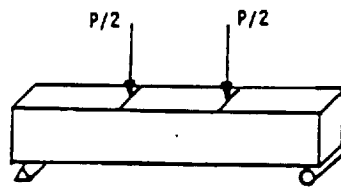
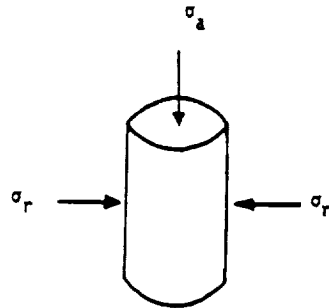


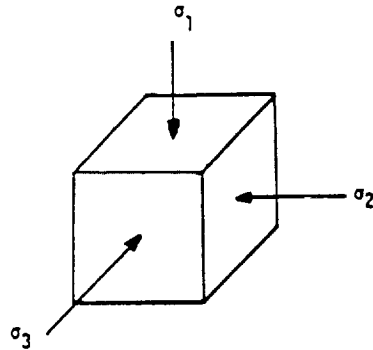
Figure 1. Grain size distribution of actual lunar soil and simulant



a) Beam bending.



b) Cylindrical triaxial.



c) Multiaxial.

Figure 2. Specimens for bending, cylindrical, and cubical tests

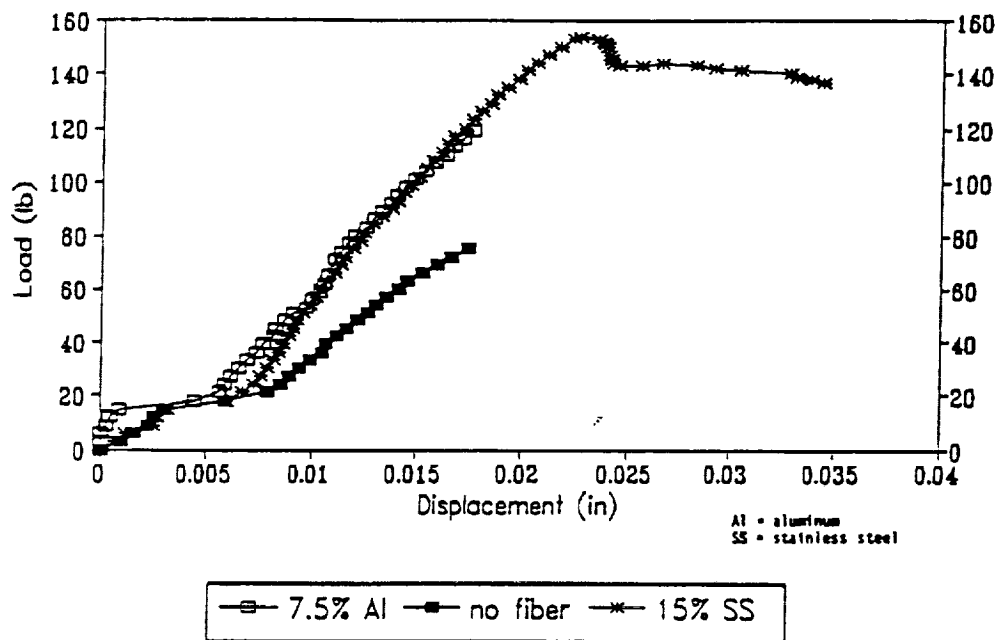
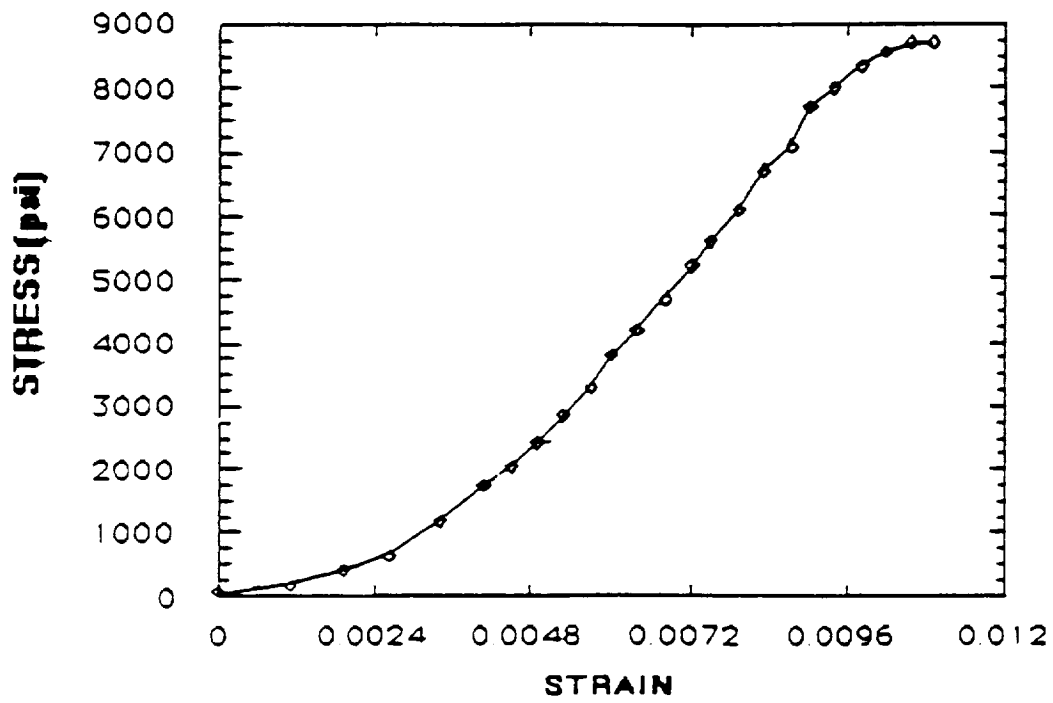


Figure 3. Load-displacement curves for typical simulant-fiber beams



1 psi = 6.895 kPa

Figure 4. Stress-Strain Curve for Compression Test

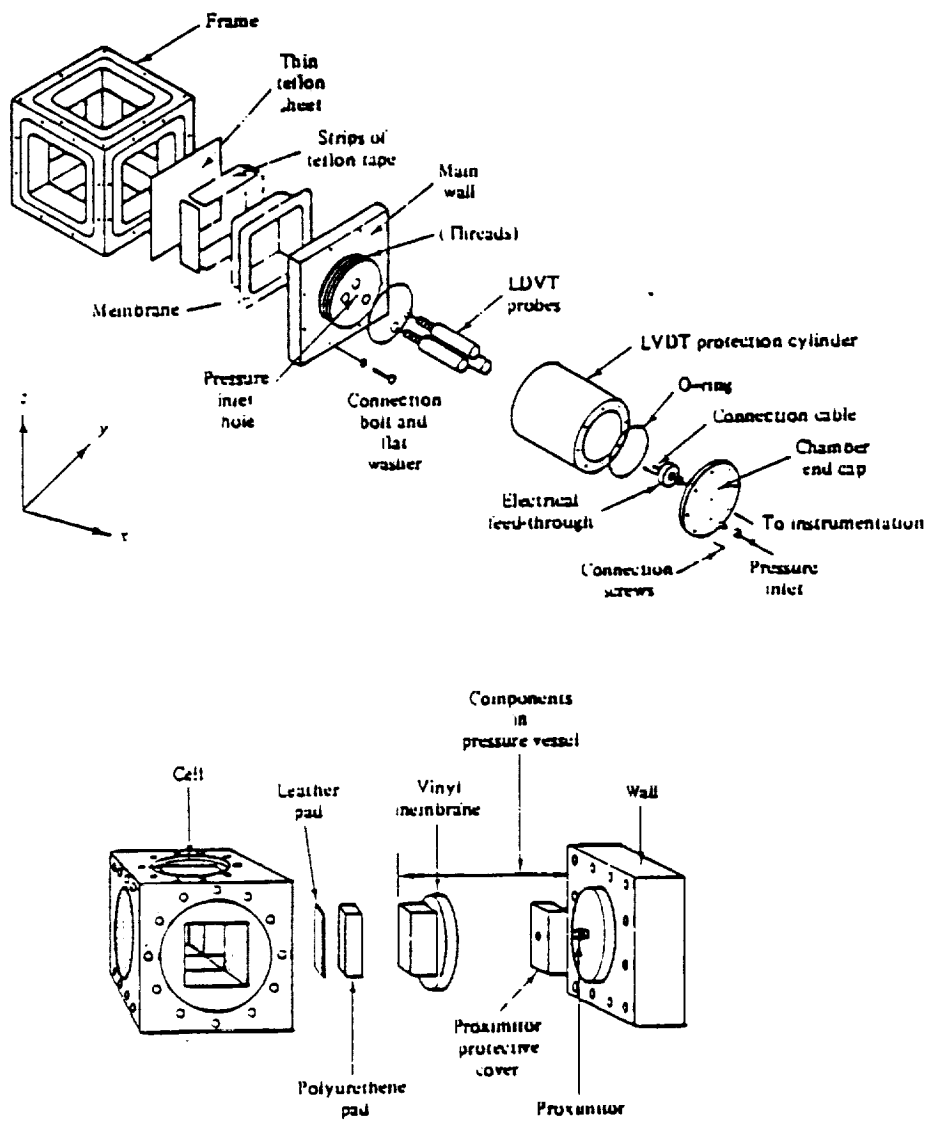


Figure 5. Multi-axial test devices

Large Area Solar Cells from Lunar Materials

Paul Calvert, Brian Fabes, Jonas Hodges and Jean Corley

Arizona Materials Laboratories

University of Arizona

ABSTRACT

Large area solar cells need a flexible and strong substrate and cover. The obvious choices for this role are polymer films such as polyester. Organic polymers cannot be made from lunar materials because of the absence of carbon and hydrogen. This project explores non-carbon polymers which might be suitable for this and other lunar applications. Few such polymers are currently known because of sensitivity to oxidation and hydrolysis. Such degradation reactions will be much less significant on the moon. Siloxane polymers have been selected for synthesis. A novel chlorosiloxane polymer has been prepared and partly characterized.

Aims

The overall goal of this research is to develop materials for the construction of large area photovoltaic cells from lunar materials. While a major focus of solar photovoltaic research has been on the semiconductor layers, many of the real problems associated with the application of cells have been more mundane. It has proved to be difficult to make large cells rugged enough to withstand long periods in the open without using grossly large and expensive packing.

Environmental stresses on solar cells include wind and hail, animal attack on insulation, degradation of polymer insulation and potting compounds due to high temperatures and intense exposure to solar UV, thermal cycling and insulation breakdown under the high DC voltages of series-connected cells. For these reasons large lightweight solar panels are not yet feasible on earth and robust installations are too expensive for any but remote or exotic locales where normal power sources are not feasible.

Clearly the lunar environment offers a set of new constraints but many of the standard problems are absent. We are assuming for the time being that our solar cells would be constructed from amorphous silicon deposited onto a flexible substrate. We are likewise assuming that conductors will be lunar-derived aluminum. Other people have given careful consideration to these aspects of lunar manufacture of solar cells [1,2].

We have focussed on the substrate material. Flexible substrates for experimental solar cells have included polyester (polyethyleneterephthalate such as DuPont Mylar) and polyimide (e.g. Kapton). The moon, unfortunately, has almost no carbon and little hydrogen both of which are essential to almost all synthetic polymers. This then raises the question of whether it is possible to make a family of polymers without C and H. Ideally these would have a range of properties from rubbery through hard plastic allowing one to make gaskets, insulation and moldings as well as substrates. Even before Columbus brought rubber to Europe, society was very dependent on polymers in the form of textiles, wood and leather. It is difficult to envisage a settlement without many forms of polymer.

Non-carbon polymers

There are three significant families of polymers with non-carbon backbones that retain the qualities of flexibility that we associate with polymers. These are the silanes, siloxanes (or silicones) and the phosphonitriles.

The phosphonitriles have a $\text{-PR}_2\text{=N-}$ structure where there are many choices for the R side group. They were developed by Allcock at the University of Pennsylvania [3] and a number

of companies, currently the Ethyl Corp., have attempted to commercialize them. The two well known non-carbon polymers have either $R=F$ or $R=Cl$. The chloride is quite reactive and can be used as a starting point for conversion to other polymers.

The silanes ($-SiR_2-SiR_2-$) are much studied at the moment as potential photolithographic materials, as precursors to silicon carbide and as non-linear optical materials. A variety of polymers with different R side groups have been made but R is invariably a hydrocarbon. Nonetheless, it is not clear that other side groups could not be used. The Si-Si bond does have considerable π character from overlap of the nominally empty d-orbitals. This results in strong UV absorption and optical sensitivity which is good for lithography but may be a problem for our purposes. A number of polysilazanes ($-SiR_2-NH-$) have been made and may find use as ceramic precursors.

The siloxanes ($-SiR_2-O-$) are well known as silicone rubber where $R=CH_3$. There is a number of other commercial materials with other hydrocarbon side groups. One experimental polymer is available with a hydrogen side group ($-Si(CH_3)H-O-$) for use as a hydrogenation reagent.

This probably exhausts the possible structures of flexible non-carbon polymers for terrestrial use. Essentially there are none. The qualification "flexible" is necessary as there are many inorganic linear chain structures such as silicates, phosphates, sulfur and selenium where the interchain bonding is strong enough to make the material effectively 3-dimensional and glass-like.

Siloxane polymers

Exterior lunar applications do open new possibilities because flammability and hydrolytic instability should not be major concerns in the absence of water or oxygen. With this in mind we have set out to investigate possible tough, flexible non-carbon polymers. We selected the siloxane backbone as the most promising from the point of view of ease of synthesis and availability of starting materials. The moon is short of univalent elements needed to form side groups on the chains. The obvious choice, in light of this, is to use hydrogen since its low mass makes it relatively cheap to transport from earth. A 1 km^2 by 100 micron substrate of the (hypothetical) polymer ($-SiH_2-O-$) would contain about 100 kilos of hydrogen. If the whole substrate was made from polyethylene it would weigh about 1000 kilos.

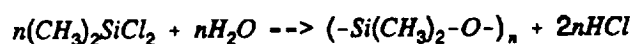
This polydihydrosiloxane should be preparable by hydrolysis of silicon dichloride, SiH_2Cl_2 , which is quite flammable. Hence we have decided to work towards this by easy, and safer, stages. The following sections describe the preparation of polydimethylsiloxane, a routine

polymerization and then extension of this to polydichlorosiloxane. Polydichlorosiloxane has not, to our knowledge, been described before. It is a carbon-free polymer and it will be most interesting to examine the properties of this new material as we characterize it.

We would expect these siloxane polymers to be rubbery. The siloxane backbone is known to rotate freely. As shown by the model in figure 1, there is very little steric hindrance between the chlorine side groups.

Preparation of polydimethylsiloxane

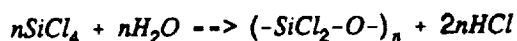
This reaction has been frequently studied [4] and was done here to build expertise. The polymerization reaction is:



The silane (0.3 mole) was mixed with dichloromethane (100 ml) and pyridine (0.6 mole), to take up the HCl, and excess water (0.6 mole) was added slowly with vigorous stirring. Reaction occurs immediately. A white solid (pyridinium hydrochloride) forms. The product was washed with water to remove the hydrochloride. The dichloromethane layer was separated and allowed to dry then heated in a vacuum oven. A polymer of honey-like viscosity resulted. The infra-red spectrum agrees with polydimethylsiloxane.

Preparation of polydichlorosiloxane

The method here is similar but only enough water to hydrolyse half the Si-Cl bonds in silicon tetrachloride must be added.



Silicon tetrachloride (0.5 mole) was added to 400 ml of cold dichloromethane. Water (0.5 mole) is slowly added while dry nitrogen was bubbled through the flask to remove the HCl. After 4 hours some white powder, probably silica, formed on the flask. The solution was allowed to evaporate to give a viscous brown liquid.

Infra-red analysis looks promising for the product to be a siloxane polymer and studies are continuing. On exposure to air the product fumed as would be expected for a chlorosiloxane.

Future Work

The identification of polydichlorosiloxane is still provisional. We have found no record of the previous preparation of this material. Preparation conditions must be varied to get high

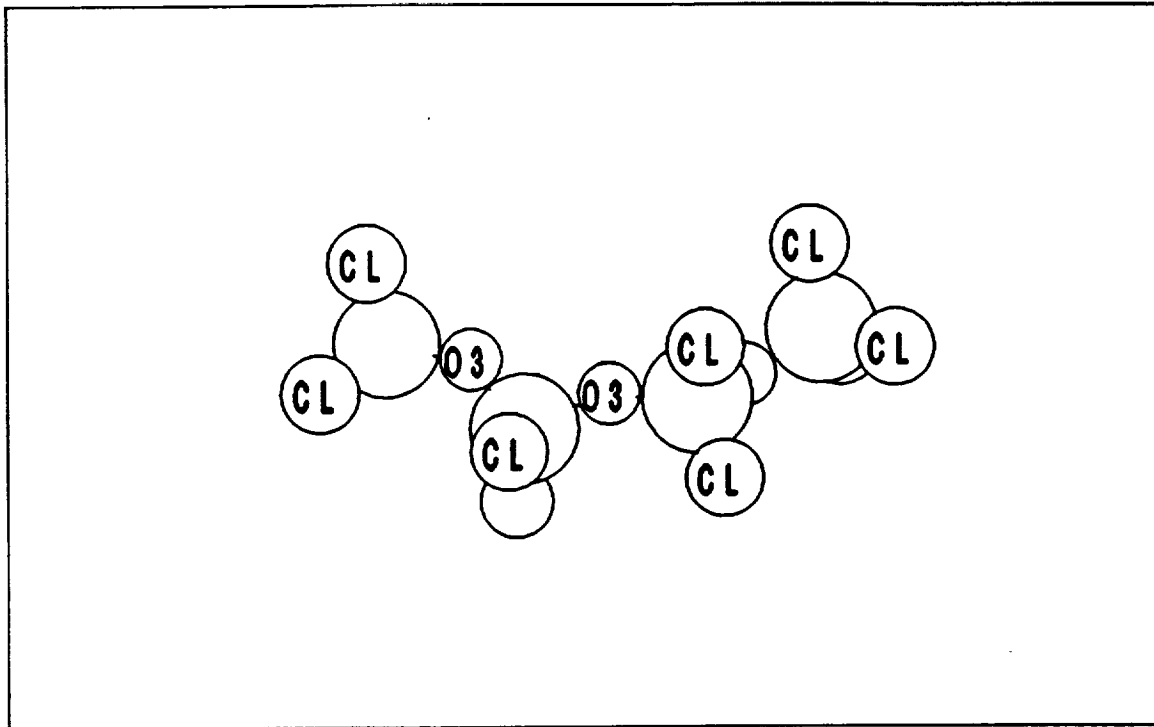
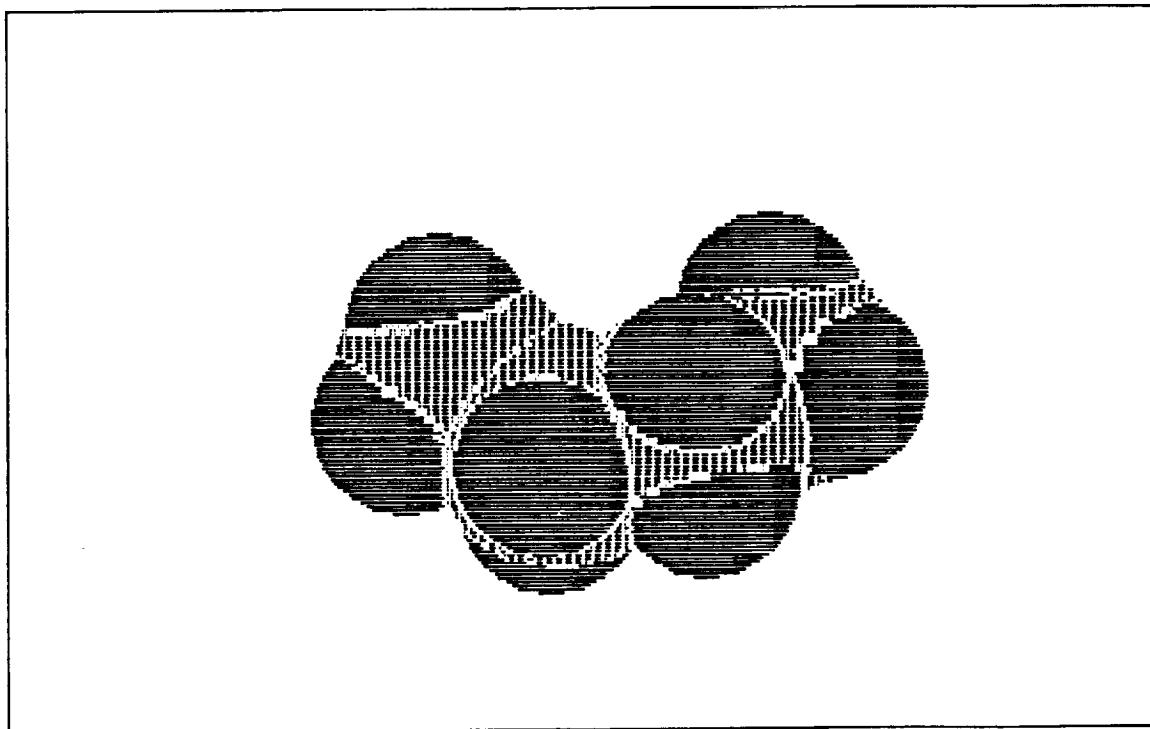
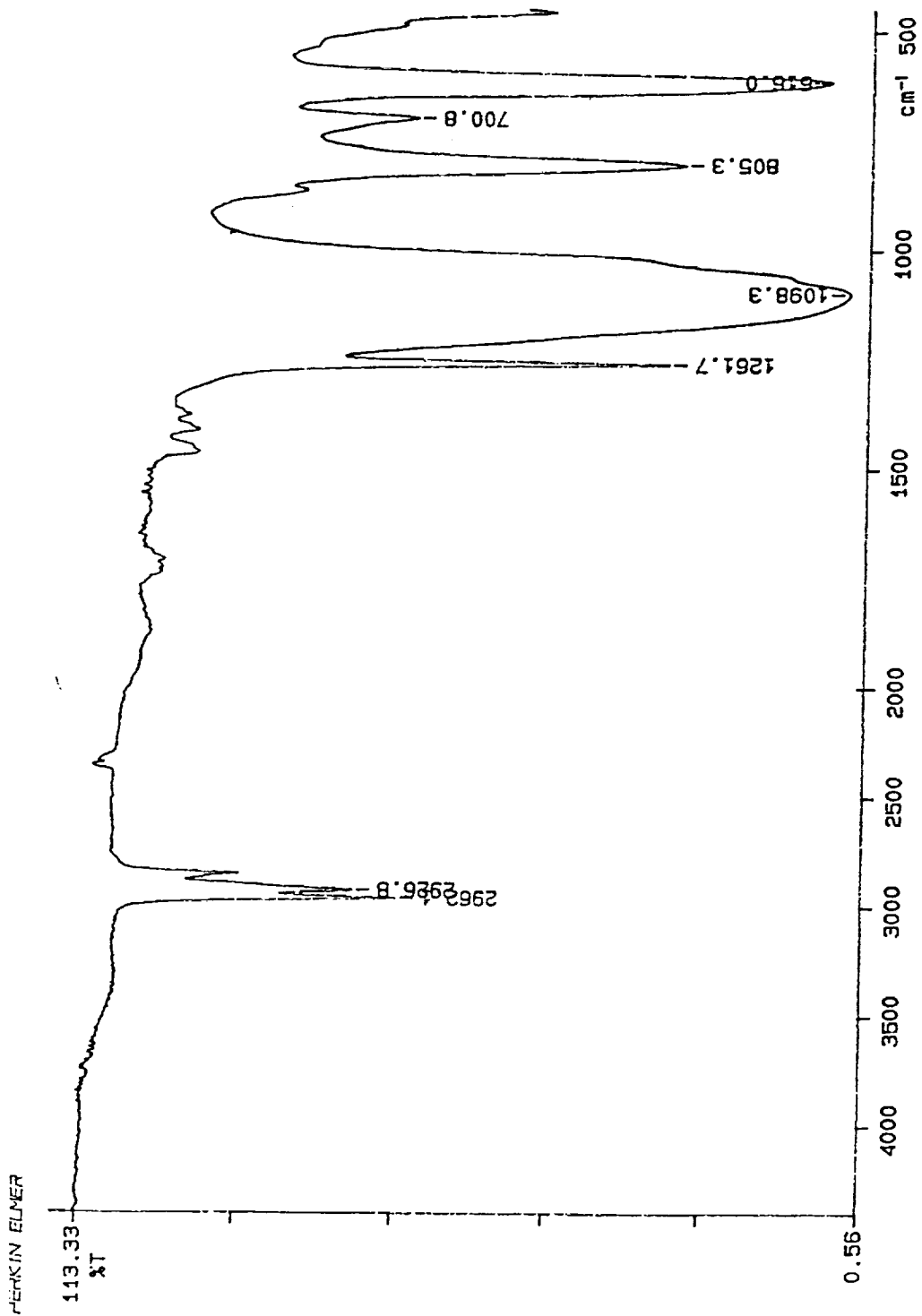


Figure 1: Model for polydichlorosiloxane





Infrared spectrum of Polydichlorosiloxane (?) product
Contaminated with dichloromethane

yields of a reproducible and pure product. This is of necessity difficult because of the water sensitivity of the polymer. The polymer will be characterized by IR, NMR and viscosity. We will then study its properties as a film.

Beyond this we plan to synthesize polydihydrosiloxane and characterize it, which will require work under an inert atmosphere. We also plan to look at the compatibility of these polymers with conventional sol-gel films as a way of introducing toughness into these glassy films.

Personnel

This work has been carried out by two undergraduate students, Jonas Hodges and Jean Corley working through the summer. As of now we plan to continue with undergraduate students and are also looking for a graduate to join the project.

References

1. G.A.Landis and M.A.Perino, NASA Tech. Memo. 102102, 1989.
2. D.Sparks, Space Power 7 235 (1988)
3. H.R.Allcock, Angew.Chem. (Intl.Ed.) 16 147 (1977)
4. E.G.Rochow, "The Chemistry of the Silicones" 2nd. ed. Wiley, New York, 1951.



Feasibility of Solar Concentrator
Fabrication From Indigenous
Lunar and Martian Materials

Roger Davenport
SAIC Applications International Corporation

ABSTRACT

Dependence upon the Earth for materials and power will make any proposed space colony very vulnerable to supply difficulties. Also, the cost and effort involved in transport of materials out of the Earth's gravitational potential well is very high. Finally, solar energy provides a ubiquitous and dependable long-term source of power in space. For these reasons, production of a solar power system in which large portions of the system are constructed of indigenous materials has promise for increasing the autonomy and security and enhancing the economics of such colonies.

In the near term, lunar colonies are of particular interest due to the moon's proximity and its likelihood as a starting point for colonization and as a debarkation point for extended excursions into space. So in 1989, with funding from NASA through the University of Arizona's Center for Utilization of Local Planetary Resources (CULPR), Science Applications International Corp. (SAIC) began to study using materials produced from lunar soil to form reflector for distributed and central receiver concentrating solar power systems. These systems may employ photovoltaic or solar thermal dynamic receivers to produce electric power for a lunar colony, or may be used to provide photons or thermal energy for chemical and materials processing needs.

The progress in the first year of this effort included materials identification, conceptual design, and limited fabrication testing. Results from that investigation were reported in Reference 1. Lunar materials and materials production processes were reviewed, and candidate materials for reflector production were identified. At the same time, lunar environmental conditions were reviewed for possible effects on the production of concentrators. Then conceptual designs and fabrication methods were proposed and evaluated for production of dish concentrators and heliostats. Finally, fabrication testing was performed on small-scale samples and models using terrestrial analogues of lunar materials.

1.0 INTRODUCTION

Dependence upon the Earth for materials and power will make any proposed space colony very vulnerable to supply difficulties. Also, the cost and effort involved in transport of materials out of the Earth's gravitational potential well is very high. Finally, solar energy provides a ubiquitous and dependable long-term source of power in space. For these reasons, production of a solar power system in which large portions of the system are constructed of indigenous materials has promise for increasing the autonomy and security and enhancing the economics of such colonies.

In the near term, lunar colonies are of particular interest due to the moon's proximity and its likelihood as a starting point for colonization and as a debarkation point for extended excursions into space. So in 1989, with funding from NASA through the University of Arizona's Center for Utilization of Local Planetary Resources (CULPR), Science Applications International Corp. (SAIC) began to study using materials produced from lunar soil to form reflectors for distributed and central receiver concentrating solar power systems. These systems may employ photovoltaic or solar thermal dynamic receivers to produce electric power for a lunar colony, or may be used to provide photons or thermal energy for chemical and materials processing needs.

The progress in the first year of this effort included materials identification, conceptual design, and limited fabrication testing. Results from that investigation were reported in Reference 1. Lunar materials and materials production processes were reviewed, and candidate materials for reflector production were identified. At the same time, lunar environmental conditions were reviewed for possible effects on the production of concentrators. Then conceptual designs and fabrication methods were proposed and evaluated for production of dish concentrators and heliostats. Finally, fabrication testing was performed on small-scale samples and models using terrestrial analogues of lunar materials.

1.2 Summary of Results

In this, the second year of effort, efforts continued on several aspects of the production of lunar concentrators. Development of processing approaches for lunar concentrators included evaluation of vacuum concrete de-watering, and evaluation of spin-molding and spin-coating. Efforts on other aspects of solar systems included further evaluation of a passive tracking system for dish concentrators and electrostatic focussing of heliostats. In addition, an evaluation of the Martian environment was begun in preparation for extending the feasibility studies to Mars.

2.0 LUNAR CONCENTRATOR DEVELOPMENT

Several aspects of lunar concentrator production were left unexamined in the first year of investigation. In the continuation of this study, several of these were further analyzed and tested. The following sub-sections describe the results of these studies.

2.1 Electrostatic Focussing of Stretched Membrane Heliostats

Since the moon lacks an atmosphere, focussing of stretched membrane heliostats using differential pressure is not possible unless a cover is placed over the reflective surface. Such a design would entail additional reflection and absorption losses, however. Therefore, a focussing system using static electric forces was proposed. In such a system, a DC voltage applied between the two membranes of the heliostat would cause a buildup of charge which would then lead to an attractive force between the membranes.

2.1.1 Analysis

The results of earlier analyses of terrestrial stretched membrane heliostats [2] was used to estimate the pressure required to focus the membranes of a 50 m² heliostat. For a heliostat with 3 mil thick stainless steel membranes and with a 6 cm center displacement of the membrane, the pressure was estimated to be 140 Pa (0.02 psi). Translating to the lunar case, this is the electrostatic force that must be generated per unit area to focus the heliostat. The thickness of the ring was taken to be 15 cm.

Assuming the membranes can be represented by parallel plates carrying uniform charges, the electric field between them is given by:

$$E = \sigma/\epsilon_0 \quad (1)$$

where σ = charge density on the plate (coulombs/m²)
 ϵ_0 = permittivity of free space ($1/4\pi\epsilon_0 = 9 \times 10^9$ Nt-m²/coul²)

The force exerted on a unit area of one membrane due to the other membrane can be expressed

$$dF/da = E \sigma \quad (2)$$

where σ = charge density (coul/m²).

Combining these two expressions, the force per unit area on a membrane can be expressed as:

$$dF/da = \sigma^2/\epsilon_0 \quad (3)$$

The required value of dF/da is just that given above, 140 Pa, so this can be solved for σ :

$$\sigma = \sqrt{(\epsilon_0 dF/da)} \quad (4)$$

Substituting for ϵ_0 and dF/da , the resulting charge density is 3.5×10^{-5} coul/m². In (1), this gives an electric field strength of 3.95×10^6 V/m between the membranes. This is a relatively strong electric field, amounting to over 100,000 V over the 3 cm gap between the membranes at the center. For comparison, Figure 2.1-1 shows sparkgap voltages versus the diameter of a conductor in air. From the figure, it can be seen that air has a breakdown dielectric strength of about 30 kV/cm. This is due to conduction breakdown of the air. In a vacuum, field emission limits the voltage gradient, and with the large flat membranes of a heliostat the 40 kV/cm predicted by the analysis should not lead to breakdown.

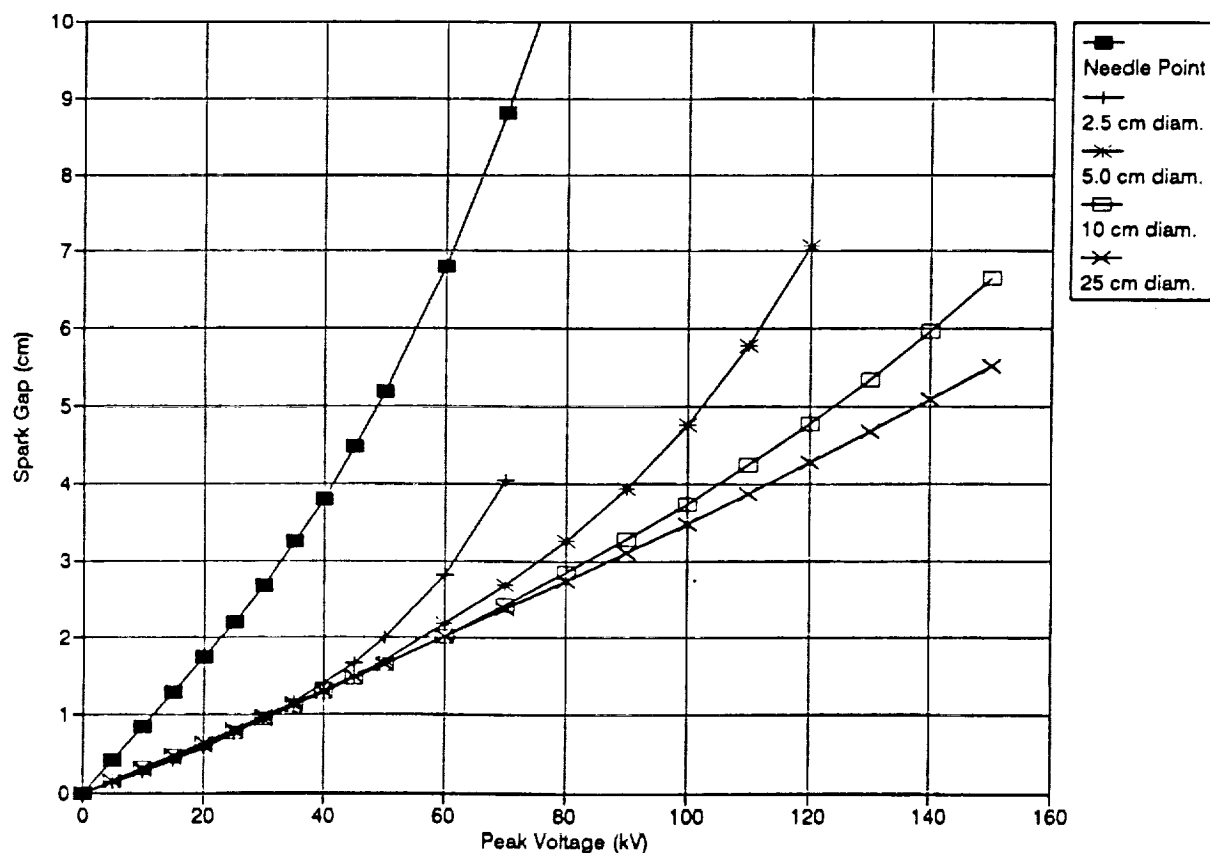


Figure 2.1-1. Spark Gap Voltages in Air

Because the estimated electric field required for focussing is very high, it is desirable to consider what could be done to reduce the required force for focussing. Two approaches come to mind immediately. First, thinner membranes would require less force to deflect them. Since there are no atmospheric forces such as wind or rain to deal with, the membranes of a lunar concentrator can be made as thin as practical based on handling and manufacturing considerations. Second, if membrane pre-tension is reduced, it decreases the force needed to deflect the membranes. Again, the lack of wind and other atmospheric effects on the moon make this a practical approach.

An unstudied effect on the focussing of a heliostat is that of non-uniform distribution of charge on the membranes. Since the membranes will be closer at their centers, charges will tend to be drawn there, increasing the force and displacement at the center of the heliostat. In effect, this is not necessarily a bad, since the form of a stretched membrane with uniform loading is slightly less deep in the center compared to an ideal parabolic surface. However, the extent of the effect has not been analyzed. The focus control approaches described in the next sub-section help to minimize this effect by giving direct control of the charge density on the rear membrane.

2.1.2 Design Approaches for Electrostatic Focussing

A preliminary examination of electrostatic focussing of space concentrators was performed in the early 1980's by Spectra Research Systems [2]. In their testing, they proposed two approaches to focussing concentrators. The first involved a plate with segmented electrodes on which the voltage could be actively controlled to adjust the shape of a stretched membrane reflector surface placed in front of the plate. The second approach used an electron gun to place patterns of charge on an insulating glass sheet in front of which was placed the membrane reflector. In a limited experimental program, both of these approaches were shown to be viable.

Of the two approaches identified by Spectra Research Systems, the second approach seems especially well suited to the lunar environment. This approach eliminates the complex electrodes and associated high-voltage wiring of the other system. Instead, a simple insulating glass plate and an elegant beamed-energy approach are used. If a lunar heliostat were made with a glass sheet forming its rear membrane, that membrane itself could become the target of the electron beam. A CRT-like electron gun would be well-suited to the vacuum of the moon's atmosphere, and could be used to supply focus control to many heliostats. The movement of the beam would be accomplished using existing CRT electronics, and the moon's low magnetic and electric fields would help minimize focussing and control complications with the beam. Finally, computer control could be used to adjust the pattern of charge laid out on the rear membrane of the heliostat in order to fine-tune the shape of the reflector.

2.2 Spin Molding of Dish Concentrators

2.2.1 Spin Molding Theory

Spin molding of dish concentrators was identified in the first year of investigations as a possible way in which to mold accurate parabolic surfaces. The University of Arizona has already used this technique for molding of glass mirrors for terrestrial telescopes with excellent success. The theory of spin molding of parabolic surfaces is as follows: At the surface of a liquid under rotational motion, the centripetal acceleration is in equilibrium with gravity at each point such that the liquid surface is perpendicular to the net apparent acceleration. Figure 2.2-1 shows a sketch of the relevant configuration, in which a liquid with a free surface is shown rotating about the y-axis at a rotational frequency of w (rad/sec).

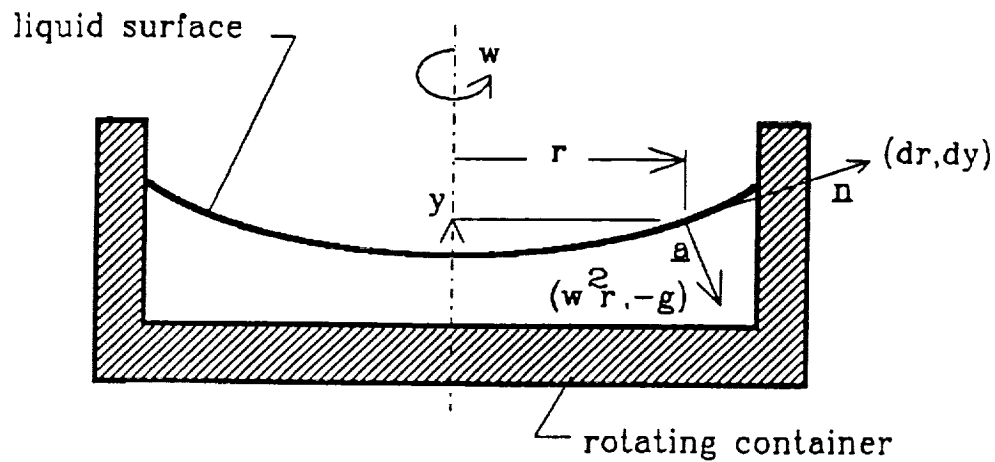


Figure 2.2-1. Geometry for Spin Molding Calculations

The condition that the surface is perpendicular to the apparant acceleration can be expressed as a dot product:

$$\underline{n} \bullet \underline{a} = 0 \quad (5)$$

Inserting the expressions for the vectors \underline{n} and \underline{a} , this becomes:

$$(dx, dy) \bullet (w^2 r, -g) = 0 \quad (6)$$

Integrating the resulting expression and applying a boundary condition that $y = 0$ at $r = 0$ results in the equation:

$$y = w^2 r^2 / 2g \quad (7)$$

This function is parabolic, curving about the y-axis with a focal length (f) given by:

$$f = g / 2w^2 \quad (8)$$

Finally, for design purposes it is useful to solve for the rotational frequency w as a function of the focal length:

$$w = \sqrt{g / 2f} \quad (9)$$

2.2.2 Spin Molding Tests

Using the results of the preceding section, a calculation was performed for lunar conditions with a dish 4 m in radius and with an f/d ratio of 0.6. The result was that a rotational speed of 3.92 RPM was required. For fabrication testing purposes, calculations were repeated for Earth gravity and a dish radius of 15 cm. It was found that a rotational speed of 49.6 RPM was required to achieve an f/d ratio of 0.6. Therefore, in order to perform fabrication testing, a turntable was acquired which gave well-regulated rotational speeds of 45 RPM and 78 RPM.

Figure 2.2-2 shows a small plaster of Paris dish that was cast on this turntable at 45 RPM. As shown in the photo, the free surface of the material formed a smooth parabolic curve. Next, a larger dish (22 cm in diameter) was cast on the turntable at 78 RPM. The surface of this dish was not as smooth as the first dish. This is believed to be attributable to roughness in the bearings of the turntable and the fact that the plaster had lumps and did not flow smoothly.



Figure 2.2-2. Spin Molded Plaster of Paris Dish

2.2.3 Spin Coating of Dish Concentrators

After the 22 cm dish was cured, its front surface was successfully coated using a spin coating approach. In the case of a lunar dish, this would be done with a thin layer of glass in order to form a smooth substrate for the reflective surface. For testing purposes in this investigation, a polyester resin was used as the coating material. Figure 2.2-3 shows the dish produced from this test. The resin flowed over the surface of the dish and coated it well, although its smoothness was limited by the roughness of the underlying surface.

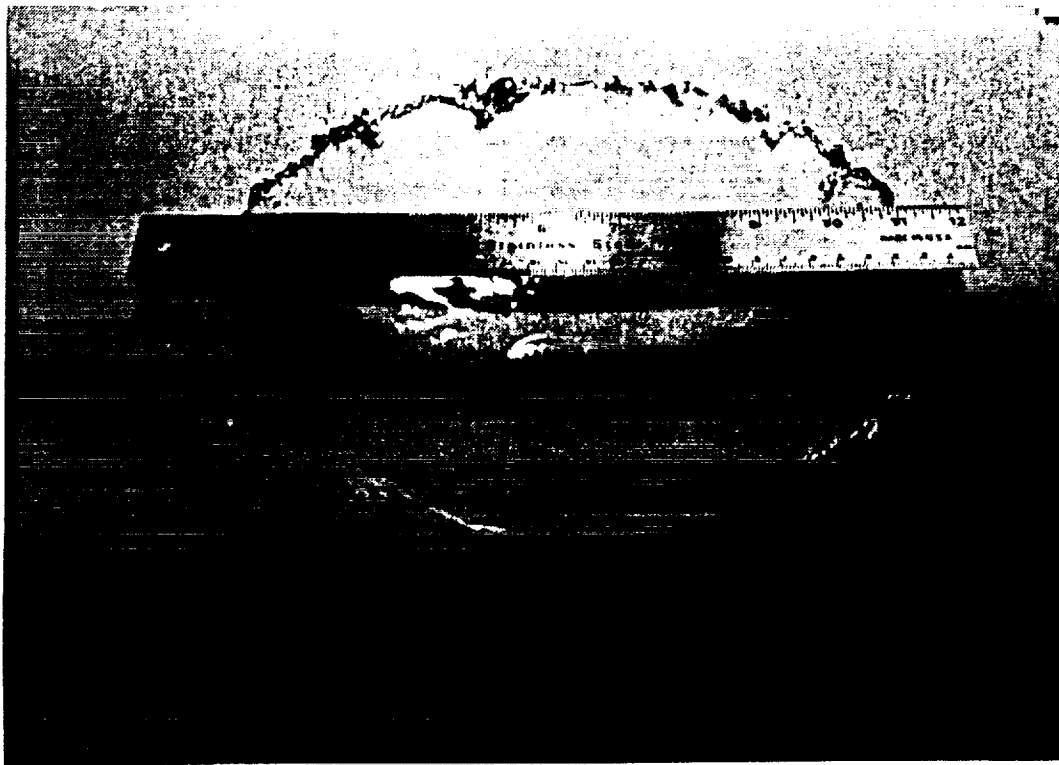


Figure 2.2-3. Spin Molded Dish with Spin Coating of Resin

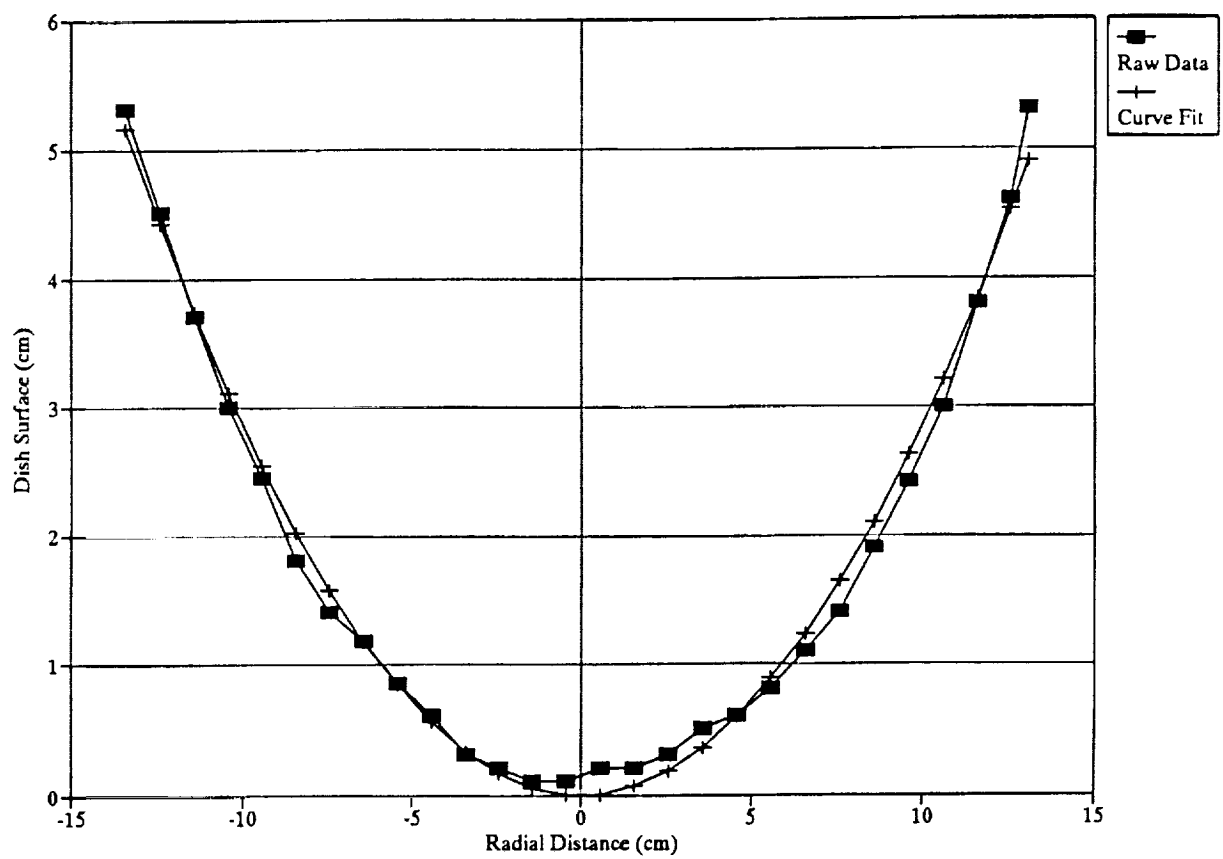


Figure 2.2-4. Comparison of Spin Molded Dish and Ideal Parabolic Shape

The surface shape of the dish shown in Figure 2.2-3 was measured across a diameter, and compared to an ideal parabola. A least-squares curve fit was used to identify the focal length of the parabola closest in shape to the dish. Figure 2.2-4 shows the comparison of the two curves. The variations of the dish surface from parabolic are mainly a few distinct lumps that remained in the dish surface. Generally, the dish shape was quite close to parabolic, supporting the viability of this method for lunar concentrator production.

2.3 Vacuum Dewatering of Concrete Dish Concentrators

One of the major problems identified with the use of concrete-like materials was the amount of water required to form the concrete mix. In order to get good flow properties and avoid formation of voids in the mix, it is even desirable to have excess water. However, on the moon water will be a very scarce and valuable commodity since it does not occur naturally, and hydrogen needed for its production will probably need to be imported from Earth. Therefore, it was suggested that vacuum dewatering of the concrete would be a means to recover and recycle the excess water in concrete concentrators. Vacuum dewatering also helps compact and strengthen the concrete by removing voids and minimizing excess water in the concrete mix.

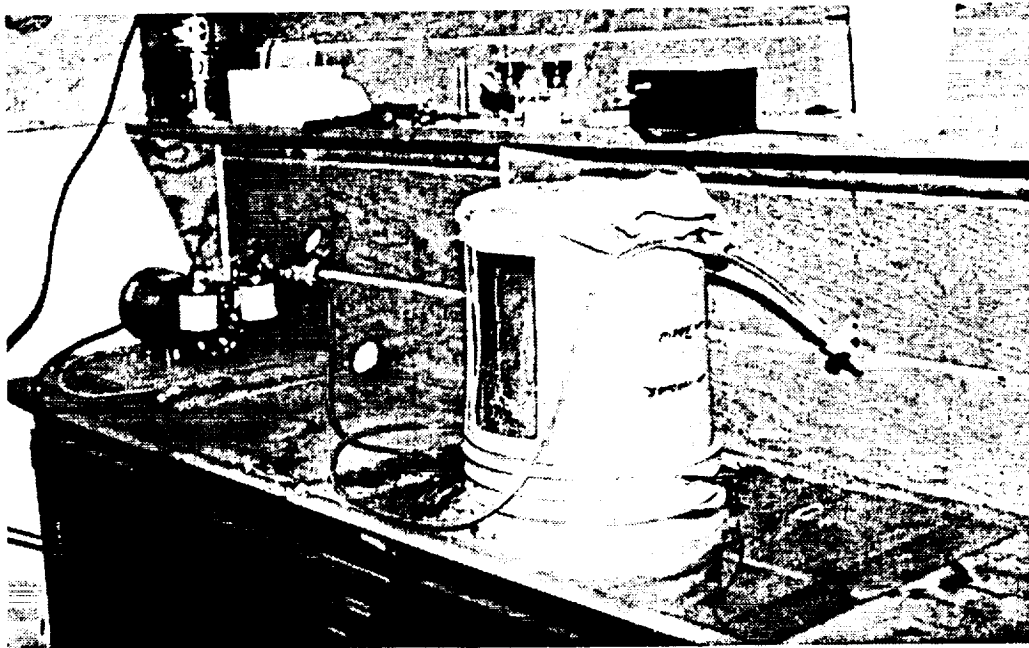


Figure 2.3-1. Vacuum Dewatering Test System

To test vacuum dewatering of concrete dish concentrators, a small test rig was constructed, consisting of a 5-gallon vacuum chamber with a viewing port and a connection to a small vacuum blower (see Figure 2.3-1). After several unsuccessful trials, a method of dewatering was arrived at in which the dish shape was formed by the same vacuum used to dewater the concrete. The procedure was as follows:

1. A concrete mixture was smoothed into a thin layer over a piece of thin, flat plastic sheet.

2. The vacuum chamber was placed over the plastic sheet so the cement was on the inside, and the plastic sheet was secured to the top of the pail.
3. The vacuum blower was activated. When this occurred, the vacuum inside the pail pulled the plastic sheet into a dish shape, forming the attached layer of concrete mix with it.
4. As the blower continued to function, the excess water was liberated from the concrete and pulled out of the system.

The molding technique described above was unfortunately not successful in producing full dishes. When the concrete mixture was pulled into a dish shape, cracks often formed in the concrete which caused the dishes to break apart. However, the dewatering technique itself was successfully demonstrated, and several fragments of dewatered concrete were successfully produced. In a production mode, the concrete would be laid up on a hard mold or on a soft mold that was pressurized separately from the vacuum system, so this problem would not arise.

2.4 Passive Tracking System

Evaluation of a passive drive system for dish concentrators was continued in this phase of investigation. A design similar to terrestrial passive tracking systems was used as the starting point. In terrestrial systems, two blackened tubes containing a condensible gas are situated behind partial shades on either side of an axis of rotation, with a manifold connecting the tubes. When the unit is off-tracked, one tube becomes shaded and the other becomes more exposed to the sun so that liquid is boiled in the sunny tube and condensed in the shady tube. The shift in the center of gravity causes the unit to rotate until it is on-track again and thermal balance is achieved once more.

Terrestrial trackers rely heavily on convective cooling of the tubes due to wind and natural circulation. This is not possible in the lunar environment, where radiation is the only heat transfer mechanism. Therefore, in order to provide more area for radiative heat transfer, the lunar tracking system was configured as a pair of banks of parallel tubes oriented nearly parallel to the incident solar radiation (see Figure 2.4-1). Banks of relatively small tubes were chosen to accommodate possible high vapor pressures in the system. The tube banks have a reflective surface towards the outside and an absorptive surface towards the inside (the dish side). No shades are employed in the lunar system, because in a radiative environment such components act as radiation shields and reduce heat transfer to the environment. Instead, the arrangement of the tube banks is such that they shade themselves progressively as the tracker is moved. The tube banks may be aligned parallel to the incident sunlight, or they may be arranged with a slight outward tilt from the center of the dish to provide smoother operation (i.e., so the tubes don't go from being fully shaded to being illuminated over such a small angular motion from the desired aimpoint).

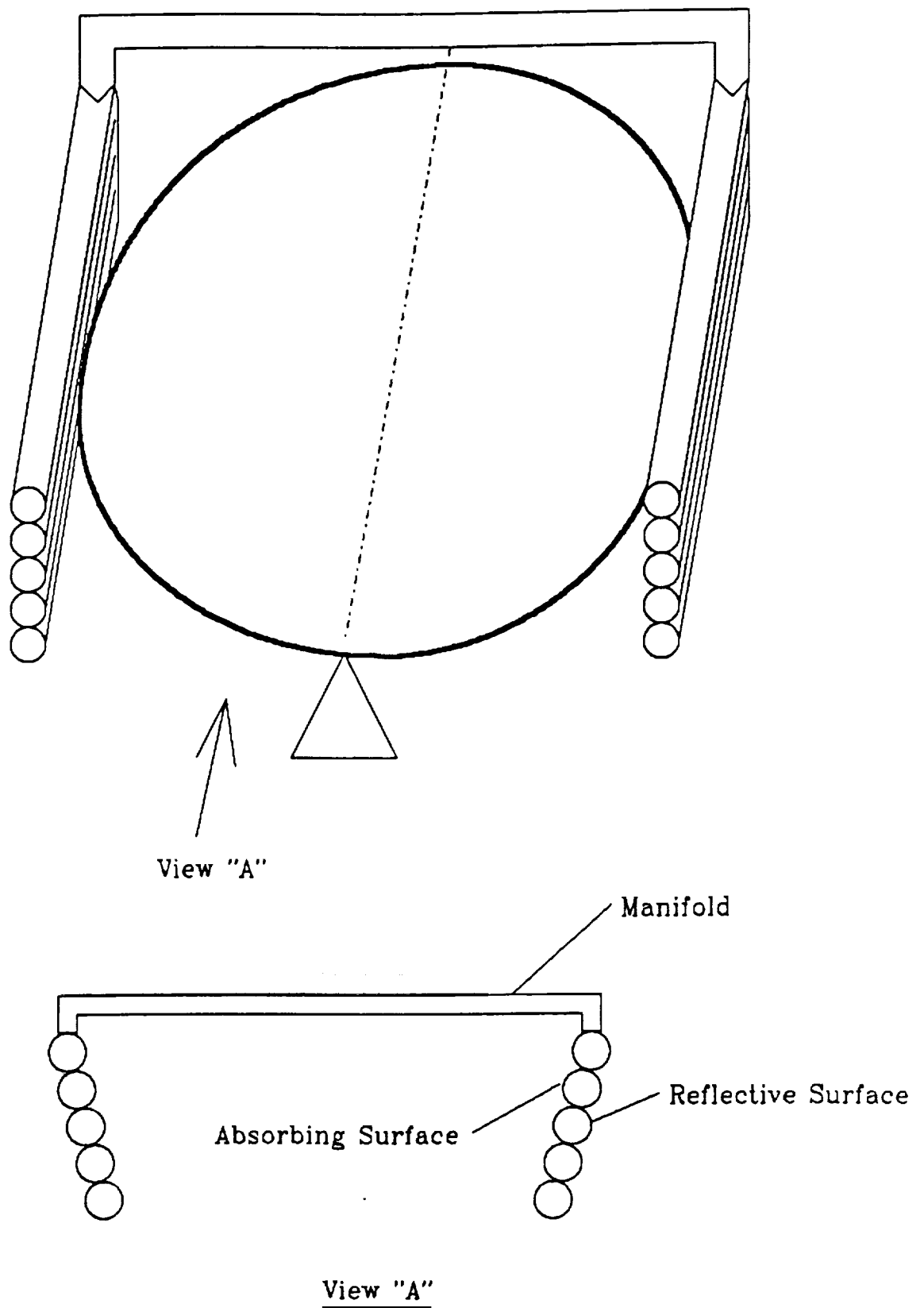


Figure 2.4-1. Lunar Dish Tracking System Concept

Calculations were performed to determine the behavior of such a system when exposed to sunlight. Equilibrium temperatures of such a system when shaded and when exposed to the sun were estimated to be in the range of 150 K to 450 K with emissivities of 0.05 and 0.95 for the absorptive and reflective components, respectively. With proper selection of materials and absorption properties, the operating temperature of the unit could be above or below that range. Considering the gases available on the lunar surface, it appears that oxygen or perhaps SO_2 would be available and appropriate for the fluid component in the system. Figure 2.4-2 shows the saturation pressures of these gases are reasonable over the desired range of temperature.

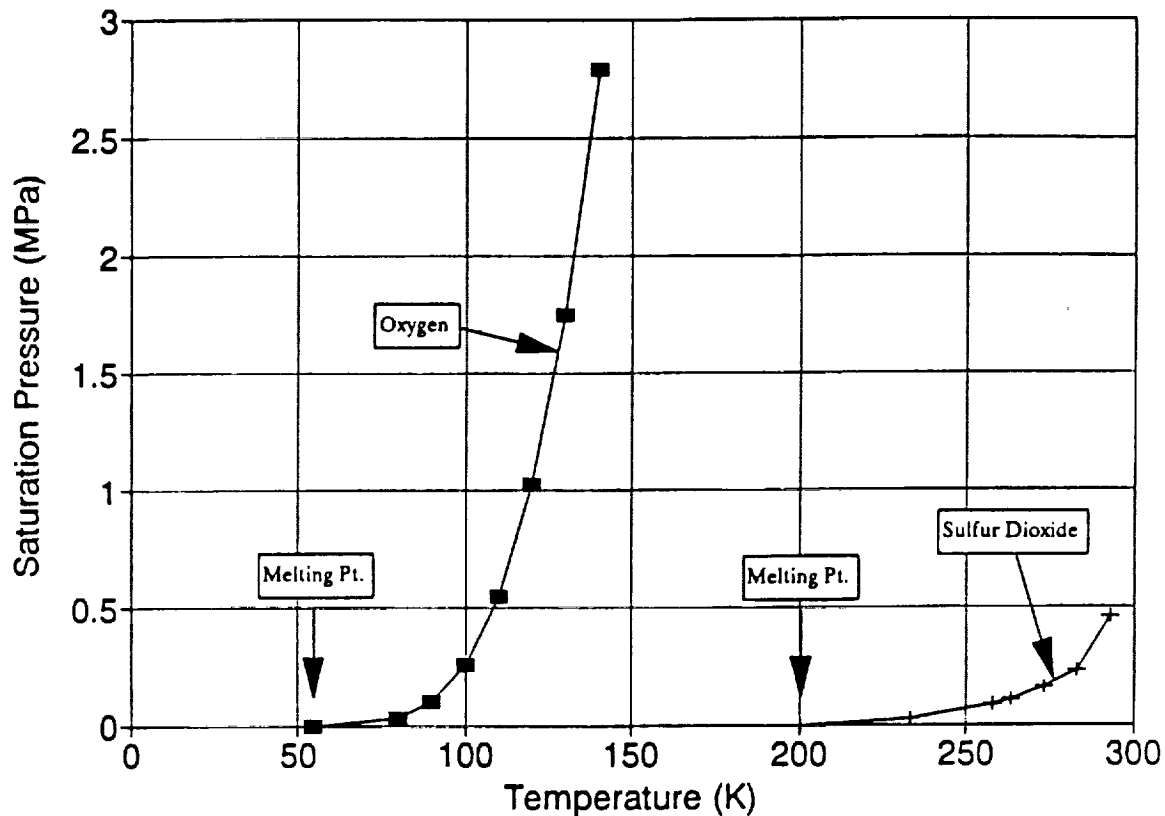


Figure 2.4-2. Saturation Pressures for Oxygen and Sulfur Dioxide

A small-scale test rig was designed and built to demonstrate the design, using copper tubes and with water as the liquid component. Figure 2.4-3 shows the test rig as it was mounted on a simple stand for testing. The test rig consisted of copper pipes soldered into manifolds to form two banks of parallel tubes. The tube banks were manifolded together at the top of the unit. Flat black paint was used on all but the outside surfaces of the tubes, which were painted white to reflect away the solar energy. The rig was mounted on bearings and balanced so that the axis of rotation was very near the center of gravity. Finally, the test unit was partially filled with water, evacuated, and sealed, leaving only water and water vapor inside the tubes. The operating pressure of the unit was therefore the saturation pressure of water, which was about 0.003 MPa at room temperature.

A thermal analysis of the test rig was performed. When operating off-axis, the absorbing side of one bank of tubes and the reflective side of the other bank, are exposed to the sun. If the two banks of tubes were separate, the absorbing bank would normally heat up relative to the reflecting bank. However, as one bank begins to heat up, water vapor is generated which travels to the cooler side and condenses. So, the entire unit acts like a heat pipe, and energy is transferred from the hot side to the cold side in a manner that maintains the unit nearly isothermal. Externally, the result of this is the heat loss from the unit is nearly evenly divided between the two banks of tubes. Internally, the transfer of liquid from one side of the unit to the other shifts the center of gravity of the unit and provides the driving force for the mechanical motion of the unit. Calculations performed for the test unit indicated that it should transfer about 1.2 g/min of water from the fully illuminated to the shaded side in full sunlight. A heat transfer analysis indicated that the system would operate at only 1.5-2.5°C above ambient temperature under those conditions.



Figure 2.4-3. Passive Tracking System Test Unit

The test rig was assembled and placed outdoors for testing. Unfortunately, several factors limited the effectiveness of its operation under these conditions. First, the solar illumination at the time of testing was insufficient due to haze and clouds. Second, the bearing drag on the test stand was found to be too high to allow the unit to swing freely; a force of 0.2-0.3 N, (e.g., equivalent to 10-15 grams of mass transfer) was required to start the unit in motion. So, the unit was difficult to get started, and tended to overshoot in its motion once it began to move. Also, since by design the unit was optimized for radiative heat transfer, it was not optimal for operation on earth where convection is dominant. Finally, because the test unit was made as simply as possible, no wicking was provided on the inside of the tubes for enhancing the wetting of water on the tubes. This limited the heat transfer capability of the unit and limited its performance. The result of these limitations was the test unit was not able to track the sun automatically by itself. However, when thermal input from a torch was used to augment solar insolation it was possible to demonstrate functionality of the unit by causing it to rotate first one direction and then the other through only the application of heat to the low side. The test rig was successful in demonstrating and providing validation of the concept; of course, it would have been more satisfying if the unit had been able to track by itself in sunlight.

3.0 MARTIAN CONCENTRATOR DEVELOPMENT

3.1 Martian Environmental Conditions

The Martian environment offers many significant challenges to the application of solar concentrators. Unlike the moon, Mars has an atmosphere and exhibits extensive global weather patterns and seasonal variations. In many ways, the atmosphere of Mars is more like that of Earth than that of the moon. A further challenge is that because of its distance from the sun, the solar insolation on Mars is only about half of the value at Earth's orbit. Thus, collection devices need to be either twice as efficient or twice as large in order to extract equivalent amounts of energy as compared to the moon. The following sub-sections describe the Martian environment and some of the concerns and conditions associated with the application of solar concentrators to Martian energy needs. Also, Martian materials are described and their application to production of solar concentrators is discussed.

3.1.1 Martian Environment

Mars is about 1.5 times as far from the sun as Earth, and as a result receives about half the solar insolation that Earth and the moon receive. Because of the eccentricity of Mar's orbit, the solar insolation also shows significant seasonal variation. The mass of Mars is about one tenth that of Earth, leading to a gravitational force of about 40% of Earth's. Mars has two satellites, Phobos and Diemos. It does not have a significant magnetic field, and its atmosphere is thin, so there are high levels of cosmic radiation, solar flare protons, and UV light. The mean temperature is 215 K, but varies considerably with latitude and season. The length of the Martian day is nearly the same as Earth, but the year is about twice as long. Mars is not thought to be seismically active at present. A summary of pertinent information regarding Mars is given in Table 3.1-1.

Table 3.1-1. General Information About Mars

Mean Solar Constant	590 W/m ²	Mean Planetary Radius	3380 km
at perihelion	718 W/m ²		
at aphelion	493 W/m ²	Length of Day	24.7 hrs
Surface Pressure	6-15 mbar	Length of Year	687 Earth-days
Mean Surface Temperature	215 K (-58°C)	Gravity	3.74 m/s ²
max.	15°C		
min.	-100°C	Inclination of Axis	25.2°
Orbital Radius	2.278 x 10 ⁸ km (1.52 AU)	Orbital Eccentricity	9.34%
Atmospheric Opacity	50%	Soil Density	1500 kg/m ³

The Martian atmosphere is composed of about 95% CO₂ and small amounts of other gases. Table 3.1-2 (with data from [3]) summarizes the main constituents of the Martian atmosphere. The Martian atmosphere is saturated with respect to water vapor at many times and in many places, and there is polar ice and evidence of subsurface water as well. As indicated in Table 3.1-1, the surface pressure varies by over a factor of two. This is due to the seasonal cycle of condensation and evaporation from the polar regions. Approximately 25-30% of the Martian atmosphere condenses at the poles each winter. This leads to strong winds in the polar regions and large air mass motions. In the northern hemisphere, cyclonic and anti-cyclonic storm systems are formed due to large temperature gradients in the atmosphere. These effects lead to significant winds and are an additional source of cloudiness. Thus the atmosphere is characterized by both CO₂ and water vapor clouds, and by dust storms. In the northern hemisphere, the so-called polar hood cloud canopy extends down to about 50°N during the fall and winter. In the southern hemisphere, dust storms are common during the summer, and they sometimes become global in size. The reason for these differences between the hemispheres is the eccentricity of the Martian orbit. Perihelion occurs about 46 days before the southern summer solstice, which means the southern hemisphere is generally warmer and receives more solar energy.

Table 3.1-2. Constituents of the Martian Atmosphere

<u>Gas</u>	<u>Concentration (% by volume)</u>
CO ₂	95.3
N ₂	2.7
Ar	1.6
O ₂	0.13
CO	0.07
H ₂ O	0.03 (variable)
Ne	2.5 ppm
Kr	0.3 ppm
Xe	0.08 ppm
O ₃	0.03 ppm (variable)

3.1.2 Concerns Related To Solar Concentrators

Several features of the Martian environment lead to concern about the application of solar concentrators on the surface of Mars. These concerns have also been raised by other researchers [4]. Some of these concerns are described in the following paragraphs.

Atmospheric Opacity: The Martian atmosphere is characterized by clouds and scattering of sunlight due to dust. One book described Martian atmospheric conditions as a "persistently high atmospheric opacity due to dust haze" [5]. Obviously, solar concentrators cannot operate effectively where the sun is obscured or where there is much scattering of the incoming solar radiation. On the other hand,

much of the scattered sunlight still reaches the surface, so that non-concentrating solar collectors could still be effective.

- Weather Effects:** The structural requirements for concentrators are increased by the possibility of high winds, and solar collection of any system will be decreased due to the existence of clouds and storm conditions. Another serious difficulty is abrasion of reflective surfaces and fouling of mechanical equipment exposed to dust storms.
- Available Insolation:** Because of Mars' distance from the sun, the available solar flux is only about 52% of the Earth-normal value. This means that solar concentrators will need to be larger and will produce less power than on the Earth or the moon.
- Sun Tracking:** The Martian planetary axis of rotation is inclined even more to the ecliptic than the Earth's, which means that solar concentrators will need to be tracked in two axes. This increases the complexity of the support and tracking systems. Martian solar concentrators will have to be similar to Earth concentrators in complexity.

3.2 Martian Construction Materials

The soil of Mars, which was analyzed by the two Viking landers, includes materials of volcanic, sedimentary, and windblown origins. The most abundant elements are silicon and iron, both assumed to be in their oxidized states (SiO_2 and Fe_2O_3). Many other useful elements and minerals were also detected. Table 3.2-1 summarizes the mineralogy of the Viking 1 lander site as inferred from the Viking analyses (from [3]).

Table 3.2-1. Minerals at the Viking 1 Landing Site

<u>Compound</u>	<u>Abundance (% by mass)</u>
SiO_2	44.7
Fe_2O_3	18.2
MgO	8.3
SO_3	7.7
Al_2O_3	5.7
CaO	5.6
TiO_2	0.9
Cl	0.7
K_2O	<0.3

Chemically, the soils from the two Viking sites were virtually identical. The conclusion that has been drawn from this fact is that global dust storms have homogenized the soil around the planet. In addition to the fines and rock, there is a salt-cemented crusty material called "duricrust." Salts comprise up to 15% of the fines; they are thought to be magnesium and

sodium sulfates with lesser amounts of NaCl and some magnesium and calcium carbonates [6].

The Martian soil contains a large assortment of useful resources for construction of solar concentrators. Metals, such as titanium, aluminum, and magnesium can be produced from molten electrolysis of their oxides. Glass and ceramic can be produced from SiO_2 , Al_2O_3 , and other ubiquitous minerals. The silicate salts in the Martian soil may provide an important building material in the form of concrete, and unlike the lunar situation, water is relatively easily available for hydration of the material. Also, plaster of Paris can be produced from gypsum/calcium sulfate present in the soil.

4.0 SUMMARY AND CONCLUSIONS

4.1 Lunar Solar Concentrators

The results of these investigations continue to support the concept of indigenous production of solar concentrators from lunar materials. Analysis and investigation of electrostatic focussing of stretched membrane heliostats continued to show promise. An approach using an electron beam to charge a non-conducting rear membrane was identified which has promise of being an elegant and easily controlled focussing system. Spin molding of dish concentrators was analyzed and found to result in a reasonable rotational speed under lunar conditions. Tests of spin molding of dish concentrators was performed successfully with plaster of Paris dishes. One of the plaster dishes was successfully spin-coated with a thin layer of polyester resin to simulate glass-coating of a dish made of concrete or other material.

Vacuum dewatering of a concrete dish concentrator was demonstrated at a bench scale. This technique allows recycling of the excess water used in collector fabrication from that material and also enhances the strength, consolidation, and toughness of the resulting concrete. The design of a passive tracking system was further refined. The design approach of using multiple parallel tubes to increase the radiative surface area of the tracker was analyzed and found to be functional. A terrestrial test unit demonstrating this design was constructed, and displayed correct operating characteristics.

Further work needs to be done on materials for lunar concentrator construction, on fabrication techniques, and on focus and tracking systems for lunar concentrators. Although contact was made with the University of Arizona about ceramic-glass composite materials, it was not possible to study their applications in solar concentrator construction. Also, in the present contract no further development of promising materials identified in the first phase was possible. Glass-glass composites, iron-glass sintered materials, foam glass, and glass fiber reinforced lunar concrete materials all require further development and testing. Scaling up of fabrication testing to larger dish sizes (e.g., 1-2 meter diameter) is also recommended in order to better simulate fabrication conditions for actual concentrators. Testing of fabrication approaches in vacuum conditions (at a scale of 20-30 cm diameter) would also yield useful information about materials and fabrication techniques. Another area where further study is needed is in reflective surface production. Testing of reflective surface deposition techniques on sample concentrator materials is needed to identify problems in this important processing step. Further testing and development of focus control systems for heliostats, based on electron beam charging, would allow lunar heliostat systems to be designed. Finally, design analysis could be refined and optimization of the passive tracking system could be completed.

4.2 Martian Solar Concentrators

Martian atmospheric conditions and the materials available for concentrator production were reviewed. Mars offers many challenges to the application of solar concentrators, including poor solar resources and relatively hostile atmospheric conditions. Materials for production of concentrators are available and plentiful in the Martian soil, including metals, glass and ceramic precursors, and cementitious materials.

In view of the difficulties in applying solar concentrator technologies on the Martian surface, other solar approaches could be found to be more appealing. Since much of the solar insolation scattered by the atmosphere eventually does reach the ground as diffuse radiation, flat-plate solar panels for both photovoltaic electricity and low temperature heat might be considered. Photovoltaic panels might be constructed from silicon and other materials found on the surface Mars, and flat plate panels could be fabricated of concrete, glass, or metal. Another approach which could be considered would be to generate power in space (on one of the moons or in orbit around Mars) and then microwave the power to the surface (a la SSPS). This would eliminate most of the concerns about atmospheric conditions mentioned above.

5.0 REFERENCES

1. Davenport, R.L., The Feasibility of Production of Solar Reflectors from Lunar Materials for Solar Power in Space, SAIC Final Report under Purchase Order 159828, 30 March 1990.
2. Bradford, R., Research on Large, Highly Accurate, Inflatable Reflectors, AFRPL TR-84-040, July 1984.
3. Meyer, T.R. and McKay, C.P., "The Resources of Mars for Human Settlement," *Journal of the British Interplanetary Society*, v. 42, pp.147-160, 1989.
4. Ramohalli, K., Lawton, E., and Ash, R., "Recent Concepts in Missions to Mars: Extraterrestrial Processes," *J. Propulsion*, v. 5, No. 2, March-April 1989.
5. Kliore, A. (ed.), The Mars Reference Atmosphere, *Advances in Space Research*, v.2, No. 2, Pergamon Press, 1982.
6. Clark, B.C., "Survival and Prosperity Using Regolith Resources on Mars," *Journal of the British Interplanetary Society*, v. 42, pp.161-166, 1989.

6.0 ACKNOWLEDGEMENTS

This project was funded by the University of Arizona (U of A) Center for the Utilization of Local Planetary Resources (CULPR), which is sponsored by NASA. The assistance of several people who contributed to this research is gratefully acknowledged, including: Dr. Kumar Ramohalli, of the U of A, who provided support, encouragement, and assistance; Steven Tellier and his colleagues at the Lunar & Planetary Institute, who provided timely and useful information about Martian materials; Dr. Chandra S. Desai, of the U of A, who provided information on ceramic composites under study at the U of A; and the libraries of the University of California at San Diego and the California Space Institute, where many reference materials were obtained.

III. RESOURCE DISCOVERY AND CHARACTERIZATION



PROGRESS REPORT

Continuous Monitoring of the Lunar or Martian Subsurface Using On-Board Pattern Recognition and Neural Processing of Rover Geophysical Data

**Charles E. Glass
Richard V. Boyd**

August 31, 1991

ABSTRACT

The overall aim of this research is to provide base technology for an automated vision system for on-board interpretation of geophysical data. During the first year's work we have demonstrated that geophysical data can be treated as patterns and interpreted using single neural networks. Research underway at this time is developing an integrated vision system comprising neural networks, algorithmic preprocessing and expert knowledge. This system is to be tested incrementally using synthetic geophysical patterns, laboratory generated geophysical patterns and field geophysical patterns.

This report presents initial results of an automated ground penetrating radar vision system which employs multiple neural networks, expert knowledge and algorithmic processing in a serial architecture. Future research is proposed which will expand the vision system to employ multiple neural networks in parallel and serial architectures.

SUMMARY OF PREVIOUS WORK

The initial aims of this research were threefold. First, develop a continuous profiling EM vision system. Second, develop a continuous profiling sonic system. Third, evaluate pattern recognition and neural network approaches for automated interpretation of continuous profile data. As funding for the first year effort (1989-1990) necessitated a reduction in scope, objectives one and three became the operative objectives for the project.

Combining SERC Funding with funding from several other projects, we purchased a ground penetrating radar (GPR) system for continuous profiling using EM radiation in the 500 MHz and 300 MHz frequency ranges. Subsequent extensive experimentation with the GPR system at our geophysical test site and at several sites in Arizona is reported in McGill et al., 1989, McGill et al., 1990, and McGill, 1990.

Research during the first year also demonstrated that radar signatures can be represented as patterns and the anomaly location interpreted automatically using a single neural network. Our increasing experience in the field, however, indicated that GPR signatures can become quite complex, with target shape and aspects of the GPR survey (such as profiling speed) strongly influencing the radar return signatures. Hence, we believe that a single neural network could rapidly become overwhelmed by actual field situations, as we ourselves are at times. This belief has led to the second year's project, which began development and incremental testing of an integrated vision system comprising neural networks, algorithmic preprocessing and expert knowledge. This latter work appears in Glass et al. (1991).

SUMMARY OF PROJECT GOALS FOR THIS REPORTING PERIOD

VISION SYSTEM

During our previous research, we have demonstrated that GPR patterns are amenable to adaptive pattern recognition using a single neural network. In these experiments a continuous output simulated neural network was used to predict the horizontal and vertical location of a buried plate given the radar signal returned from the irradiated plate.

Results from generating synthetic radar signatures over regular geometric shapes, however, showed that, theoretically at least, far more than the target's spatial location can be derived from the radar pattern. The target shape can be ascertained from the slope of the signature arms, and the vertical and horizontal extent of the target can be calculated from the length

and shape of the signature arms. Hence, neural network-based pattern recognition systems should be able to provide more information than our previous experiments have asked of them.

In the field, though, several factors combine to complicate the GPR patterns. First, attenuation in the surrounding soils will limit the radar penetration, thus truncating the anomaly arms. Second, the EM wave velocity of the background soils and the speed of the GPR profile can compress the radar pattern, making shape determination difficult. And third, heterogeneities in the background soils can superimpose noise on the desired GPR patterns.

Because of these difficulties, we have undertaken a program to design a more complex vision system able to incorporate the advantages of neural networks, knowledge base and algorithmic paradigms into a single unit. Neural networks, for example, appear to work best on simple (toy) problems. That is, the simpler the pattern, the more successful neural networks are in recognizing it. Furthermore, the scale of the "toy" (Minsky and Papert, 1968) problem is at a level at which most of the functioning of the human visual system seems to work, i.e., the human visual system appears to be composed of numerous simple neural networks working, for the most part, independently on specific aspects of a pattern.

The complexity of the human visual system seems to reside not as a single huge network, but rather in the complex (and so far little known) way in which the component networks interact or are coordinated. The focus, then, should not be on constructing a single large and complex neural network, but rather on organizing several simple systems into a more effectively complex larger one. Although we are still experimenting with some fundamental uncertainties related to the specifics of how to go about such an organizational task, the following discussion outlines our general approach.

Applying the concept of encapsulation found in object oriented programming, particular domains of the pattern recognition function have been isolated from others to keep the level of inter-model complexity down. Higher level objects are being employed to coordinate, or manage, the interaction of simpler objects. Research on the visual system of the horseshoe crab, for example, indicates that the information flow into the crab's visual cortex from its brain exceeds the information flow into its visual cortex from the system of neural networks constituting its optic nerve. Hence, even in simple visual systems there appears to be significant management of image information through knowledge gained from heredity or experience.

The basic idea is to use neural network paradigms and expert system paradigms as separate objects within the object oriented programming environment. Nets for associative memory, nets for self organization and back-propagation nets for discrimination, are guided and directed in terms of access and activation by expert system modules. At the time of the last progress report,

a preliminary knowledge base had been assembled, the components (expert system shell, neural network simulation package, and small talk based object oriented programming environment) had been implemented on a Sun Sparcstation, and software to generate synthetic data for neural network training had been written.

Goals for the current reporting period were to:

1. Create Vision System

Coordinate the components of the vision system, embed them in the object-oriented environment, and begin incremental testing.

2. Synthetic Patterns

Test the vision system on synthetic patterns, supervising the training until it performs well.

PROGRESS DURING CURRENT REPORTING PERIOD

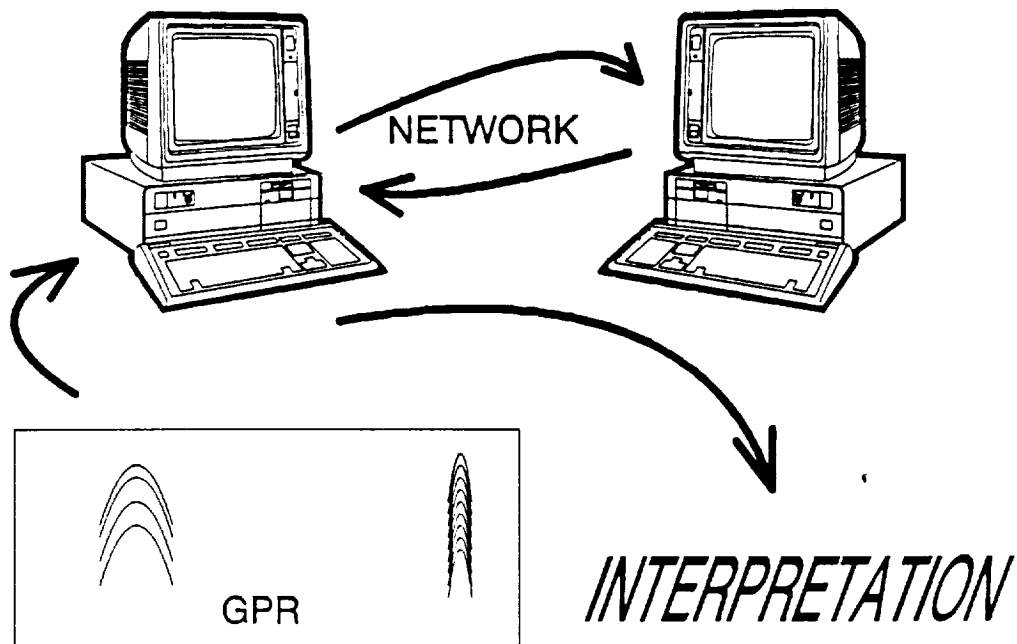
All milestones established for the current reporting period will be achieved by 30 September 1991, and progress is finally moving rapidly.

Create Vision System

Achieving this goal involved coordinating the interaction of three computer paradigms, algorithmic, symbolic and neural, within a distributed object-oriented environment. Conceptually, such a coordination effort is straightforward and can be described using Figure 1.

The subsurface profile pattern is acquired on a mobile rover and preprocessed on the on-board computer (Figure 1, left) system using object-oriented programming (small talk) and procedural and algorithmic programming implemented using "C". The resulting patterns are then sent to a remote computer system (Figure 1, right system), either on-board or at a nearby base station, for pattern recognition, pattern integration and, finally, pattern interpretation, using a combination of neural networks and expert systems. The final interpretation is then returned to the rover for action.

We initially underestimated the difficulty in embedding the neural network and expert system software within a controlling smalltalk program. Despite initial company claims to the contrary, our premier neural network software (Neural Works Professional II) can not be so implemented. Neither, for that matter, could any other neural network software. The typical corporate response to our queries was, "My,nobody has ever tried that. Let me know if you can do it."



1. *OBJECT ORIENTED* PROGRAMMING (SMALLTALK-80)
2. *PROCEDURAL* PROGRAMMING (C)
3. *EXPERT SYSTEMS*
4. *NEURAL NETWORKS*
5. *DISTRIBUTED* PROCESSING

Figure 1. Conceptual diagram of distributed vision system.

It took an heroic effort for Richard Boyd to finally achieve the task. It has been this breakthrough that has permitted the rapid progress in the past several weeks.

The system is now working as illustrated in Figure 1 and shown in more detail in Figure 2. Tests of the system during this phase of research have concentrated on the following:

- 1) Test the system's ability to recognize anomaly spatial location and detailed shape using characteristics of a synthetic GPR pattern.
- 2) Given several possible interpretations for the anomaly, test these using:
 - a) image context
 - b) global context
 - c) expert knowledge.
- 3) Finally, arrive at an interpretation and assign a probability.

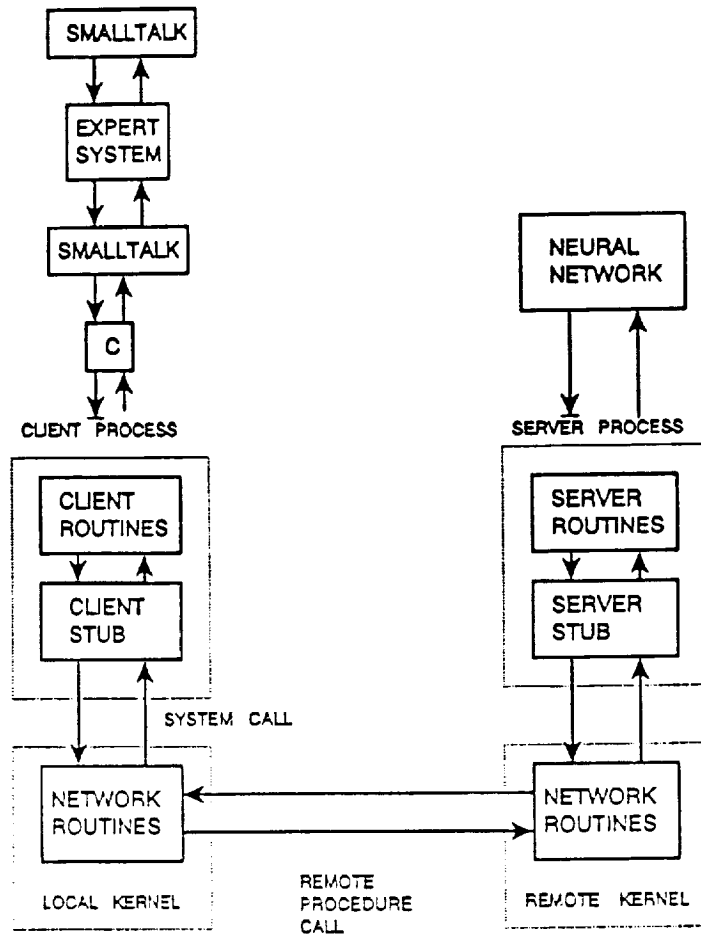
Test Pattern Recognition Ability

Our previous research applied single neural networks for recognizing the spatial location of anomalies using the GPR pattern. To do this, processing was needed that removed many shape aspects of the GPR pattern.

More recent research, funded by The University of Arizona Space Engineering Research Center, however, has demonstrated that the very shape aspects that the preprocessing removed carry important information on characteristics of the anomaly shape, characteristics that help to produce the GPR pattern. We simply were not asking enough of the vision system.

Our initial strategy, the one that is running at this time, uses several neural networks and expert knowledge in a serial implementation, such as that shown in Figure 8. This strategy has been implemented using synthetic data. Training data for the first neural network (BP in Figure 8) consist of the patterns derived from the 19 anomaly shapes contained in Figures 3 through 7. A total of 8 pixels were used to describe each input pattern generated by these anomaly shapes. These pixels contain the following information:

1. Anomaly arm length
2. Anomaly arm slope
3. "V"shape (If the anomaly is opaque, no return is generated from the inside edge.)
4. Intensity of "V"shape (To what degree is the anomaly opaque?)
5. "V"plateau width
6. "V"plateau intensity
7. "M"shape (If the anomaly is transparent, a signal is returned from the inside edge.)
8. Intensity of "M"shape.



1. *SMALLTALK* (OBJECT ORIENTED LANGUAGE)
2. EMBEDS *HUMBLE EXPERT SYSTEM* WITHIN ITS OBJECTS
3. EXPERT SYSTEM CALLS *SMALLTALK CODE*
4. WHICH MAKES CALLS TO *C* (PROCEDURAL LANGUAGE)
5. WHICH CALLS *NETWORK* ON ONE *SUN SPARCSTATION*
6. WHICH MAKES NETWORK CALL TO SECOND *SUN SPARCSTATION*
7. WHICH CALLS *REMOTE C CODE*
8. WHICH CALLS *REMOTE NEURAL NETWORK*
9. WHICH PROCESSES INPUT VECTOR AND SENDS RESULT *BACK*

Figure 2. Detailed algorithm for the current vision system.

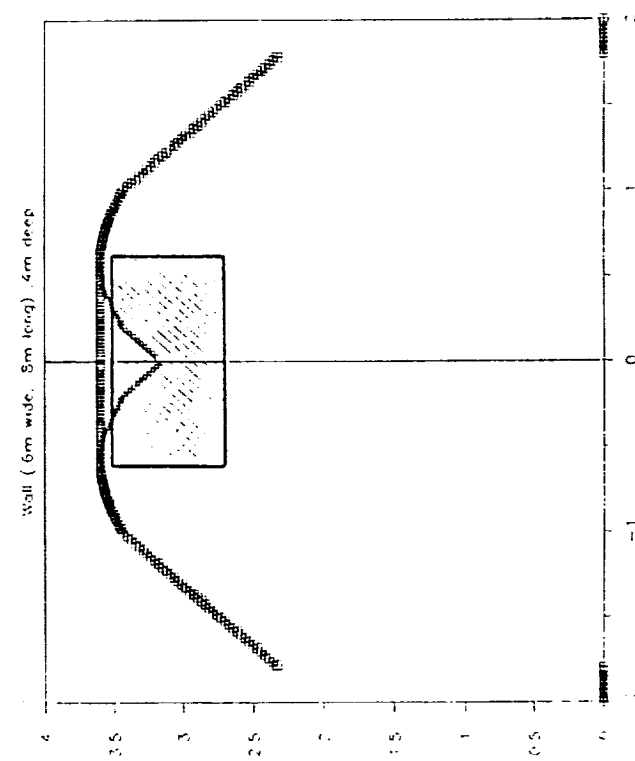
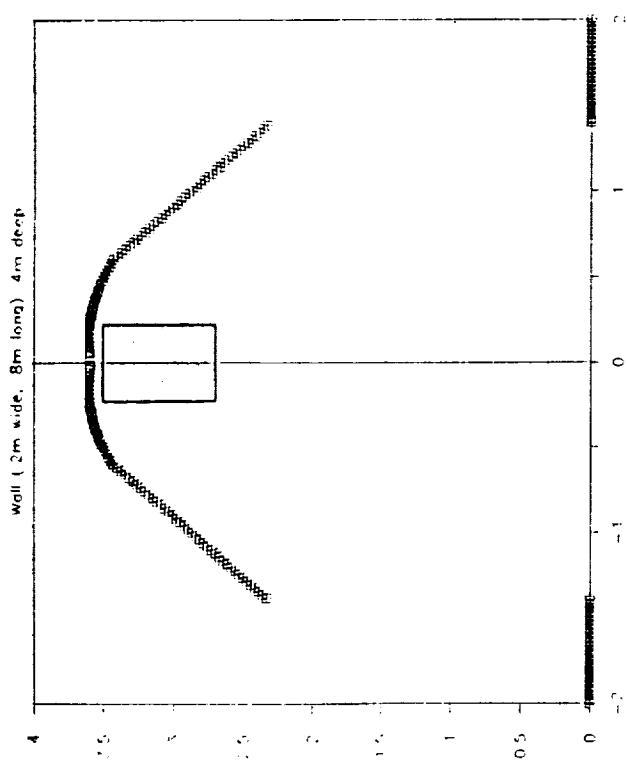
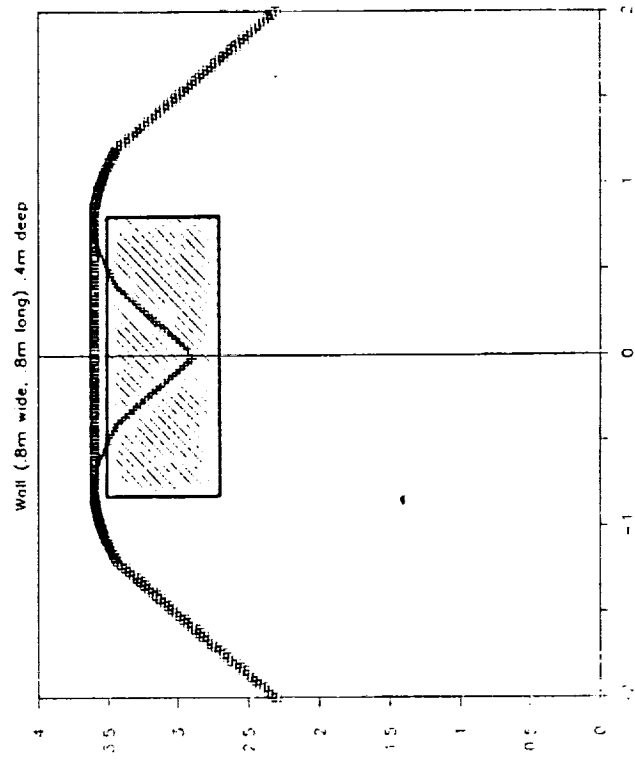
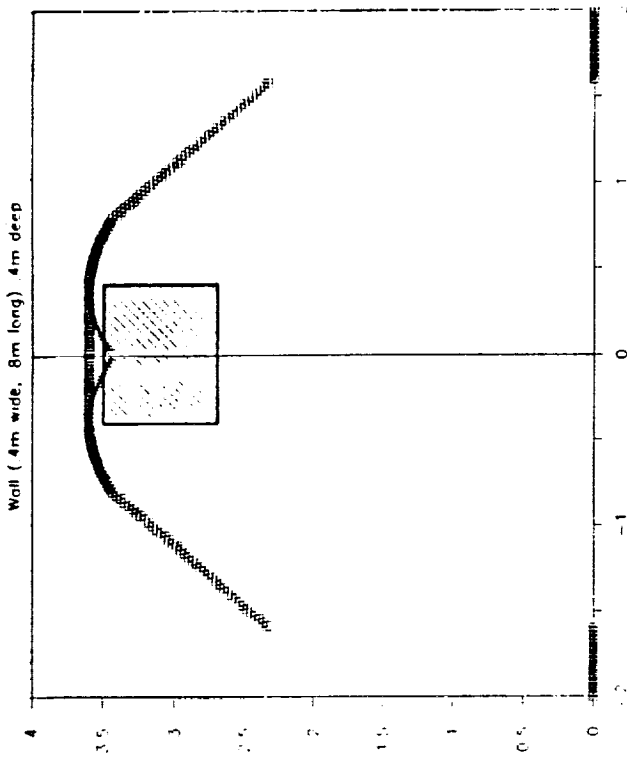


Figure 3. Synthetic GPR profiles over blocks having vertical sides and varying widths, (a) 0.4m, (b) 0.8m, (c) 1.2m, and (d) 1.6m. Reflections from top (squares) and inside surfaces (crosses) are shown.

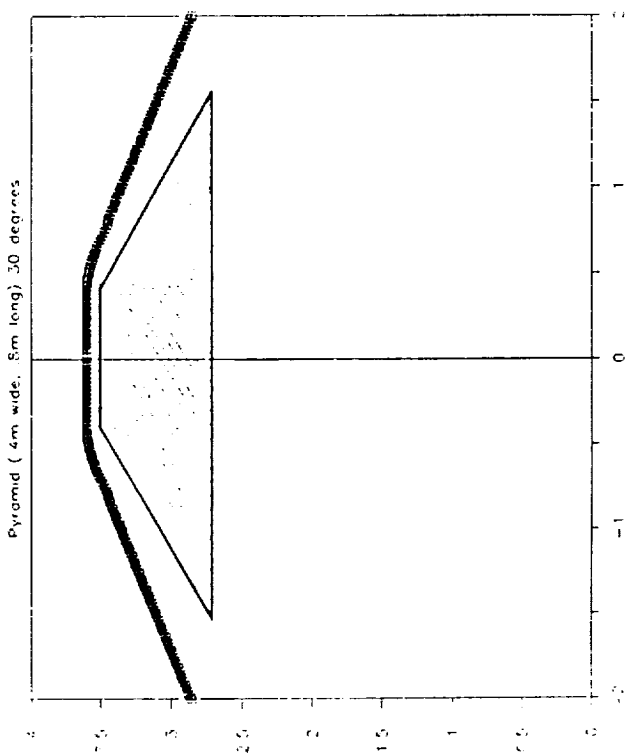
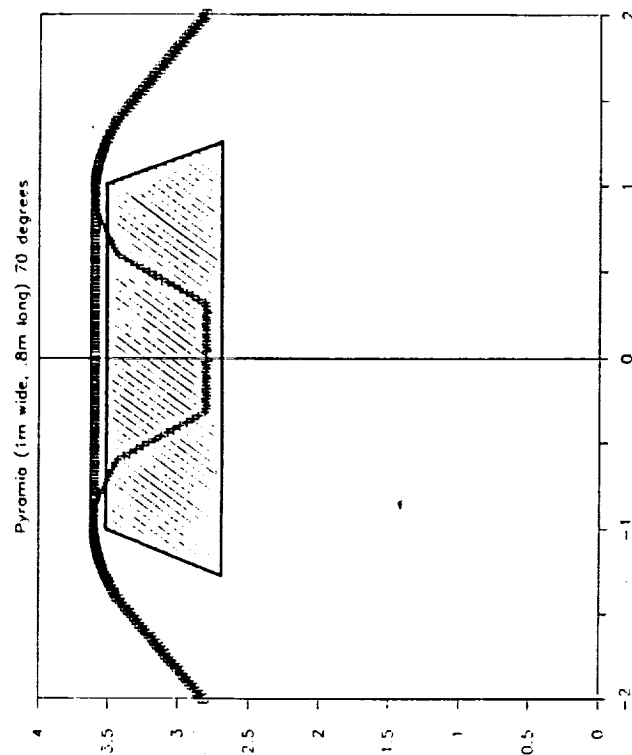
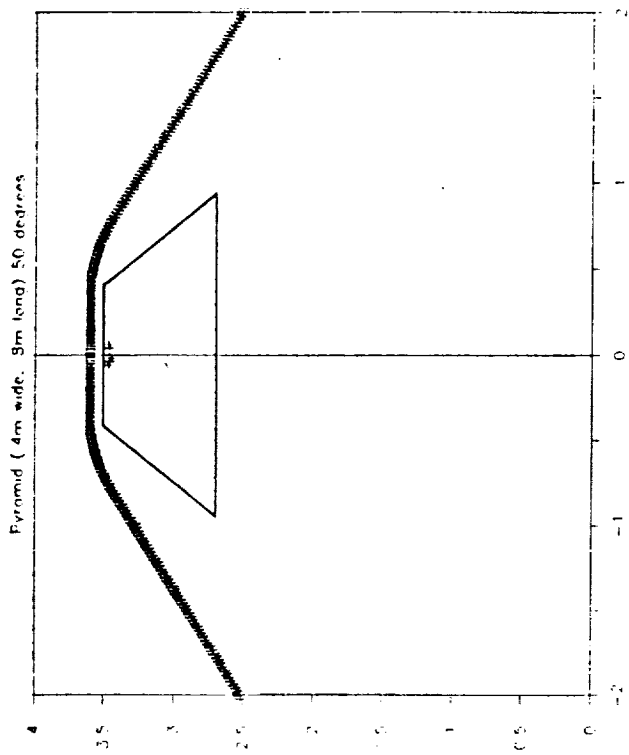
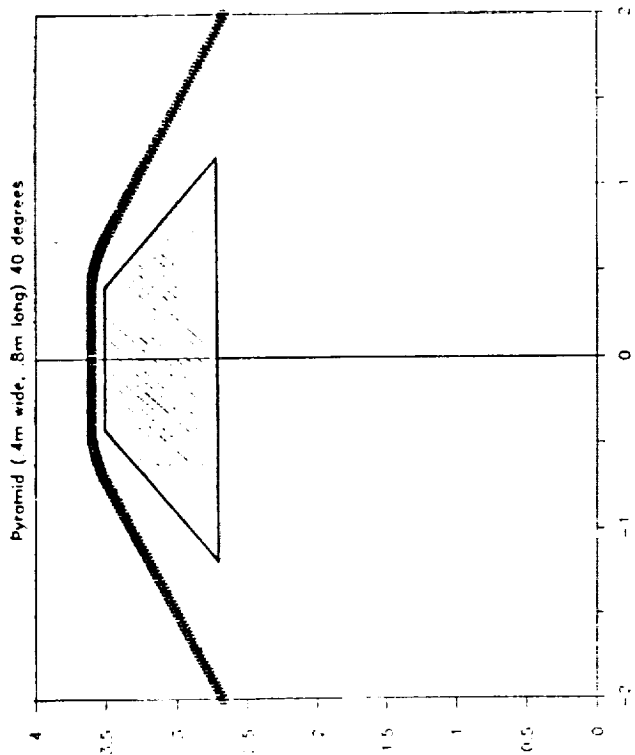


Figure 5. Synthetic GPR profiles over blocks having varying slope angles and widths, (a) 0.8m wide, 50 degrees, (b) 0.8m wide, 40 degrees, (c) 0.8m wide, 30 degrees and (d) 1m wide, 70 degrees. Symbols are described in Figure 3.

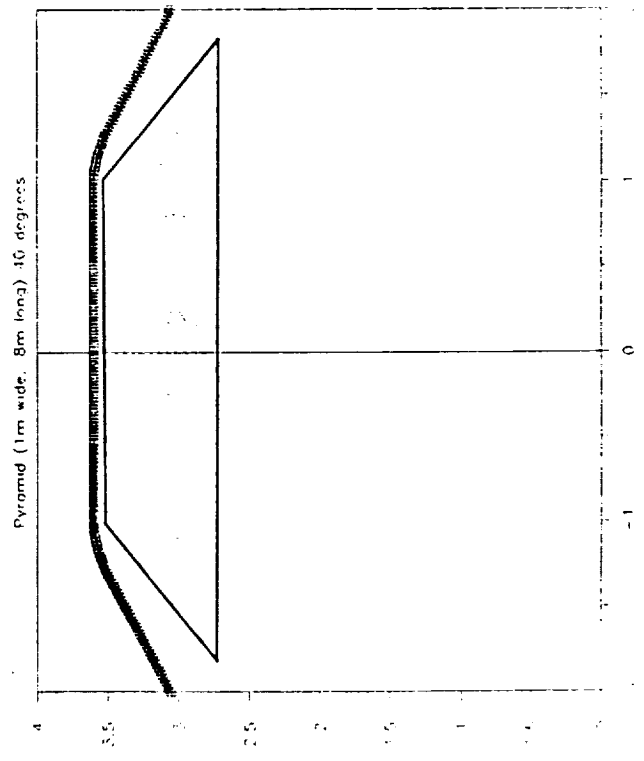
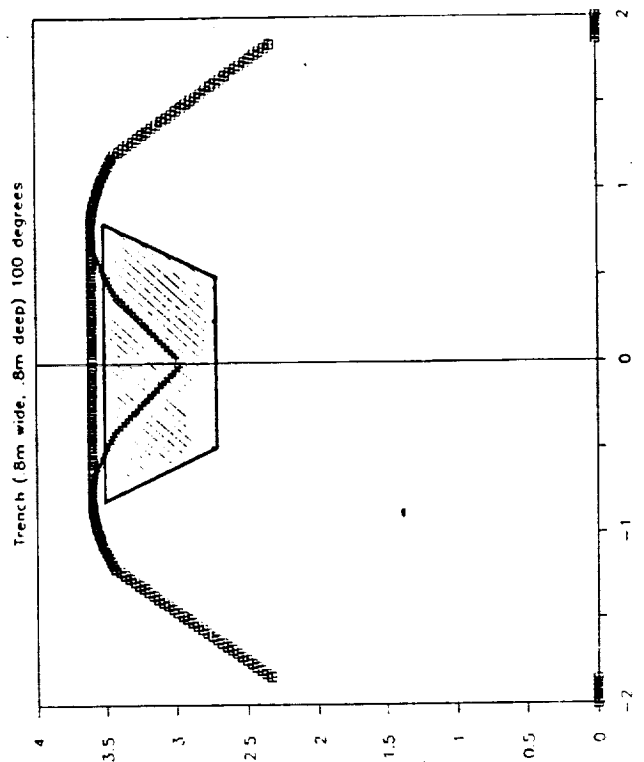
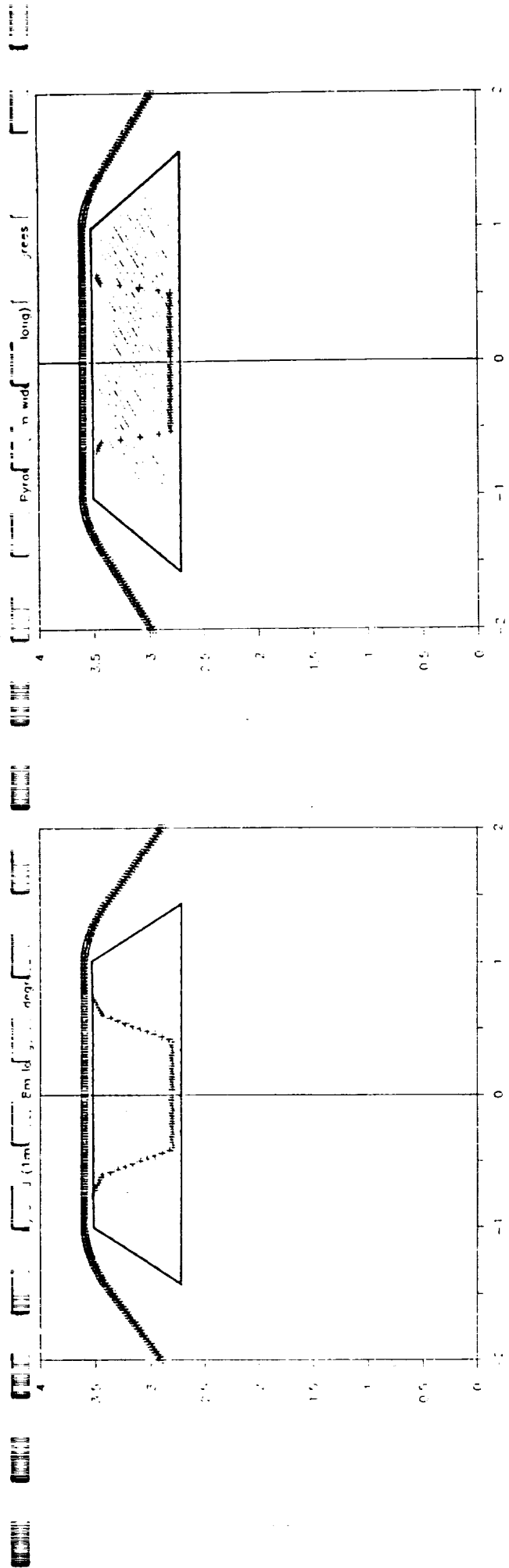


Figure 6. Synthetic GPR profiles over blocks having varying slope angles, (a) 60 degrees, (b) 50 degrees, (c) 40 degrees and (d) 100 degrees. Symbols are described in Figure 3.

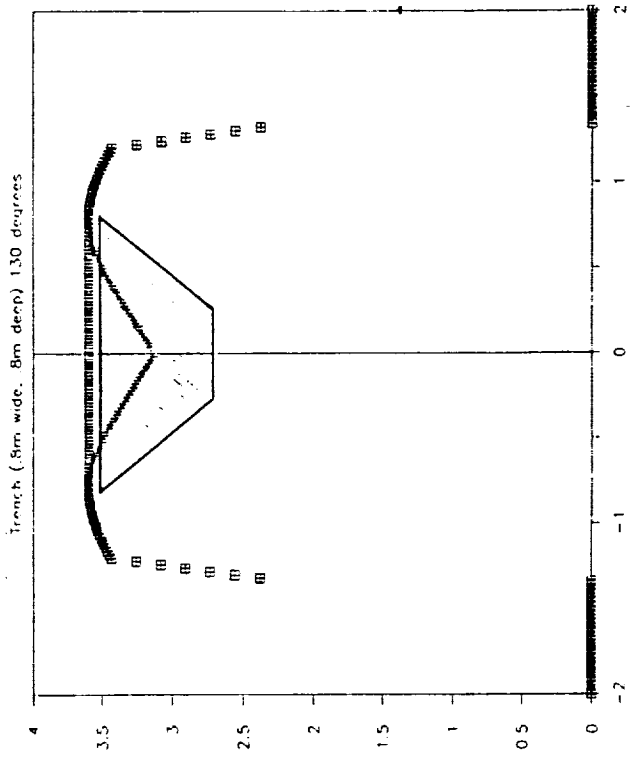
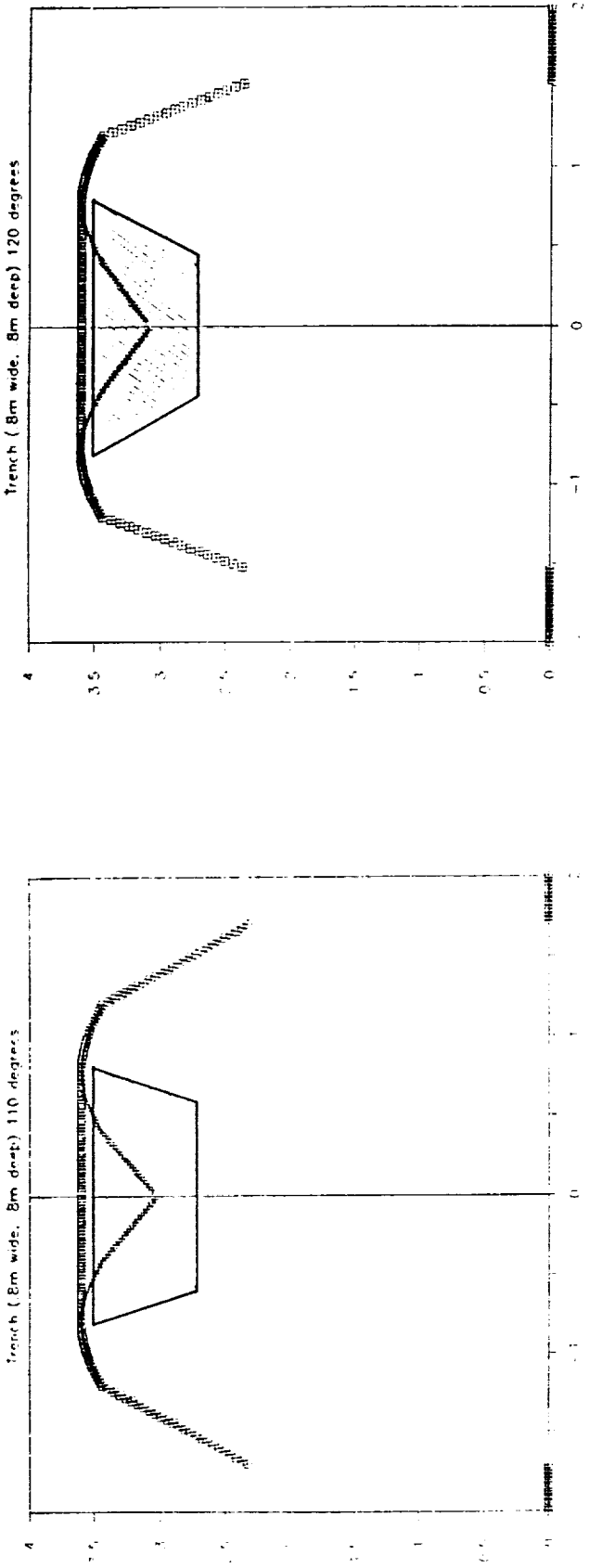


Figure 7. Synthetic GPR profiles over blocks having varying slope angles, (a) 110 degrees, (b) 120 degrees and (c) 130 degrees. Symbols are described in Figure 3.

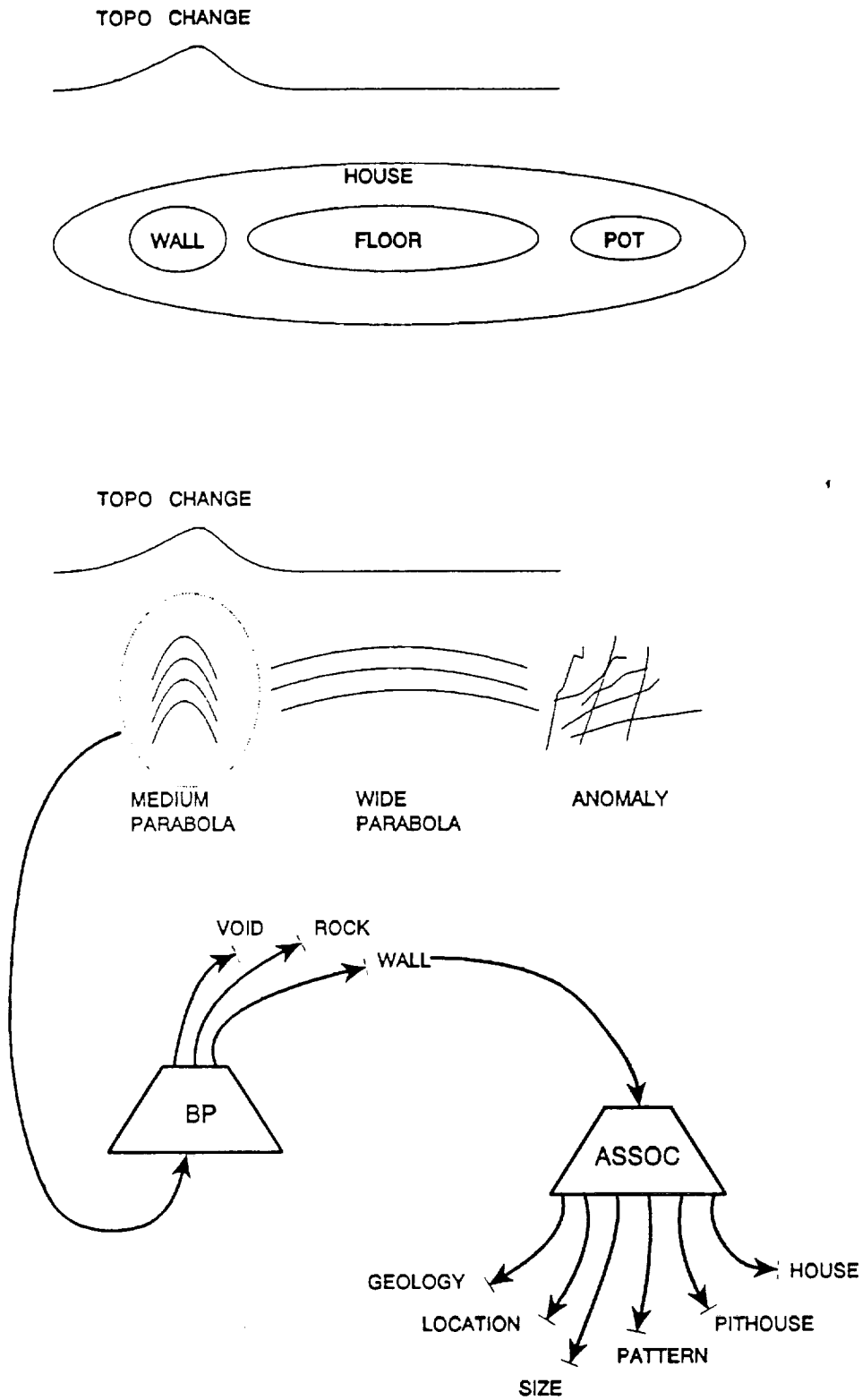


Figure 8. Serial strategy used in the currently operating vision system.

Four pixels represent the desired output. These pixels represent the following aspects of the anomaly shape:

1. Width of anomaly
2. Length of anomaly
3. Depth below surface
4. Angle of anomaly sides.

The output patterns for each of the 19 anomalies are shown in Table I.

TABLE I Output Training Pixels

Anomaly Shape	Anomaly Width	Anomaly Length	Anomaly Depth	Anomaly Angle
3.1	0.2	0.8	0.4	90
3.2	0.4	0.8	0.4	90
3.3	0.6	0.8	0.4	90
3.4	0.8	0.8	0.4	90
4.1	1.0	0.8	0.4	90
4.2	0.4	0.8	0.4	80
4.3	0.4	0.8	0.4	70
4.4	0.4	0.8	0.4	60
5.1	0.4	0.8	0.4	50
5.2	0.4	0.8	0.4	40
5.3	0.4	0.8	0.4	30
5.4	1.0	0.8	0.4	70
6.1	1.0	0.8	0.4	60
6.2	1.0	0.8	0.4	50
6.3	1.0	0.8	0.4	40
6.4	0.8	0.8	0.4	100
7.1	0.8	0.8	0.4	110
7.2	0.8	0.8	0.4	120
7.3	0.8	0.8	0.4	130

Results of training the BP neural net (Figure 8) are shown in Table II, and results using interpolated input patterns are shown in Table III. We are at this time generating test patterns in order to more rigorously test the initial neural network. These tests will be completed by 30 September 1991.

The output from BP in Figure 8 is an abstract shape. For example, shape 3.1 is a rectangular body having a width of 0.4 m and a length of 0.8 m, and buried 0.4 m deep. At this stage we know what the anomaly looks like, but not what the anomaly is. It could be any number of things - a wall, a boulder, a void, among others. At this point the object-oriented programming environment calls another neural network object that assigns a probability to a number of possible hypotheses (e.g. wall, void, boulder, etc.), based on the global context within which the rover is operating. Armed with these probabilities, object-oriented programming pursues the most likely interpretation, using what we shall call image context.

Image Context

Image context involves searching for ancillary patterns within the image, patterns that would tend to support the current, or operating, hypothesis. For example, the neural net labeled ASSOC in Figure 8 would, if it corresponds to an archaeological network within a cultural global context, look for other image patterns that would support the hypothesis that the GPR patterns constitute patterns from a buried house. Other walls, plaster floors, hearths and postholes are but some of the ancillary patterns ASSOC look for. There is naturally some uncertainty involved in this, and not all of these patterns can be found in all houses. Should none of the ancillary patterns be found, the assigned probability for a house is low. This is the first stage in which expert knowledge is used with the neural nets. In our current implementation, control is then passed from ASSOC back to the object-oriented programming environment and another hypothesis is tested using another ASSOC network.

Our current strategy calls for this iteration to continue until all possibilities are exhausted, at which time the interpretations are ranked, and the one having the highest likelihood is passed back to the rover.

At the time of this report all but the last phase, the image context phase, has been completed and tested. The image context phase will be completed and tested by 30 September 1991.

TABLE II Training Results. The first line of each corresponds to the input pixel values.

NETWORK CONFIGURATION
8 Input, 7 Hidden, 4 Output

Statistics: 0.003932 0.079356
Iter, cPat, Iterations: 1001 100 100100

FIGURE 3

0.5330	0.7860	0.6000	1.0000	0.3680	1.0000	0.0000	0.0000
Output:	0.2238	0.8039	0.4030	89.0776			
0.5560	0.7860	0.5000	1.0000	0.5260	1.0000	0.1000	1.0000
Output:	0.4498	0.8036	0.4072	90.8096			
0.5560	0.7860	0.4000	1.0000	0.6320	1.0000	0.5000	1.0000
Output:	0.6219	0.7938	0.3781	89.5417			
0.5560	0.7860	0.3000	1.0000	0.8420	1.0000	0.8000	1.0000
Output:	0.8802	0.8179	0.4288	90.1920			

FIGURE 4

0.5440	0.6070	0.2000	1.0000	1.0000	1.0000	1.0000	1.0000
Output:	0.9576	0.8134	0.4245	88.8857			
0.5000	0.8570	0.5500	1.0000	0.4470	1.0000	0.1000	1.0000
Output:	0.3624	0.7983	0.4006	79.9764			
0.4560	0.9290	0.5500	1.0000	0.4470	1.0000	0.1000	1.0000
Output:	0.3793	0.7970	0.3985	69.9889			
0.4110	1.0000	0.5500	1.0000	0.4470	1.0000	0.1000	1.0000
Output:	0.3976	0.7956	0.3969	59.6641			

FIGURE 5

0.3670	1.0000	0.6000	1.0000	0.4210	1.0000	0.0000	0.0000
Output:	0.3622	0.8168	0.4351	52.1432			
0.3110	0.9640	0.5500	1.0000	0.4470	1.0000	0.0000	0.0000
Output:	0.4002	0.7941	0.3855	39.1103			
0.2560	1.0000	0.5500	1.0000	0.4470	1.0000	0.0000	0.0000
Output:	0.4241	0.7900	0.3793	29.3596			
0.4560	0.5360	0.2000	1.0000	1.0000	1.0000	1.0000	1.0000
Output:	0.9639	0.7976	0.3995	70.1151			

FIGURE 6

0.4110	0.5000	0.2000	1.0000	0.9740	1.0000	1.0000	0.8000
Output:	0.9596	0.7857	0.3751	59.8533			
0.3670	0.5000	0.2000	1.0000	1.0000	1.0000	1.0000	0.7000
Output:	0.9695	0.7933	0.3927	50.7770			
0.3220	0.5710	0.2000	1.0000	1.0000	1.0000	0.0000	0.0000
Output:	0.9536	0.8023	0.4002	40.0512			
0.6220	0.7140	0.3000	1.0000	0.7890	1.0000	0.8000	1.0000
Output:	0.8137	0.8040	0.3941	101.4100			

FIGURE 7

0.6890	0.6790	0.3000	1.0000	0.7890	1.0000	0.7000	1.0000
Output:	0.7888	0.8106	0.4051	110.6656			
0.7890	0.6070	0.2000	0.9000	0.8160	1.0000	0.7000	0.9000
Output:	0.7895	0.7938	0.3754	120.1961			
0.9220	0.5710	0.1000	0.7000	0.8160	1.0000	0.7000	0.7000
Output:	0.7864	0.7929	0.3929	126.7778			

TABLE III Test Pattern Results. The first line of each corresponds to the input pixel values.

FIGURE 3 INTERPOLATED

0.5450	0.7860	0.5500	1.0000	0.4470	1.0000	0.0500	0.5000
Output:	0.3252	0.8069	0.4100	90.2459			
0.5560	0.7860	0.4500	1.0000	0.5790	1.0000	0.3000	1.0000
Output:	0.5359	0.7995	0.3939	90.2728			
0.5560	0.7860	0.3500	1.0000	0.7370	1.0000	0.6500	1.0000
Output:	0.7755	0.8057	0.4023	89.8405			

FIGURE 4 INTERPOLATED

0.5220	0.7320	0.3750	1.0000	0.7240	1.0000	0.5500	1.0000
Output:	0.7731	0.8046	0.4084	84.1993			
0.4780	0.8930	0.5500	1.0000	0.4470	1.0000	0.1000	1.0000
Output:	0.3708	0.7976	0.3995	75.0279			
0.4340	0.9640	0.5500	1.0000	0.4470	1.0000	0.1000	1.0000
Output:	0.3880	0.7964	0.3978	64.9207			

FIGURE 5 INTERPOLATED

0.3390	0.9820	0.5750	1.0000	0.4340	1.0000	0.0000	0.0000
Output:	0.3809	0.8057	0.4100	45.4248			
0.2840	0.9820	0.5500	1.0000	0.4470	1.0000	0.0000	0.0000
Output:	0.4117	0.7921	0.3825	34.0834			
0.3560	0.7860	0.5500	1.0000	0.4470	1.0000	0.0000	0.0000
Output:	0.3843	0.7878	0.3783	49.8434			

FIGURE 6 INTERPOLATED

0.3890	0.5000	0.2000	1.0000	0.9870	1.0000	1.0000	0.7500
Output:	0.9649	0.7896	0.3839	55.2821			
0.3440	0.5360	0.2000	1.0000	1.0000	1.0000	0.5000	0.3500
Output:	0.9622	0.7978	0.3957	45.0504			
0.4720	0.7920	0.2500	1.0000	0.8940	1.0000	0.4000	0.5000
Output:	0.9004	0.8134	0.4105	71.1546			

FIGURE 7 INTERPOLATED

0.7390	0.6430	0.2500	0.9500	0.8020	1.0000	0.7000	0.9500
Output:	0.7882	0.8022	0.3894	116.0878			
0.8560	0.5890	0.1500	0.8000	0.8160	1.0000	0.7000	0.8000
Output:	0.7877	0.7933	0.3841	124.3598			

Statistics: 0.004476 0.080128

Iter, cPat, Iterations: 0 100 0

Global Context

Global context oversees the design and implementation of the entire vision system in terms of probability assignments. We have, for instance, ample examples of prehistoric and historical cultural patterns within driving distance of the University; hence, rooms, hearths and other cultural activity present viable hypotheses for GPR patterns, and are important for testing the vision system. The global context for a lunar rover, though, would possess a different global context which would emphasize its own sets of hypotheses.

STRATEGY FOR PROJECT CONTINUATION

Parallel Neural Networks

At the present time, the vision system is implemented serially.¹ The vision systems of the higher life forms, however, are massively parallel. Continuation funding will be used to model this parallel processing using Neural Windows. This strategy will permit the implementation of up to 128 neural networks running simultaneously in parallel. This research will have the following milestones:

1. Implement the image context phase of the vision system using parallel neural networks.
2. Test the parallel system on the same synthetic GPR data used to test the serial system.
3. Implement parallel neural networks throughout the vision system.

Continue Incremental Testing

Incremental testing using our laboratory test tank will follow synthetic data testing. The final milestones for project continuation will be to:

1. Laboratory Test Tank

This phase will test the system in a more natural environment, but still in a well controlled, laboratory situation.

The modeling scheme will be chosen to provide an attenuation per wavelength similar to that found in the field. In this way, the same conditions encountered in the field can be modeled in a controlled environment. Using this unique facility, the influence of EM wave velocity, profiling speed and background attenuation on GPR patterns can be assessed while still maintaining homogeneous background conditions. The research during this phase will evaluate the ability of the GPR vision system to extrapolate from synthetic patterns to real, but still ideal, patterns. This phase will also be interactive as the system is adjusted to improve performance.

2. Field Test

As a final test, the GPR system will be applied using the GPR test facility at the San Xavier Geophysical Test Site. Details of this site are provided in McGill (1990).

REFERENCES

- Glass, C.E., B.K. Sternberg, and M.M. Poulton, 1991, Continuous profiling subsurface monitoring using adaptive pattern recognition, Proc. Inter. Symp. on Mine Mechanization and Automation, Vol. 2, pp. 17-29 to 17-38, Golden, CO, June 10-13.
- McGill, J.W., 1990, Ground penetrating radar investigations with applications for southern Arizona, M.S. Thesis, The University of Arizona, Tucson, AZ 85721.
- McGill, J.W., B.K. Sternberg, and C.E. Glass, 1989, Applications of ground penetrating radar in southern Arizona, Report of the Laboratory for Advanced Subsurface Imaging, LASI-89-2, The University of Arizona, Tucson, AZ 85721.
- McGill, J.W., B.K. Sternberg, and C.E. Glass, 1990, GPR research at the University of Arizona, 3rd Internat. Conf. on Ground Penetrating Radar, Poster Presentation, Lakewood, CO.
- Minsky, M.L. and S. Papert, 1958, Perceptions, MIT Press, Cambridge.



**DETERMINATION OF LUNAR ILMENITE ABUNDANCES FROM
REMOTELY SENSED DATA : 3/91-9/91 REPORT**

Robert B. Singer, Stephen M. Larson, Jeffrey R. Johnson, and David E. Melendrez
Department of Geosciences/Lunar and Planetary laboratory
University of Arizona

ABSTRACT

Quantitative large area survey mapping of the TiO₂ abundance on the lunar nearside mare at 5.3 km resolution has been completed, identifying the areas of highest concentrations (>10 wt %) in Mare Tranquillitatis and Oceanus Procellarum. Complementary 330-1000 nm spectroscopy of a variety of compositional units confirms the abundance values at higher spatial and spectral resolution. We have identified a more sensitive spectral ratio for TiO₂ mapping and applied it to high spatial resolution imaging with an experimental 2048² CCD giving a scale of 240 m/pixel on the moon. These high resolution maps provide far more detail on the spatial distribution of the high TiO₂ deposits. Tests of the response properties of the CCDs in the near-ir show that they are far superior to the vidicons used in the past for remote sensing applications.

DETERMINATION OF LUNAR ILMENITE ABUNDANCES FROM
REMOTELY SENSED DATA : 3/91-9/91 REPORT

Robert B. Singer, Stephen M. Larson, Jeffrey R. Johnson and David E. Melendrez
Department of Geosciences/Lunar and Planetary Laboratory
Planetary Image Research Laboratory
University of Arizona

BACKGROUND

The mineral ilmenite (FeTiO_3) was found in abundance in lunar mare soils returned during the Apollo project. Lunar ilmenite often contains greater than 50 weight-percent titanium dioxide (TiO_2), and is a primary potential resource for oxygen and other raw materials to supply future lunar bases. Chemical and spectroscopic analysis of the returned lunar soils produced an empirical function that relates the spectral reflectance ratio at 400 and 560 nm to the weight percent abundance of TiO_2 (Charette et al., 1974). This allowed mapping of the lunar TiO_2 distribution using telescopic vidicon multispectral imaging from the ground (eg. Johnson et al., 1977). However, the time variant photometric response of the vidicon detectors produced abundance uncertainties of at least 2-5%. Since that time, solid-state charge-coupled device (CCD) detector technology capable of much improved photometric response has become available.

We have been continuing an investigation of the lunar TiO_2 distribution utilizing groundbased telescopic CCD multispectral imagery and spectroscopy. The work has been approached in phases to optimize the results based upon initial experiences. The goal is to achieve the best possible TiO_2 abundance maps from the ground as a precursor to lunar orbiter and robotic sample return missions, and to produce a better idea of the peak abundances of TiO_2 for benefaction studies. These phases and the results thus far are summarized below.

A. Low spatial resolution global survey producing a photometrically homogeneous TiO_2 map of the entire lunar near-side using the traditional 400/560 nm ratio. This involved constructing a Newtonian focus on the Tumamoc Hill 0.5 m telescope to produce an appropriate scale on the CCD, and a filter wheel to facilitate rapid cycling between filters. With this arrangement, the visible lunar disc could be covered with a mosaic of 5 CCD fields with 5.3 km pixels on the moon. The resulting map shows that the highest TiO_2 regions are in Mare Tranquillitatis and Oceanus Procellarum. Where they overlap, most of this map is consistent with the Apollo Gamma Ray Spectrometer data, but with much better spatial resolution.

Maps based on 950/560 nm ratios were also made to define the location of locally mature mare soil for which the spectral TiO_2 abundance relation is considered valid. In this ratio, fresh craters appear dark because of abundant pyroxene grains which produce strong absorption near 950 nm due to Fe^{2+} crystal field transitions. Micrometeoroid impacts over time increases the agglutinate content and a weakening of the 950 nm pyroxene absorption band. We obtained substantial differences from previous 950/560 nm ratio maps which seem to result from inexact correction of scattered light in the silicon vidicon tubes. The silicon substrate becomes transparent at wavelengths longward of 800 nm, and because of the high index of refraction causes "light piping" within the CCD. This scattering can substantially alter the effective modulation transfer function of the detector preferentially for the longer wavelengths. Previous investigators attempted to correct for this by subtracting a constant "DC level" from the 950 nm image. Studies of the lunar limb profiles and laboratory testing of our CCD

shows that the thinned silicon substrate does not exhibit significant scattering. Because of this, we feel that we can better identify regions of various relative soil maturity.

B. Medium resolution (1 nm) 330-870 nm spectrophotometry of high TiO₂ regions to investigate a broader spectral range and identify spectral signatures which might alter the interpretation of the image ratio values. Using the all-reflecting Larson IHW CCD spectrograph on the Tumamoc Hill 0.5 m telescope, we adopted a technique of dividing the spectrum of the region of interest by a spectrum of the standard area MS-2 taken within 10 - 30 seconds to correct for terrestrial atmospheric extinction, instrumental response, solar Fraunhofer absorption lines and the general red spectral slope of the moon. With relative photometric uncertainties of only 0.1%, the resulting spectra can be readily compared and show many new spectral features, especially in the near-ultraviolet region. Follow-up spectrophotometry was obtained with better spatial resolution on the Catalina 1.5 m telescope of all of the Apollo sites (for "ground truth" checks with returned samples), the high TiO₂ areas and other relevant locations on the moon.

C. Absolute spectral calibration of the standard area MS-2 with respect to flux calibrated solar analog stars is underway with data obtained with the Catalina 1.5 m telescope to convert the ratio spectra to absolute reflectivity for more direct comparison with the laboratory spectra of Apollo samples. The long slit spectra also permitted determination of the spatial extent of the spectrally uniform MS-2 standard area, and what errors are introduced by imprecise pointing of the spectrograph slit aperture.

D. Investigation of laboratory spectra of lunar samples in the Brown University RELAB database to clarify apparent inconsistencies and uncertainties in the empirical abundance relationship. High spatial resolution groundbased spectra of the Apollo landing sites are needed to test the consistency between spectra of returned samples and groundbased data.

E. As a result of B and D, we have found that the use of 400/730 nm image ratios appear to show the same feature distribution as the 400/560 nm ratios but at higher spectral contrast. The 400/730 nm image ratios may thus yield better TiO₂ abundance accuracy due to higher spectral contrast.

F. To make the best possible TiO₂ abundance maps from the ground, we have applied an experimental 2048 by 2048 pixel CCD built by Photometrics Ltd. of Tucson. A successful observing run on the Catalina 1.5 m telescope on 1990 Dec. 1-2 yielded good images with 240m pixel size of 7 areas on the moon at .36, .40, .56, .73 and .95 nm. These selected areas include all of the Apollo landing sites, MS-2, and the high TiO₂ regions in Mare Tranquillitatis and Oceanus Procellarum. The resulting ratio images will help determine the sharpness of composition boundaries and compositional variations in the Apollo landing sites. The smaller sample size shows more localized areas of higher TiO₂ abundance.

PROGRESS IN THE 3/91 - 9/91 REPORTING PERIOD

This reporting period is shorter than the usual 12 months due to an adjustment in anniversary date.

A. The results of the global mapping phase is now in press after substantial refinement of the lengthy paper (Johnson et al., 1991a). and a paper on the scattering properties and suitability of CCDs for multispectral imaging in the near-IR was also submitted

(Larson et al., 1991b). Papers and abstracts relating to this work have already been extensively referenced by other groups. The global digital data are now in the public domain, and have been requested and supplied to a number of other research groups.

B. The Tumamoc spectrophotometry has been confirmed with the additional observations with the Catalina 1.5m telescope. Reductions have progressed to combining red and blue sections giving 320-1000 nm spectra relative to the standard area MS-2. We placed the UV part of the spectrum closer to the center of the CCD as a precaution against instrumental effects on the important spectral slope changes in that region. These spectra, besides giving quantitative ratio values for the Apollo ground truth sites and high TiO₂ locations, contain interesting new spectral features possibly caused by Fe-bearing minerals. The long slit data permit a quantitative determination of the spatial extent of compositional homogeneity, which we have done for all of the targets. We find, for example, that the spectra of the standard MS-2 area is consistent to the 0.1% level over an area of 40km.

C. With the Catalina 1.5m telescope spectra reduced, we are now able to determine the absolute bidirectional reflectance of MS-2 over the 320-1000nm range. This will enable the other areas to be directly compared to laboratory spectra of the returned Apollo samples.

D. The Brown University RELAB spectra were analyzed to better understand the basis for the Charette et al. TiO₂ relation and to help derive a more sensitive relation using the 400/730 nm ratio (see E).

E. The 400/730 nm image ratio provides an improvement in sensitivity resulting from a 37% increase in spectral contrast. These results have been presented (Johnson et al., 1991b) and are in press (Johnson, et al, 1991c).

F. All of the high resolution 2048² CCD images have now been reduced, registered, and ratioed. Conversion to weight percent TiO₂ is currently underway. Some of the fields appear to be as good as the best full moon photographic images yet obtained from the ground. Preliminary results have been given (Melendrez et al., 1991), and a paper on these results is currently in preparation.

Partly in response to our results, C. Pieters at Brown University has undertaken a program to remeasure spectra of Apollo soil samples for a range of phase angles. The phase function variation with wavelength is one outstanding problem which may alter the Charette et al. TiO₂ abundance relation. Pieters' preliminary results indicate a measurable phase effect, but the laboratory samples do not mimic the mechanical configuration of soil grains on the lunar surface. To help minimize any phase effect in the data obtained so far, we have made all of our observations within a day or two of full moon. Measurements of a few selected lunar sites over a range of phase angles are needed to ensure that there is not a significant phase effect on ratio values. The Tumamoc Observatory 0.5m telescope now has a new, dedicated CCD permanently mounted that can be used whenever the sky is clear. It will be possible to obtain the phase function data with a minimum of effort this fall.

REFERENCES

- Charette, M.P., McCord, T.B., Pieters, C and Adams, J.B. (1974). Application of remote spectral reflectance measurements to lunar geology classification and determination of titanium content of lunar soils. *J. Geophys. Res.* 79, 1605.

- Johnson, J.R., Larson, S.M., and Singer, R.B. (1990a). Estimates of lunar mare titanium and ilmenite abundances from CCD imaging and spectroscopy. Abstracts of the LPSC XXI, 567-568.
- Johnson, J.R., Larson, S.M., and Singer, R.B. (1990b). Remote compositional mapping of potential lunar resources. Bull. Am. Astron. Soc., 22, no. 3, 1048.
- Johnson, J.R., Larson, S.M., and Singer, R.B. (1991a). Remote sensing of potential lunar resources: I. Global compositional mapping. J. Geophys. Res., in press.
- Johnson, J.R., Larson, S.M., and Singer, R.B. (1991b). Spectral ratio methods for telescopic lunar TiO₂ mapping. LPSC XXII Abs. 647.
- Johnson, J.R., Larson, S.M., and Singer, R.B. (1991c). A Reevaluation of spectral ratios for lunar TiO₂ mapping. Geophys. Res. Lett., in press.
- Johnson, T.V., Saunders, R.S., Matson, D.L. and Mosher, J.A. (1977). A TiO₂ abundance map for the northern maria. Proc. Lunar Sci. Conf. 8th, 1029-1036.
- Larson, S.M., Johnson, J.R. and Singer, R.B. (1991a). Mapping lunar soil maturity using groundbased CCD multispectral imagery. LPSC XXII Abs. 783.
- Larson, S.M., Johnson, J.R., and Singer, R.B. (1991b). An evaluation of the near-infrared scattering properties of CCD detectors in lunar remote sensing applications. submitted to Geophys. Res. Lett.
- Melendrez, D.E., Larson, S.M., Johnson, J.R., Singer, R.B., Schempp and P. Doherty (1991). High spatial resolution mapping of lunar titanium abundances using groundbased multipsectral CCD images. LPSC XXII Abs. 887.
- Swindle, T.D., Johnson, J.R., Larson, S.M., and Singer, R.B. (1991). Systematic variations in solar wind fluence with lunar location: Implications for resource utilization. DPS abstract submitted.



Compositions of Near Earth Asteroids

Larry A. Lebofsky and Marcia L. Nelson
Lunar and Planetary Laboratory
University of Arizona
Tucson, AZ 85721

ABSTRACT

The goal of this study is to determine whether any of the near-Earth asteroids contain hydrosilicate minerals. If these minerals are present, they would provide a ready source of water for propellant generation and use in life support systems. Some of the dark asteroids in the main asteroid belt have been shown to contain hydrated phyllosilicate minerals. Some of the near-Earth asteroids are also dark, but telescopic detection of water on the near-Earth asteroids is complicated because thermal emission masks the diagnostic absorption features for objects close to the sun. High resolution telescopic spectra, and sophisticated models will be necessary to determine whether the water adsorption features are present on any of the near-Earth asteroids. This year, we have continued development of these models.

Introduction

The CI1 and CM2 carbonaceous chondrite meteorites are known to contain hydrated phyllosilicate minerals in their matrix materials, although the fine grain size has made it difficult to determine the specific minerals present. Some of the CI1 meteorites even contain evaporite minerals which are believed to have been deposited when a heating event allowed liquid water to migrate through the parent body, eventually depositing evaporates. Asteroidal size bodies with these compositions would prove rich source of water and oxygen, and the resources might be easier to extract from phyllosilicates than other oxides.

Reflectance spectra of the hydrated carbonaceous chondrite meteorites are similar to telescopic spectra of some of the dark asteroids in the main asteroid belt, implying similar mineralogy. Unfortunately, it is difficult to obtain accurate telescopic spectra of dark asteroids, and the dark components in their surface mask the diagnostic, near-infrared absorption features of the silicate minerals presumed to be present. The major water-of-hydration absorption feature at approximately 3 micrometers is sufficiently strong that it is not masked by the dark components of the surface, which makes it possible to determine whether hydrated phases are present, even if it is not possible to determine the exact mineral species. Detection of water on Ceres by Lebofsky confirmed both the presence of water in the asteroid belt, and the feasibility of detecting it telescopically. It also led to the general idea that all dark asteroids were primitive and volatile rich.

Telescopic surveys by Lebofsky and coworkers have shown that some of the dark asteroids do contain hydrated minerals, but not all, which has forced a re-evaluation of the simple idea that dark necessarily means volatile rich. They have proposed that the dark asteroids in the main asteroid belt accreted from water ice and anhydrous silicates, and heating events later melted the water in some of them, producing hydrated silicates. If this explanation is correct, then at least the dark asteroids in the outer asteroid belt probably do contain volatiles, even if they are no longer present at the surface. An additional complication for the inner asteroid belt has been proposed by Dan Britt who has shown that black chondrites, which are shock darkened ordinary chondrites (which are totally anhydrous) are spectrally indistinguishable from some of the dark asteroids in the visible and near-infrared. Both ideas together explain many problems in interpreting the history of the asteroid belt, but they complicate the determination of the composition of individual asteroids tremendously.

The near-Earth asteroids are dynamically much easier to reach than the main belt asteroids, which would make them more feasible resource targets. Most of the taxonomic types known in the main asteroid belt have been found in the near-Earth asteroid population, as well as

one which has not yet been detected in the main belt. Unfortunately, as the previous paragraph mentioned, asteroids which are the same taxonomic type may well be compositionally different because the taxonomy was defined using only visible and extremely-near-infrared wavelengths, which do not include the wavelengths which are sensitive to hydrated minerals. This makes it impossible to predict which dark near-Earth asteroids will contain water without more extensive telescopic spectra. In addition, the near-Earth asteroids are nearer to the sun than the main belt, which makes them warmer, which in turn moves the peak of their thermal emission to shorter wavelengths. This is particularly true of the dark asteroids. For the dark near-Earth asteroids, the thermal emission is large enough to mask the absorption feature caused by hydrated minerals. Simple thermal models can be used for the main belt asteroids because they are much cooler, but these models are insufficient to correct the near-Earth asteroids for thermal emission.

Bruce Hapke has proposed the first theory that models the reflected light and emitted radiation simultaneously, which offers the best opportunity for modeling the spectra of the near-Earth asteroids. The model is an application of radiative transfer theory to particulate surfaces. It includes terms for the absorption and scattering properties of the component minerals, the photometric geometry, and the physical properties of the surface. Reflectance spectra can be calculated from the model and compared to measured spectra, or the model can be fit to observational data, making appropriate assumptions for the unknown parameters. Parts of this theory have been, and are being tested extensively, but the thermal terms are new and relatively untested. We have proposed to investigate this theory to determine its validity and applicability to the problem of analysis of near-Earth asteroid spectra.

Results for this Year

This year, Marcia Nelson has continued to explore the applications of Hapke theory. She has continued to build on her work with the grain size that she began last year. In most of the applications of interest to this project, the grain size of the components is unknown. She is investigating the effects of this uncertainty on the model results starting with the mineralogically simple asteroid Vesta. (Vesta is much simpler than the dark asteroids because it is essentially basalt, which doesn't include the dark components which make working with the dark asteroids so difficult.) The modeling has been complicated because laboratory spectra of well characterized and chemically appropriate minerals are not available in the literature and the University of Arizona has not yet been able to obtain funding to purchase a laboratory spectrophotometer. She is varying the grain sizes of the components through reasonable ranges to determine the range of plausible

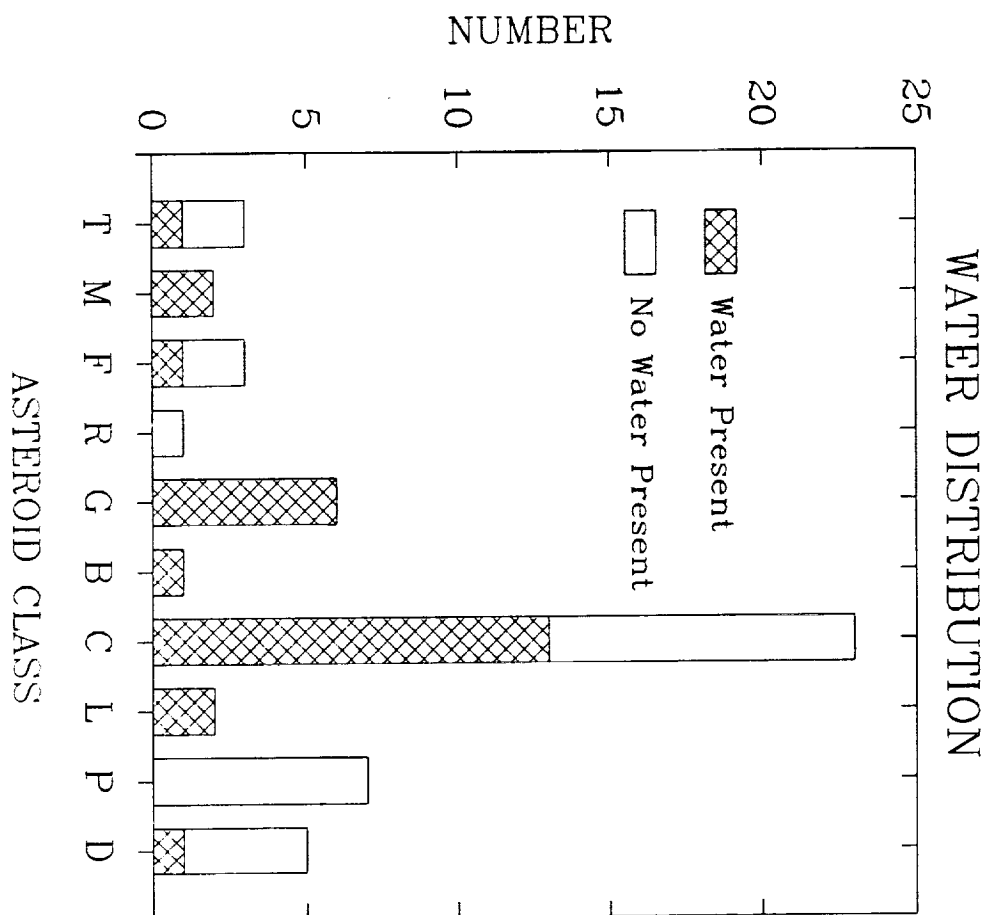
compositions and trying to determine ways to decide which of these are most probable. This will be more difficult for the dark asteroids because the matrix material is so fine-grained that it will have to be treated as a single, composite component. The Vesta work will help determine how to deal with this problem.

We have also prepared a review paper on asteroid composition for the Resources of Near-Earth Space book, in conjunction with Dan Britt. The paper will update the existing review papers on asteroid compositions, and provide comprehensive spectral figures of all the asteroid and meteorite types in one place for the first time.

Publications

Nelson, M.L., D. Britt, and L.A. Lebofsky, "Overview of the Asteroids", Resources of Near-Earth Space, (submitted).

Lebofsky, L.A., E.S. Howell, and D.T. Britt, "Characterization of Low Albedo Asteroids", Presented at the Meteoritical Society Meeting, Palo Alto, CA, (1991).





SPACEWATCH DISCOVERY OF NEAR-EARTH ASTEROIDS

Tom Gehrels

Lunar and Planetary Laboratory

Abstract

Spacewatch discovered 15 near-Earth asteroids by automatic detection. Papers were published describing the Spacewatch programs and the analysis of the data. Many public presentations were made. In the range of diameters 100-10 meters, a cometary contribution comes in in a dominant manner. The Spacewatch techniques are being developed further.

1991 Progress Report
to the
Space Engineering Research Center
by
Tom Gehrels

Our principal accomplishment since February 1991 has been in three areas, namely the discovery of near-Earth asteroids, the presentation of our results to peers and public, and the development of new techniques.

Discovery

This was the first season of automatic discovery of near-Earth asteroids, which began in a spectacular way in September 1990 and was carried through the month of June, 1992, after which we stopped for refurbishment during the monsoon months. We will start observing again on August 30, 1991. The Table below gives the complete listing of our discoveries of near-Earth asteroids to date.

We had made two predictions before September 1990, namely by Rabinowitz that we would find 13 and by Gehrels that we would find 17 during these 10 lunations. We found 15. The success of our predictions means that we have used the proper magnitude-frequency relation which is the one that we know for the asteroid belt from the Palomar Leiden Survey, namely that the number increases by a factor of 2.5 for each magnitude fainter. This is correct in first approximation and it is the magnitude-frequency relation for fragmentation. However, we were able to derive important effects at the smaller sizes.

Publications and Presentations

The paper by Rabinowitz "Detection of Earth-Approaching Asteroids in Near Real Time", Astron. J. 101 of April 1991 has come out, and we have reprints for it. The review paper "Scanning with Charge-Coupled Devices" by T. Gehrels will appear in Space Science Reviews in November 1991. A general description of the project was also presented and will be published by the "Asteroids, Comets and Meteors Conference" in Flagstaff in June. Furthermore, Rabinowitz presented a paper there which will be published in the same book, and also in more extended form in Icarus with the title "The Flux of Small Asteroids Near the Earth."

The last paper is the most important because it comes to the

Spacewatch Discoveries to Date

Identification	Perihelion distance (AU)	Aphelion distance (AU)	Incl. nation (deg)	dia- meter (km)	Date of Discovery	Remarks
1989 UP	0.98	2.7	3.9	0.3	27 Oct., 1989	elongated; perihelion at Earth orbit
1990 SS	0.89	2.5	19.4	0.9	25 Sep., 1990	
1990 TG1	0.77	4.2	9.1	4.6	14 Oct., 1990	Discovered at 2.9 AU from Sun
1990 UN	0.81	2.6	3.7	0.09	22 Oct., 1990	H-23.5
1990 UO	0.30	2.2	29.3	0.4	22 Oct., 1990	perihelion at Mercury orbit
1990 UP	1.10	1.5	28.1	0.4	24 Oct., 1990	Amor; slow rotation
1990 VA	0.71	1.3	14.2	0.6	9 Nov., 1990	Aten; perihelion at Venus orbit
1991 AM	0.51	2.8	29.7	2.3	14 Jan., 1991	crosses Venus orbit
1991 BA	0.71	3.8	2.0	0.009	18 Jan., 1991	smallest object found so far
1991 BN	0.87	2.0	3.4	0.5	19 Jan., 1991	
1991 CB1	0.64	2.7	15.8	1.3	15 Feb., 1991	
1991 EE	0.84	3.6	9.8	1.5	13 Mar., 1991	
1991 FA	1.08	3.0	3.2	1.5	17 Mar., 1991	Amor
1991 FE	1.07	3.5	4.5	5.8	18 Mar., 1991	Amor
1991 JR	1.04	1.8	10.1	0.14	8 May, 1991	Amor
1991 LH	0.37	2.3	51.1	1.0	14 June, 1991	

In addition to the discoveries, Spacewatch "rediscovered" 1990 UP (twice), (1865) Cerberus, P/Kopff, P/Taylor, P/Helin-Roman-Alu 2, and P/Hartley 1. Also, five objects were followed because of their apparent fast motion, but the eventual orbit indicated they were on the inside of the asteroid belt, and two were in geocentric orbit.

conclusion that objects smaller than about 100 meters are increasingly overabundant compared to the above extrapolation from larger sizes. Near 10 meters, the most probably flux near the Earth is 2 orders of magnitude higher. This is in agreement with the flux extrapolated from observations of bright meteors and fireballs. It is likely that processes other than collisional breakup of asteroidal material begin to supply the population of small objects near the Earth at sizes near 100 meters. This contribution is probably due to fragmentation from comets.

A science writer for the New York Times wrote an article on the hazards of near-Earth asteroids which has drawn worldwide attention. Subsequently we were interviewed on a few dozen radio and television shows. The effect of this is still rippling around the world such that we get reports from faraway places as India and Scotland. Even distinguished people as Alistair Cooke have been talking about Spacewatch!

At the urging of the American Institute of Aeronautics and Astronautics, the U.S. Congress has instructed NASA to hold two workshops, namely on the discovery of near-Earth asteroids in view of their hazard, and the other one to study what to do about those hazards. The first meeting of the first workshop was held at San Juan Capistrano in California. The 1.8-m Spacewatch Scannerscope was adopted as the prototype for four more such instruments which may be located in India, Western Australia, Chile, and Hawaii.

Development of New Techniques

In the first place we are refining our techniques at the 0.9-m Spacewatch Telescope. There was an extended period this summer with the Solbourne computer in Tucson. A series of improvements was made to the software.

The CCD was installed in another dewar which holds vacuum better so that the rather dangerous operation of pumping every second or third night will no longer be necessary. Also, the dewar will hold liquid nitrogen all night. There will no longer be delays in the observing due to refilling of liquid nitrogen.

We expect an improved efficiency of about 20 percent such that during the next ten lunations of observing we should be finding 18 near-Earth asteroids.

The ultimate discovery rate with the 0.9-m Spacewatch Telescope is expected to be about 36 near-Earth objects per year. The improvement of a factor of 2 will be obtained from the usage of a new CCD of twice the quantum efficiency. With support from other funds we plan to buy that CCD and have it in operation by 1994.

We have considered moving the 0.9-m Spacewatch Telescope on the sky, faster than when the drive is turned off, to speed area coverage. However, this old telescope may be too deficient in quality of bearings and gears to be able to do this without disproportional expenditure of funds.

The ultimate gain from 36 to 200 near-Earth asteroids per year can only be obtained by replacing the 0.9-m Spacewatch Telescope with the 1.8-m Scannerscope. The gain will come from the combination of the larger area of the primary mirror and from the fact that this telescope will be designed to move on the sky at rates as high as 2 degrees per day. We are active in fund raising for this refurbishment. Some design work has also been accomplished. We hope to obtain NASA approval for the refurbishment shortly.



ABUNDANCE OF ^3He AND OTHER SOLAR-WIND-DERIVED VOLATILES IN LUNAR SOIL

Timothy D. Swindle
Lunar and Planetary Laboratory
University of Arizona

Progress report, August 30, 1991

Abstract:

On the Moon, solar wind implantation is the primary source of potentially valuable volatiles such as ^3He , H, C, and N. We have evaluated geometric effects and the effects of shielding by the Earth's magnetosphere to determine the magnitude of systematic variations in total solar wind fluence with location. We find that the central nearside, the location from which all of the well-studied Apollo samples come, has probably been exposed to less than half as much solar wind as equatorial locations near the limb and on the farside. Assuming that the variations in solar wind fluence lead to comparable variations in volatile abundances (an assumption we plan to test more rigorously in the coming year), we have generated maps of estimated abundances of volatiles. For most volatiles, fluence variations are expected to be the only systematic effect. For ^3He , soil chemistry is also important, so we have combined our calculations of fluence variations with maps of estimated Ti abundance to produce estimates of ^3He abundances.

Volatiles implanted into the lunar regolith by the solar wind are potentially important lunar resources. Wittenberg et al. (1986) have proposed that lunar ^3He could be used as a fuel for terrestrial nuclear fusion reactors. They argue that a fusion scheme involving D and ^3He would be cleaner and more efficient than currently-proposed schemes involving D and T. However, since the terrestrial inventory of ^3He is so small, they suggest that the lunar regolith, with concentrations of the order of parts per billion (by mass) would be an economical source of ^3He . Solar-wind implantation is also the primary source of H, C and N in lunar soil. These elements could also be important, particularly for life support and for propellant production.

In a SERC study of the feasibility of obtaining the necessary amount of ^3He , Swindle et al. (1990) concluded that the available amount is sufficient for early reactors, at least, but that the mining problems, while not necessarily insurmountable, are prodigious. The volatiles H, C, and N, on the other hand, come in parts per million level abundances (Fegley and Swindle, 1992). The differences in abundances mean that a) a comparable amount of H, C and/or N could be extracted with orders of magnitude smaller operations than required for ^3He and b) if ^3He extraction ever becomes important, huge quantities of H, C, and N will be produced as by-products.

Some work has been done on identifying promising sites for ^3He mining. Most of this work has focussed on identifying sites where ilmenite content (and hence Ti content) is high (e.g., Cameron, 1991), since ilmenite retains a higher fraction of the implanted He than do other common lunar minerals. Discussions of the abundances of H, C, and N, which are less dependent on mineral chemistry, generally assume that these volatiles are rather uniformly distributed in the lunar regolith, with only local variations as a result of local impact cratering history (Haskin, 1989; see also Taylor, 1991).

However, there are geometric factors affecting the abundance of all solar-wind-derived volatiles that have not been previously considered in discussions of resource utilization. In particular, since the Earth's magnetosphere shields the Moon from the solar wind during the portion of each month in which the subsolar point is at the central nearside, that region has been exposed to considerably less solar wind than has the central farside. In addition, equatorial regions should receive more solar wind than polar regions because the direction of the flow of the solar wind is close to the plane of the Moon's equator. Whether this translates into a difference in volatile content depends on how important saturation effects are: if the surfaces of samples from the central near side (such as the well-studied Apollo samples) are saturated with solar-wind derived volatiles, additional exposure will not lead to higher volatile contents.

During the six months of the current grant, calculations have been made of the expected size of variations in the solar wind fluence, and some of the implications have been considered. In the next year, we plan to perform analyses on some crucial lunar samples to test the importance of saturation effects.

Variations in solar wind fluence

As a first step, we have calculated how the integrated solar wind fluence varies with latitude and longitude on the Moon. The latitude effect is simply proportional to the cosine of the latitude. The longitude effect is more complicated, since it depends on the details of the Earth's magnetotail and magnetosheath. According to Neugebauer et al. (1972), the Moon is in the magnetotail about four days each lunar cycle, and spends about four or five more days in the magnetosheath. In the magnetotail, the solar wind flux is essentially zero, while in the magnetosheath it varies from a few percent of the unshielded flux to values comparable to the unshielded flux. Rather than modeling the magnetosheath in detail, we have assumed that the Moon is completely shielded for 25% of the lunar cycle. Under those conditions, the central near side receives less than 30% of the fluence that the central far side receives, and only about 35% of the fluence received by the limbs. A map of the relative fluence is given in figure 1.

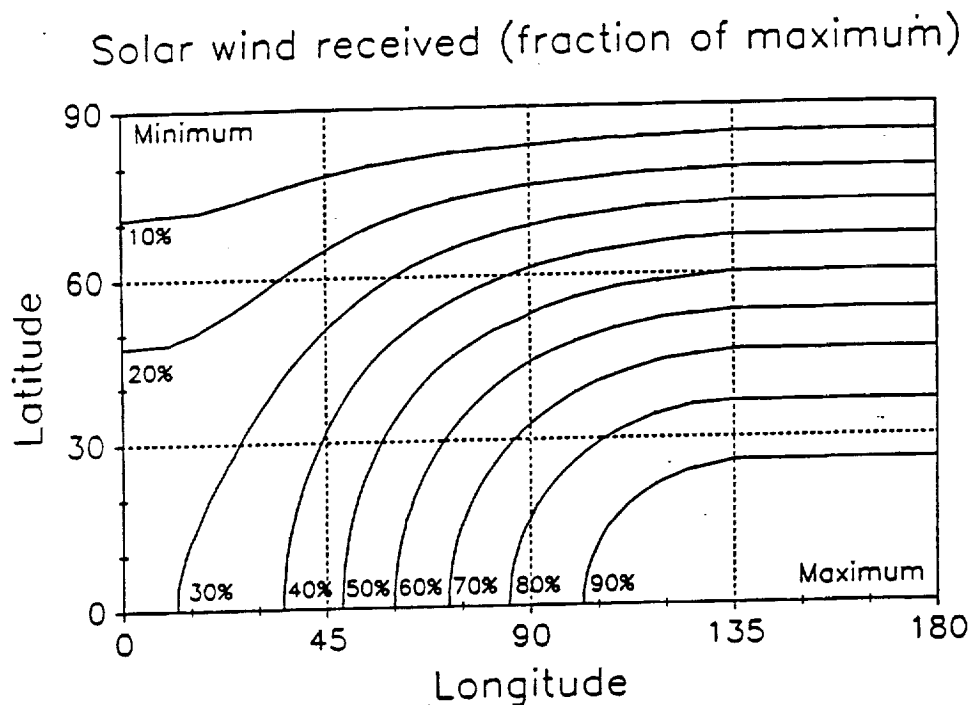


Figure 1: Fraction of maximum solar wind fluence as a function of lunar latitude and longitude. The distribution is symmetric about the equator and nearly so about the 0° meridian.

Changing the details of the shielding (i.e., changing the amount of time shielded, or including partial shielding for the whole duration of the magnetosheath passage, rather than total shielding for part of the duration) will change the details of the map, but not the overall pattern. For elements for which soil chemistry is not important (probably all the elements of interest except He), a global abundance map should look nearly the same (except for local variations in impact history).

From this, we can make some simple, but important, observations about siting of mining facilities. The most obvious observation is that equatorial sites are likely to be preferable to high-latitude sites, and that central nearside sites are likely to be poorer in resources (by a factor of a few) compared to the best sites on the Moon. However, it is not necessary to go to the farside to get to sites that have high solar wind fluences, since the fluence at the limbs is more than 80% of the central farside fluence.

For ^3He , we must include soil chemistry to estimate abundances. Jordan (1989) has shown that the abundance of ^3He in Apollo (central nearside) samples is proportional to the product of a parameter called I_p/FeO (which measures duration of surface exposure, and will be discussed in more detail below) and Ti content. This is reasonable, since the first factor should be proportional to the amount of solar wind received, and the second is proportional to the fraction retained (since ilmenite retains far more than other minerals). Generalizing to consider fluence variations, we would expect the abundance to be proportional to the product of the fluence and the Ti content. We have generated a map of estimated ^3He abundance based on that assumption, using the fluence variations calculated as described above, and maps of estimated Ti abundance based on spectrophotometry of the Moon (Johnson et al., 1991). We are also in the process of generating a map using the Apollo gamma-ray spectrometer Ti results (Davis, 1980), which are also available in the Planetary Imaging Research Laboratory (PIRL) computers.

Since the highest Ti abundances are concentrated in the central near side, where the solar wind fluence is lowest, the two effects tend to cancel each other. It turns out that Mare Tranquillitatis, with its very high Ti content, but low longitude, is still one of the best places to look for ^3He , but some other areas with moderate Ti content but higher longitudes (e.g., western Oceanus Procellarum, Mare Fecunditatis, Mare Smythii) are potentially as promising. With a few exceptions (most notably in and around Mare Smythii on the eastern limb), there are few promising sites on the far side, despite the higher solar wind fluence.

Testing the importance of saturation effects

We have noted that we can convert solar wind fluence to estimated volatile abundance only if saturation effects are not important. In the lunar sample literature, the question of whether or not some grain surfaces are saturated is not settled. The best solar-wind simulation studies were performed recently by Futugami et al. (1990), who bombarded pure mineral samples with He ions. They concluded that saturation of a free grain in space could occur in about 10 years of completely unshielded exposure (corresponding to a few decades of exposure on the Moon). Under these conditions, saturation of He, at least, would be expected to be important. In a study of actual lunar samples, Wieler et al. (1980) concluded that He saturation of grain surfaces occurs for "a considerable fraction" of the grains they analyzed. However, they also concluded that saturation of Ar occurs for few samples. Since Ar abundances correlate well with abundances of C and N (and, with poorer data, H), even at high abundances, it seems likely that these species are not saturated either.

To test for saturation effects, we should compare volatile abundances in samples from locations which we would predict to have a range of solar wind fluences. The Apollo samples all come from a limited geographic range on the central near side. The location with the highest estimated fluence (Apollo 17) would have only 50% more than the location with the lowest fluence (Apollo 15), and only 15% more than the mean of the Apollo samples. The ideal samples would be ones from documented locations on the central farside, but such samples are, of course, not available. The best samples, then, are the Russian Luna samples, which come from closer to the eastern limb of the nearside, and hence would be expected to have about twice the solar wind fluence as the average Apollo sample, and more than 60% more than even Apollo 17.

Samples of two soils each from Luna 16 and Luna 20 soils have been allocated by NASA (though not yet physically transferred) for ferromagnetic resonance (FMR) and noble gas analyses. The FMR analyses, which will be performed by R. V. Morris of NASA Johnson Space Center, are essential to determining the ratio of reduced to oxidized iron (I_0/FeO), a widely-used, probably impact-driven, measure of "maturity" or exposure history (Morris, 1976). The I_0/FeO ratio has not been determined for any Luna 16 or Luna 20 samples. The noble gas analyses will be performed at the University of Arizona. The He analyses are obviously relevant to the question of 3He abundances, while the analyses of the heavier noble gases (Ar, Kr and Xe), whose abundances are not affected by the chemistry of the soil, provide a good analog for volatiles such as C and N. One of the four soils has not been analyzed previously for noble gases, while the others have all had some analyses, but not all have been analyzed by any single lab.

Even with the data available now, there are hints that the geometric factors may be observable in the Luna samples. Luna 16 samples have average He contents that are comparable to mature, high-Ti Apollo 11 and Apollo 17 samples, despite having less than half the Ti content. And the Luna 24 samples, where I_0/FeO has been measured, have about twice the He content that would be predicted for an Apollo sample with that Ti content and maturity. We hope to make these comparisons more quantitative, and to extend them to the other noble gases.

Bibliography

- Cameron E. N. (1988) Mining for helium -- site selection and evaluation. In Lunar Helium-3 and Fusion Power (NASA Conference Pub. 10018), pp. 35-63.
- Cameron E. N. (1991) Helium resources of Mare Tranquillitatis. In Resources of Near Earth Space Abstracts (UA/NASA Space Engineering Research Center AIS/A-90), p. 16.
- Davis P. A. Jr. (1980) Iron and titanium distribution on the Moon from orbital gamma ray spectrometry with implications for crustal evolutionary models. J. Geophys. Res. **85**, 3209-3224.
- Fegley B. Jr., and Swindle T. D. (1992) ^3He and other lunar volatiles. Submitted to Resources of Near Earth Space (J. S. Lewis and M. S. Matthews, eds.). University of Arizona Press, Tucson.
- Futugami T., Ozima M. and Nakamura Y. (1990) Helium ion implantation into minerals. Earth Planet. Sci. Lett. **101**, 63-67.
- Haskin L. A. (1989) The Moon as a practical source of hydrogen and other volatile elements (abstract). Lunar Planet. Sci. XX, pp. 387-388.
- Johnson J. R., Larson S. M., and Singer R. B. (1991) Remote sensing of potential lunar resources: I. Global compositional mapping. J. Geophys. Res., in press.
- Jordan J. L. (1989) Predictions of the He distribution at the lunar surface. In Space Mining and Manufacturing (abstracts of papers submitted to the Annual Invitational Symposium of the UA/NASA SERC, Tucson).
- Morris R. V. (1976) Surface exposure indices of lunar soils: A comparative FMR study. Proc. Lunar Sci. Conf. 7th, 315-335.
- Neugebauer M., Snyder C. W., Clay D. R., and Goldstein B. E. (1972) Solar wind observations on the lunar surface with the Apollo-12 ALSEP. Planet. Space Sci. **20**, 1577-1591.
- Swindle T. D., Glass C. E., and Poulton M. M. (1990) Mining lunar soils for ^3He . UA/NASA Space Engineering Research Center TM 90/1.

Taylor L. A. (1991) Helium abundances on the Moon: Assumptions and estimates. In Resources of Near Earth Space Abstracts (UA/NASA Space Engineering Research Center AIS/A-90), p. 40.

Wieler R., Etique Ph., Signer P., and Poupeau G. (1980) Record of the solar corpuscular radiation in minerals from lunar soils: A comparative study of noble gases and tracks. Proc. Lunar Planet. Sci. Conf. 11th, 1369-1393.

Wittenberg L. J., Santarius J. F., and Kulcinski G. L. (1986) Lunar source of ^3He for commercial fusion power. Fusion Technology 10, 167-178.

Publications supported by the current grant (March 1-August 30)

Fegley B. H. Jr. and Swindle T. D. ^3He and other lunar volatiles. Submitted to Resources of Near-Earth Space (J. S. Lewis and M. S. Matthews, eds.). University of Arizona Press, Tucson.

Johnson J. R., Swindle T. D., Larson S. M., and Singer R. B. Systematic variations in solar wind fluence with lunar location: Implications for resource utilization. Submitted to the meeting of the Division of Planetary Sciences of the American Astronomical Society, Palo Alto, CA, November, 1991.



IV. SYSTEM AUTOMATION AND OPTIMIZATION



FURTHER DEVELOPMENT OF A FIGURE-OF-MERIT IN SPACE MISSIONS

Bruce Preiss and Kumar Ramohalli

Aerospace and Mechanical Engineering

University of Arizona

ABSTRACT

The concept of a Figure-of-Merit (FoM) is developed to assess specific mission designs. The variables for a mission plan are so numerous and interdependent that a single parameter cannot accurately represent the overall design performance. The introduction of in-situ resource utilization (ISRU) and the use of advanced modular engines further complicate the problem. For these reasons, the FoM approach has been proposed to provide a more comprehensive look at the overall picture. The analysis encompasses the important design parameters in addition to the less tangible aspects such as long-term effects, reliability and reparability of the hardware, and the risks that are inevitably associated with new technologies. FoM's have been examined in detail for historical missions and for a proposed Mars Sample Return (MSR) mission. Results are presented for a conventional MSR mission along with missions incorporating ISRU and modular engines for comparison. It is concluded that this quantitative FoM approach may well become a key tool in the analysis and design of future space missions.

INTRODUCTION

The Figure-of-Merit is a quantitative number that represents a measure of success of the mission planning. The FoM methodology is unique because it focuses on overall mission architecture while still placing importance on detailed design. The philosophy behind the FoM is that specific spacecraft and support details will continually change throughout development. The FoM concept concentrates on identifying promising mission architectures in the early planning stages, but readily accommodates changes throughout the entire planning process. As the mission becomes better defined, the FoM becomes more accurate. The FoM methodology ultimately identifies the most efficient overall mission plan. Unlike other approaches, specific component optimization will not be considered individually. Instead, the components are optimized within a larger framework consisting of all mission details. Because of the high degree of component integration within a spacecraft, optimizing the performance of one component may degrade the performance of another. As missions become increasingly complex, there is a greater need to factor in all possible details to accurately define the mission and determine its relative merit. The FoM is most effective when comparing similar missions. It fulfills a need for an improved methodology of comparing mission strategies by providing enough detail to make the results significant.

In order for the FoM to be meaningful, it must have a clear definition. Other than for global comparisons, the FoM should not be limited to just one general definition that applies to all types of missions. Instead, the definition should remain flexible so it can be tailored to a specific type of mission. The most basic FoM definition is presented in equation 1. This FoM definition assumes that the mission begins in low Earth orbit (LEO) and focuses on the mass of the sample to be returned back to LEO. The definition also includes an R-factor ranging from zero to one which assesses the relative risk, reliability, and reparability of a mission plan.

$$FoM = \left[\frac{M_{sample}}{M_{LEO}} \right] \times (R\text{-factor}) \times 10^4 \quad (1)$$

The R-factor is calculated as:

$$R\text{-factor} = \text{Inverse Risk} \times \text{Reliability} \times \text{Reparability} \quad (2)$$

Although this number can be somewhat subjective, great care is taken to provide accurate numbers in a relative sense.

SOFTWARE DEVELOPMENT

A spreadsheet program has been developed to calculate the FoM for a given planetary mission. Flexibility and convenience were the key factors for choosing a spreadsheet approach

over a programming language. Spreadsheets provide a simple means for data input which is then instantly factored into a new FoM calculation. The processed numerical data in the spreadsheet can easily be converted to a color coded graphical format. The graphical representation can even be generated automatically if desired. The spreadsheet also serves as an interface for access to any supplemental databases. A liquid propellant database has been utilized to incorporate reliable rocket engine performance parameters.

The three-dimensional capabilities of the spreadsheet have been fully exploited by using separate sheets as a convenient means for grouping the inputs within the separate design modules. The input parameters have been divided into distinct categories: mission details, spacecraft design, rocket performance, support components, and ISRU components. The spreadsheet requires approximately 150 separate inputs for each FoM calculation.¹ These inputs are combined through strict governing equations to provide a detailed analysis. An effort was made to maintain a suitable balance between an effective use of engineering approximations and detailed design calculations in the spreadsheet equations. The approximations are useful and sometimes necessary when using unknown parameters or when using rapidly changing technology.

A major feature of the spreadsheet is its incorporation of detailed coefficient dependencies for the structural elements and the engine components. It is important to realize that changing one design aspect may have significant effects on other components. In the spreadsheet, a given structural element is not assumed to be strictly a fixed percentage of the total spacecraft mass. Instead, the component mass is calculated from the design variables where possible. Therefore, each component must have somewhat detailed calculations of its mass based upon all of the independent parameters which may affect it. These interdependencies need to be considered in the design stages to predict the projected mission capabilities as accurately as possible.

The numerous governing equations combine to form a powerful spreadsheet for analyzing the FoM of space missions, but the underlying strength of the FoM spreadsheet approach is found elsewhere. The real differentiation between the FoM concept and other methods of analysis is the ability of the FoM spreadsheet to manage supplementary data. By incorporating a rocket propellant database, detailed data on hardware for the use of ISRU, and modular engine integration techniques, the program is more flexible and applicable to a broader range of mission types. By integrating all of the available information, the FoM represents an accurate approximation of the efficiency of a planned mission.

MARS SAMPLE RETURN MISSION RESULTS

In order to determine the credibility and accuracy of a given FoM definition, historical data was gathered and analyzed for previous U.S. space missions. A distance factor (Distance of mission/Distance to Moon) is incorporated into the FoM definition for historical lander missions to

Increase the merit of missions involving greater complexities and longer durations. Missions required to traverse greater distances will invariably require more propellant and subsequently have a greater initial mass at launch. With the inclusion of the distance factor, it is shown that the FoM increases with time as the technology and mission planning become more sophisticated.

Curve fits were applied to the observed trends of past missions in an effort to predict the FoM for future space missions. Figure 1 shows lander missions with the calculated power equation superimposed. The resulting trend is plotted on a normalized time line in which the relative year is the base year minus the launch year. The base year is the year in which the first successful lander mission was launched. In the figure, the FoM value has been placed at the launch year of the specific mission. Once the fit constants were calculated for the highest possible correlation, the function was extrapolated to span the estimated time frame for a MSR mission. The FoM values have been separately calculated in the spreadsheet for comparison. A MSR mission was planned utilizing two different propellant combinations and both are shown in the figure to be consistent with the historical data. A power fit is used since it is assumed that technological advances will not increase linearly, but will approach a certain limit over time.

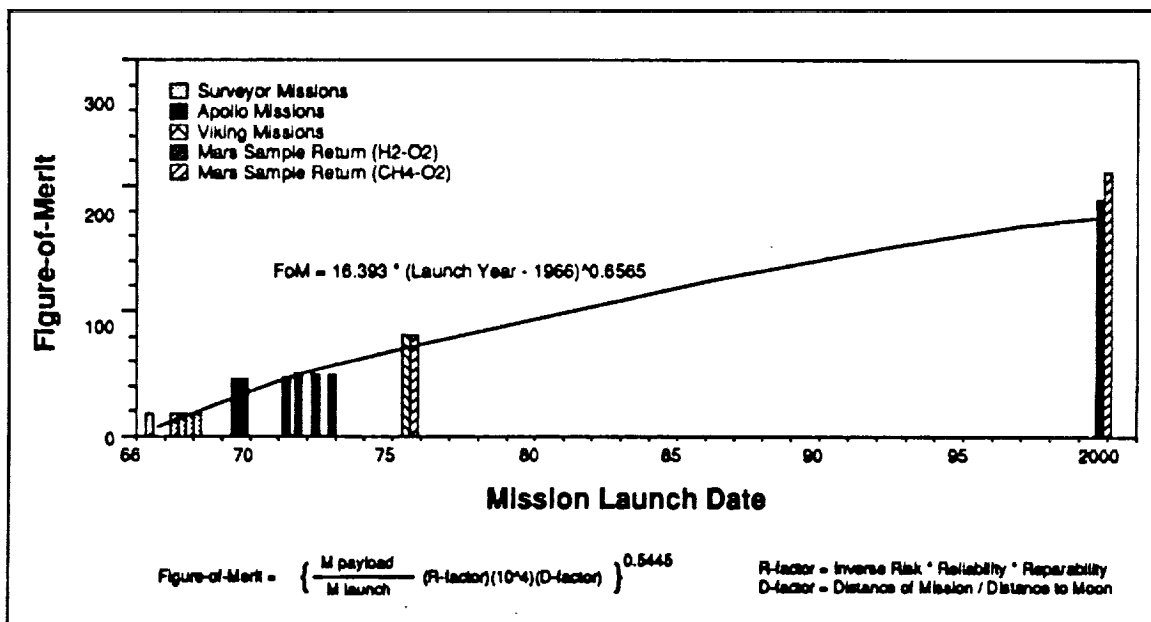


Figure 1 - Historical Lander Figure-of-Merit

The Figure-of-Merit spreadsheet can be used to analyze a large variety of missions because it can accept a wide variety of propellant combinations for propulsion. While many fuel and oxidizer combinations have been tested in terms of rocket performance, the comparisons usually stop there. Comparisons must be made in an overall system approach, like the FoM, in order to adequately weigh the advantages and disadvantages of each specific combination. Consequently, a propellant database has been utilized so the spreadsheet can be used to analyze a large variety of possible

propellant combinations for a given space mission.

The main premise behind in-situ resource utilization is to use local resources wherever possible to help fulfill the mission needs. Mission planning has thus far been unduly restricted in that everything used in the mission must be initially carried from the Earth. ISRU may lead to numerous benefits in mission planning with the primary advantage being the substantial reduction of the initial launch mass of the spacecraft. In general, reductions would be realized for cases in which the total plant mass is less than the mass of the propellant it will produce. Because of the exponential decreases in mass involved in orbital mechanics, ISRU may reduce the initial spacecraft mass for a typical mission to Mars by thousands of kilograms. Although the processed propellant may not always yield optimum performance, the benefits of ISRU may outweigh any disadvantages in terms of overall mission planning. Accurate comparison studies have been completed to determine which strategies will be most influenced by ISRU. The argument in favor of certain propellants using ISRU is convincing, but the actual implementation of this strategy must prove to be both practical and reliable. The complexity of the production plant depends on the available resources, their initial state, and the type of processing required to obtain a useful product. It is important to consider both the complexity and the necessary conditions for the driving chemical reaction. A simple reaction which only proceeds at a high temperature and pressure may be less favorable than a more complicated reaction which occurs under ambient conditions. The driving design factors will be the total system mass and the reliability of the components. The hardware should be kept as simple and light-weight as possible. Figure 2 details the relative benefits of decreasing the plant mass. The FoM values for the ISRU configuration assumes that oxygen is being processed from atmospheric carbon dioxide on the surface of Mars through an electrochemical conversion process. The mass estimates for a plant of this type are taken directly from the oxygen plant design project being conducted at SERC. Previously, the total plant mass was projected to be 197 kg, but the technological advances that have occurred since the inception of the oxygen plant project have lowered the predicted mass to approximately 100 kg. The necessary production rate will dictate the total system mass, and as a general rule, the system mass will be a function of the production rate raised to the two-thirds power.² The power source will ultimately account for a large percentage of the total production plant mass. Consequently, further effort should be focused on the reduction of both the plant power requirements and the specific weight of the power source.

The term "modular" refers to physical components which are interchangeable. In the case of rocket engines, it implies that one engine used for a particular stage could be replaced with an identical engine from another stage without any measurable loss in performance. The modular engine concept focuses on both the engine design and the engine integration between successive stages in order to optimize the overall performance of the vehicle. The optimum engine design

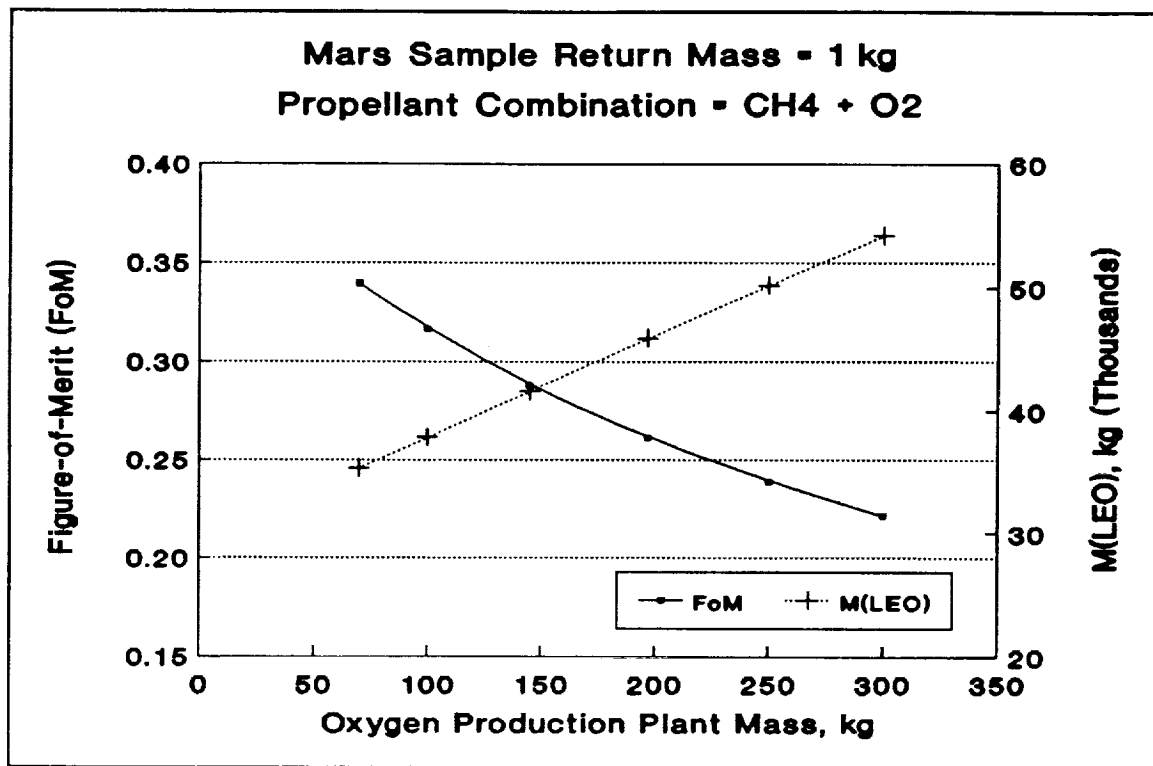


Figure 2 - Plant Mass Variations

achieves a maximum specific impulse while maintaining a minimum engine mass. The modular engine concept simplifies the engineering to one basic design which can supply all of the specified thrust requirements. Larger thrusts are obtained by linking several modular engines in a parallel arrangement so that the thrust is additive. Engine clusters of decreasing number can provide the necessary thrust for each subsequent stage of the spacecraft.

The benefits realized through the utilization of modular engines are increased reliability, reduced risks, simpler reparability, and reduced design and production costs. The total mass of the propulsion system will be somewhat greater for a modular engine design than for one using a conventional design, but the multitude of benefits far outweigh this one liability. If desired, an additional engine could be included in the modular design to account for a possible failure. The increased mass would be minimal, and the greater reliability for the mission could make the inclusion worthwhile. Including an extra engine in the traditional design case would substantially increase the initial mass and would not be practical. The redundancy available from the modular strategy is highly desired and should be included in the early planning stages for any mission.

The ability to use modular engines has been included in the spreadsheet. The spreadsheet has been designed so modular engines can only be used for the inbound return flight. This is a realistic limitation since modular engines typically do not provide enough thrust for the outbound legs of a mission. The thrust capabilities and mass of the modular engines are sized according to

the final thrust requirement upon return to LEO. If the engines are fueled from the same propellant tanks, the complexity of the rocket design would be increased because of the multiple number of feed lines and duplicity throughout the feed system. The complexity is instead reduced by integrating the engines as discrete packages. Each engine will function independently of the others although the electronic controls will be linked. The modular engine scheme will have an increased mass in terms of the propellant tanks over a conventional design, but this mass will be partially offset by the savings in nozzle weight. A pressure feed type liquid propulsion design is used for the modular engines because it provides the least amount of complexity and is very efficient in terms of small thrust requirements. The spreadsheet fully summarizes the design details for the modular engine to be utilized in the mission.

Figure 3 shows the increase in the FoM that results from the use of modular engines. A methane and liquid oxygen propellant combination is presented for comparison and the mass of the soil sample returned is 2 kg. The conventional mission with all Earth carried propellants is shown along with the ISRU case. Superimposed on the plot are the FoM's if the R-factor is set to unity. In an absolute sense, the FoM values for the missions using modular engines decrease

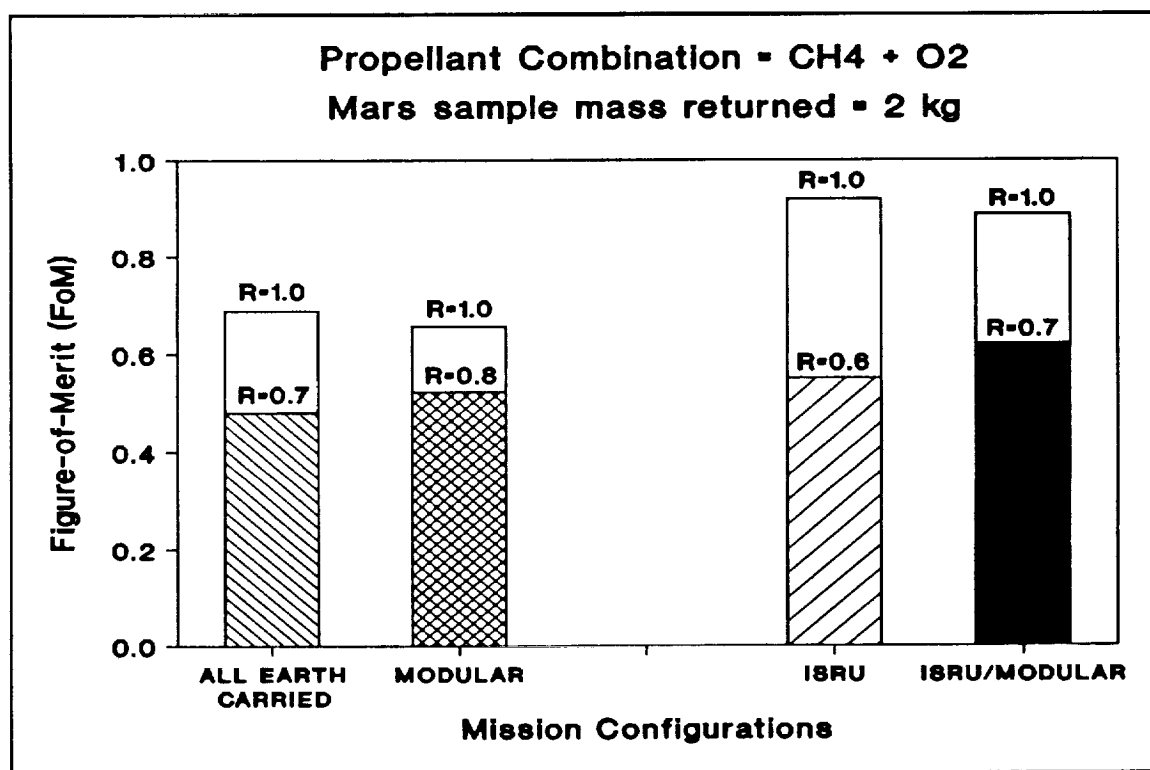


Figure 3 - Technology Benefits

because the initial mass will increase. Although the resulting masses are greater, the FoM has a relative increase after the appropriate R-factors are included. The risk has decreased as a result an increase in the reliability and reparability. For missions utilizing modular engines, the R-factor is

incremented by 0.1. Conversely, the plot shows that the inclusion of ISRU will decrease the R-factor by 0.1. The initial mass savings are so great, however, that even the added risks will not reduce the favorability of the mission.

Table I summarizes the relative changes for the mission variations using the conventional mission as a basis. Both the changes in the initial mass at LEO and the FoM values are presented. The results show that the most effective mission plan is to use a methane and liquid oxygen propellant combination utilizing both ISRU and modular engines. A 2 kg sample could be returned back to LEO for an initial spacecraft mass in LEO of approximately 45,000 kg. The payload includes an oxygen production plant for the surface of Mars which weighs 100 kg and produces 10 kg of oxygen per day. The separate use of modular engines will increase the FoM by 9%, while the separate use of ISRU will increase the FoM by 13%. Combining both technologies, the FoM can be increased by a full 29%. This translates into an initial spacecraft mass savings of 21%.

FUTURE WORK

Using a modular engine architecture has been shown to increase the FoM for a given mission plan. The total initial mass of the spacecraft could be reduced even further through the use of an advanced modular engine scheme which would reuse engines in successive staging maneuvers whenever possible. The secondary propellant tanks would be jettisoned along with the extraneous engines after each ignition. Further work is necessary to quantitatively estimate the mass savings that could be achieved through an advanced modular staging technique. Currently, only the conventional modular staging approach is supported in the FoM spreadsheet.

The refrigeration calculations contained within the spreadsheet are based upon a simple heat transfer model. This basic model provides worst case estimates for the mass of the refrigeration units that must maintain low enough temperatures to ensure that the working propellants remain in a liquid state. A more sophisticated model could be used which would include either multiple insulation layers for the tanks or the use of special cryogenic storage tanks with an evacuated lining. A more refined model would decrease the mass of the refrigeration masses and

<u>Mission Variation</u>	<u>$\Delta M(\text{LEO})$</u>	<u>ΔFoM</u>
All Earth Carried	-	-
Modular Engines	+6.4%	+8.9%
ISRU	-25.3%	+12.7%
ISRU/Modular Engines	-21.2%	+28.8%

Table I - Mission Variation Summary

provide more realistic comparisons between the all-Earth carried propellant missions and ISRU missions.

The oxygen plant mass figures must be continually updated as work progresses on breadboard unit. The production rate must still be scaled upward and additional components are in the process of being integrated. As additional hardware becomes more well defined, the values used in the spreadsheet must be continually updated to reflect these changes. The oxygen plant built in the laboratory will not address the power source issue directly, and more analytical work must be accomplished to estimate changing power requirements and keep pace with technological advances in the energy field.

1. Preiss, B., "A Quantitative Figure-of-Merit Approach for Optimization of an Unmanned Mars Sample Return Mission," Master of Science Thesis, University of Arizona, December 1991.
2. Preiss, B., Pan, T., and Ramohalli, K., "Further Applications of a Figure-of-Merit to Space Missions," AIAA/SAE/ASME/ASEE 27th Joint Propulsion Conference, Sacramento, CA, June 1991, AIAA Paper #91-2330.

AUTOMATION AND CONTROL OF AN OXYGEN EXTRACTION PLANT

L. Schooley, F. Cellier, A. Doser, G. Farrenkopf, J. Kim, Y. Pan, and B. Williams

The University of Arizona

Abstract

This report documents progress on the continuation of a previous project for the development and implementation of automation and remote supervisory control of process plants used to produce oxygen from local planetary resources. A distributed architecture is being developed and implemented so that an oxygen production plant can be reliably controlled over an extended time period in a high-autonomy mode with high-level task-oriented teleoperation from a remote location.

The main effort during this reporting period was the automation of a prototype oxygen production plant. This section describes the details of the instrumentation and control system design, relates it to the overall architecture planned for the future, and discusses performance during a particular incident which occurred during a 100 hour test of continuous oxygen production without human intervention. Progress in the areas of communications system protocol development and modeling and simulation is also reported.

INTRODUCTION

This is the continuation of a previous project for the development and implementation of automation and remote supervisory control of process plants used to produce oxygen from local planetary resources. A distributed architecture is being developed and implemented so that an oxygen production plant can be reliably controlled over an extended time period in a high-autonomy mode with high-level task-oriented teleoperation from a remote location. The components of this architecture include computer communication, smart sensors, sensor fusion techniques, and distributed intelligent real-time algorithms for task planning, plant operation, fault detection, fault diagnosis, and fault recovery.

The ultimate result of this research will provide the capability for teleoperation of such process plants that may be located on Mars, Luna, an asteroid, or other objects in space. Communication protocols previously developed for NASA's Telescience Testbed Pilot Project (Schooley and Cellier, 1988) are being adapted to teleoperating the prototype plants located at the Space Engineering Research Center from remote commanding computers located at the University of Arizona main campus. Key assignment protocols are being implemented that will enable multiple remote commanders/observers to simultaneously interact with the teleoperated plant.

Various static and dynamic computer simulations of the process plant are also being developed. These will eventually be used as the world model for the artificial intelligence applications used in the hierarchical control scheme. In the interim, they also provide a modeling/simulation tool that can be used to analyze the dynamics of the plant and to design or test control algorithms or alternate plant designs.

A report of previous work on this project may be found in Schooley and Cellier (1991).

CONTROL ARCHITECTURE FOR HIGH-AUTONOMY OPERATION

The main effort during this reporting period was the automation of a prototype oxygen production plant. This section describes the details of the instrumentation and control system design, relates it to the overall architecture planned for the future, and describes performance during a particular incident which occurred during a 100 hour test of continuous oxygen production without human intervention.

According to NASA (1985), 'automation' is defined as "the ability to carry out a pre-designated function or series of actions after being initiated by an external stimulus without the necessity of further human intervention." In contrast, 'autonomy' is defined as "the ability to function as an independent unit or element over an extended period of time performing a variety of actions necessary to achieve pre-designated objectives while responding to stimuli produced by integrally contained sensors."

Automation of a process is usually viewed as designing a (feedback) controller that reduces the plant sensitivity to parameter variations and/or the influence of disturbances. Parameter variations may be due to minor variations in the manufacturing process that is used to generate the plant, to thermal effects, or to the influence of external environmental variations. Mostly, these variations are minor (a few percent). Feedback control architectures have helped to make plant operation more robust (less sensitive) to such types of variations in comparison with open-loop command architectures.

Traditional control engineers hardly ever concern themselves with abnormal situations such as failures that occur within a subsystem of the plant to be controlled or --even worse-- within the controller itself. Reliability of a controlled system over long periods of time is rarely mentioned among the items on the desired performance parameter list of a control engineer. The engineer is concerned with such properties as stability, steady-state accuracy, percent overshoot, and settling time, not failure rate, down time, or repair activities.

Such factors must be considered, however, for high-autonomy system operation. They add a new dimension of complexity to the overall system design. A high-autonomy system contains an additional hierarchy layer around the control architecture. It usually contains several alternative control architectures. It knows which of them to choose at any particular moment, and it knows when to switch between different controllers. It contains a task planning module that computes the set points for active controllers, and sequences the tasks to be executed. It reasons about both plant and controller integrity, it detects faults (symptoms) as they occur, localizes the faults within the system (discovers failures), and thinks about means of recovery from such faults (initiates repair activities). It furthermore collects statistics on symptoms, failures, and successful (as well as unsuccessful) repair activities (learns from past experience).

An architecture for high-autonomy systems was recently proposed by Zeigler (1991) and Chi (1991). Our oxygen production plant prototype, while still fairly primitive, contains all elements of a high-autonomy system. In the sequel, these elements will be described, and it will be shown how they cooperated during a recent incident which occurred during a long test. The plant itself is described elsewhere in this report, but the primary elements are supplies of carbon dioxide and helium gas (for purging), a heater, one or more zirconia cells, and associated instrumentation sensors and control actuators. Figure 1. shows the physical configuration of the single-cell prototype used during the 100 hour experiment.

Task Planning: Task planning refers to the activity of sequencing commands issued at task level to the control architecture. The task planner does not concern itself with the details of task

execution. All it does is to determine which tasks should be executed (and in what sequence) and with resource management. That is, the planner knows what resources are required by each task, and makes sure that those resources are available during task execution. Finally, it concerns itself with time management; it knows how much time each task is supposed to consume and makes sure that real-time constraints are satisfied.

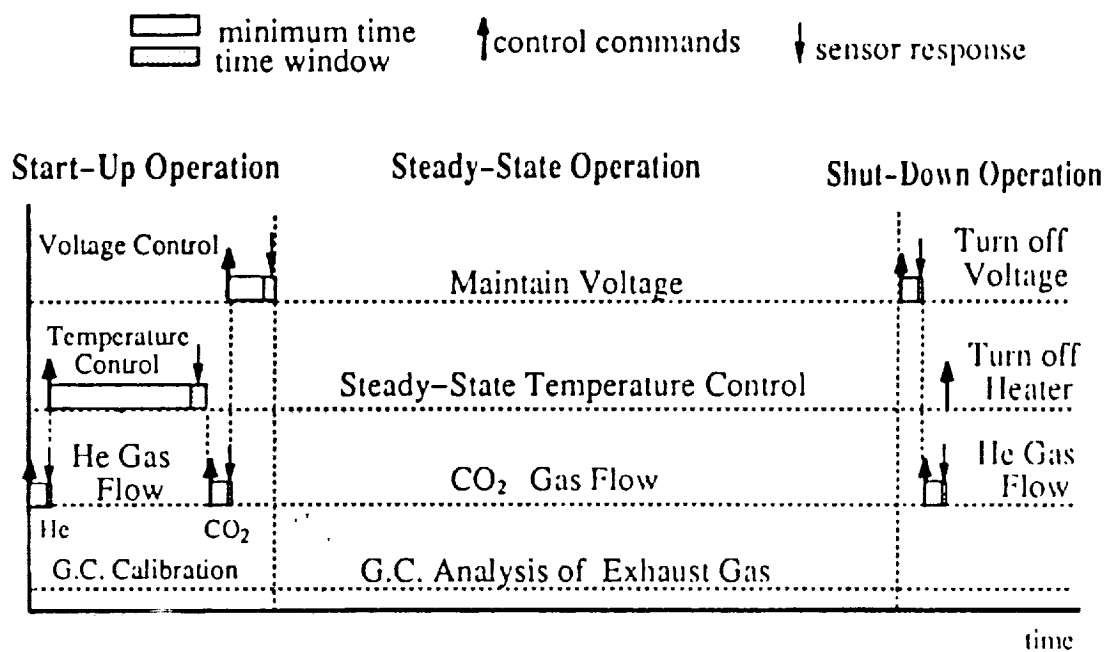
In our testbed, the task planner was fairly rudimentary. Since only one type of experiment was planned (the 100 hour test of continuous oxygen production without human intervention) an elaborate task planner was not required. Figure 2. shows how the task planner manages the resource and time umbrellas for four different control loops during the start-up sequence, the steady-state operation, and the shut-down procedure. The four control loops are concerned with voltage control, temperature control, flow rate control, and control of a gas chromatograph.

The first control loop is concerned with the voltage applied across the wall of the zirconia cell. During the separation of oxygen and carbon monoxide, a voltage of approximately 2 VDC must be applied to the zirconia cell for the electrocatalytic reaction to take place. In the presence of zirconia the hot oxygen gas is ionized by borrowing four electrons from the cathode located at the inside wall. The oxygen ions are sufficiently small to migrate through the porous zirconia wall. Upon arrival at the other side, they shed the electrons to the anode, and the free oxygen is released.

The oxygen production rate is very sensitive to the applied voltage. Below 0.6 V (Nernst voltage), no oxygen is produced at all. For higher voltages, the oxygen produced is linear in the applied voltage. However, at 2.3 V, the zirconia cell is permanently destroyed. However, there is also a relation between voltage and temperature. No voltage should be applied to the cell before steady-state temperature and gas flow rate have been reached, and the voltage should be switched off at the beginning of the shut-down sequence.

Temperature control is also essential. A temperature of at least 850 K is necessary for thermal disassociation of the carbon dioxide to take place. However, at temperatures between 1000 K and 1200 K, the zirconia cell is permanently damaged (the critical temperature depends on the material used for electrodes and seals). There also exists a relation between temperature control and gas flow. Obviously, the proper gas flow rate must be established before heating can take place. However, around 600 K, there is a risk of carbon deposition along the walls of the zirconia cell. For that reason, the cell is being purged with helium gas during start-up and shut-down. The helium gas is only replaced by carbon dioxide gas after the zirconia cell has reached its operational temperature of approximately 900 K.

The third control loop is concerned with maintaining the appropriate gas flow rate and with



System State Variable Table		
temperature		25
	upper bound	30
	lower bound	20
flow rate		0.07
	upper bound	0.08
	lower bound	0.06
voltage		0
	upper bound	0
	lower bound	0
input gas type		He

Start-Up Operation

System State Variable Table		
temperature		900
	upper bound	915
	lower bound	885
flow rate		0.07
	upper bound	0.08
	lower bound	0.06
voltage		2.00
	upper bound	2.05
	lower bound	1.95
input gas type		CO ₂

Steady-State Operation

System State Variable Table		
temperature		25
	upper bound	30
	lower bound	20
flow rate		0.07
	upper bound	0.08
	lower bound	0.06
voltage		0
	upper bound	0
	lower bound	0
input gas type		He

Shut-down Operation

Figure 2: Task Planning for OPP.

operating the electronically controlled valve that switches between the helium and carbon dioxide gas.

The fourth control loop operates the gas chromatograph that is used to analyze the various gases during the experiment. During start-up, the gas chromatograph needs to be calibrated, and during steady-state, various gas samples can be routed through the gas chromatograph by appropriately setting several valves.

While our task planner is currently still very simple, this part of the program will need to be drastically expanded before the full scale plant can be launched. Task planning is not only responsible for setting the pace for normal operation, but also for recovering the plant after a fault has occurred. The Martian task planner must be able to deal with sand storms, contaminated membranes and tubes, leakage of seals, and tripped circuit breakers, to mention just a few of the types of failures that are expected to occur during long-term operation of this high-autonomy control system. Chi (1990 and 1991) has proposed an intricate hierarchical task planning architecture that should suffice for controlling such an expedition.

Command Execution: The command executor is an independent agent that resides in the local controlling computer. It accepts the next command to be executed from the task planner and prepares the control architecture for its execution. The task executor selects the appropriate low-level control algorithm from a set of precoded algorithms, downloads the selected controller into the smart sensor that physically houses the low-level control loop, and initiates the control activity.

The command executor is also responsible for receiving and processing sensory events that signal task completion. It is responsible for maintaining the appropriate time-window information that allows it to judge success or failure of task execution. Consequently, the command executor is responsible for fault detection during transient operational phases, such as the start-up and shut-down phases that were previously discussed. In case of a failure (the sensory event has arrived too early or too late), it starts the fault diagnoser to reason about the nature of the observed fault so as to relate the observed symptom to the failure that caused it.

Time windows are intimately linked to our event-based control logic. They ensure early detection of faults during transient operational phases, and thereby provide the high-autonomy system with sufficient reliability to allow the system to operate adequately over an extended period of time. Figure 3 explains the time-window mechanism.

Each command issued by the command executor is accompanied by an expectation as to how much time the commanded task will require for its completion, i.e. before the goal state is reached. Due to plant parameter uncertainties and external disturbances, the time cannot be

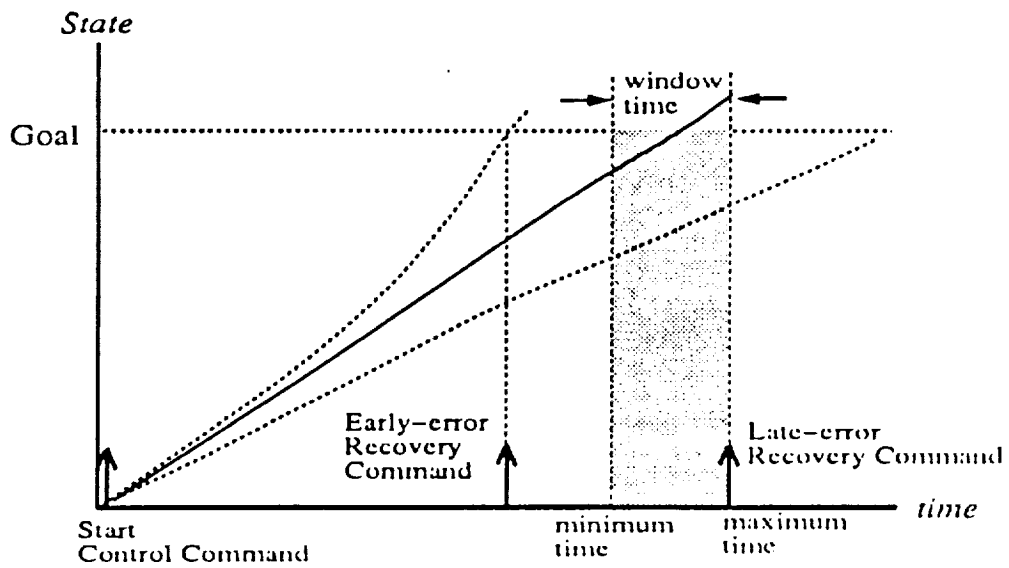


Figure 3: Time-Window Mechanism.

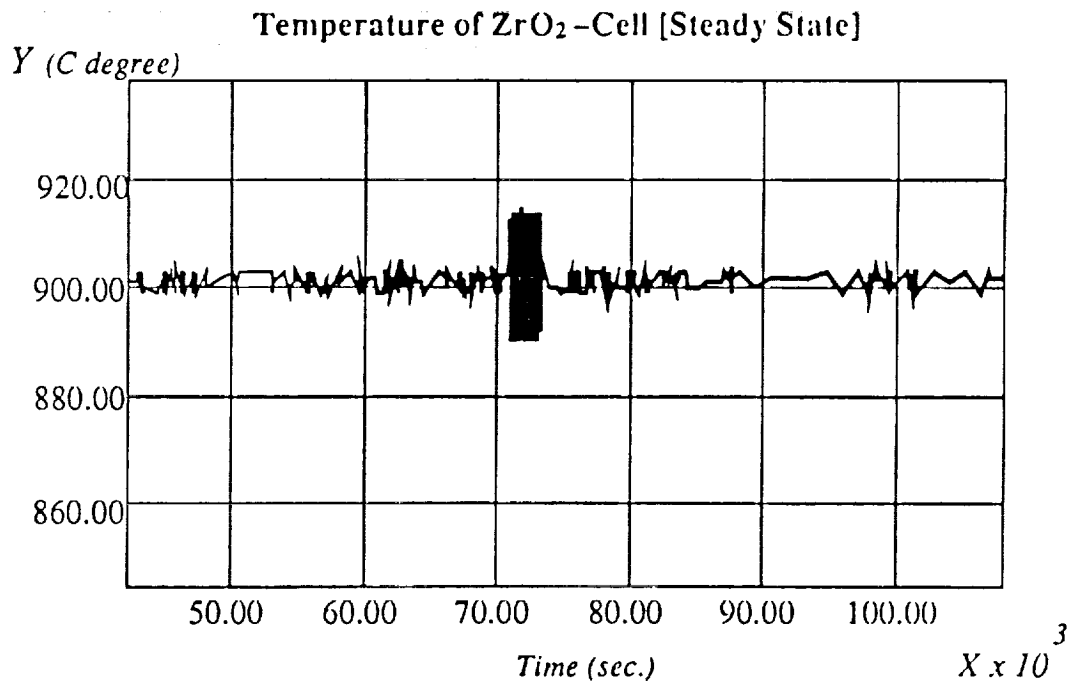


Figure 5: ZrO_2 Temperature Plotted over Time.

estimated precisely. Instead, the uncertainty is captured in a so-called time window. A sensor should record the fact that the next goal state has been reached, and should report the time of task completion to the task executor. If the sensory event arrives too early or too late, a fault diagnoser is activated. The objective of the diagnoser is to relate the observed symptom back to its cause, the failure. It then calls upon the failure recovery agent to come up with a new command sequence that will put the high-autonomy system back on track. Once the failure recovery agent has decided what to do, it calls upon the task planner to work out a new command sequence that implements the suggested recovery action. The time-window mechanism has been described in detail in Wang and Cellier (1991). The time windows associated with the 100 hour run are shown on Fig.2.

Plant Operation: The actual low-level control is implemented in a microcontroller called a smart sensor. Once the command executor has downloaded a control program to the smart sensor, the low-level controller is activated. This can be a classical controller of any vintage. Figure 4 shows the two-level local control architecture employed in this example. The smart sensor accepts sensory information from the plant. Sensory signals are then time-multiplexed before they are forwarded to the local controlling computer, which is a PC/AT in this implementation. The smart sensor also receives multiplexed control signals from the PC, unpacks them, and sends them out through its actuator channels to the plant. In this mode, the smart sensor does not perform any control at all, but only serves as an interface between the plant and the local controller. However, the smart sensor can be programmed to either preprocess the sensory signals before sending them to the PC (sensor fusion), or postprocess the actuator signals before sending them to the plant (actuator expansion), or compute actuator signals directly from the sensory information received.

In the latter case, the smart sensor acts as a microcontroller, and that is the mode in which we operate. The memory of the smart sensor used here is very limited. Therefore, the microcontrol programs must be short. For that reason, different control programs are downloaded into the smart sensor from the PC during various operational phases. However, using the smart sensor as a microcontroller (programmable logic controller), we can ensure high-speed control, relieve the PC from low-level control activities, and reserve its computing cycles for the higher-level intelligent control decisions.

In our case, all control activity was event-based, but there is nothing in our methodology that would force such a solution upon us. Notice that the control programs are indeed different during different phases. For example, the voltage is carefully ramped up in the start-up phase by one control program (to avoid overshoot), whereas the voltage control program operates quite differently during steady-state operation.

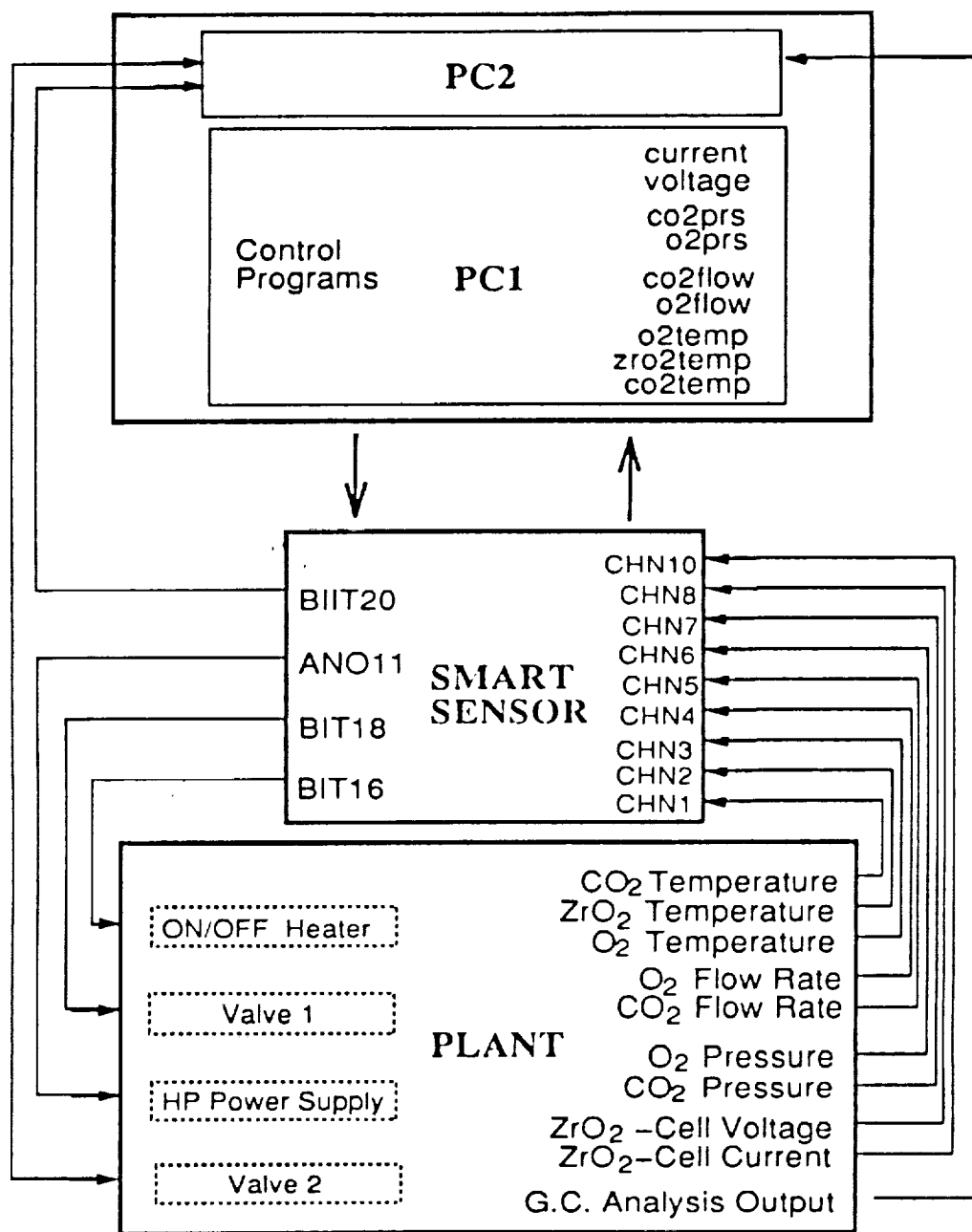


Figure 4: Two-Level Local Control Architecture.

For purposes of describing the incident which occurred during the test, it is useful to discuss temperature control in a little more detail. During start-up, the heater is simply switched on. When the temperature reaches a value of 890 K, a threshold sensor detects this fact, and sends a sensory event back to the smart sensor that is then forwarded to the PC. The PC compares the time of arrival with the time window specified for (electrically) heating the system. If the completion event arrives too early, something bad must have happened. Since the electrical heater is operating at its maximum power, the completion event should never arrive too early. If this is nevertheless the case, the fault diagnoser concludes that there must be something drastically wrong in the system, the recovery unit decides that this fault is not repairable and instructs the task planner to design a graceful shut-down sequence starting from the current state. If the completion event arrives too late (or rather, it doesn't arrive in time), the fault diagnoser concludes that either the power supply or the heater is not functioning properly. In this case, the recovery agent switches both the power supply and the heater off and back on, sends another command to the power supply to set its voltage, and instructs the task planner to try again with a new time window. If the second attempt fails also with a too late indication, the recovery unit concludes that the situation is hopeless and instructs the task planner to design a graceful shut-down. During steady-state operation, temperature control is governed by three rules:

- Rule 1: Heating. If the current temperature is below 890 K, turn the heater on and enable Rule 3.
- Rule 2: Cooling. If the current temperature is above 915 K, turn the heater off and disable Rule 3.
- Rule 3: Approach. If the current temperature is between 890 K and 898 K, turn the heater on, estimate the expected remaining heating time τ , which is proportional to the difference of the goal temperature, 900 K, and the current temperature and schedule a turn-heater-off event to occur τ time units into the future.

The rationale behind this event-based control logic is simple: since the temperature sensor is not directly attached to the heat source, a certain overshoot behavior is possible. To prevent the temperature from overshooting, we use Rule 3. This rule functions similarly to a corrective maneuver of a spacecraft: we compute the amount of necessary correction beforehand and then fire the vernier engine for a precomputed period of time. To avoid problems with local heat storage, we always approach the goal temperature from below, i.e. we disable Rule 3 during cooling periods until the temperature has fallen safely below the goal temperature everywhere.

Watchdog Monitors: Notice that there are no time windows shown on Figure 2 during steady-state operation of the oxygen production plant. This is understandable since, during normal steady-state operation, the same control algorithms are constantly active, and neither the task planner nor the command executor have anything to do.

Watchdog monitors are independent intelligent agents that monitor the high-autonomy system during steady-state operation. They have knowledge of some components of nominal system behavior during steady-state, and compare their expectations with the actually observed behavior. If a significant discrepancy is found, the "disquieted" watchdog alerts a fault diagnoser to come up with an explanation for the observed anomaly.

The watchdog monitor philosophy has been advocated in Kury (1990). In our case, it was one of the watchdogs that got aroused and triggered off the event chain that ultimately led to the restoration of the "distressed" temperature controller.

Fault Diagnosis: Contrary to the watchdog monitors that are active demons throughout the steady-state operational phase, fault diagnosers are dormant sequential routines. They are activated only after an anomaly has been detected. The purpose of a fault diagnoser is to relate an observed symptom back to the failure most likely to have caused it.

In our testbed, we employ only a global rule-based fault diagnoser that is extremely simple. Those failures from which the high-autonomy architecture can recover are indicated by clear symptoms, and therefore, no complex fault diagnosers are needed. However, before an actual plant can be launched, we must make sure that the high-autonomy system can recover from all foreseeable sorts of mishap. It will then become essential that the precise nature of any observed failure is well understood before an automated repair activity is initiated. For that purpose, we shall need a multi-level hierarchical model-based diagnoser. Such an architecture was first proposed by Sarjoughian (1990). It has meanwhile been elaborated upon by Chi (1991).

Fault Recovery: The findings of the fault diagnoser are forwarded to a fault recovery agent. It is the task of that agent to decide whether something can be done about the failure or not. If recovery is possible, it is the job of the recovery agent to compute a new goal state. It then provides the task planner with the current state and the desired goal state, and requests that a new command sequence be computed that moves the high-autonomy system from the current state to the desired goal state.

If no recovery is possible, the recovery agent will provide the task planner with the current state only and request computation of a command sequence for graceful shut-down.

The Chain of Events: The following section uses actual data from a portion of the 100 hour test to illustrate the operation of the agents described above.

Figure 6 shows the zirconia cell temperature between 58,000 seconds and 102,000 seconds from start of the test. This is a portion of the steady-state operation. It is immediately visible that around 71,000 seconds, something strange happened. The system recovered from the anomaly roughly 2,000 seconds later.

What happened? The anomaly started while a heavy thunderstorm took place. This was during the evening, and no human observer was at the plant site. From other curves, we know that at that time, there was a short power failure (less than 2 seconds). The backup power supply took over, but there are signs of a temporary power surge. Somehow, this transient upset the smart-sensor-based temperature controller.

It is still not clear exactly what happened. Our best guess is that the power transient stopped the real-time clock of the smart sensor. Thus, when Rule 3 was fired, it computed the remaining heating time, but the turn-heater-off event never arrived since the real-time clock wasn't working. Thus, the heater stayed on until Rule 2 fired, which disabled Rule 3. Consequently, the system cooled down until Rule 1 fired, which reenabled Rule 3, which computed a new remaining heating time, etc.

It should have been easy to detect this anomaly immediately. However, the software being used did not require that the value of the real-time clock of the smart sensor be reported back to the PC, and thus the watchdog monitor did not suspect any trouble. In normal operation, Rule 2 should never be fired. Thus, the first firing of Rule 2 should have sufficed to alert the fault diagnoser --- but this case had not been foreseen, and the occurrence of Rule 2 during steady state operation had not been declared as an anomalous event. Finally, one of the watchdogs got suspicious --- unnecessarily late. Since temperature change is normally such a slow phenomenon, that particular watchdog was executed only once in a while to save computing cycles on the PC. This is a serious problem with the watchdog monitor philosophy: since watchdogs are demons, they must be executed repetitively even if nothing is wrong. If they are executed rarely, they aren't very effective, but if they are executed frequently, they consume lots of computing power. Fortunately, since they are demons, they run asynchronously and could be installed on separate CPUs, even though that was not done in this case.

Fault diagnosers are harmless. They are sequential routines and don't consume any computing cycles unless an anomaly has been observed. In our case, the fault diagnoser, once invoked, worked beautifully. It concluded that the failure had to be in the smart-sensor program. It did not conclude that the bug was in the real-time clock, but this wasn't necessary. As an

analogy: if a computer is down, the repair person will identify the fault only up to the board level and exchange the entire board. The faulty board can then be taken back to the lab where it can be further analyzed down to the chip level. There is no need to perform the second type of fault diagnosis on-line and in real time.

The recovery agent then decided to reload the control program once more into the smart sensor memory. If our assumption about the true cause is correct, it would probably have sufficed to restart the smart sensor without replacing any programs, but the additional action performed was harmless and didn't consume much time anyway.

Lessons Learned: What are the lessons learned from this incident? Let us enumerate them:

1. Proper functioning of the real-time clock is crucial to any event-based controller. Consequently, we should report the value of the real-time clock of the smart sensor back to the PC, and install an additional watchdog that compares the two real-time clocks with each other and gets aroused when they start to diverge.
2. Some of the events that do not normally occur during steady-state operation, such as Rule 2 above, can be declared as anomalous events. While no separate immediate recovery action is needed (it is inherent in the event handler itself), anomalous events should nevertheless start a fault diagnoser.
3. While either of the two previous lessons could have improved results in the given situation, the watchdog that finally caught on should have been executed a little more frequently.
4. Event-based control is well suited for post-fault analysis. However, to this end it is necessary to remember which rules were fired when, why, and by whom. This was omitted in order to save computing cycles. Due to this oversight, it wasn't possible to conclude without a grain of a doubt what really had happened during the incident.
5. Similarly, while the smart sensor is equipped with means to download into it programs on the fly, nobody ever thought of the need to upload a program from the smart sensor back into the PC to save it for post-fault analysis.
6. We are confident that the lessons learned from this incident will ensure that the same incident will never happen again. These sorts of experiments will help us increase the reliability of the high-autonomy system until we have a system that is reliable enough for long-term operation on planet Mars. However, we are still far from reaching that ultimate goal.

Future Work: During the next phase, we shall replace the single-tube prototype by a 16-cell prototype. Also, several more electronic valves must be added to the system, and the gas chromatograph needs to be replaced by more modern equipment. This will increase the complexity

of the control task, and consequently, also the fault diagnoser will have to be made more complex than was necessary so far. We shall also add several more watchdogs to improve the reliability of the system.

COMMUNICATION

Until now, the system was operated under local control. However, the system was designed such that it can be easily interfaced to a remote commander for teleoperation. The necessary technology was developed during another NASA funded research activity: the Telescience Testbed Pilot Program (Schooley and Cellier, 1988). At least conceptually, it has already been adapted to the task at hand (Marner, 1990). Figure 7 shows the proposed overall command and control architecture.

Notice our usage of the terms "remote" and "local." We call "local" the plant site, whereas "remote" is used to denote the human commander. This nomenclature comes naturally to control engineers who view their plant as central. Psychologists have a tendency to view the human commander as central, and therefore call that location "local" and the plant site "remote."

At the local (plant) site, the command and control architecture is enhanced by a local "command and communication center" (CCC). The CCC is responsible for communicating with one or several remote controllers and/or observers, receiving their requests, and passing them on to the local controlling computer (LCC) for further processing. It is also responsible for packing telemetry data received from the plant into packages, and mailing them to the remote sites. The CCC can be used to manage several LCCs simultaneously controlling several different pieces of equipment. At the remote end, only one commander is allowed to issue intrusive commands to the plant at any one time. This workstation is called the remote commanding computer (RCC). However, one or several other remote sites can obtain telemetry packages from the plant. They are also allowed to send non-intrusive commands to the plant. These sites are referred to as remote observing computers (ROCs). A key assignment mechanism is used to determine who, among the remote participants, is the commander. The rationale behind this decision is the following: several human experts may be located at several different sites on Earth. If a particular type of expert knowledge is required during a particular phase of the operation the most knowledgeable person will be given the command key, while all other participants become passive observers. They can communicate with the momentary commander through "open microphones." If, during a later phase of the experiment, another participant becomes more knowledgeable, the command key can be passed on to that individual, and the former commander becomes now one of the observers.

Work on this part of the architecture was deferred in order that the automation described

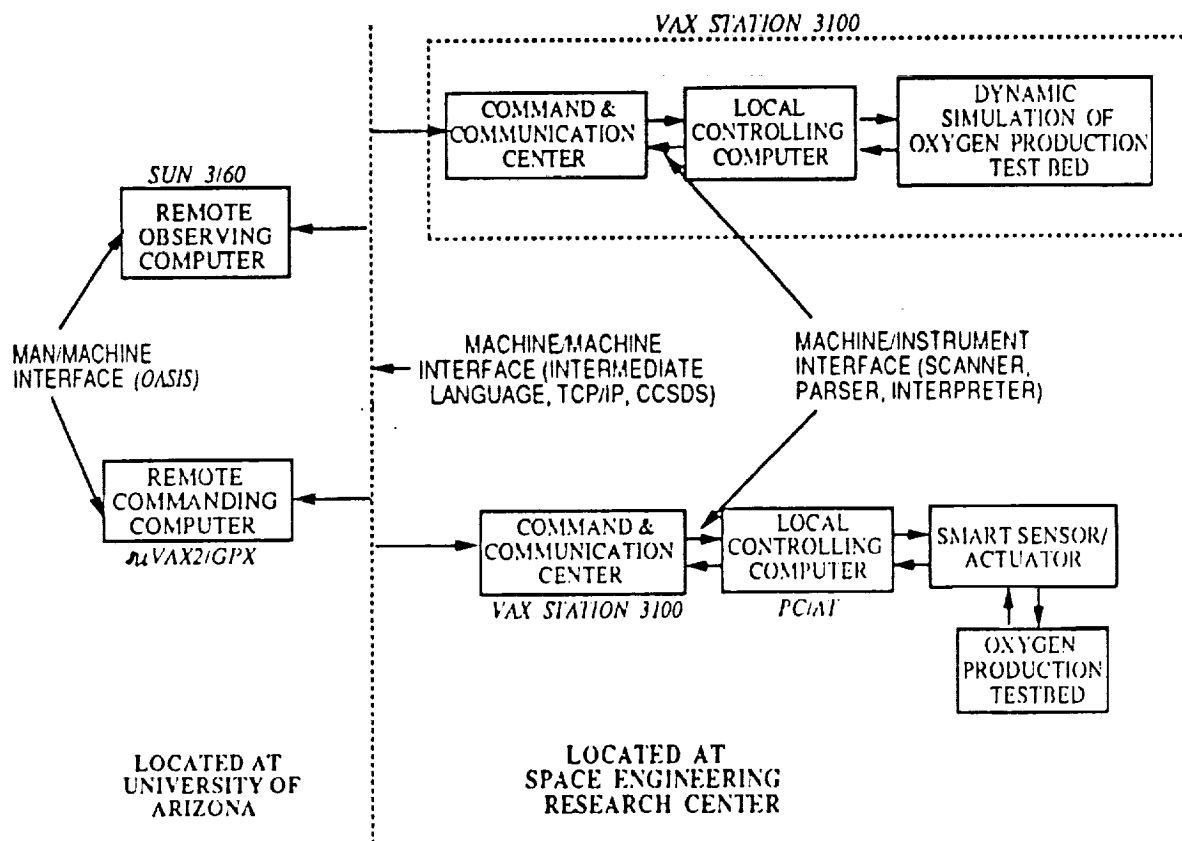


Figure 6: Command and Control Architecture.

above could be installed and tested prior to the 100 hour test. Nevertheless, some progress was made during this reporting period.

The software modifications required to support alternate commanders and multiple observers have been completed. This entailed developing a scheme to assign a key. A key is a pass lent to a user that enables the ability to issue intrusive commands. The other ROCs remain observers. When the current commander is finished with the key, it can be given to another, on a first-come, first-served basis. In this application, mailboxes are used to handle key holder and non-key holder commands. Currently, the only command that can be issued by a non-key holder is a key request, but this will be extended to include requests for data display changes and other non-intrusive commands.

The TCP/IP software is found at the transport layer in the OSI protocol set. The modifications required here involve the actual connections. The previous routines allowed for only one telemetry channel, so another had to be added. The routines also had to be able to associate channel numbers with the key holder and non-key holders. This required interfacing with higher tasks to obtain current key holder information. When presented with an outgoing packet, the scheme had to be able to choose the appropriate channel. These additions have also been completed.

The entire system is currently being tested with a subset of the architecture shown in Figure 6. The MicroVax and SUN workstations located on the main campus serve as alternate RCC and ROC. A VaxStation 2000 located at the Space Engineering Research Center serves as the CCC, and also houses the static simulations of the oxygen plant. As soon as this communication system is demonstrated, the LCC, smart sensor, and prototype oxygen plant will be connected and remotely controlled.

SIMULATION AND MODELING

Three simulation models of the oxygen production system are of particular interest: a static mass flow model, a flow-equilibrium energy balance model, and a complete dynamic model. The static mass flow model is based on conservation of mass principles. The production rate of O₂ and CO depends on the input flow rate of CO₂, and on the efficiency parameters associated with the Zirconia cell and the CO₂/CO separator. From this simulation we can estimate what the production rate of oxygen will be in steady-state, and what various system pressures and temperatures can be expected to be. This model has been completed and tested.

Of course, thermodynamic properties which can greatly affect system operation cannot be determined by this model. For example, we have found that as the Zirconia cell temperature rises, the cell efficiency increases, but if the cell temperature becomes too high (above about 1000C), the cell begins to degrade, thus decreasing system efficiency. In the mass flow model, these effects

can only be included by manually entering new data values for the efficiency parameters.

The flow-equilibrium energy balance model is based on thermodynamic and conservation of energy principles. This simulation shows how different pressures, temperatures, and flowrates vary with the input CO₂ flow rate and with system efficiency parameters. This model has also been completed and tested, but for reasons similar to the above example, it is useful for simulating performance only for small variations from a given set of steady-state conditions.

The third simulation model describes the dynamics of the system, and is based on a modeling and design methodology involving the use of Bond graphs. The use of the Bond graph modeling method is advantageous because the power that moves throughout the system is topologically as well as mathematically represented in the model. This will permit the simulation of startup and shutdown scenarios, as well as large excursions from steady-state operating conditions that might be caused by system anomalies or control system malfunctions.

Work on the dynamic model was deferred in order to concentrate on the timely completion of the automation of the single cell testbed described in the previous section. Some progress has been made, however.

Complete models have been developed for the heater, heat exchanger, and compressor. The models of these components are generally comprised of cell-like elements with similar thermodynamic properties. For example, the physical realization of the heater model consists of a series-connected group of heating elements, which pass heat to gas that flows in a series-connected group of pipe sections. Similarly, the heat exchanger model consists of two groups of connected pipe sections, and the pipe that carries the hotter gas passes heat to the other pipe. Using this "construction-by-cells" modeling approach allows for a high degree of modularity, and the size and thermodynamic properties of the model can be freely and easily varied.

A partial model of the Zirconia cell has been developed. When this model is finished, the different modular components will be connected to form the first dynamic simulation model of the entire oxygen production plant. Simulations will then be run to ensure model validity, and refinements to the model components will be made as necessary. Valuable information can then be learned about system startup and shutdown, and the performance of the system can be easily evaluated for different configurations.

In the next period, the dynamic simulation model will be completed, model validation will be carried out, and the simulation predictions will be used to give insight into which system configuration will result in optimum performance. This dynamic model will also be used as the "world model" in the next generation of artificial intelligence applications for high-autonomy remote supervisory control.

ACKNOWLEDGMENTS

The authors of this paper are only responsible for designing, implementing and testing the intelligent control architecture of the oxygen plant. Many others are involved in the overall project. While this report mainly discusses the design of the high-autonomy architecture, our results would not have been possible without a close cooperation with these other individuals. In particular, we wish to acknowledge the support of Prof. Kumar Ramohalli and his students, as well as of Prof. K.R. Sridhar and his students of the Aeronautical and Mechanical Engineering Department.

Finally, we wish to acknowledge the invaluable contributions of our Ph.D. student SungDo Chi who, while not directly involved with the oxygen plant or even the NASA/UA SERC, has laid the groundwork for the high-autonomy architecture employed in this project. His research was funded through NASA-Ames Cooperative Agreement No. NCC 2-525, "A Simulation Environment for Laboratory Management by Robot Organizations."

REFERENCES

- Chi, S. 1991. "Modelling and Simulation for High Autonomy Systems, Ph.D. Dissertation, Department of Electrical and Computer Engineering, University of Arizona, Tucson, Ariz.
- Chi, S., B.P. Zeigler, and F.E. Cellier. 1990. "Model-Based Task Planning System for a Space Laboratory Environment," Proceedings SPIE Conference on Cooperative Intelligent Robotics in Space, Boston, Mass.
- Kury, P.M. 1990. "An Intelligent Fault Diagnoser for Distributed Processing in Telescience Applications", MS Thesis, Department of Electrical and Computer Engineering, University of Arizona, Tucson, Ariz.
- Marnier, W.J., J.W. Suitor, L.C. Schooley, and F.E. Cellier. 1990. "Automation and Control of Off-Planet Oxygen Production Processes," Proceedings SPACE'90: Engineering, Construction, and Operation in Space, Albuquerque, N.M., Vol.1, pp. 226--235. NASA. 1985. "The Space Station Project."
- Sarjoughian, H.S., F.E. Cellier, and B.P. Zeigler. 1990. "Hierarchical Controllers and Diagnostic Units for Semi-Autonomous Teleoperation of a Fluid Handling Laboratory," Proceedings IEEE Phoenix Conference on Computers and Communication, Scottsdale, Ariz., pp. 795--802.
- Schooley, L.C. and F.E. Cellier. 1988. "Telescience Testbed Pilot Program --- Final Report", NASA Grant NAGW-1073, Technical Report TSL-021/88, Department of Electrical and Computer Engineering, University of Arizona, Tucson, Ariz.
- Schooley, L.C. and F.E. Cellier. 1991. "Modeling, Simulation and Control of an Extraterrestrial Oxygen Production Plant," in Annual Progress Report 1990-91, NASA Space Engineering Research Center for Utilization of Local Planetary Resources, The University of Arizona, Tucson, Arizona, April

1991.

Wang, Q. and F.E. Cellier. 1991. "Time Windows: An Approach to Automated Abstraction of Continuous-Time Models into Discrete-Event Models," *International Journal of General Systems*, in press.

Zeigler, B.P., S. Chi, and F.E. Cellier. 1991. "Model-Based Architecture for High Autonomy Systems," *Proceedings EURISCON'91 --- European Robotics and Intelligent Systems Conference*, Corfu, Greece, June 23--28, 1991.

Quantitative Simulation of Extraterrestrial Engineering Devices

A. Arabyan, P.E. Nikraves and T.L. Vincent

Department of Aerospace and Mechanical Engineering

University of Arizona

Abstract

This is a multicomponent, multidisciplinary project whose overall objective is to build an integrated database, simulation, visualization and optimization package for the proposed oxygen manufacturing plant on Mars. Specifically, the system allows users to enter physical description, engineering and connectivity data through a uniform, graphical interface and stores the data in formats compatible with other software also developed as part of this project. These latter components include programs to simulate the behavior of various parts of the plant in Martian conditions; an animation program which, in different modes, provides visual feedback to designers and researchers about the location of and temperature distribution among components as well as heat, mass and data flow through the plant as it operates in different scenarios; a control program to investigate the stability and response of the system under different disturbance conditions; and an optimization program to maximize or minimize various criteria as the system evolves into its final design. All components of the system are interconnected so that changes entered through one component are reflected in the others.

Quantitative Simulation of Extraterrestrial Engineering Devices

A. Arabyan, P. E. Nikraves and T. L. Vincent

Department of Aerospace and Mechanical Engineering

University of Arizona

(Progress report for 3/1/91 - 8/31/91)

This is a multicomponent, multidisciplinary project whose overall objective is to build an integrated database, simulation, visualization and optimization package for the proposed oxygen manufacturing plant on Mars. Specifically, the system allows users to enter physical description, engineering and connectivity data through a uniform, graphical interface and stores the data in formats compatible with other software also developed as part of this project. These latter components include programs to simulate the behavior of various parts of the plant in Martian conditions; an animation program which, in different modes, provides visual feedback to designers and researchers about the location of and temperature distribution among components as well as heat, mass and data flow through the plant as it operates in different scenarios; a control program to investigate the stability and response of the system under different disturbance conditions; and an optimization program to maximize or minimize various criteria as the system evolves into its final design. All components of the system are interconnected so that changes entered through one component are reflected in the others.

Introduction

The design of complex mechanical systems which are required to operate reliably and autonomously in alien environments is an intricate and iterative process which requires extensive testing in a wide range of hypothetical scenarios. Given the impossibility or the high cost of recreating alien environments on earth, such scenarios have to be generated by computers and applied to simulated versions of the actual mechanical systems. As a result, computer simulation has become an essential and integral part of designing and building mechanical systems to be used in space or extraterrestrial environments.

This specific project was initiated with the aim of providing the essential simulation capability for the oxygen manufacturing plant that the Space Engineering Research Center at the University of Arizona has undertaken to build on Mars. Because of the multidisciplinary nature of the plant's design process, this integrated software project was designed to provide data storage, classification, access and visualization services for all the different groups working on the design and testing of the plant. This project consists of the following principal components

- i) A relational bill of components database;
- ii) A visualization system for animation of the plant's dynamics;
- iii) A control design system associated with data collection equipment connected to an experimental setup;
- iv) An optimization system to maximize specified performance criteria while meeting weight, thermal, cost and other constraints.

The technical features and current status of these principal components are briefly outlined below.

Current Project Status

Relational Bill of Components Database

The design and implementation of the database entry, organization and storage program has been completed. A brief description of the program and its objectives and design philosophy were provided in an earlier progress report [1]. In essence, components of the plant are abstracted into simple functional databases which are then connected in a compatible manner to produce necessary connectivity data to other programs. The program, implemented in the FoxPro 1.02 environment on 80386-based personal computer, now features five different types of components and four different types of connections which can be combined to model virtually any type of physical connection between any two components. The databases for components and connections are being continually improved and updated to include component and connectivity properties that are being encountered in more novel devices (e. g. zirconia-based reduction cells). In addition the database system is now capable of exporting specially-formatted files for an optimization package (see next section).

A complete report about the design and use of the database program has been written and is available at the Computer-Aided Engineering Laboratory [2].

Optimization Software

A new customized software system has been produced to optimize the packaging of the oxygen manufacturing plant. The principal purpose of this system is to ensure that the components of the plant are located relative to each other in such a way that user-defined cost functions are minimized. The system reads all the information it needs about the properties and connections of the components in the plant from the relational database and then relocates the components iteratively until the cost or objective function that has been defined is minimized. At the present time, the objective function consists of a weighted sum of all heat and pressure losses that occur within the plant through radiation between components and from connecting pipes, convection through fluid flow, conduction along pipes and fluid friction within pipes. Because of the different types of losses included in the function, system parameters (e.g. temperatures at desired points or surfaces or pressures at certain inlet or outlet positions) occur in nonlinear form in the function. This function will be modified in the future to include component weights, pipe lengths and costs. The optimization program currently works with nine components which are connected to each other in an arbitrary manner.

Because of the relatively large number of components that the oxygen plant is expected to feature, the probable complex connectivity among them and the unknown nature of constraints or desirable characteristics, a novel method has been used to abstract the state of the system in the space of the variables that are included in the objective function. The optimization program initially constructs a connected graph on the basis of the connectivity and physical property data it obtains from the relational database. This graph consists of nodes that define the state of the system for any configuration and arcs which define paths to other nodes. Each arc emanating from each node is marked as "desirable" or "undesirable" depending on whether it leads to a state that is desirable or undesirable in terms of the objective function. Quantitatively the desirability or undesirability of any given path is represented by a "resistance" value for each arc. The program then tries to traverse the tree in such a way that the "resistance" from the top to the end of the graph is

minimum. This type of abstraction was necessary because it allows the inclusion of system parameters other than physical ones in the procedure.

The program can currently implement various optimization schemes (e.g. bisection or fastest descent methods) to relocate components to their optimal locations while maintaining their connectivity properties. The program's output can be viewed interactively as it searches for the optimal configuration or graphically whereby the program displays the initial (nonoptimal) and final (optimal) configuration of the plant, together with figures for total heat and pressure losses. As of now, the heat and pressure losses in the optimal configuration are guaranteed to be the minimum possible because the program does a brute force search of all possible configurations, but that will not necessarily be the case when the program operates on a full-blown system with many more components than the current nine that are being used as a test bed.

The system is currently being enhanced to export data about the optimal configuration it finds to the relational database program so that it can update its appropriate databases and export them to other programs that make up the integrated system.

A complete report about the design, operation and current status of the optimization program has been written and is available at the Computer-Aided Engineering Laboratory [3].

Visualization/Animation System

The status of this component of this project remains as it was described in the previous progress report [1]. At present the system is being connected by hardware and software links to the relational database. This is being done by reprogramming the relational database program so that it can produce the files that the animation system uses.

Control/Data Collection System

The purpose of this component of the project is to construct a control design and data collection system to investigate the stability, sensitivity and response of the plant system to external disturbances and changes in operating parameters. Progress on this component of the project was limited due to unexpected cuts in funding and subsequent departure of personnel assigned to this task.

Over the next year, this component will be developed to perform data collection and basic control functions and to interact with the relational database and animation and visualization software.

References

1. Arabyan, A., Nikraves, P. E., and Vincent, T. L., "Quantitative Simulation of Extraterrestrial Engineering Devices," NASA/SERC Annual Progress Report 1990-91, APR-91, pp IV-7-12.
2. Krishnasamy, A., Arabyan, A., and Nikraves, P. E., "An Integrated Design Database for the Mars Oxygen Manufacturing Plant," CAEL-91-6, Computer-Aided Engineering Laboratory, Tucson, Az., July 1991.
3. Santhanam, V., Arabyan, A., "Optimization of the Packaging of the Mars Oxygen Manufacturing Plant," CAEL-91-9, Computer-Aided Engineering Laboratory, Tucson, Az., August 1991.

Title
In Situ Materials Processing Systems and Bioregenerative Life Support Systems
Interrelationships

Progress Report
August 30, 1991

By
Robert Frye and George V. Mignon

Abstract

This project is to investigate the synergy and linkages between bioregenerative life support systems and the materials produced by in-situ materials processing systems. Such systems produce a broad spectrum of byproducts such as hydrogen and other volatiles, metals, ceramics, refractories and cements (materials for making shielding, piping and building blocks) and direct products such as O₂. Certain of the processes are capable of generating the chemical components of fertilizers and the base stocks of arable soils. Many of these substances are required by a bioregenerative life support system.

Two phases of work were proposed: an initial bibliographic literature search and an analysis of the requirements of life support and the availability of in situ resources for satisfying these requirements. As this is still early in the development of this project we are currently concentrating on the bibliographic literature search. This is being conducted in several ways. The first is the organization of the extensive literature compiled by Environmental Research Laboratory during its involvement of in the Biosphere 2 project. This material is both of domestic and foreign (primarily translated documents from the U.S.S.R.) origin. It includes both published material and unpublished reports developed for the Biosphere 2 project and other projects associated with controlled environment agriculture by Environmental Research Laboratory staff and consultants. These bibliographies compiled by researchers at Environmental Research Laboratory are being merged and organized. Second, computer based searches of N.T.I.S. documents available have been made and a bibliography compiled. Third, computer based literature searches are being made of the general scientific literature of for any new work on bioregenerative life support system requirements and a bibliography is being compiled. The bibliographies completed will be annotated for the relevance and importance of each document for the project. This first phase of the project is in progress and should be completed by early September.

In addition to the biological system requirements literature search a literature search has been initiated into the types and forms of raw materials available on the Moon and Mars. A detailed assessment of these materials will be conducted in September. We will also be seeking information from the scientific and engineering researchers working on materials processing projects at the UA/NASA SERC/culpr during this time period.

The first phase of this project is basically a literature search and review of new and/or ongoing research in the area of Bioregenerative systems and CELLS type systems. Once the information is

reviewed and collated from both the biological and materials perspective a detailed analysis will follow.

The second phase of the project which includes analysis of the bibliographic materials is just beginning through annotation and collation of the bibliographic material. We have begun to define lists of the bioregenerative life support needs (elements, compounds, life system attributes, quantities of these materials needed, and potential sources for these materials). We anticipate completion of this work in late September.



V. DATABASE DEVELOPMENT



THE STEWARD OBSERVATORY ASTEROID RELATIONAL DATABASE

Mark V. Sykes and Elizabeth M. Alvarez del Castillo
Steward Observatory
The University of Arizona

ABSTRACT

The Steward Observatory Asteroid Relational Database (SOARD) has been created as a flexible tool for undertaking studies of asteroid populations and sub-populations, to probe the biases intrinsic to asteroid databases, to ascertain the completeness of data pertaining to specific problems, to aid in the development of observational programs, and to develop pedagogical materials. To date SOARD has compiled an extensive list of data available on asteroids and made it accessible through a single menu-driven database program. Users may obtain tailored lists of asteroid properties for any subset of asteroids or output files which are suitable for plotting spectral data on individual asteroids. A browse capability has been added allowing the user to explore the contents of any data file. In addition an asteroid bibliography containing about 12,000 references has been incorporated into SOARD. The program has online help as well as user and programmer documentation manuals. Already SOARD has provided data to fulfill requests by members of the astronomical community. SOARD continues to grow as data is added to the database and new features are added to the program.

INTRODUCTION

Asteroids are characterized by their diversity. We study them using a wide variety of remote sensing techniques in an attempt to determine their composition and physical properties, and relate this information to processes effecting asteroids and other solar system bodies over the age of the solar system. Observations are obtained through groundbased telescopes and radar, and spacecraft such as the Infrared Astronomical Satellite (IRAS). These observations are focussed on individual objects of particular interest or dedicated surveys. SOARD incorporates the data obtained from these various observations into a single database.

In order to evaluate and exert some quality control over the data, it is critical to be able to trace each datum to its origin. In addressing scientific issues it is important also to have a knowledge of and access to the existing literature on the subject. Towards this end, SOARD now contains an asteroid bibliography containing about 12,000 references, from the 19th century to the present.

In addition to being objects of scientific investigation, asteroids are potential resources to be utilized in support of the expansion of humans into the solar system. The most accessible of these are the Near Earth Asteroids (NEA's) whose motions around the Sun bring them within reach of low-energy transfer orbits from the Earth. Until recently, the information available on the NEA's has been relatively limited, but with increased rates of discovery and greater numbers of observational programs focussing on these objects, this information is expected to grow rapidly. Since NEA's derive from the main asteroid belt (though some may be extinct comets), knowledge of their source populations provides additional insight into the nature and physical properties of NEA's.

SOARD's goal is to incorporate ALL published asteroid data into one generally accessible database for use in research and in expanding our general and specific understanding of asteroid populations.

SOARD is a menu-driven asteroid database management system which utilizes dBase IV software in a fashion transparent to the user. It allows four basic system outputs at this time: (1) files of designations of asteroids satisfying range criteria for parameters or functions of parameters, (2) subsets of database parameters for subsets of asteroids, (3) files of multiband photometry or spectroscopy for individual asteroids (for plotting), and (4) files of bibliographic references satisfying users' search criteria. Any data file now may be examined using a SOARD browse capability.

SOARD DATA

Table 1 lists the individual data sets which are currently online and accessible through SOARD. It combines ground based observations which were published in ASTEROIDS II, radiometric data collected by IRAS, ancillary IRAS data sets of groundbased polarimetry, lightcurve, and spectroscopic observations, Jeff Bell's 52-color near-IR survey, osculating

TABLE 1. SOARD DATA SETS

ASTEROIDS II

- Proper Orbital Elements
- Taxonomic Classifications
- Family Designations
- Pole Orientations
- Magnitudes, UBV Colors, Albedos, and Diameters

IRAS

- Radiometric Diameters and Albedos
- Individual IRAS Observations
- Polarimetry file
- Lightcurve file
- UBV Observations
- 8-Color Spectroscopy
- 24 Color Spectroscopy

MISCELLANEOUS

- 52-Color Spectroscopy (J. Bell)
- Osculating Orbital Elements (E. Bowell)
- Preliminary Designations and Discovery Circumstances (MPC)
- Photometric Parameters (MPC)
- Proper Elements (Milani and Knezevic)
- Radar Observations (S. Ostro et. al.)

ASTEROID BIBLIOGRAPHY (C. Cunningham)

TABLE 2. DATA SETS IN THE PROCESS OF BEING ADDED

- CCD Spectroscopy (L. McFadden, F. Vilas)
- Near-IR Spectra (Lebofsky, Bus, et. al.)
- Families (Zappala, et. al.)

orbital elements for 17,415 asteroids, discovery information and photometric parameters published through the Minor Planet Circulars (MPC), ground based radar observations, and 11,961 literature references. As data is incorporated into SOARD, it receives a reference to its source in the literature which is listed in the bibliography file. This provides online information on the origin of the data and allows maximum understanding of data quality. Data evaluation is critical to its use in an engineering context.

SOARD REFERENCE CAPABILITY

SOARD has acquired and incorporated Clifford Cunningham's asteroid bibliographic reference file. Cooperation over the last eight months has led to suggestions for expansion of his original file. Fields which have been added include a keyword field and a field which lists the asteroids to which the reference pertains. This expansion which has been implemented already for the major journals and for recent publications is currently a part of SOARD. Full implementation for all citations is expected to take a longer time. Cliff Cunningham has been very helpful in agreeing to alter his file format so that it is more compatible with SOARD requirements. Although he is marketing his database as a salable product, he has generously given permission to distribute it as part of SOARD to the test sites. In its implementation in SOARD, a user can search the reference file by author, title, date, publication, keyword, asteroid numbered designation, some subset of authors or words in a title, or any combination of these parameters. We regard this utility as a powerful addition to SOARD and will seek to contract with Clifford Cunningham in developing a licensing agreement.

UPDATING THE DATABASE

SOARD is expanding to include the data sets listed in Table 2. Some of the data such as CCD spectroscopy of certain asteroids has been published. Some data is collected and needs to be reduced and published. Monthly updates to SOARD include data available through literature searches, data sent by individual observers, and data obtained from the Minor Planet Circulars (MPC). Ongoing observations and research promise a continually growing body of data which will be added to SOARD.

EXPANDING SOARD

Additional programming will expand the features available through SOARD. A fourth main menu item will allow the user to concatenate functions of asteroid parameters. If a file contains orbital elements such as semi-major axis and eccentricity, the user may calculate the perihelion distance as an output parameter of specific interest. This feature will minimize data which must be distributed with the system while allowing the user maximum choice for customized output of asteroid parameters.

Another main menu item being investigated is the ability to run external code. Specific programs such as code to generate ephemerides, to run standard thermal models, or to calculate magnitudes would be accessible without leaving the main SOARD program. Files generated through SOARD would be available for direct input into the external code and the output of the external code would be in a form accessible to SOARD.

TESTBED ACTIVITIES

The program has online help as well as user and programmer documentation manuals. SOARD has greatly expanded its testbed activities to include the following sites: the California Space Institute in La Jolla, California (Dr. Lucy-Ann MacFadden); the Institute for Astronomy in Honolulu, Hawaii (Dr. David Tholen); the Lunar and Planetary Laboratory at the University of Arizona in Tucson, Arizona (Dr. Larry Lebofsky and Ellen Howell), and the Park School in Brookline, Massachusetts (Dr. Linda French). A transportable execution version of the relational database has been distributed to these sites to test without the assistance of prior tutoring but with the help of online documentation only. Already they have provided substantial input into the overall user friendliness of the system and made suggestions for improving the SOARD environment. With the addition of a test site at the Park School the educational applications of SOARD at the pre-collegiate level are being explored.

COMMUNITY SUPPORT

We respond to all moderate requests from the community and have provided data in support of observing, research, and teaching programs. For instance, this past April SOARD supplied pedagogical materials for the University of Arizona's Steward Observatory run Adult Space Camp and was subsequently asked to provide similar materials for the Beginning and Advanced Teen Space Camps in June.



Near-Earth Asteroids:

Observer Alert Network and Physical Observations

Donald R. Davis and Clark R. Chapman

Planetary Science Institute

Abstract

The Planetary Science Institute (PSI) developed a communication network to alert observers of newly discovered near-Earth asteroids (NEAs). This network is intended to encourage observers to obtain physical observations of NEAs, which are needed in order to characterize and assess the resource potential of these bodies. This network was declared operational in October, 1990 via an announcement to the asteroid observing community. Unfortunately, funding was discontinued by SERCuplr after February, 1991, due to bureaucratic problems, and we have barely been able to keep the network functioning since then. We propose to fully re-establish our network which we have expanded in recent months to include European observers. We also propose to capitalize on recent upgrades to the Tumamoc Hill Observatory and establish an observing program to acquire spectrophotometric colors on newly discovered near-Earth asteroids that require a rapid response time.

Task 1: Observer Alert Network

Near-Earth asteroids are being discovered at an increasing rate; however, usually only a preliminary orbit and an estimate of the brightness of the asteroid is obtained during the discovery apparition. This is due to the brief interval (typically days to weeks) that the asteroid is bright enough to be observed by workers at 1-2 meter class telescopes. Unfortunately, it is usually several years before a newly discovered NEA makes another close approach to Earth; thus little is known about the physical properties of NEAs until long after their discovery and no physical data at all exist for most NEAs. However, as NASA is becoming increasingly interested in NEAs as potential mission targets and as a source of resources for expanded space activities, it is essential to learn more about these bodies as early as possible in order to meet the needs of the space program.

The importance of timely observations during the discovery apparition was recently emphasized by Wisniewski of the Lunar and Planetary Laboratory, who found that over the next few years, roughly twice as many newly discovered NEAs will be bright enough for physical observation as there will be "old" NEAs this bright. The Planetary Science Institute established an Observer Alert Network in October, 1990; Appendix A contains the announcement letter that was sent to 111 observatories and individual observers. We have twenty observers on our active list that we communicate with whenever an appropriate NEA is discovered. We also assist in alerting observers of the need to obtain positions of high priority newly discovered fast moving objects, both prior to and following the release of an IAU circular. In the ten months following establishment of our network, we have responded to eight requests to alert observers via the network.

The number of active observers continues to increase, although not as fast as the number of newly discovered NEAs is increasing. This past summer, for example, we interested Dr. Alan Fitzsimmons of the Dublin Observatory in the problem of acquiring physical observations of NEAs. He carried out a test run, following alert by our Observer Alert Network in August 1991, to acquire a spectrum of the newly discovered asteroid 1991OA using the 2.5m telescope at La Palma. We were just informed that the spectrum was acquired and that our test was successful. Buoyed by this success, Dr. Fitzsimmons will propose to establish a target-of-opportunity program to acquire spectra of as many newly discovered NEAs as possible in the future. His program is the only major European participation in the observer network at this time, but we hope that other individuals and institutions will become interested as they learn more about near-Earth asteroids.

We propose to continue operation of the Near-Earth Asteroid Observer Alert Network and to further expand efforts to add international observers in order to enhance the acquisition of physical observations during the discovery apparition.

Task 2: Physical Observations of Newly Discovered Near-Earth Asteroids

The resource potential of Near-Earth Asteroids is well recognized, but what is lacking for most of these objects are physical observations that will aid in identifying the possible compositions of these bodies. This problem has been widely recognized and was discussed at the recent conference on NEAs held in San Juan Capistrano this past summer; however, the question of how to actually increase the physical observation rate was not resolved. The major problem with obtaining observations is that newly discovered NEAs are usually observable for at most a few weeks following their discovery and unless an asteroid observer just happens to have telescope time with an appropriate instrument and is willing to divert time from his/her officially approved program to try to obtain physical observations of the newly discovered body, then it will not be observable until its next close approach, which often does not occur for many years.

Because of these factors, good physical data exist for very few NEAs. At this time, there are no observational programs devoted to acquiring physical observations of NEAs during their discovery apparition on a regular basis. Ostro attempts to obtain radar observation of NEAs that come close to Earth; however, this is only a small fraction of the total number discovered in any given year and is only one of the several complementary techniques necessary for inferring NEA mineralogy.

We propose to capitalize on recent developments in the past year that have made the Tumamoc Hill Observatory a potentially usable site for obtaining physical observations for many NEAs. This 20" telescope has been used only sporadically in the past, due to the lack of instrumentation, the poor state of the tracking and acquisition system, and the bright sky at the observatory which is located at the western edge of the city of Tucson. However, many of the difficulties have been corrected in the past year: 1) Photometric Corporation, Ltd., has loaned a CCD camera and controller to the Observatory and this instrument is now permanently mounted on the telescope. 2) The University of Arizona (S. Larson) provided a computer for data acquisition and storage. 3) Encoders are being added to the drive to aid in pointing the telescope and in acquiring faint objects. 4) The Planetary Science Institute provided a rack and pinion dome drive. All of these improvements are either in place or will be in place in the next few weeks. Tests by S. Larson have already established that a 19th magnitude(V) star can be detected with this CCD/telescope using a 2 minute integration time.

We propose to test this telescope and CCD camera to see if it is suitable for acquiring spectrophotometric colors(in the 8-color system of Tholen) for newly discovered NEAs. Not all of the 8 colors will be observed, as studies by Britt have shown that 5 or 6 of the 8 colors are adequate to reliably classify most of the asteroids. Taxonomic classification will indicate if an object

is unusual or particularly interesting and should be pursued with further high resolution infrared spectra which is needed to obtain band information required for detailed compositional information. We will test the system to determine the quality of colors that can be measured using known asteroids whose colors have been measured. We will also take data on newly discovered NEAs which are sufficiently bright to be observed with this system. We will also develop procedures for obtaining colors using a CCD system to observe rapidly moving objects.

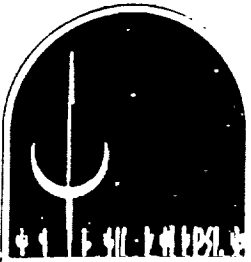
During the year 1991/2 we will develop procedures to determine what the real capabilities of this telescope/CCD system are for observing NEAs. If it proves to be as useful, then Tumamoc Hill will be a major asset for NEA studies since it is conveniently located for rapid response to newly discovered objects. Telescope time will be available since there are few observers using this telescope and priority will be given to time critical observations. Thus we expect that this project could provide a major new source of physical observations on newly discovered NEAs that will enable us to better assess the resources available in this population of solar system objects.

REFERENCE

Lagerkvist, C.-I., et al. (1988). *Asteroid Photometric Catalogue: First update*. Consiglio Nazionale Delle Ricerche: Rome.

APPENDIX A

Announcement: Notification Network for Physical Observations of Near-Earth Asteroids



Planetary Science Institute

Announcing...

Notification Network for Physical Observations of Near-Earth Asteroids

The Planetary Science Institute wishes to announce that, effective 29 October 1990, we will be operating a network designed to alert observers concerning especially interesting near-Earth asteroids for which *physical observations* are desired. The service is supported by the NASA/University of Arizona Space Engineering Research Center for the Utilization of Local Planetary Materials. The effort is headed by Dr. Donald R. Davis, with participation by Dr. Clark R. Chapman and Mr. David H. Levy.

We solicit the names and communications channels for all observers interested in being notified about important near-Earth asteroids. We will be asking them, and major observatories, to provide us with advanced observing schedules so that we will know who to contact when an important object is discovered. We will also ask the individuals who work on discovering Earth-approaching objects to notify us when particularly important objects are discovered, and we will also be regularly checking the *IAU Circulars*.

We will notify observers concerning unusually important objects for which physical observations are desired. We will give priority to those objects that (a) are likely radar targets, (b) have B brighter than 15, (c) will be well-placed for a short but adequate duration to make physical observations possible but timely notification desirable, (d) have sufficiently good orbits/ephemerides to make acquisition fairly reliable, and (e) have other unusual traits of particular interest. We anticipate, based on unofficial, partial operation of this service during the past year, that an object might meet our criteria every month or so.

The service will be an *active* supplement to the normal IAU announcements of discoveries. We encourage observers to subscribe directly to the *IAU Circulars* and to check them regularly. If you hear from us, you will know that the object is deemed to be particularly important and that an "observing campaign" is underway. We thereby hope to enhance the quantity of physical data available for these important objects that often fade so rapidly. We will be coordinating with Dr. Brian Marsden of the IAU Central Bureau to ensure that our alerts are based on sound orbits, in order to minimize wasted time at the telescope. We will be evaluating the effectiveness of the network after seven months of operation.

Our goal is to alert observers within twelve hours of when we receive notice of an important discovery (usually morning, Mountain Standard Time) but certainly within 48 hours; our response may be slower on weekends and holidays than on normal workdays. We will check *IAU Circulars* and our phone messaging service once a day, including weekends. We will send announcements out by electronic mail and telephone. While our primary goal is to alert physical observers, we will also assist when needed to alert astrometric observers about critical needs for positions.

If you have questions or suggestions about the service, or if you wish to sign up, please contact:

Dr. Donald R. Davis
Planetary Science Institute
2421 East Sixth Street
Tucson AZ 85719 USA

Telephone: 602/881-0332 (Logistical details can be handed by Ms. Elaine Owens at this number; during off-hours, a 24-hour message service is in operation for this telephone number.)

E-mail: PSKEY::PSKEY (on SPAN)

Fax: 602/881-0335

19 Oct 1990

